Alma Mater Studiorum

Università degli Studi di Bologna

FACOLTÀ DI INGEGNERIA

DIEM - Dipartimento di Ingegneria delle Costruzioni Meccaniche, Nucleari, Aeronautiche e di Metallurgia

SCUOLA DI DOTTORATO IN INGEGNERIA INDUSTRIALE

Dottorato di Ricerca in **Meccanica dei Materiali e dei Processi Tecnologici**

XIX Ciclo

Settore scientifico disciplinare:

ING-IND/14: PROGETTAZIONE MECCANICA E COSTRUZIONE DI MACCHINE

SIMULATION MODELS IN BIOMECHANICS AND EXPERIMENTAL MECHANICS

Ph.D. Thesis

MODELLI DI SIMULAZIONE NELLA BIOMECCANICA E NELLA MECCANICA SPERIMENTALE

Dissertazione finale

Autore

Dott. Ing. Barbara Reggiani

Coordinatore

Chiar.mo Prof. Ing. Tullio Trombetti

Relatori

Chiar.mo Prof. Ing. Luca Cristofolini

Chiar.mo Prof. Ing. Gabriele Vassura

Chiar.mo Prof. Ing. Alessandro Freddi

Esame finale anno 2007

Table of contents

Chapter 3 ***Surveying on the flexural stiffness of a close-wound coiled spring for a novel joint of robotic hands by means of the Finite Element Method***

Chapter 4 **A contribution to the method of the fatigue life prediction in components by local stress concept**

Indice

Capitolo 3 <u>***Indagine sulla rigidezza flessionale di una molla in configurazione a pacco per un nuovo giunto di mani robotiche attraverso il metodo agli Elementi Finiti***</u>

Capitolo 4 ***Un contributo al metodo della predizione della vita a fatica in componenti basato sul concetto di tensione locale***

Chapter 1

Introduction

Introduzione

Presentation and contents of the work

"Simulation model" is a general term that indicates computational and analytical tools able to cope, characterize and predict physical events.

To date, in the engineering field, computational mechanics has been enormously successful allowing the simulation of complex physical events and the use of sophisticated simulation tools to design engineering systems.

In this direction, the Finite Element Method has played a fundamental role showing an unprecedented predictive power. Complex real systems can now be modelled by discretized versions of the theories of mechanics which are amenable to digital computation.

The common effort is to improve the computational tools in order to limit the role of experimentation to a preliminary value of comparison. Nevertheless, the crucial importance of experimental tests is still recognized. The sentence "simulation models in experimental mechanics" in the title of this work, although apparently contradictory, just refers to this still needed methodological synergy.

The present thesis shows three applications of the computational mechanics in the fields of biomechanics, robotics applied to biomechanics and in problems related to the fatigue life predictions.

An exciting modern area of computational mechanics applicability under development is the predictive surgery. In the ***2nd Chapter*** is presented the FE model of an implanted cementless hip stem purposely-developed to allow the surgeon to estimate the primary stability during the pre-operative planning.

In the ***3rd Chapter***, in the context of a novel solution of robotic hands made with compliant mechanisms, the flexural stiffness of a close-wound helicoildal spring is investigated by means of the FE Method.

The latest part of this work, in the ***4th Chapter,*** aims to assess a modern formulation proposed in literature to predict the local fatigue life of complex components with uneven stress distributions with the aid of the FE method.

An attractive future application of this work could be the fatigue life prediction of the joint of robotic hands made with close-wound helicoidal springs by means of the analytical-numerical method assessed by means of the FE analysis.

Presentazione e contenuti del lavoro

"Modelli di simulazione" è un termine che vuole genericamente indicare strumenti analitici e computazionali sviluppati per predire e caratterizzare eventi fisici.

Nel campo dell'ingegneria, alla meccanica computazionale, è stato riconosciuto un enorme successo, la stessa permettendo la simulazione di complessi eventi e sistemi fisici reali altrimenti difficilmente analizzabili.

In questa direzione, il Metodo agli Elementi Finiti (MEF) ha giocato un ruolo fondamentale mostrando un potere predittivo senza precedenti. Sistemi reali continui complessi possono ora essere modellati attraverso versioni discretizzate delle teorie della meccanica accessibili tramite calcolo digitale.

Obiettivo è quello di un progressivo miglioramento degli strumenti computazionali ad oggi in uso con lo scopo di limitare il ruolo di una comunque sempre onerosa (in termini di costo e tempi) sperimentazione al solo valore preliminare di confronto. Tuttavia, ad oggi, viene ancora attribuita e riconosciuta una cruciale importanza alla fase sperimentale. L'espressione "simulation models in experimental mechanics" nel titolo della Tesi presentata, sebbene apparentemente contraddittorio, vuole riferirsi proprio a questa ancora forte esigenza di sinergia metodologica.

Il presente lavoro mostra tre applicazioni della meccanica computazionale nei campi della Biomeccanica, della robotica applicata alla Biomeccanica ed in problemi di predizione della vita a fatica di componenti.

Una recente stimolante applicazione della meccanica computazionale è la chirurgia predittiva. Nel ***Capitolo 2*** *viene presentato un modello FE di un impianto di protesi d'anca non cementata sviluppato con lo scopo ultimo di fornire al chirurgo uno strumento di predizione della stabilità primaria in fase di pianificazione pre-operatoria.*

Nel ***Capitolo 3****, nell'ambito di una nuova soluzione di mani robotiche realizzate con meccanismi compliant, viene investigata, attraverso il metodo agli Elementi Finiti, la rigidezza flessionale di una molla in configurazione a pacco.*

L'ultima parte di questo lavoro, nel ***Capitolo 4****, è finalizzata alla valutazione e verifica di una moderna formulazione proposta in letteratura per predire la vita a fatica locale di componenti complessi con qualunque distribuzione irregolare di tensione con l'aiuto del metodo FE.*

Un'attraente applicazione futura di questo lavoro potrebbe configurarsi nella predizione della vita a fatica del giunto della mano robotica con molle a pacco tramite il metodo numerico-analitico verificato proposto in letteratura.

Chapter 2

The primary stability of a cementless hip stem: A Finite Element simulation model

Stabilità primaria di un
impianto protesico d'anca non cementato:
un modello di simulazione agli Elementi Finiti

Chapter 2.1

Introduction

The ultimate goal of this work was to develop numerical models that allow the surgeon to estimate the primary stability ***during*** *the pre-operative planning session. Finite element models accounting for patient and prosthetic size and position as planned by the surgeon have been validated.*

For this purpose, the finite element model of a cadaveric femur was generated starting from the CT scan and the anatomical position of a cementless stem derived by a skilled surgeon using a pre-operative CT-based planning simulation software. In-vitro experimental measurements were used as benchmark problem to validate the bone-implant relative micromotions predicted by the patient-specific Finite Element model. In addition, the sensitivity of the primary stability prediction to the differences observed between the planned and the achieved pose was also verified. The present study confirms that it is possible to accurately predict the level of primary stability achieved for cementless stems using numerical models that account for patient-specificity and surgical variability. It also confirmed that while the implant position does have an effect on primary stability, the estimate we can get from the planned position provides a correct order of magnitude for the bone-implant relative micromotion.

Scopo ultimo di questo lavoro era lo sviluppo di modelli numerici che consentano al chirurgo di stimare la stabilità primaria durante la sessione di pianificazione pre-operatoria. Nel presente lavoro sono stati validati modelli agli Elementi Finiti che tengano conto della specificità del paziente così come della taglia e della posizione dello stelo della protesi d'anca come pianificate dal chirurgo.

Il modello agli Elementi Finiti di un femore di cadavere è stato generato a partire da dati di tomografia computerizzata. La posizione anatomica di uno stelo non cementato è stata derivata da un chirurgo esperto tramite un software di simulazione di pianificazione pre-operatoria basato su dati TC. I micromovimenti relativi protesi-osso predetti dal modello FE "subject-specific" sono stati validati su dati sperimentali in-vitro. In aggiunta, si è proceduto alla verifica della sensibilità della predizione della stabilità primaria alla posizione dello stelo pianificata ed ottenuta.

Il presente studio conferma come sia possibile la predizione accurata del livello di stabilità primaria ottenuto per steli d'anca non cementati utilizzando modelli numerici che considerino la variabilità del paziente e della tecnica chirurgica. Viene inoltre confermato che mentre la posizione dell'impianto ha un effetto sulla stabilità primaria, la stima che possiamo fare a partire dalla posizione pianificata fornisce un corretto ordine di grandezza dei micromovimenti relativi osso-protesi.

Chapter 2.2

Why this study? An overview to the state of the art

In this chapter the evolution of the knowledge and of the techniques of surveying for the prediction of the primary stability in cementless hip implants is presented. Attention is paid on the crucial meaning of an accurate pre-operative prediction of the primary stability, context in which the contribution of this study wants to be inserted.

Nel presente capitolo viene presentata l'evoluzione delle conoscenze e delle tecniche di indagine per la predizione della stabilità primaria di impianti protesici d'anca non cementati.

Viene data attenzione al ruolo cruciale di un'accurata predizione pre-operatoria della stabilità primaria, contesto nel quale vuole inquadrarsi il contributo di questo studio.

The term *primary stability* usually refers to the bone-implant relative micromotions induced by the physiological joint loading that occur immediately after the operation before any biological process takes place. It means that the primary stability merely presents mechanical characteristics differing from the so-called secondary, or long-term, stability which is the micromotion under load once the biological adaptation process is completed.

The implant of an uncemented hip stem into the femoral medullary cavity consists of six main steps (Figure 2.1) and the steadiness with which a cementless stem is stabilized against the host bone during the operation (that's the primary stability) is a critical factor for the success of the operation.

The most common reason for the aseptic loosening of cementless hip prostheses is the lack of primary stability (Maloney et al., 1989; Manes et al., 1996; Philips et al., 1990; Sugiyama et al., 1989). Excessive relative micromotion at the bone-implant interface may inhibit the bony in-growth and the secondary long-term fixation (Burke et al., 1991; Schneider et al., 1989a), promoting the aseptic loosening of the implant (Pilliar et al., 1986; Søballe et al., 1993a,b), which is the primary factor of failure for cementless hip stems (Manes et al., 1996; Stea et al., 2002; Various Authors, 2004, 2005a, 2005b) (Table 2.1).

	Number of events	%
Aseptic loosening	16,730	59.7 %
Dislocation	3,109	11.1 %
Deep infection	2,435	8.7 %
Periprosthetic fracture	1,944	6.9 %
2-stage procedure	1,172	4.2 %
Miscellaneous	1,027	3.7 %
Technical error	901	3.2 %
Implant fracture	399	1.4 %
Pain only	290	1.0 %
Secondary infection	1	0.0 %
(missing information)	37	0.1 %
Total	**28,045**	**100 %**

Table 2.1: Reasons for revision of the primary operation from 1979 to 2004 (Swedish National Hip Arthroplasty Register)

Undesirable high bone-implant relative micromotion could actually lead to a looping degenerative process that prevents the osseointegration:

- only a small fraction of the stem surface is in contact with the completely mineralized bone tissue; the rest of the implant is in contact with different types of soft tissue, mainly marrow or blood;

- up on the extension and localization of the soft tissue, the mechanical stability of the stem could be reduced leading to excessive bone-implant relative micromotions under physiological loading;

- excessive micromotions prevent the calcification process leading to a tissue differentiation and increasing the fibrous tissue extension at the bone-implant interface with the main effect of increasing the micromotions.

The described aseptic loosening process thus involves both mechanical (stresses and micromotions) and biological (fibrous tissue formation) factors.

A relevant number of experimental works estimated the amount of micromotions and shear stress that could prevent the osseointegration. While a number of studies (Engh et al., 1992; Maloney et al., 1989) analysed the achieved bone-implant interface conditions without affecting the natural process, other works (S∅balle et al., 1991, 1992, 1993, 1994; Pilliar et al., 1985, 2001; Bragdon et al., 1996; Jasty et al., 1997) a priori imposed the boundary conditions of the implant (stress and micromotions) then estimating the consequences.

Engh (Engh et al., 1992) and Maloney (Maloney et al., 1989) carried out studies on human cadaveric femora assessing the micromotions amount compatible with the osteointegration process. Under simulated physiologic loading (single-limb stance, stair climbing), micromotions between the implant and the bone were measured using electrical displacement transducers. In the former study, 13 of 14 implanted femora were found osteointegrated measuring a peak micromotion of 40 μm; for the single case of failed bone ingrowth it measured 150 μm. All the 11 femurs analysed by Maloney et al. were osteointegrated.

Contemporary studies (Søballe et al. 1991,1992,1993,1994) were conducted on dogs to study the influence of micromovements on bony ingrowth in titanium alloy and hydroxyapatite coated implants. An ad-hoc device producing movements of 500 microns during each gait cycle was developed. The implants were inserted into all 4 femoral condyles in each of 7 mature dogs. After 4 weeks histological analysis revealed the nature and the amount of tissue on the interface bone-implant showing that micromotions among 150-500 μm were associated with fibrous tissue.

By use of similar device, Pilliar (Pilliar et al., 1985, 2001) proved that relative micromotions lower than 50 μm allow bone-implant osteointegration while the histological analysis conducted by Jasty (Bragdon et al., 1996; Jasty et al., 1997) on mature dogs revealed that at a value of 20 μm the interface tissue is osteointegrated; for a value between 20 and 40 μm the tissue is fibrous- cartilaginous and for an imposed value over 150 μm the tissue is fybrotic.

Conversely, excessive press fitting may produce intra-operative bone fractures (Fishkin, et al., 1999; Schwartz et al., 1989; Taylor et al., 1978) which are known to drastically reduce the primary stability (Monti et al., 2001).

To achieve a good level of primary stability the surgical technique plays a fundamental role. An inaccurate implant size and/or position, creating a potentially unstable condition, may result in the formation of a fibrous tissue layer around the prosthesis deteriorating the mechanical characteristics of the interface. Hence, the amount of relative micromotion that the physiological loads will induce at the bone-implant interface would be an essential information for the surgeon while he or she is planning a cementless total hip replacement.

Thus, it would be extremely useful to know in advance what it would be the primary stability achievable with a *certain stem size* in a *certain position* for a *specific patient*.

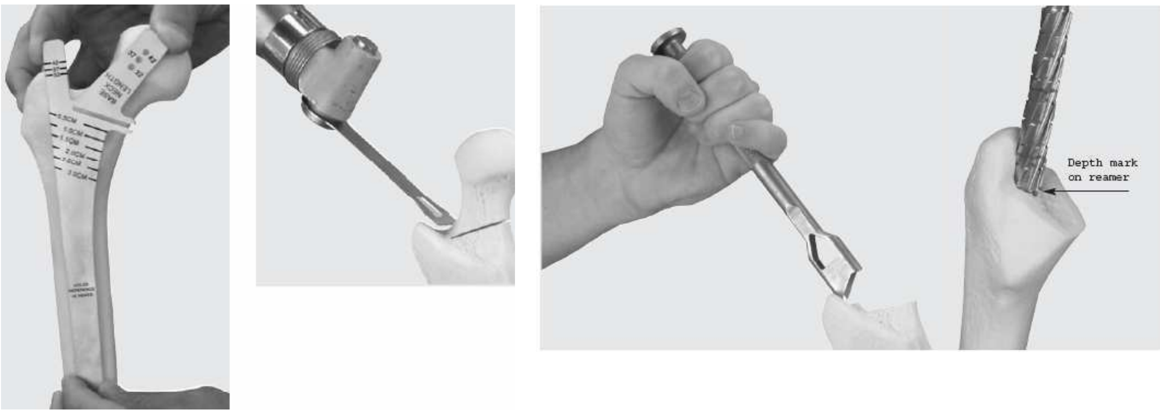

a) Femoral neck resection *b) Femoral canal preparation*

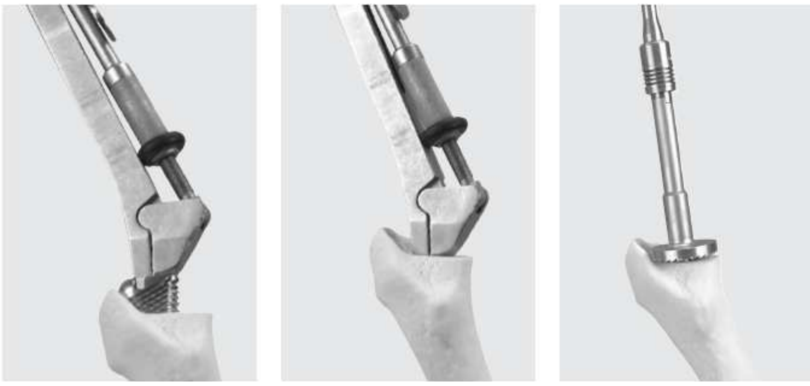

c) Broaching/ Calcar preparation

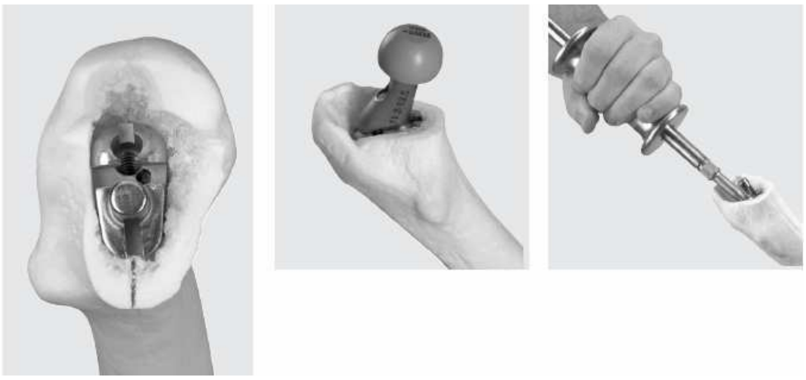

d) Trial reduction

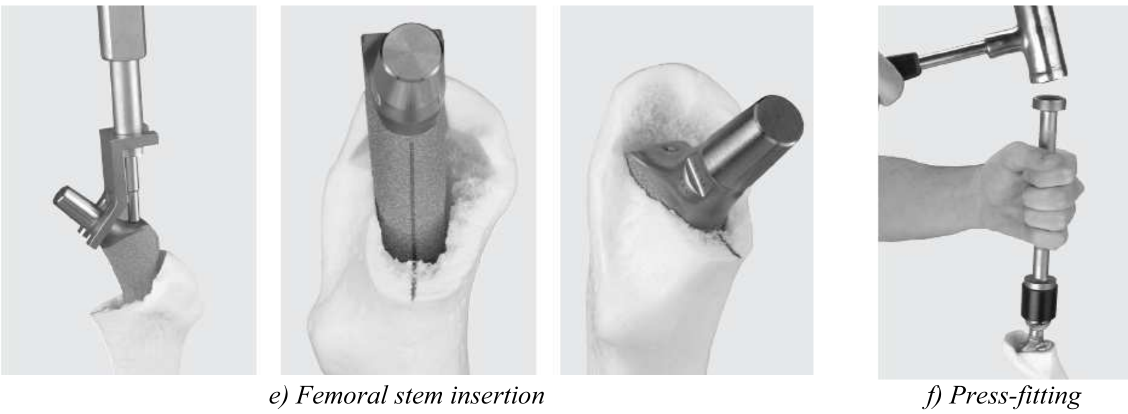

e) Femoral stem insertion *f) Press-fitting*

Figure 2.1: Steps of the implant of an uncemented hip stem into the femur medullary cavity
(Images taken from "Perfecta Rs femoral Stems-Surgical Technique, Wright Medical Technology, Inc)

In the last few years, computer-based protocols of pre-clinical evaluation of joint prostheses have remarkably improved and Finite Element Method (FEM) has become a widely used tool by researchers in assessing the level of achieved primary stability. This is an attractive opportunity to train the surgeon to reliably assess operative planning.

The first application of the Finite Element method in orthopaedic (Huiskes et al., 1983) dates from 1972 (Brekelmans et al., 1972).

Contrary to experimental methods, fully validated finite element models can provide a complete map of the interface micromotions (Dammak et al., 1997; Tissakht et al., 1995) showing the location of the peak value. A number of studies have extensively analysed the interface modelling parameters (Bernakiewicz et al., 2002; Viceconti et al., 2000), and the level of accuracy needed to predict the primary stability of cementless hip implants was established (Viceconti et al., 2000). Similar works were carried out for the pelvic component (Spears et al., 2001). The impact of inaccurate implant positioning on various biomechanical indicators has been investigated (Viceconti et al., 2004b). A statistical finite element analysis recently demonstrated that, over a simulated population of 1000 cases, a mismatch up to 1 mm between the stem and the host bone at random locations of the interface is sufficient to produce a grossly loosened stem in 2% of the patients, while for another 3-5% the high level of predicted micromotion is likely to prevent any substantial osseointegration (Viceconti et al., 2005). These figures are surprisingly close to the failure rate for aseptic loosening reported in the most recent outcome reports (Stea et al., 2002; Various authors, 2003).

From these results it appears important to make sure that the prosthetic component perfectly fits the host bone, in order to further improve the clinical outcomes of cementless total hip replacement. However, even using one of the most sophisticated CT-based pre-operative planning software, the Hip-Op software, (Lattanzi et al., 2002) the repeatability of the anatomy-based implant sizing for the same patient by the same surgeon is worse than 1 mm (Viceconti et al., 2003). We may conclude that the surgeon needs to know not only the anatomical information but also the functional/biomechanical information in order to take the proper clinical decision; in this case the surgeon needs to know the primary stability of the cementless component.

This need can be addressed in two ways. Intra-operatively, using adequate measurement tools (Cristofolini et al., 2002a, Cristofolini et al., 2002b; Cristofolini et al., 2006; Varini et al., 2004). Pre-operatively, using numerical simulation models able to estimate the primary stability that the planned prosthetic size, placed in the planned position, will have under physiological loads. But, to date, in our knowledge, none of the pre-operative planning software applications currently available on the market is able to predict the primary stability.

Moreover, even though the latest progresses in the field of the computer aided surgery allow a perfect surgical planning, there is still the practical problem of the correct positioning of the stem in the femur during surgery. Thus a fundamental question arises: is the prediction of primary stability obtained on the planned pose (position and orientation) representative of the stability we should expect *in vivo* where the prosthesis will be placed in a different position?

The *planned-Vs-achieved accuracy* (PVA) may be higher for computer aided procedures (DiGioia et al., 1998) or lower for conventional, unassisted procedures (Lattanzi et al., 2003), but some differences will always be there. What we predict during planning is not exactly what it will be achieved in the operative room.

The ultimate goal of this research work was to develop numerical methods designed in a way that allows the surgeon to estimate the primary stability *during* the pre-operative planning session, possibly in an interactive environment that permits to explore various configurations and pick the best one. Specifically, this paper focuses on the development and validation of patient-specific finite element models created using the CT-scan data and the planned position.

Finite element models predicting bone stresses and strains of specific patients can be generated starting from the same CT scan that some surgeons use to plan the operation (Taddei et al., 2003). These *patient-specific* modelling protocols provide the automation, accuracy, robustness and generality required by clinical applications (Viceconti et al., 2004a). However, the possibility to develop an implanted model starting from a pre-operative CT scan and a CT-based pre-operative planning defining the stem position has never been explored. Moreover, this can be considered as the first attempt where experimental micromotions prediction are validated against measurements in a cadaver specimen.

Furthermore, once the accuracy of a subject-specific finite element model in predicting the primary stability of a cementless stem had been investigated, the present study aimed also to establish if the prediction made on the pre-operative pose is representative of the primary stability that will be achieved intra-operatively. Specifically, we investigated the sensitivity of the prediction of primary stability to the difference in pose between the planned and the achieved configurations.

Chapter 2.3

The Finite Element modelling of the intact femur

The procedure used to generate the Finite Element model of the femur from CT-data before the hip stem implant is presented.

The error technique adopted to verify the numerical accuracy of the FE model is also shown together with the results of the convergence test.

Viene presentata la procedura utilizzata per generare il modello agli Elementi Finiti del femore prima dell'impianto della protesi a partire da dati di tomografia computerizzata.

Si mostrano inoltre la tecnica dell'errore adottata per verificare l'accuratezza numerica del modello FE ed i risultati dell'analisi di convergenza del modello.

An intact right cadaver femur of a 69 years old female donor (specimen lab code #78) was scanned in the transverse direction with a Computed Tomography (CT) system (mod. HiSpeed, General Electric Co., USA). A scanning protocol specifically designed to optimise the 3D reconstruction and to maintain the same radiation level of conventional protocols (Lattanzi et al., 2004) was used. The CT exams were taken in the helical mode, with the slice thickness set to 3 mm in the epiphyseal regions and 5 mm in the diaphyseal regions, and with a pitch of 1.5. The CT dataset were reconstructed with spacing of 2 mm in the epiphyseal regions and of 4 mm in diaphyseal ones. This differentiation account for a greater variability of the bone distribution in the diaphyseal regions. The scanner was set to 120 KvP and 160 mA of tube current; the selected field of view produced a pixel size of 0.625 mm.

The 3D solid model of the intact cadaver femur was generated from the CT dataset using a previously validated procedure (Taddei et al., 2003; Viceconti et al., 1999, 2004a). The procedure mainly consists of three steps:

- extraction of the 3D bone surface;
- generation of the FE mesh;
- mapping of the inhomogeneous bone tissue mechanical properties onto the mesh

The CT images were segmented (Amira, TGS, France) to extract the external contours of the bone and the resulting polygonal surface was converted into a NURBS model (Geomagic, Raindrop Inc., USA) (Figure 2.2). As the last step, the intact femur was imported into a modelling program (Unigraphics MX, Unigraphics Corp, USA), and converted into solid model.

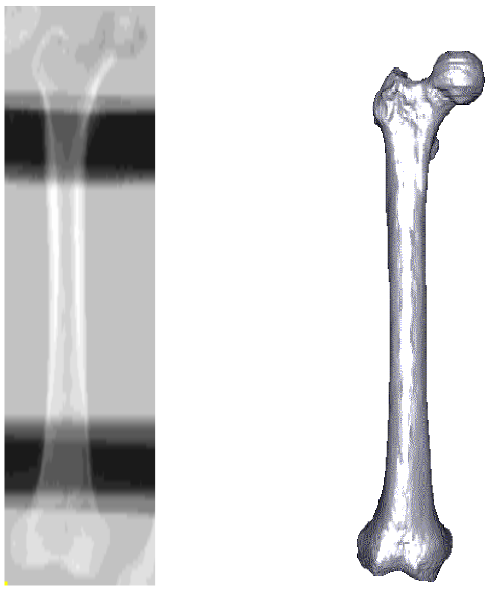

CT scan *3D solid model*

Figure 2.2: The process of the 3D solid model reconstruction

The operator plays a role only in the segmentation of the CT images, and this aspect has already been analysed in term of sensitivity (Testi et al., 2001; Taddei, 2006); for the uncertainties related to the femur geometry and the bone density, the latter study showed that the sensitivity of stress and strain predictions is affected by these factors for less than 9%, suggesting a minimal sensitivity to this factors. The rest of the procedure is totally automatic, and it would yield the same results regardless of the operator.

The generated solid model of the intact femur was afterwards meshed with an advancing front automatic mesh generator (Ansys, Ansys Inc, USA).

2.3.1. Error assessment *(Ansys Theory Reference)*

The finite element method provides an approximation to the true solution of a mathematical problem. From the analyst's standpoint, it is important to know the magnitude of the error involved in the solution. Through suitable mathematic techniques, it is possible to a posteriori estimate the solution error due to mesh discretization. In synthesis, the method involves the calculation of the energy error within each finite element expressing this error in terms of a global error energy norm. The error approximation technique is similar to the one given by Zienkiewicz and Zhu (Zienkiewicz et al., 1987) and it is based on the discontinuity of the stress field between adjacent elements. To obtain an acceptable value of stress, an average of the element nodal stress is done:

$$\overline{\sigma}_n^a = \frac{\sum_{i=1}^{N_e^n} \sigma_n^i}{N_e^n} \tag{2.1}$$

where

N_e^n : number of elements connected to node n;
$\overline{\sigma}_n^i$: stress vector computed at node n of element i.

The difference between the averaged and the unaveraged nodal stresses gives the nodal stress error vector:

$$\Delta\overline{\sigma}_n^i = \overline{\sigma}_n^a - \overline{\sigma}_n^i \tag{2.2}$$

This provides a rough estimate of the element error by computing the related strain energy. For each element the error energy e_i is defined as:

$$e_i = \frac{1}{2} \int_{Vol} \Delta\overline{\sigma}^T \overline{\overline{D}}^{-1} \Delta\overline{\sigma} d(Vol) \tag{2.3}$$

where:

Vol : element volume;
$\overline{\overline{D}}$: stress-strain matrix;
$\Delta\overline{\sigma}$: stress error vector .

By summing all element error energies, the global energy error in the finite element model can be determined:

$$e = \sum_{i=1}^{Nr} e_i \tag{2.4}$$

where:

N_r: total number of element in the model.

This can be normalized against the strain energy, calculable for one or more elements or for the overall model, and expressed as a percent error in energy norm, E:

$$E = 100 \cdot \left(\frac{e}{U + e} \right)^{\frac{1}{2}} \tag{2.5}$$

The percent error in energy norm E is a good overall global estimate of the discretization or mesh accuracy; it should suggest the regions where mesh needs a refinement.

2.3.2. Verification of convergence

Verification is a crucial step intended as the process to ensure that a Finite Element model is able to accurately predict the theoretical model which it is based on (Viceconti, 2004c).

A linear convergence test on six unstructured meshes with increasing refinement levels, consisting of parabolic tetrahedral elements, was developed to ensure the numerical accuracy of the model. This type of element is commonly used to mesh irregular solid structures under the conditions of great displacements and deformations (Ansys, Theory Reference). The increasing average dimension of the element used in the convergence test is well-established by previous protocols. In Table 2.2 the average dimension and the resulting total number of elements for each model are shown. The meshes used for the convergence test are represented in Figure 2.3 .

	Average dimension (mm)	Number of elements
Model_1	3.0	88149
Model_2	3.5	57536
Model_3	3.8	46138
Model_4	4.0	39895
Model_5	4.5	26441
Model_6	5.0	20670

Table 2.2: The average dimension and the total number of elements for each FE model used for the linear convergence test

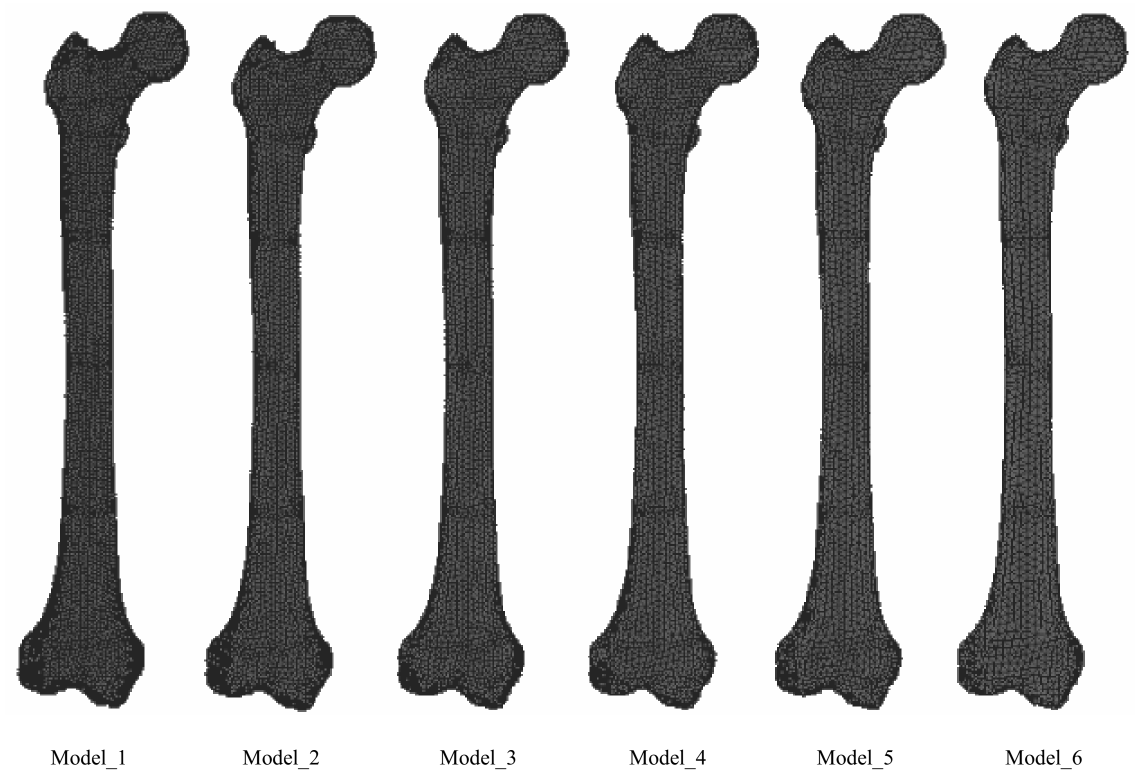

Figure 2.3: Finite element meshes of the femur considered in the present study.

Homogeneous elastic material properties were assigned to all FE models (E=1000MPa, ν= 0.3).

A simplified compression-bending loading condition, consisting of a single force of 1000N directed along the femur longitudinal axis, was applied to the models in the same location on the femoral head. The most extreme femur distal diaphysis was constrained (Figure 2.4) and the same region of interest in the diaphyseal region was selected.

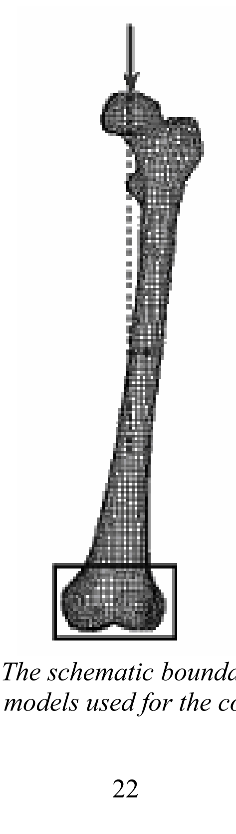

Figure 2.4: The schematic boundary conditions applied to the models used for the convergence test.

The following parameters were recorded over the increasing number of elements:

- Mean percentage error (E%)
- Peak strain energy error (e %)
- Peak tensile stress (σ_1) (MPa)
- Peak compressive stress (σ_3) (MPa) (absolute value)
- Peak tensile strain (ε_1) (μstrain)
- Peak compressive strain (ε_3) (μstrain) (absolute value)
- Peak Von Mises stress (σ_{EQVM}) (MPa)
- Peak displacement (U) (mm)
- Computational Time (CP) (*s*)

The computational time is the total time required to reach the solution convergence.

The percentage shifts of the parameters versus the corresponding values of the most refined model (e.g. *Model_1*), assumed as reference, are shown in Figure 2.5 over the total number of elements.

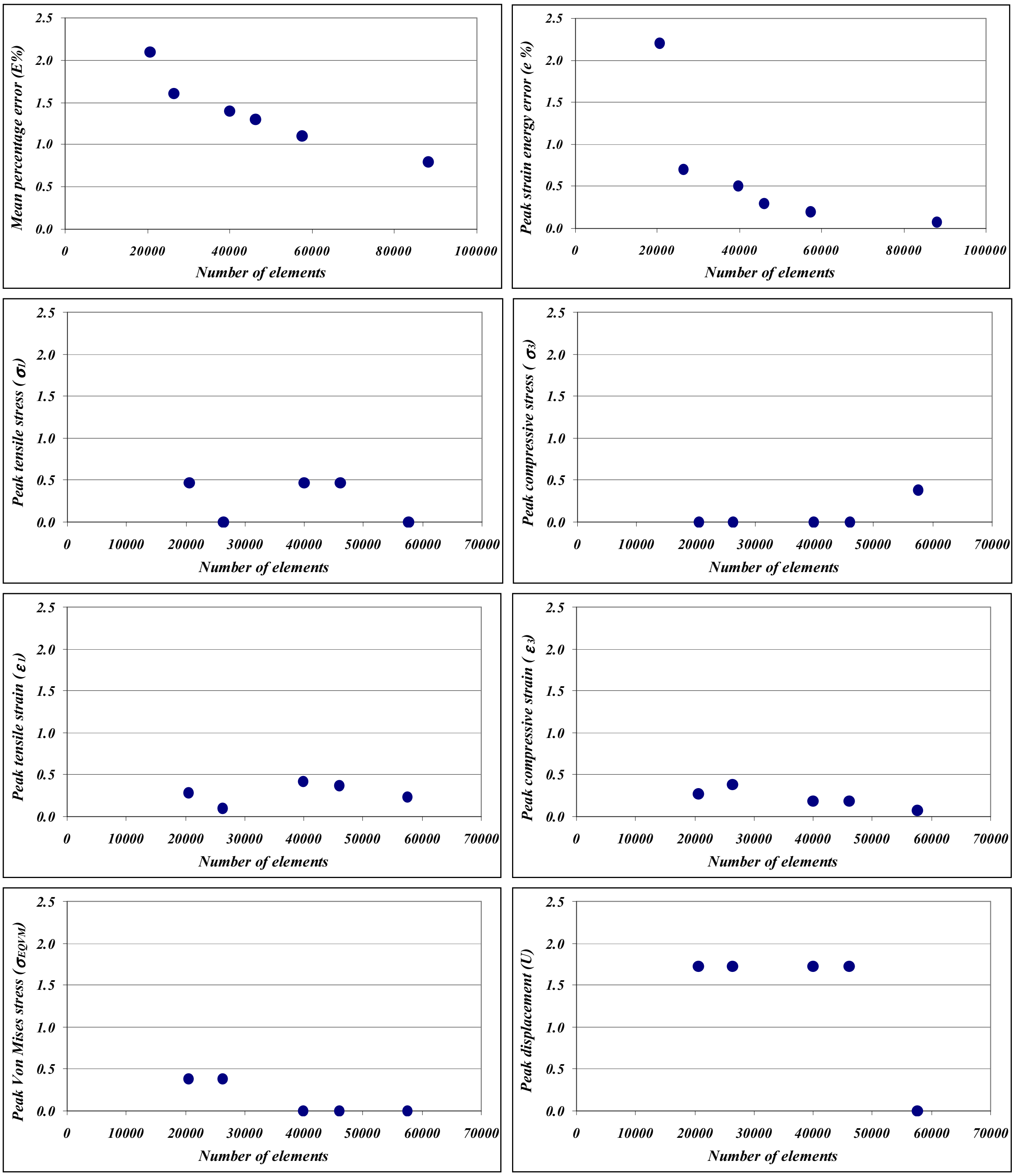

Figure 2.5: History of the parameters percentage shift from the most refined model assumed as reference over the increasing number of elements

As it can be observed, the percentage error in energy norm and the differences in terms of stress, strain and displacement were less than 2.2%. The model that guaranteed the best compromise among computational time and accuracy was therefore chosen (*Model_4*). In addition, the 95% confidence interval of the strain energy error distribution, 0.002J, was found close to the values previously reported for models derived from data collected in vivo (Viceconti et al., 2004).

Chapter 2.4

The Finite element modelling of the implanted femur

In this section the modelling of the human femur implanted with a cementless hip stem is shown.

A discussion on the value of the yield strain of bone that has to be used is also reported.

In questa sezione viene mostrata la modellazione del femore protesizzato con uno stelo d'anca non cementato.

Si riporta, in aggiunta, una discussione sul valore della deformazione di snervamento dell'osso da utilizzare.

2.4.1. Cemented and uncemented prosthesis

Bone mineralization status and patient age are the prevailing parameters that affect the choice of the prosthesis. As a general rule, in young patient the uncemented prosthesis are normally favourite due to a better chance of bone remodelling; on the other side, in old patient, or in patient suffering from pathologies of bone metabolism, uncemented prosthesis are used.

The chances of success for a cemented prosthesis are strictly correlated with the bone and implant ability to integrate each other. Bone is in endlessly evolution whilst the prosthesis presents a mechanical structure stressed by both the chemical surrounding environment and the physiological loading. Since the total integration is still unthinkable, the best achievable goal is to alter less as possible the physiological load and stress distribution of bone ensuring a stable anchorage of the implant.

The clinical knowledge of the osteosynthesis processes, prosthetic and dental surgery, as well as the histological studies, has shown the bone capability to integrate with titanium devices. The bone cells and the mineralised matrix of the bone lie directly on the implant surface without interposition of other tissues.

The main potential problems related to cemented implants are the following (Justy et al., 1992):

- Bone necrosis caused by heat generated during the cement set (bone cement is made by an acrylic resin that hardening with an exothermic polymerisation reaction produces temperature of 80°);
- Poor mechanical fatigue strength of cement;
- Loss of mechanical characteristics of cement (cracking and crumbling that lead to the implant loosening);
- High stresses at the bone-implant interface due to a significant difference in terms of elastic modulus between cement (3000 *MPa*) and implant (210000 *MPa* for Cr-Co alloy and 107000 *MPa* for titanium alloy).

As well, uncemented implants have some critical aspects:

- Achievable primary stability (mechanical stability);
- Achievable secondary or long-term stability (biological stability);
- Stress-shielding.

Nevertheless, if uncemented implants reach the osteointegration, they show better long-term results. The general trend is therefore to use uncemented implant (Various authors, 2005) (Table 2.3).

Operation year	**Primary operation**	
	Cemented prosthesis	**Uncemented prosthesis**
2000	14.2 %	62.1 %
2001	14.4 %	65.4 %
2002	12.1 %	70.0 %
2003	11.0 %	71.7 %
2004	8.6 %	76.2 %

Table 2.3: Percentage of cemented and uncemented prosthesis implanted from 2000 to 2004 (Registro dell'Implantologia protesica)

2.4.2. Pre-operative planning

An anatomic cementless hip stem (AncaFit, Cremascoli-Wright, Italy) was chosen for the implant. This is the most used stem in Emilia-Romagna (Table 2.4).

Stem	Primary operation				
	2000	2001	2002	2003	2004
ANCAFIT-Cremascoli	15.0 %	15.8 %	17.2 %	15.4 %	15.9 %
CLS- Sulzer, Centerpluse, Zimmer	12.5 %	10.1 %	10.6 %	10.5 %	9.7 %
CONUS- Sulzer, Centerpluse, Zimmer	8.4 %	9,1 %	9.5 %	9.5 %	8.3 %
ABGII-Howmedica	0.9 %	4.8 %	5.8 %	6.1 %	7.0 %

Table 2.4: Percentage history of the 4 most used stems in Emilia-Romagna over 4 years (Registro dell'Implantologia protesica)

The hip stem is made in titanium alloy, a material widely used in biomedical applications due to its higher elastic modulus, that means high flexibility, than other biomaterial. This ensures that the elastic deformations of stems and bone are similar, reducing potential stress concentrations. Moreover, titanium is highly biocompatible. On titanium implant surfaces, the natural presence of oxygen induces the formation of a thin film of dioxide, protecting against corrosion.

The hip stem was positioned in space inside the femur by a skilled surgeon using a simulation pre-operative CT based software (Hip-Op, B3C, Italy) (Figure 2.6).

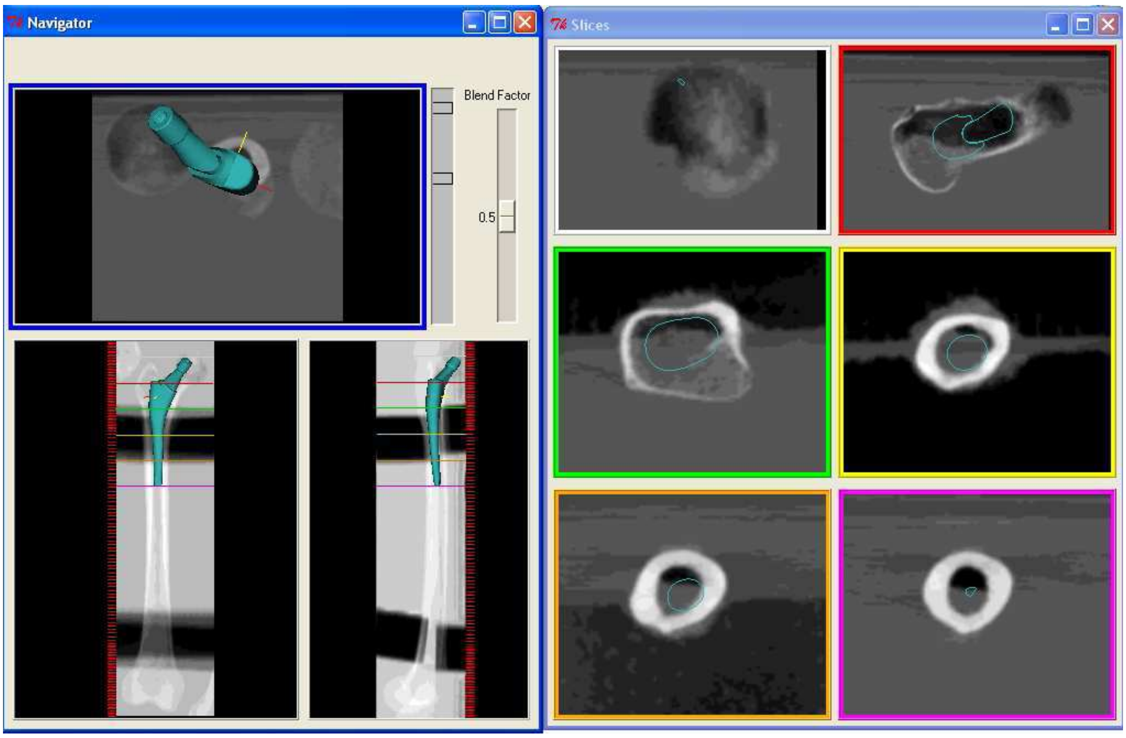

Figure 2.6: Pre-operative planning of the femur with the Hip-Op software

To guarantee the accuracy of the stem positioning and size choice by means of the pre-operative planning, it was asked to 4 subjects with different skills and level of knowledge of the Hip-Op software to replicate the planning of the AncaFit into the femur. This was done 3 times for each subject spreaded in time, except for the surgeon (subject 3), so that no memory was kept of the previous planning. The results are shown in Table 2.5.

	Stem size	**Stem planned pose**					
		Tx	Ty	Tz	Rx	Ry	Rz
Subject1	12	148.005	164.089	-118.081	-2.987	1.478	164.445
Subject1	12	149.665	163.984	-115.434	-3.101	0.283	167.334
Subject1	12	149.192	163.601	-112.076	-3.262	0.517	167.334
Subject2	12	148.945	164.450	-120.319	-1.533	2.085	150.000
Subject2	13	149.349	163.740	-114.687	-3.534	0.359	166.575
Subject2	13	149.254	164.844	-117.698	-1.087	2.535	150.000
Subject3	13	148.000	164.885	-119.000	-3.000	2.000	158.000
Subject3	14	150.000	165.371	-116.000	-2.000	2.000	150.000
Subject4	12	146.505	165.675	-119.433	-2.892	2.172	163.843
Subject4	12	148.653	164.688	-116.688	-2.447	1.413	162.000
Subject4	12	147.788	164.577	-114.474	-3.262	1.103	160.000
	Mean	148.669	164.537	-116.704	-2.646	1.450	159.957
	St. dev	1.013	0.652	2.477	0.786	0.791	7.024

Table 2.5: Planning of the AncaFit stem into the femur used in the present study

In order to generate the femur cavity hosting the hip stem, a 3D solid model of a rasp was generated starting from the solid model of the stem (Figure 2.7).

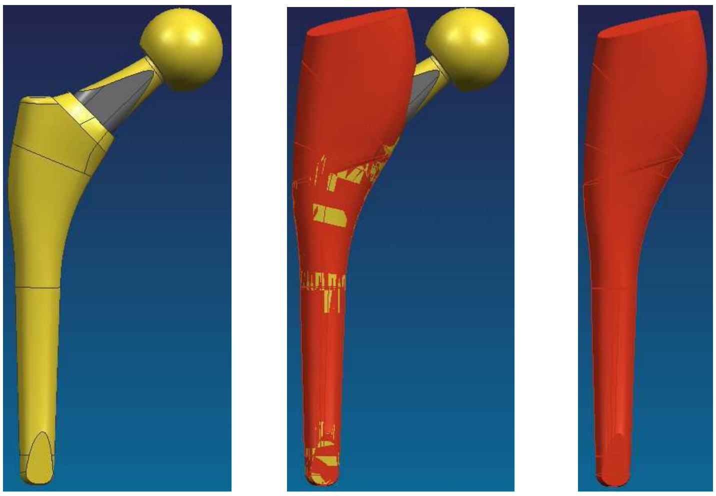

Figure 2.7: From left to right: the solid model of the AncaFit stem; creation of the solid model of the rasp; the resulting rasp

The femur cavity was then created by Boolean subtraction of the solid model of the rasp, loaded in the modelling program (Unigraphics), from the 3D model of the intact femur.

Surgical parameters and hip stem geometry were imported within the solid model of the hollow femur. The femur neck was resected at the level chosen by the surgeon through the Hip-Op software.

Afterwards, the model of the implanted femur was meshed resulting in 38,441 tetrahedral elements (Figure 2.8).

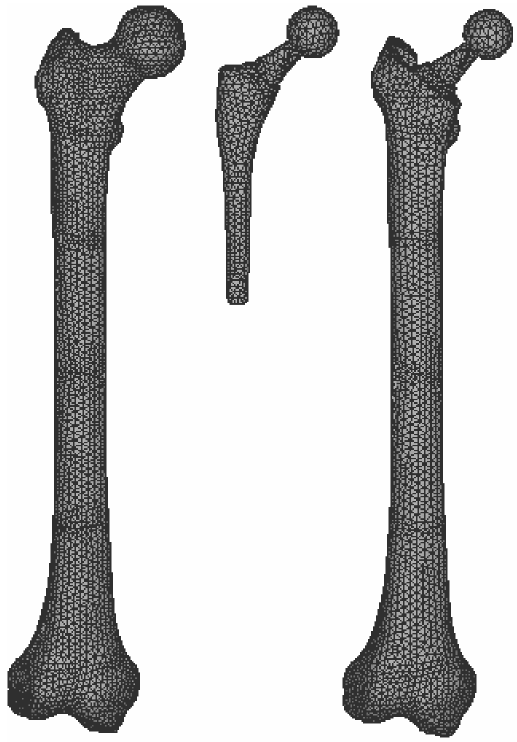

Figure 2.8: Finite element meshes of the femur (frontal view). From left to right: the intact femur, the hip stem (AncaFit) and the implanted femur.

The convergence test was not repeated for the FE model of the implanted femur where a contact exists. The convergence theorem is not valid for boundary non linearities and inhomogeneous material; thus, nothing ensures that any contact parameter, such as relative sliding, monotonically converges to a given value for increasing refinement, which makes any convergence test on contact parameters pointless. This explains why direct experimental validation is mandatory in these problems. For the contact, the peak compenetration has to be monitored since it must be minimal; the adequacy of the mesh refinement with respect to stress and strain predictions is also verified.

The post-hoc indicator proposed by Zienkiewucz and Zhu was therefore computed for the FE model of the implanted femur. An homogeneous elastic modulus of 10000 *MPa* was assigned to the femur and the always-bonded contact was set for the bone-implant contact. The always-bonded contact is used to simulate frictionless contact where no separation occurs between the bodies. The maximum error for the femur was found 11% while for the prosthesis it was 7%.

2.4.3. Material properties assignment

The bone tissue was modelled as a non-homogeneous material (Taddei et al., 2004), deriving the tissue mineral density from the radiographic density of the intact femur CT. Actually, a few studies (M.J. Ciarelli, et al., 1991, R.J. McBroom, et al., 1985, J.Y. Rho, et al., 1995) have shown that the Hunsfiled Units of a CT image and the bone tissue density are linearly correlated.

A calibration phantom with three bone-equivalent (solution of hydroxyapatite) insertions of different densities embedded in a water-equivalent resin-based plastic was scanned (The European Spine Phantom, Kalender, 1992) (Figure 2.9). It was used to calibrate the CT data to correlate the Hounsfield units into mineral density using a linear calibration equation (Kalender, 1992) here computed for the specific patient: $\rho = 0.8082HU - 5.6409$ (Table 2.6). The same scanner parameters used for the femur were set for the phantom scanning.

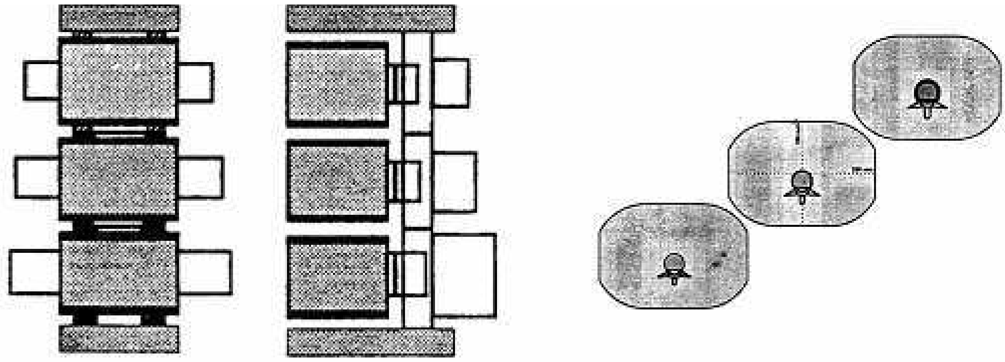

Figure 2.9: Lateral, anteroposterior (LEFT) and section (RIGHT) view of the European Spine Phantom

	HU	**Mineral Density (mg/cm^3)**
Low density vertebra	68.846	51.8
Medium density vertebra	138.063	103.1
High density vertebra	258.871	204.6

Table 2.6: Values used to compute the linear calibration equation: Hunsfield Units (HU) of the European Spine Phantom and Mineral density taken from the Keller study

The Young's modulus (E) was related to mineral density (ρ) in the form of power relationship (Keller, 1994):

$$E = 10.5\rho^{2.57}\,(R^2 = 0.965) \tag{2.6}$$

Both mineral density and elastic modulus were then mapped onto each element of the generated mesh using in-house shareware software Bonemat (Taddei et al., 2004).

This software required the following parameters as input data:

- CT dataset of the intact femur in .vtk format, that is a single file containing complete information on the Hounsfield Units (number and coordinates) of every single dataset voxel;
- Keller and Kalender equations coefficients;
- Interval amplitude within which all obtained elastic modulus values are associated with the peak value in the interval.

The resulting range of elastic modulus was $E = 9.25 \div 25101\,MPa$ and $\rho = 0.046 \div 1.46\,g/cm^3$ for the mineral density. A map of the aforementioned properties is showed in Figure 2.10. High modulus is assigned to the medial and lateral cortex, whilst on the anterior aspect, the modulus is low in comparison. Multiple CT scans were checked on, founding a similar pattern in many other femurs. Thus it can be concluded that this is not an error or an artefact, but it is just the density distribution in the bone under examination.

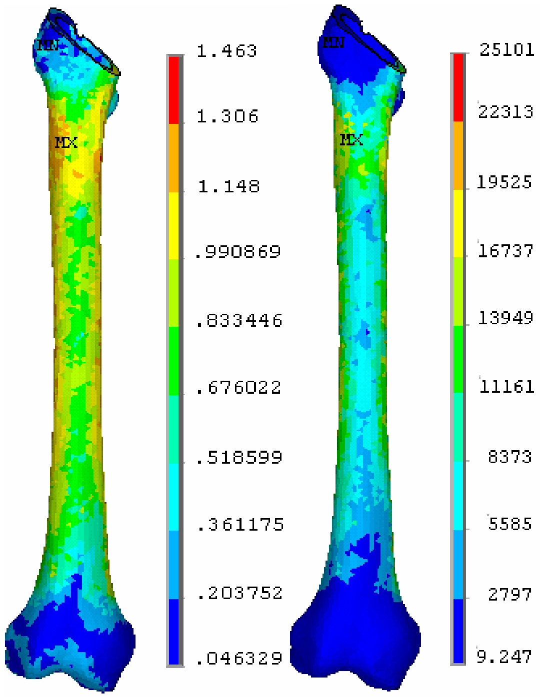

Figure 2.10: Distribution of the mapped material properties on the Finite Element model of the femur used in the present study: modulus of elasticity (MPa) (left) and mineral density (g/cm^3) (right).

As previously mentioned, the stem implant was made in Titanium alloy ($E = 105000\ MPa$; $\nu = 0.3$).

2.4.4. Contact and solution parameters setting

Frictional contact was modelled at the bone-implant interface by means of asymmetric face-to-face contact elements. This type of element is commonly used for arbitrary bodies that have large contact areas and is very efficient for bodies that experience large amounts of relative sliding with friction. These elements are the most accurate when compared to experimental measurements and allow accounting for large sliding (Hefzy et al., 1997; Mann et al., 1995; Viceconti et al., 2000).

In detail, the contact was set flexible-to-flexible, that is it occurs between two deformable bodies having similar stiffness since, as previously noted, titanium hip stem and bone show comparable deformability.

The coefficient of friction was set to 0.3 (Viceconti et al., 2000; Pancanti et al., 2002). A sensitivity analysis of the predicted micromotion at the calcar level over the variations of the coefficient of friction value within the range of uncertainty (0.1-0.5) produced differences of less than 35 microns.

An augmented Lagrangian approach with a full New-Raphson iterative scheme on residual force, combined with line search technique, was chosen to solve the contact problem. For force convergence, 1% tolerance based on Euclidean L_2 norm was used. As mentioned, the peak compenetration was monitored, since it must be very small to get a good level of numerical accuracy. Setting a contact normal stiffness of 9000 N/mm involved a peak compenetration of 3.2 microns which is smaller then previously reported values (Viceconti et al., 2000).

2.4.5. Boundary conditions

In the last few years, a large amount of devices and protocols have been developed to predict the primary stability of hip stems (Harris et al., 1991; Monti et al., 1999). These methods have been also used to pre-clinically validate new prosthetic designs. In this context, however, we considered more adequate to use as reference measurements those obtained from an intra-operative device for the assessment of the primary stability (Cristofolini et al., 2002a, Cristofolini et al., 2002b; Cristofolini et al., 2006; Varini et al., 2004).

In-vitro measurements taken with the Intra-operative Stability Assessment Console (ISAC) (Figure 2.11) were used as reference to validate the predictions obtained from the patient-specific finite element models.

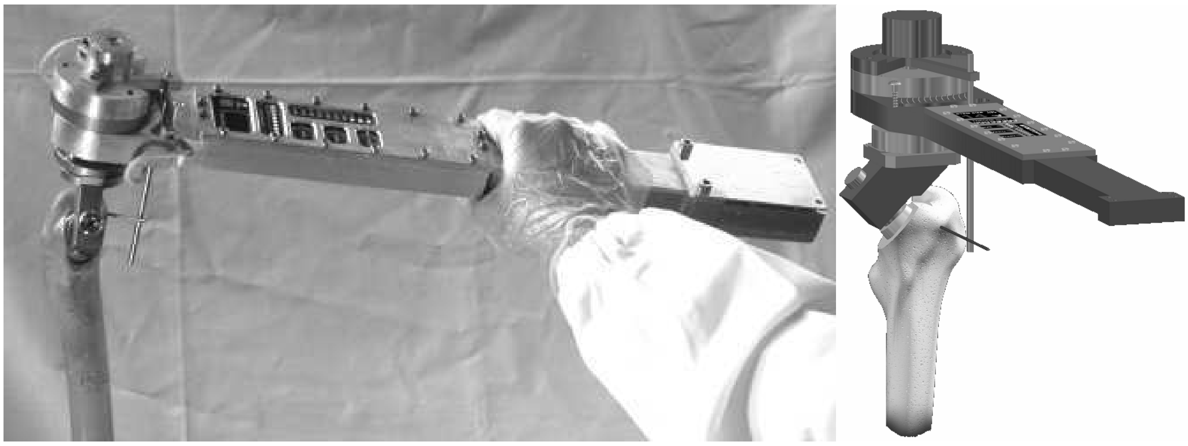

Figure 2.11: Intra-operative Stability Assessment Console (ISAC).

The device mainly consists of two transducers with high accuracy, a torsional load cell and a RVDT angular sensor measuring respectively the torque applied and the stem-bone rotation. All the components are rigidly connected to minimize the effects of non-torsional load components.

A handle, hosting all electronics, allows the surgeon to apply the torque whilst a series of led gives information on the entity of the torque applied and on the level of implant stability. Tangential micromotion is measured at the calcar level.

The boundary conditions of the experimental set-up were therefore replicated in the model. A maximum internal rotation of 11.4 Nm was applied to the proximal part of the hip stem and solution data recorded every 0.5 Nm (22 sub-steps). The distal-most femoral diaphysis was constrained (Figure 2.12).

The stem in reality is press-fitted into the reamed canal; nevertheless a previous validation study showed that the main effect of press-fit is to regularise the contact interface, and, if this is assumed in ideal conditions in the model, the mechanical effect of press-fit can be neglected while retaining a very good level of accuracy (Viceconti et al., 2000). Thus, this condition was not considered in the numerical simulation.

Due to limitations of the original software control in the ISAC System at the time when the measurements were carried out, the device started to control for torque above 1.21 Nm. Thus experimental data acquisition was not available for the first fraction of the applied torque.

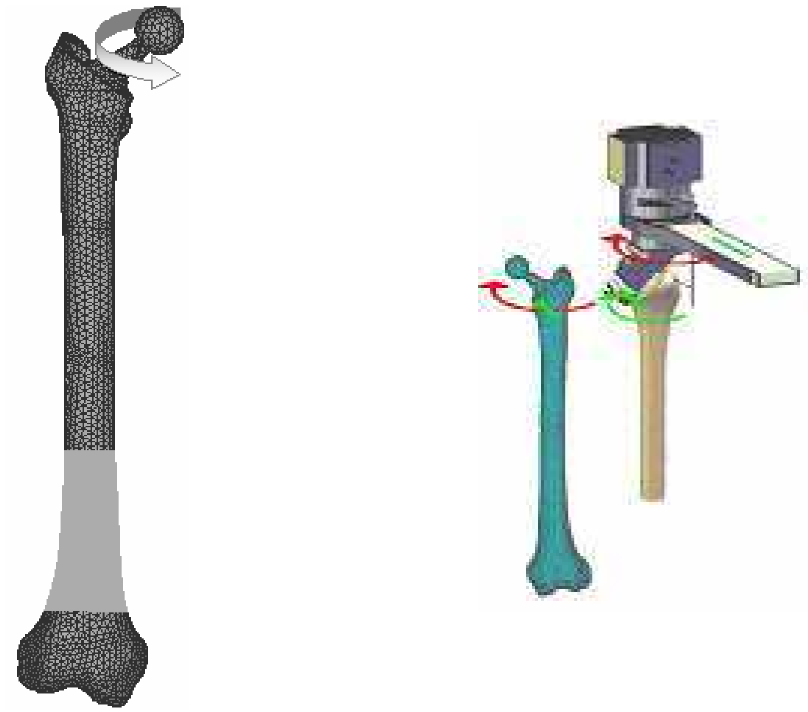

a) Frontal view b) Posterior view

Figure 2.12: Boundary conditions applied on the Finite element model of a right femur. a) The light area is the constrained region. The arrow represents the internal rotation imposed to the stem of the prosthesis; b) Green arrow points towards the region where micromotions are measured, e.g. the calcar level

A torsional load, such as that applied by the ISAC set-up on the hip stem, and replicated in the FE model, was found the most critical for the primary stability in terms of induced micromotion in a number of experimental and numerical studies (Callaghan et al., 1992; Davy et al., 1988; Gustilo et al., 1989; Harman et al., 1995; Harris et al., 1991; Ishiguro et al., 1997; Kotzar et al., 1991; Maloney et al., 1989; Martens et al., 1980; Mjoberg et al., 1984; Nistor et al., 1991; Nunn et al., 1989; Philips et al., 1991; Schneider et al., 1989b; Sugiyama et al., 1989). From these, in-vitro tests performed to measure the primary stability of cementless prostheses have shown that the highest values of micromotion at the bone-stem interface arise when torsional moment, in the range of 15-29 Nm, around the femur axis prevails (Bergmann et al., 1995). A smaller value of torque is applied to the ISAC device, as well as to the FE model, to account for the fact that patients apply reduced loads in the immediate post-operative period (Monti et al., 1999).

The procedure used to compute the bone-implant relative micromotion is described elsewhere (Pancanti et al., 2003). A monitoring element was selected to carry out the comparison at the same location where the micromotion sensor was located in the experiment set-up, e.g. the calcar level.

2.4.6. Post-hoc indicators

Two indicators were selected to judge the quality of the model: the root mean square (RMS) error and the peak error of predicted micromotion with respect to experimental measurements. The slope of the curves, opportunely partitioned, was also compared. Additionally, non-linear behaviour of experimental micromotion over the applied torque was investigated. To this purpose, two additional cadaver femur specimens (lab code #82, #993) were tested to state the generality of this observed non-linearity. Since the experimental curve presented, within a range of torque values, a marked non-linearity, the slope of the torque-micromotion curve between the measured and the predicted values was compared non only globally but also over the four spans that go from 0 to 1.2, 1.2 to 2, 2 to 7.6 and 7.6 to 11.4 Nm.

Afterwards, the equivalent Von Mises strain was recorded at every sub-step of the FE model solution and compared to the yield strain reported in literature for the bone.

2.4.7. Failure criterion of bone: a still controversial literature

Few studies indicate the need of using yield rather than ultimate strain for trabecular (Bayraktar H.H. et al., 2004; Niebur G.L. et al., 2000) and cortical bone (Biewener AA., 1993) although a single study suggests that the damage of the trabecular bone can occur at lower value of strains (Yeh O.C. et al., 2001). Moreover, the functional strains reported for normal (Bone Mechanics Hand Book, 2nd edition, Cowin S.C., 2001; Van Rietbergen B. et al., 2003) and abnormal activities of human femur (Verhulp E. et al., 2003) are much lower than the average value of yield strains.

Trabecular bone:

While the weak dependency of the yield strain on apparent density has been widely reported (Rohl et al., 1991; Keaveny et al., 1994; Hvid et al., 1985, 1989; Hansson et al, 1987; Mosekilde et al., 1987), at the same time it has been stated that tension and compressive yield strains vary among anatomic sites (Kopperdahl and Keaveny, 1998; Morgan and Keaveny, 2001). It is therefore unclear if, when developing a computational model of a whole femur, the yield strain have to be taken as a constant parameter rather than variable within the range of apparent density since different sites (great trochanter, femoral neck, etc.) are co-present. The only study that reports a regression equation between compression yield strain and trabecular density overestimates the experimental results (Kopperdahl and Keaveny, 1998) for upper values of the apparent density than those reported for the human vertebral trabecular bone (Morgan et al., 2001). Thus, to the aim of the present study, the slight inter-site variation of the yield strain within a bone segment was neglected assuming a single average value.

The value of the yield strains reported in the literature for the femur are shown in Table 2.7 with reference to the anatomic site:

	Anatomic site	**Yield strain (%)**	**Reference**
Tension	12 human femoral neck	0.61 ± 0.03	Bayraktar et al., 2004
	23 greater trochanter	0.61 ± 0.05	Morgan et al., 2001
	27 femoral neck	0.61 ± 0.03	Morgan et al., 2001
	6 Human femoral neck	0.62 ± 0.04	Bayraktar et al., 2004
	Human proximal femur	0.57	Verhulp E. et al, 2003
Compression	12 human femoral neck	0.86 ± 0.1	Bayraktar et al., 2004
	23 greater trochanter	0.70 ± 0.05	Morgan et al., 2001
	27 femoral neck	0.85 ± 0.1	Morgan et al., 2001
	6 Human femoral neck	0.86	Bayraktar et al., 2004

Table 2.7: The yield strain reported in literature for trabecular bone

Cortical Bone:

There are only few studies on the analysis of the yield strains for cortical bone that are reported in Table 2.8:

	Anatomic site	Yield strain (%)	Reference
Tension	Human femoral neck	0.73 ± 0.05	Bayraktar et al., 2004
	Human femur	1.02	Currey J.D., 2004
	Human femur	0.88	Currey J.D., 2004
	Human femur	0.72	Currey J.D., 2004
Compression	Human femur	1.10	Burstein et al. 1996
	Human femur	1.10	Reilly et al., 1975

Table 2.8: The yield strain reported in literature for cortical bone

Just averaging the values above reported, it should be therefore reasonable to assume the following values:

	Yield strain
Trabecular tensile yield strain	0.60 %
Trabecular compressive yield strain	0.82 %
Cortical tensile yield strain	0.83 %
Cortical compressive yield strain	1.10 %

Table 2.9: Summarizing average value of the yield strain for trabecular and cortical bone

As shown, tensile yield strain results 27% and 22% lower than compressive yield strain for trabecular and cortical bone respectively.

In the present study, a reference value was calculated as the weighed average of the yield strain for trabecular and cortical on the respective percentage in contact with the hip stem; thus, the bone was assumed to yield at a constant yield strain of 0.7% strain in tension and 0.95% strain in compression.

Chapter 2.5

Sensitivity of the predicted primary stability to the stem pose

This section aims to evaluate if the predictions made on the pre-operative pose are representative of the primary stability that will be achieved in the operative room. For this purpose, a second FE model of the implanted femur is generated with the stem pose derived by the post-implant CT scan.

In questa parte del lavoro viene valutato se le predizioni fatte a partire dalla posizione dello stelo pianificata sono rappresentative della stabilità primaria che sarà ottenuta in sala operatoria. A questo scopo, viene generato un secondo modello FE del femore protesizzato con la posizione dello stelo derivata dalla scansione TC post-opertaoria.

The micromotion measurements are taken on a physical specimen, in which the stem position with respect to the bone may differs some millimetres from the one the surgeon planned using the Hip-Op software. It is therefore necessary to answer to a fundamental question: is the prediction of primary stability obtained on the planned pose (position and orientation) representative of the stability we should expect *in vivo* where the prosthesis will be placed in a different position?

The *planned-Vs-achieved accuracy* (PVA) may be higher for computer aided procedures (DiGioia et al., 1998) or lower for conventional, unassisted procedures (Lattanzi et al., 2003), but some differences will always be there. What is predicted during planning is not exactly what it will be achieved in the operative room.

The next step of the present study was therefore aimed to establish if the prediction made on the pre-operative pose is representative of the primary stability that will be achieved intra-operatively. To this purpose, an additional Finite Element model of the same femur till now considered was generated in which the stem position was this time defined from the post-implant CT scan. In other term, the sensitivity of the prediction of the primary stability to the difference in pose between the planned and the achieved configurations was investigated.

After intact femur CT scanning and hip stem implantation, a second CT scan was performed on the same specimen using the same radiological parameters of the former CT. The subject-specific FE model of the femur as derived by the post-operative CT scan was generated using the same validated procedure previously explained for the implanted femur as derived by the pre-operative planning.

Here the cavity of the femur due to the physical presence of the stem was preliminary filled to create a solid model of the intact femur (Figure 2.13). The 3D solid model of the stem was also generated starting from the post-operative CT scan (Figure 2.15(1)) since this was the only source of information for the achieved pose.

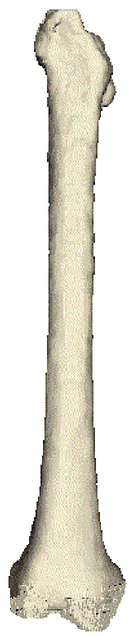

Figure 2.13: Frontal view of the solid model of the femur as derived by the post-operative CT scan.

This second model was aimed to replicate the position achieved during surgery (ACHIEVED). As previously mentioned, two CT scan of the femur were performed: before and after the stem implant operation. The two CT scans and the pose the surgeon planned with the Hip-Op software (PLANNED) were use to determine the differences between the Planned and the Achieved poses.

To the purpose, a method that involves the mutual registration of both the femurs and the stems in the reference systems defined by the two separate CT acquisitions was used (Popescu et al., 2003).

More in detail, since CT datasets had different spatial references, in order to get the relative position of the stem as derived from the planned and the achieved surgery, the ACHIEVED model was superimposed to the PLANNED model using an in-house developed software (Multimod Data Manager). This was performed trough the automatic registration of the same set of anatomical landmarks previously manually defined on both models (Figure 2.14).

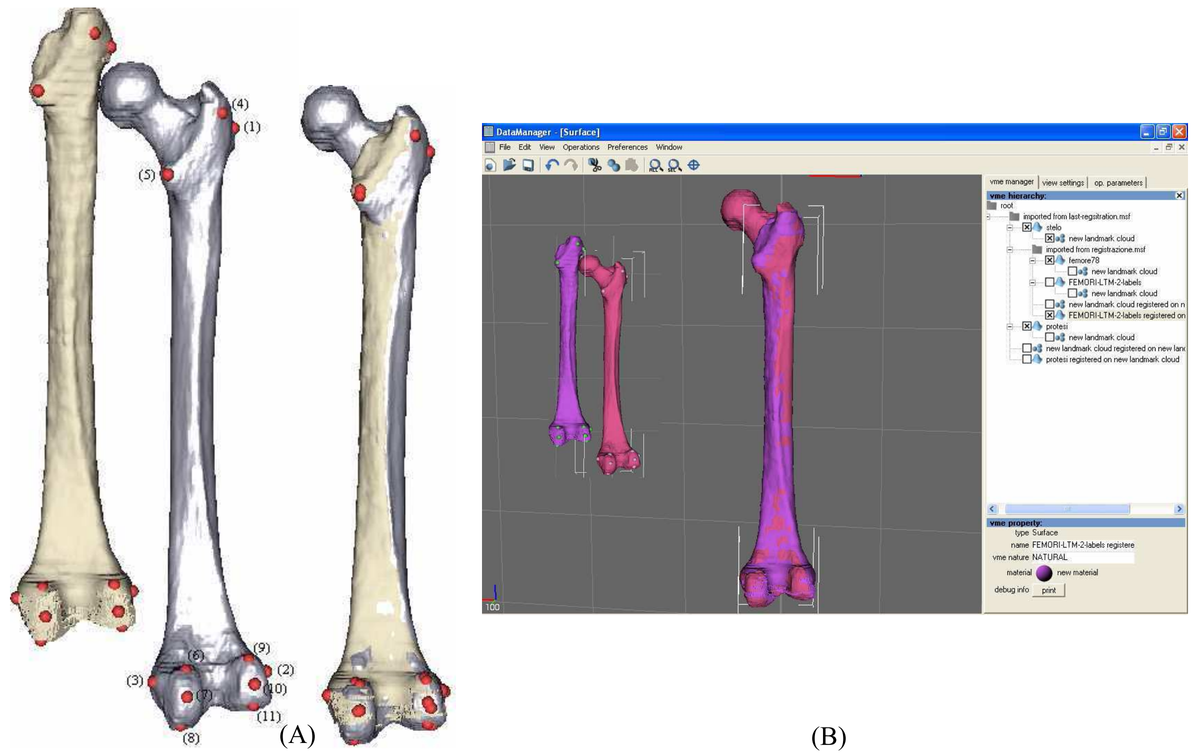

Figure 2.14: The definition of the set of anatomical landmarks (red spots) used for the automatic registration of the solid models of the femur (Posterior view): one generated from the post-operative CT scan (A-LEFT showed in the original spatial reference) and one from the CT scan of the intact femur (A-RIGHT). Landmarks: (1) most lateral point on great trochanter, (2) most lateral point on later epicondyle, (3) most medial point on medial epicondyle, (4) lateral posterior prominence of greater trochanter, (5) most prominent point on lesser trochanter, (6) most superior point on medial condyle, (7) most posterior point on medial condyle, (8) most inferior point on medial condyle, (9) most superior point on medial condyle, (10) most posterior point on medial condyle, (11) most superior point on medial condyle. (B) the two solid models superimposed one each other in the spatial reference of the CT scan of the intact femur.(B) Multimod Data Manager interface

Once the two solid models of the femur were registered each other, the roto-translation matrix for superimposing the two stem positions was derived using the same procedure with a different set of landmarks (Figure 2.15).

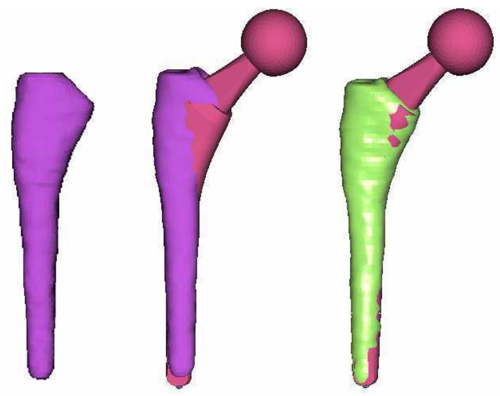

(1) (2) (3)

Figure 2.15: Frontal view of the solid models of the stem: (1) the stem as derived by the post-operative CT scan; (2) the solid model of the stem in the original achieved (violet) and planned (pink) positions; (3) the achieved position (green) superimposed to the planned position (pink)

The roto-translation matrix that expresses the change in pose between Planned and Achieved (Table 2.10) with respect to the reference system of the intact femur is well within the peak shifts of the Planned versus the Achieved position of the stem reported in a previous study (Lattanzi et al., 2003).

Translations (mm)			Rotations (Deg)		
Tx	**Ty**	**Tz**	**Rx**	**Ry**	**Rz**
10.53	-10.5	4	-0.05	-0.6	4

Table 2.10: The roto-translation matrix for superimposing the pose of the stem into the femur cavity as derived by post-operative CT scan (ACHIEVED) and by the pre-operative planning with the Hip-Op software (PLANNED).

The stem was therefore moved to the Achieved pose (Figure 2.16) and imported in the solid model of the femur as derived by the post-operative CT scan, so as to have a further solid model of the implanted femur.

The solid models of the femur and the stem were meshed using the same procedure and the same element size previously described. The resulting FE model of the implanted femur consists of 41,097 ten-node tetrahedral elements (Figure 2.16)

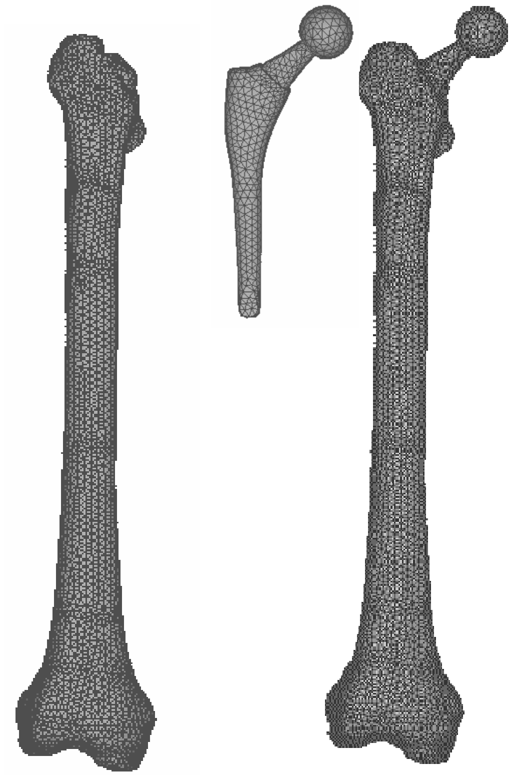

Figure 2.16: The generated FE models of the femur as derived by the post-operative CT scan. From left to right: intact femur; stem; implanted femur with the stem pose achieved during surgery.

A post-hoc indicator (Zienkiewicz et al., 1987) was computed also for this second FE model. The percentage error in the energy norm was 9% for both the femur and the stem. The peak compenetration was also monitored to guarantee a good level of numerical accuracy resulting in a peak value of 19 microns.

Once more, the same procedure to map the material properties was followed for the ACHIEVED model. In the Table below the resulting values of the mineral density and the Young's modulus are reported and compared to those obtained for the PLANNED model.

	Number of Materials	**Density (g/cm^3)**		**Young's modulus (MPa)**	
		Min	**Max**	**Min**	**Max**
PLANNED	460	0.046	1.46	9.2	25101
ACHIEVED	466	0.037	1.47	5.7	25589

Table 2.11: The mechanical material properties mapped onto the meshes of the two FE models of the femur (PLANNED and ACHIEVED). The minimum and the maximum values of the Mineral density and the Young's Modulus are shown. The number of the materials resulting in each mesh is reported as well.

The applied boundary conditions, as well as the solution parameters, were set identical to those used for the FE model derived by the pre-operative planning.

The relative percentage error assessed the differences between the PLANNED and ACHIEVED models in predicting the equivalent Von Mises stress and strain.

Chapter 2.6

Results

The main results of the FE model simulations are here presented. In the first part of the chapter, the bone-implant micromotions predicted by the FE model derived by the pre-operative planning are confronted to experimental measurements.
Then, the stresses, the strains and the micromomevements predicted by ACHIEVED and the PLANNED FE models are compared.

Vengono presentati in questo capitolo i principali risultati delle simulazioni FE. Nella prima parte, i micromovimenti osso-impianto predetti dal modello FE generato a partire da dati di pianificazione pre-operatoria sono comparati con misure sperimentali.
Successivamente, vengono confrontati le tensioni, le deformazioni ed i micromovimenti predetti dai modelli FE ACHIEVED (derivato da dati post-operatori) e PLANNED (derivato da dati pre-operatori).

2.6.1. FE model derived from the pre-operative planning

At an applied torque of 11.4Nm the ISAC System measured 171 μm and the Finite Element model predicted 150 μm. When compared over the entire loading range from 0 to 11.4 Nm, the model predicted the sliding micromotion measured experimentally with an average (RMS) error of 12 μm and a peak error of 21 μm (Figure 2.17).

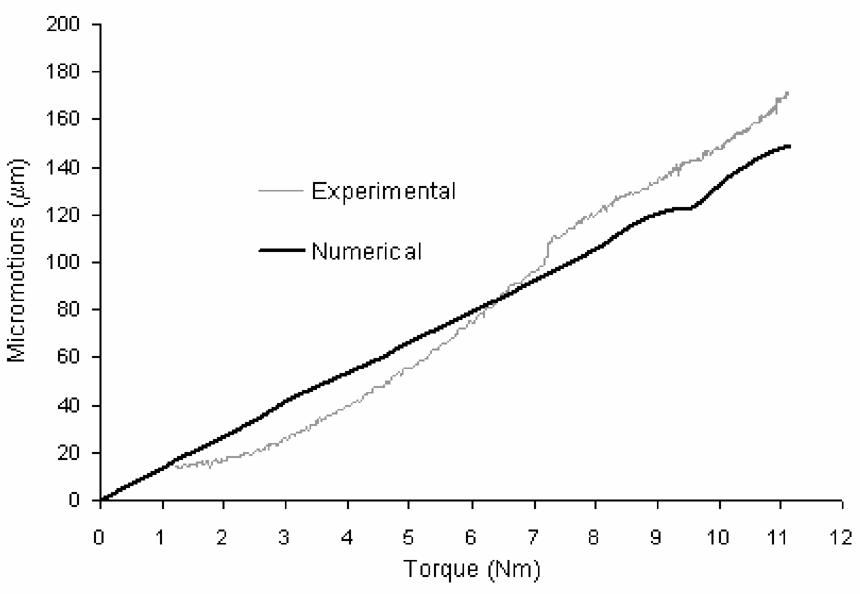

Figure 2.17: The experimental micromotions compared to those predicted by the numerical finite element model over the entire range of the applied torque from 0 to 11.4 Nm.

The torque-micromotion curve predicted by the model was linear, with only a minimal non-linearity in the predicted micromotion between 9 and 10 Nm.

Conversely, the experimental curve showed a marked non-linear relationship between torque and micromotion in the range 1-7 Nm and a linear relationship for higher values of torque. This non-linearity was not incidental; the same non-linear behaviour was observed in the other two analysed specimens (Figure 2.18).

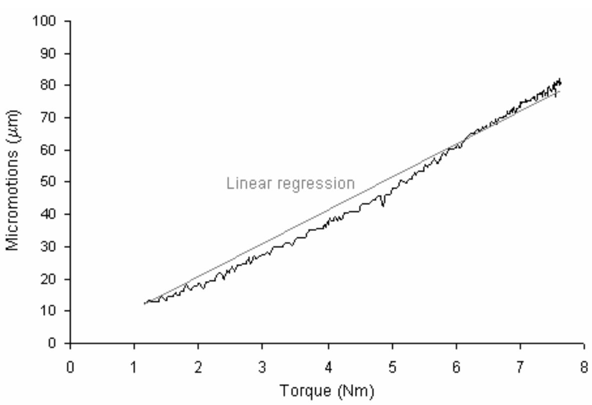

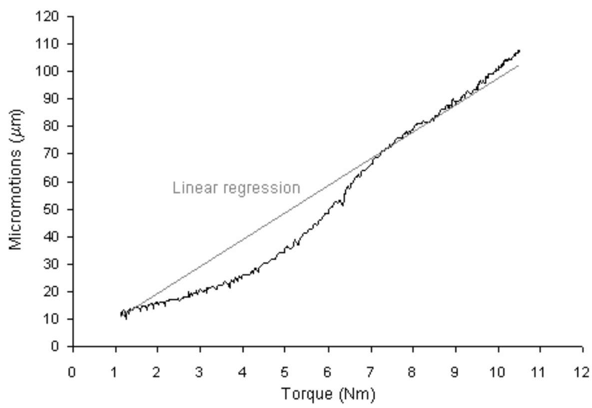

Figure 2.18: The experimental micromotions over the applied torque for the other two femurs tested (specimen lab code #82, top, and #993 at the bottom) here used to state the generality of the observed non-linearity. The comparison with the reported slope of the linear regression let to better understand the magnitude of the non-linearity.

There was a good agreement between the slope of the experimental and the numerical curve in the two extreme regions (error of 10 and 12 % respectively in the first and last portion, Table 2.12, Figure 2.19).

Conversely, the intermediate region of the curves showed a significant discrepancy of the slope. However, the overall difference between the slope of the linear regression of the experimental data and the finite element predictions was less then 9%.

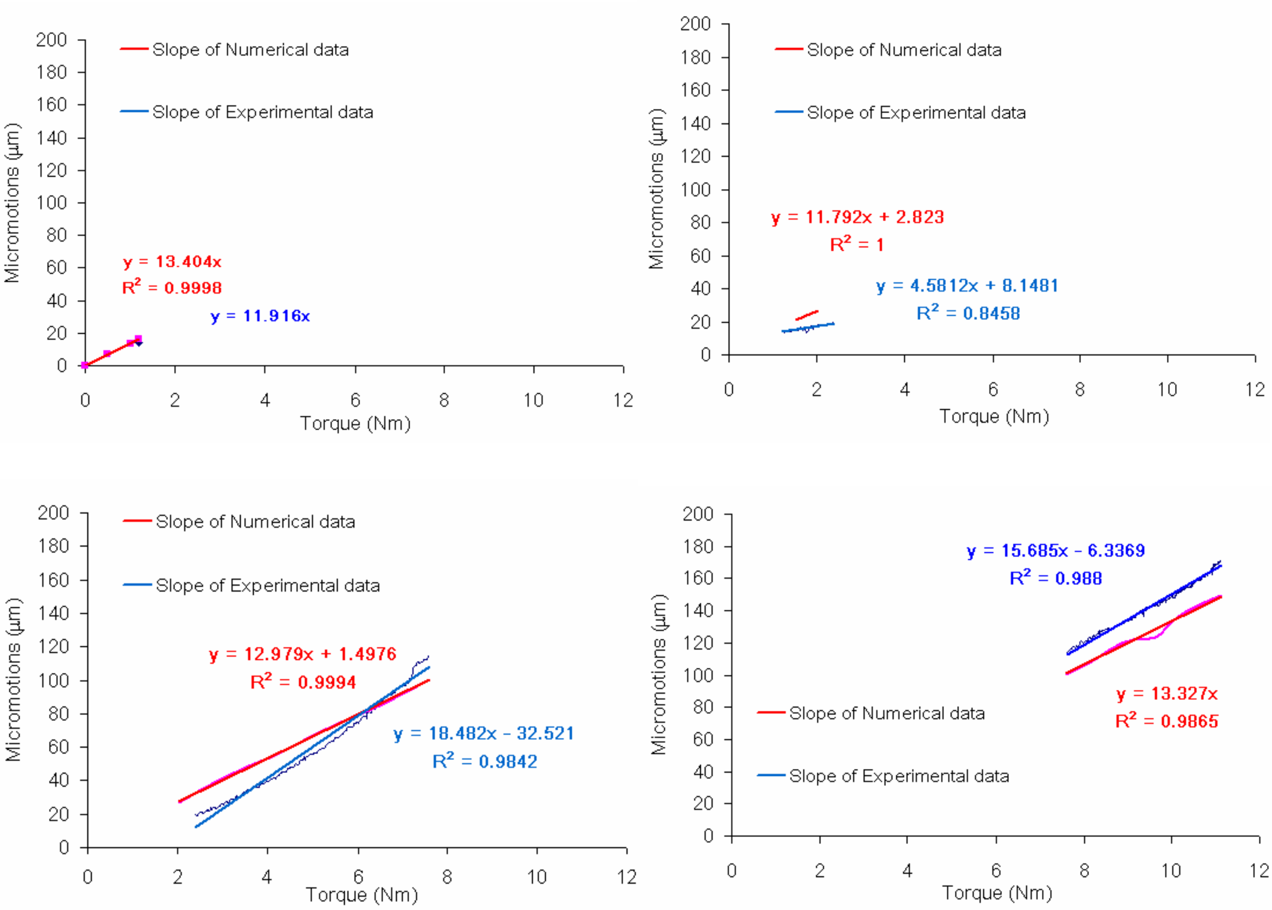

Figure 2.19: Comparison between the slope of the experimental and numerical curves for the 4 analysed spans. Regression equations and the goodness of fit indicators (R^2) are reported for each span.

Range of torque (Nm)	Slope (µm / Nm) Experimental	Slope (µm / Nm) Numerical	% Error
0.0 ÷ 1.2	13.4	12	10 %
1.2 ÷ 2.0	4.6	11.8	157 %
2.0 ÷ 7.6	18.5	13	30 %
7.6 ÷ 11.4	15.7	13.8	12 %

Table 2.12: Slope of the experimental and numerical curves for the four analysed spans. The relative percentage error is also shown.

The observed non-linearity in the range between 1 and 7 Nm (Figure 2.17) for the experimental micromotions could be explained by a compressive yielding of small regions of cancellous bone directly in contact with the distal tip of the stem, producing an increase of micromotion less than proportional to the increase of applied torque. When the cancellous bone yields, stem motion is due partly to additional interface sliding, but also to the (permanent) bone deformation. Only when the yield volume reaches the point called *densification* (Gibson et al., 2005) the local stiffness of the small volume of bone material drastically increase. Then relative motion is again mainly due to interface sliding, and micromotion is proportional to the applied torque. In the Finite Element model, where the bone material is assumed perfectly elastic, the micromotion is linear with the torque at all values. In support of this theory we noticed that small volumes of soft cancellous bone near the interface with the stem exceed the yield strain limit in the FE model. This occurs for torques greater than 1 Nm (Figure 2.20, 2.21), which is the value where the non-linearity in the experimental measurements starts to appear.

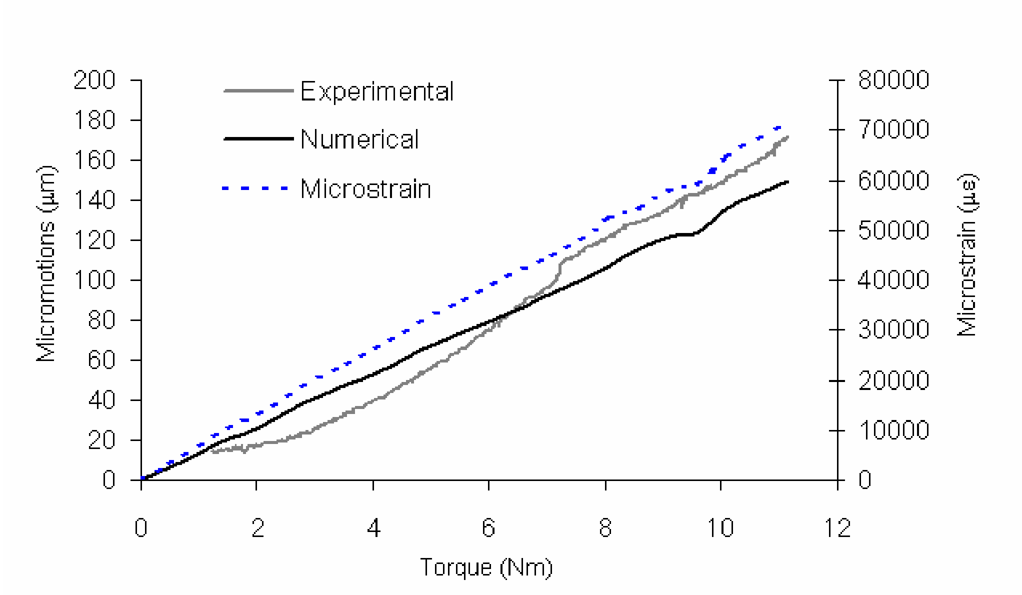

Figure 2 20: History of the relative bone implant micromotions by numerical and experimental measures over the applied torque. In addition, the peak microstrain predicted by the FE model is reporter as function of the torque.

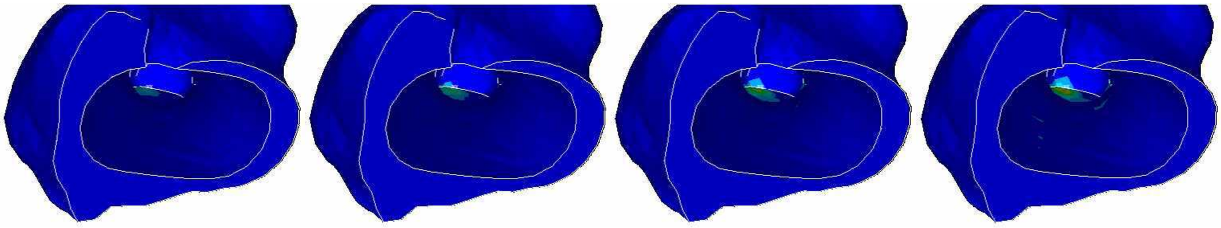

2.3 Nm *4.6 Nm* *6.9 Nm* *9.2 Nm*

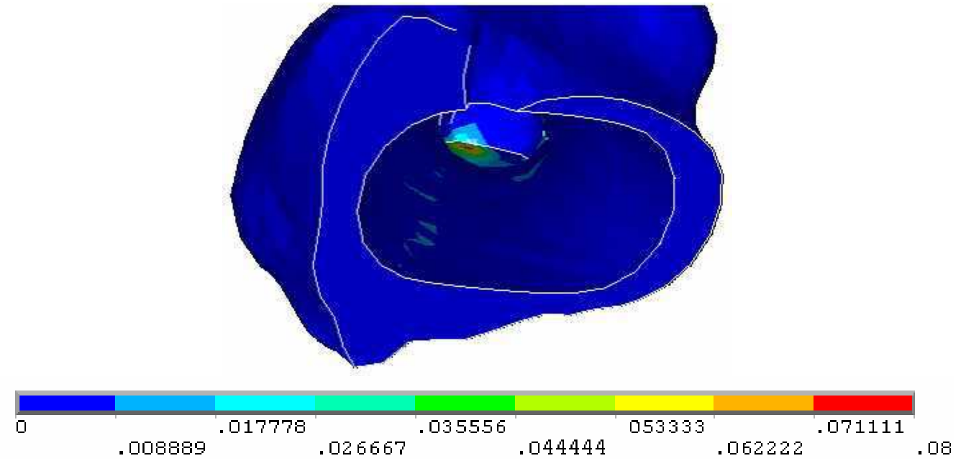

11.4 Nm

Figure 2 21: The Von Mises strain-history in the distal tip of the femoral cavity, due to the stem impingement, is shown over four subsequent increment of the applied torque (0.08 in the legend means 80,000$\mu\varepsilon$, 8%)

2.6.2. Comparison of the ACHIEVED and the PLANNED FE models

At the maximum applied torque of 11.4 Nm, the ACHIEVED FE model predicts 170 μm (Figure 2.22). Experimental micromotions were predicted with an average (RMS) error of 13 μm and a peak error of 26 μm. Thus, a difference of only 20 microns between the ACHIEVED and the PLANNED models, although the stem position differed more than a millimetre, was found.

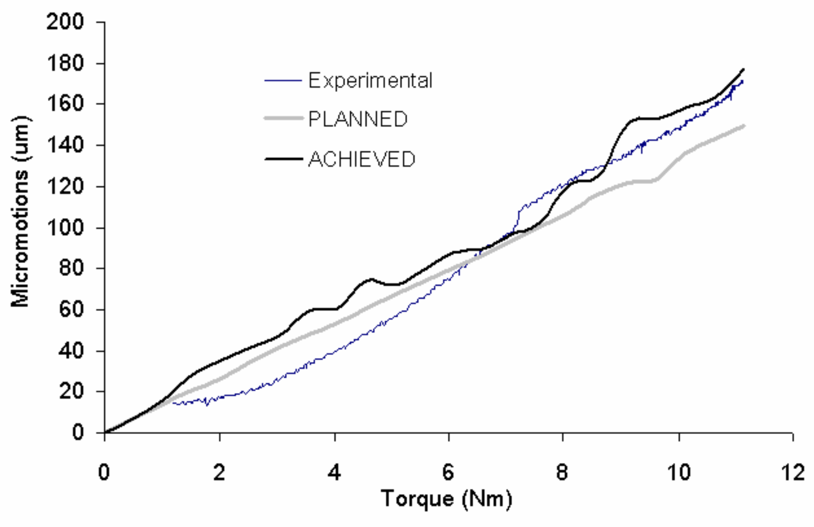

Figure 2.22: The comparison of the history of the relative bone-implant micromotions over the entire rage of the applied torque as predicted by the two developed FE models (PLANNED and ACHIEVED) with the experimental data.

A few elements in the contact region with the highest value of compenetration influence the contact kinematics in a way that arises in the non-perfect linearity of the micromotions history over the applied torque for the model derived by the post-operative CT scan, e.g. the ACHIEVED model (Figure 2.22).

The peak relative percentage error on the Von Mises stress was less than 12% with a predicted maximum value of 10.2 *MPa* by the PLANNED model and 11.5 *MPa* by the ACHIEVED FE model (Figure 2.23).

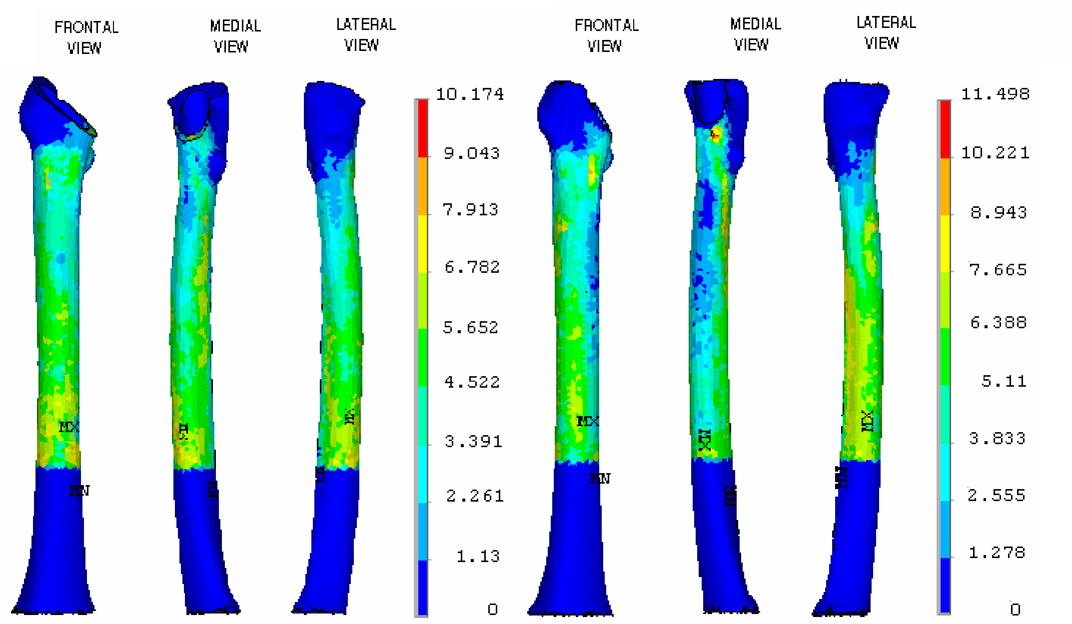

Figure 2.23: The peak Von Mises stress reported for the two developed FE models, PLANNED (left) and ACHIEVED (right), in the frontal, medial and lateral views.

In both cases, the peak equivalent Von Mises strain was located at the bone, at very low density, in contact with the distal tip of the implant. (Figure 2.21 and 2.24). The peak value for the ACHIEVED model was 81000με; the percentage error with respect to the Von Mises strain predicted by the PLANNED model was therefore 14 %.

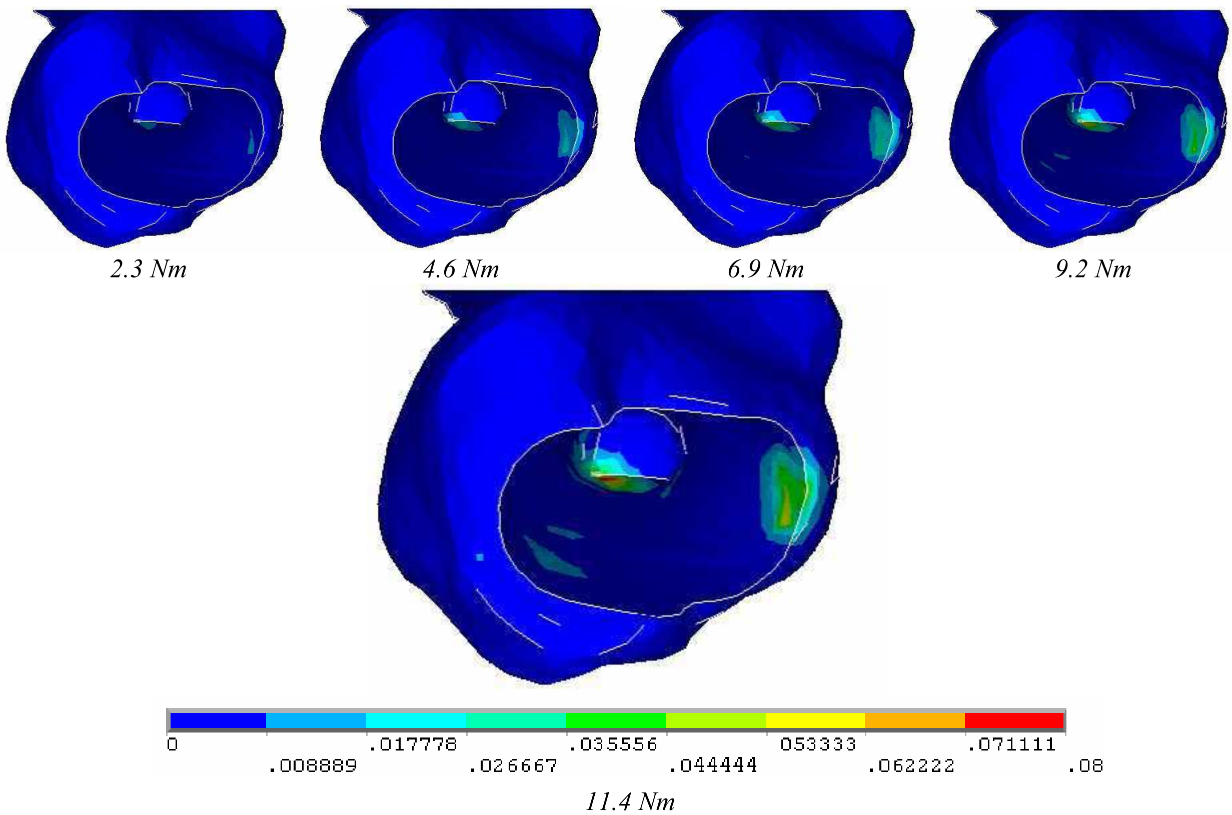

Figure 2 24: The Von Mises strain-history in the distal tip of the femoral cavity of the post-operative model over four subsequent increment of the applied torque (0.08 in the legend means 80,000$\mu\varepsilon$, 8%)

Chapter 2.7

Discussion

The present work was aimed to develop patient-specific Finite Element models of the proximal femur implanted with a cementless anatomical stem and to verify the accuracy with which these models predict the bone-implant relative micromotion. To this purpose, the finite element model of a cadaver femur, implanted with an anatomic cementless hip stem (AncaFit), was developed deriving the anatomy and the material properties from the CT scan of the patient's hip region. The implant position inside the femur was derived from the pre-operative plan that a skilled surgeon performed using a pre-operative planning CT-based software. The comparison of the micromotion at the calcar level as predicted by the numerical model with experimental measurements over the entire range of the applied load was thus carried out.

A good agreement, both in terms of average and peak value, was observed between predicted versus experimental micromotion. The error on the maximum predicted micromotion was only 12% of peak micromotion experimentally measured. The average error over the entire range of applied torques was only 7% of peak measurement.

Also the model predicted the slope of the torque-micromotion curve very close to that experimentally measured. The observed little discrepancy was ascribable to the non-linearity of the experimental micromotion that was not predicted by the model (that incorporated only linear-elastic materials). To preserve the study from the analysis of a singularity, two further specimens were tested, producing the same pattern of the micromotion over the applied torque.

Direct comparison of the reported results with previous studies from the literature is difficult since, to the authors' knowledge, this is the first attempt to predict the relative bone-implant micromotion by means of finite element models without considering an average patient. Additionally, the applied boundary conditions aimed to replicate the specific experimental set-up of the ISAC System were not previously simulated.

The errors found for the predicted micromotion are comparable to those reported in studies with synthetic femurs and clearly acceptable for most applications (Viceconti et al., 2000).

The main limit of the present study is that only one bone was tested. Nevertheless, as previously mentioned, to the knowledge of the authors, no previous study reports a validation of the relative bone-implant micromotion predictions of a FE model against a controlled experiment *in vitro*. In this study, or in previous related studies conducted by our group, we explored the sensitivity of the predictions accuracy to almost all factors related to the surgeon, to the patient, or to the modelling methods, always finding that the results, at least for this prosthetic model, are only mildly sensitive to these factors; because of this, it can be concluded that the present validation should stand true even if it is obtained on a single specimen.

A further limit is the assumption of the bone material as perfectly elastic. This simplified constitutive equation prevents the model from replicating the post-elastic behaviour that is likely to occur. While the inclusion of an elasto-plastic material model would be relatively simple, to date the literature is still controversial on the definition of the yield and the ultimate strength values for both the cortical and the cancellous bone (Keaveny 2001; Ostrowska et al., 2005). This is probably why also in many other numerical studies bone is assumed to be perfectly elastic (El' Sheikh et al., 2003; Senapati et al., 2002; Simōes et al., 2005; Viceconti et al., 2000, 2001, 2004a, 2005).

Aim of the second part of the study was to assess if the subject-specific FE model of an implanted femur as derived by the parameters planned by the surgeon before the operation is able to predict the conditions of the achieved stability of the implant. For this purpose, a second FE model of the implanted femur was generated in which the pose of the stem with respect to the femur was defined using the post-operative CT scan. The predictions of this further model (ACHIEVED) were confronted to those obtained by the FE model derived by the pre-operative planning (PLANNED). Under the same boundary conditions, the peak bone-stem micromotion and the peak Von Mises stress and strain predicted by the two models were then compared.

As first result, the errors found for the predicted micromotion in both FE models, from the comparison with experimental data, are comparable to those reported in studies with synthetic femurs and clearly acceptable for most applications (Viceconti et al., 2000). The difference between the two models was 20 μm in terms of the peak predicted micromotion with a relative percentage error of 12% (PLANNED) and 0.6% (ACHIEVED) with respect to experimental data.

The Von Mises stress was found in close agreement as well, both in terms of distribution and peak value with a peak relative error of less than 12%. The percentage difference in terms of the predicted Von Mises strain was 14%.

The difference of the evolution of the peak micromotion as the applied torque is increased between the Planned and the Achieved models, is due to a mild chattering between a few contact elements that was observed in the Achieved model. This was probably due to small imperfections in the mesh for that model, which produced significant initial compenetration at the interface. However, this phenomenon did not affect the results at convergence and thus can be neglected.

Chapter 2.8

Conclusions

Even with the limitations discussed in the chapter 2.7, the present study confirms that it is possible to create a patient-specific Finite Element model using a pre-operative CT scan and a CT-based pre-operative planning of the stem size and position. This FE model can predict the primary stability of a cementless stem with an accuracy sufficient to draw clinically-relevant conclusions. It is thus confirmed that this type of model can be used as a secondary reference for the validation of less accurate but faster predictive models able to provide a gross estimate of primary stability interactively during pre-operative planning.

The predictions of two FE models of the same implanted femur, one generated from the post-operative CT scan and the other from the pre-operative planning, in terms of micromotion, stress and strain were found in good agreement. Thus, it can be concluded that predictions of primary stability based on the planned position can be used to judge what will happen in vivo, even if the stem is posed slightly differently from what was planned.

Anche con le limitazioni discusse nel capitolo 2.7, il presente studio conferma la possibilità di creare un modello FE “subject-specific” utilizzando da una parte dati TC pre-operatori per derivare l’anatomia e dall’altra un software di pianificazione pre-operatoria per la taglia e la posizione dello stelo. Tale modello FE può predire la stabilità primaria di uno stelo non cementato con un livello di accuratezza sufficiente per guidare decisioni clinicamente rilevanti. Viene quindi confermato che questo tipo di modello può essere utilizzato come riferimento secondario per la validazione di modelli predittivi meno accurati, ma più veloci, in grado di fornire una stima grossolana della stabilità primaria interattivamente durante la pianificazione pre-operatoria.

Le predizioni dei due modelli FE dello stesso femore protesizzato, l’uno generato a partire da dati TC post-operatori, l’altro da dati di pianificazione pre-operatori, in termini di micromovimenti, tensioni e deformazioni, sono state trovate in buon accordo. Può essere pertanto concluso che le predizioni della stabilità primaria basate sulla posizione pianificata dello stelo posso essere utilizzate per giudicare ciò che accadrà in vivo, anche se la posizione dello stelo ottenuta differisce leggermente da quanto pianificato.

References

[1] Bergmann, G., Graichen, F., Rohlmann, A., 1995. Is staircase walking a risk for the fixation of hip implants?. Journal of Biomechanics 28, 535-53.

[2] Bernakiewicz, M., Viceconti, M., 2002. The role of parameter identification in finite element contact analyses with reference to orthopaedic biomechanics applications. Journal of Biomechanics 35, 61-67.

[3] Brekelmans, W.A.M., Poort, H.W., Sloof, T.J.H., 1972. A new method to analyse the mechanical behaviour of skeletal parts. Acta Orthopaedica Scandinava 43, 301-317.

[4] Burke, D.W., O'Connor, D.O., Zalenski, E.B., Jasty, M., Harris, W.H., 1991. Micromotion of cemented and uncemented femoral components. Journal of Bone and Joint Surgery 73B, 33-37.

[5] Callaghan, JJ., Fulghum, CS., Glisson, RR., Stranne, SK., 1992. The effect of femoral stem geometry on interface motion in uncemented porous-coated total hip prostheses: Comparison of straight-stem and curved-stem designs. Journal of Bone Joint Surgery Am 62, 839-848.

[6] Ciarelli, M.J., Goldstein, S.A., Kuhn, J.L., Cody D. D., Brown, M.B., 1991. Evaluation of orthogonal mechanical properties and density of human trabecular bone from the major metaphyseal regions with materials testing and computed tomography. Journal of Orthopaedic Reserches 9, 674-682.

[7] Cristofolini, L., Pelgreffi I., Cappello A., Toni A., 2002a. Intra-operative measurement of cementless hip stem torsional stability. In Proceedings of the 13th Annual Meeting of the European Society of Biomechanics, Wroclaw, Poland, 263-264.

[8] Cristofolini, L., Pelgreffi I., Cappello A., Toni A., 2002b. Intra-operative assessment of the primary stability of cementless hip stems. In Proceedings of the 12th Annual Meeting of the European Orthopaedics Research Society, Lausanne, Switzerland, 90-95.

[9] Cristofolini, L., Varini, E., Pelgreffi, I., Cappello, A., Toni, A., 2006. Device to measure intra-operatively the primary stability of cementless hip stem. Medical Engineering & Physics 28, 475-482.

[10] Dammak, M., Shirazi-Adl, A., Zukor, D.J., 1997. Analysis of cementless implants using interface nonlinear friction-experimental and finite element studies. Journal of Biomechanics 30, 121-129.

[11] Davy, D.T., Kotzar G.M., Brown, RH., Heiple, KG, Goldberg, VM:, Heiple, KGJ., Berilla, J., Burstein, AH., 1988. Telemetric force measurments across the hip after total arthroplasty. Journal of Bone Joint Surgery 70 (A), 45-50.

[12] DiGioia, A.M., Jaramaz, B., Blackwell, M., Simon, D.A., Morgan, F., Moody, J.E., Nikou, C., Colgan, B.D., Aston, C.A., Labarca, R.S., Kischell, E., Kanade, T., 1998. Image guided navigation system to measure intraoperatively acetabular implant alignment. Clinical Orthopaedics and Related Research 355, 8-22.

[13] El' Sheikh, H.F., MacDonald, B.J., Hashmi, M.S.J., 2003. Finite element simulation of the hip joint during stumbling: a comparison between static and dynamic loading. Journal of Materials Processing Technology 143-144, 249-255.

[14] Engh, C.A., O'Connor, D. et al., 1992. Quantification of implant micromotion, strain shielding, and bone resorption with porous-coated anatomic medullary locking femoral prostheses. Clinical Orthopaedics and Related Research (285), 13-29.

[15] Fishkin, Z., Han, S.M., Ziv, I., 1999. Cerclage wiring technique after proximal femoral fracture in total hip arthroplasty. The Journal of Arthroplasty 14 (1), 98-101.

[16] Gustilo, RB., Bechtold, JE., Giacchetto, J., Kyle, RF., 1989. Rationale experience and results of long-stem femoral prosthesis. Clin Orthop 249, 159-168.

[17] Harman, MK., Toni, A., Cristofolini, L., Viceconti, M., 1995. Initial stability of uncemented hip stems: an in vitro protocol to measure torsional interface motion. Medical Engineering Phys 17, 163-171.

[18] Harris, W.H., Mulroy, R.D., Jr., Maloney, W.J., Burke, D.W., Chandler, H.P., Zalenski, E.B., 1991. Intraoperative Measurement of Rotational Stability of Femoral Components of Total Hip Arthroplasty. Clinical Orthopaedics and Related Research 266, 119-126.

[19] Hefzy, M.S., Singh, S.P., 1997. Comparison between two techniques for modelling interface conditions in a porous coated hip endoprosthesis. Medical Engineering & Physics 19,50-62.

[20] Huiskes, R., Chao, E.Y.S., 1983. A survey of finite element analysis in orthopaedics biomechanics: the first decade, Journal of Biomechanics 16, 385-409.

[21] Ishiguro, N., Kojima, T., Ito, T., Saga, S., Anma, H., Kurokouchi, K., Iwashori, Y., Iwase, T., Iwata, H., 1997. Macrophage activation and mogration in interface tissue around loosening total hip artrhoplasty components. Journal of Biomedical Materials Research 35, 339-406.

[22] Jasty, M., Burke, D., Harris, W.H., 1992. Biomechanics of cemented and cementless prostheses. La chirurgia degli organi di movimento 77(4), 349-58.

[23] Bragdon, C.R, Burke, D., Lowenstein, J.D., O'Connor, D.O., Ramamurti, B., Jasty M., Harris, W.H., 1996. Differences in stiffness of the interface between a cementless porous implant and cancellous bone in vivo in dogs due to varying amounts of implant motion. The Journal of arthroplasty 11(8), 945-951.

[24] Jasty M., Ramamurti B. et al., 1997. Factors influencing stability at the interface between a porous surface and cancellanous bone: a finite element analysis of a canine in vivo micromotion experiment. Journal of Biomedical Materials Research 36(2), 274-280.

[25] Kalender, W.A., 1992. A phantom for standardisation and quality control in spinal bone mineral measurement by QCT and DXA: Design considerations and specifications. Medical Physics 19, 583-586.

[26] Keller, T. S., 1994. Predicting the compressive mechanical behaviour of bone. Journal of Biomechanics 27(9), 1159–1168.

[27] Keaveny, T.M., 2001. Strength of trabecular bone. In: Cowin, S.C, (Edt.), Bone Mechanics Handbook, 2ND Edition. CRC Press, Inc., Boca Raton, FL. P.16-5.

[28] Kotzar G.M., Davy D.T., Goldberg, VM., Heiple, KG., Berilla, J., Heiple, KGJ., Brown, RH., Burstein, AH., 1991. Telemeterized in vivo hip koint force data: A report on two patients after total hip surgery. Journal of Orthopaedics Researches 9, 621-633.

[29] Lattanzi, R., Viceconti, M., Zannoni, C., Quadrani, P., Toni, A., 2002. Hip-Op: an innovative software to plan total hip replacement surgery. Medical Informatics and the Internet in Medicine 27(2), 71-83.

[30] Lattanzi, R., Grazi, E., Testi, D., Viceconti, M., Cappello, A., 2003. Accuracy and repeatability of cementless total hip replacement surgery in patients with deformed anatomies. Medical Informatics 28(1), 59-71.

[31] Lattanzi, R., Baruffaldi, F., Zannoni, C., Viceconti, M., 2004. Specialised CT scan protocols for 3-D pre-operative planning of total hip replacement. Medical engineering & physics 26, 237-45.

[32] Maloney, W.J., Jasty, M., Burke, D.W., O'Connor, D.O., Zalenski, E.B., Bragdon, C., Harris, W.H., 1989. Biomechanical and Histologic Investigation of Cemented Total Hip Arthoplasties. A Study of Autopsy-Retrieved Femurs After In Vivo Cycling. Clinical Orthopaedics and Related Research 249, 129-140.

[33] Maloney W.J. and Burke D.W., 1989. Biomechanics of femoral total hip components in simulated stair climbing. Clinical Orthopaedics, 229.

[34] Manes, E., Arancione, V., Andreoli, E., Celli, V., Erasmo, R., 1996. Incidenza delle revisioni dopo 20 anni. Atti II Convegno Internazionale "Attualità e prospettive nella protesi d'anca-i reimpianti". Roma, 16-17 Maggio.

[35] Mann, K., Bartel, D., Wright, T., Burstein, A., 1995. Coulomb frictional interfaces in modeling cemented total hip replacements: a more realistic model. Journal of Biomechanics 28, 1067-1078.

[36] Martens M., Van Audekercke, R., De meester, P., Mulier, JC., 1980. The mechanical characteristics of the long bones of the lower extremity in torsional loading. Journal of Biomechanics 13, 667-676.

[37] McBroom, R.J., Hayes, W.C., Edward, W.T., Goldberg, R.P., 1985. Prediction of vertebral body compressive fracture using quantitative computed tomography. Journal of Bone Joint Surgery [Am] 67(8), 1206-1214.

[38] Mjoberg B., Hansson. LI., Selvik, G., 1984. Instability of total hip prosthesis at rotational stress: A roentgen stereophotogrammetric study. Acta Orthop Scand 55, 504-506.

[39] Monti, L., Cristofolini, L., Viceconti, M., 1999. Methods for quantitative analysis of the primary stability in uncemented hip prostheses. Artificial Organs 23(9), 851-859.

[40] Monti, L., Cristofolini, L., Toni, A., Ceroni, R.G., 2001. In vitro testing of the primary stability of the VerSys enhanced taper stem: a comparative study in intact and intraoperatively cracked

femora. Proceedings of the Institution of Mechanical Engineers. Part H, Journal of engineering in medicine [H] 215(1), 75-83.

[41] Nistor, L., Blaha, JD., Kjellstrom, U., Selvik, G., 1991. In vivo measurements of relative motion between an uncemented femoral hip component and the femur by roentgen stereophotogrammetric analysis. Clinical Orthopaedic 269, 220-227.

[42] Nunn, D., Freeman, MA., Tanner, KE., Bonfield, W., 1989. Torsional stability of the femoral component of hip artrhoplasty: Response to an anteriorly applied load. Journal of Bone Joint Surgery 71, 452-455.

[43] Ostrowska, A., Scigala, k., 2005. The influence of in vitro factors on the bone properties values determination. In Proceeding of the 4th Annual Meeting of Youth Symposium on Experimental Solid Mechanics, Castrocaro Terme, Italy, 93-94.

[44] Pancanti, A., Bernakiewicz, M., Viceconti, M., 2003. The primari stability of cementless stem varies between subjects as much as between activities. Journal of Biomechanics 36, 777-785.

[45] Philips, T.W., Messieh, S.S., McDonald, P.D., 1990. Femoral stem fixation in hip replacement. A biomechanical comparison of cementless and cemented prostheses. Journal of Bone and Joint Surgery 72(3), 431-434.

[46] Philips, T.W., Nguyen, LT., Munro, SD., 1991. Loosening of cementless femoral stems: A biomechanical analysis of immediate fixation with loading vertical, femur horizontal. Journal of Biomechanics 24, 37-48.

[47] Pilliar, R.M., Lee, J.M., Maniatopoulos, C., 1986. Observations on the effect of movement on bone ingrowth into porous-surfaced implants. Clinical Orthopaedics and Related Research 208, 108-113.

[48] Popescu, F., Viceconti, M., Grazi, E., Cappello, A., 2003. A new method to compare planned and achieved position of an orthopaedic implant. Computer Methods and Programs in Biomedicine 71(2), 117-27.

[49] Rho, J.Y., Hobatho, M.C., Ashman, R.B., 1995. Relations of mechanical properties to density and CT numbers in human bone. Medical Engineering and Physic 17, 347-355.

[50] Schneider, E., Eulenberger, J., Steiner, W., Wyder, D., Friedman, R.J., Perren, S.M., 1989a. Experimental method for the in vitro testing of the initial stability of cementless hip prostheses. Journal of Biomechanics 22 (6-7), 735-744.

[51] Schneider E., Kinast, C., Eulenberger, J., Wyder, D., Eskilsson, G., Perren, SM., 1989b. A comparative study of the initial stability of cementless hip prosthesis. Clinical Orthopaedics and Related Researches 248, 200-210.

[52] Schneider, E., Eulenberger, J., Steiner, W., Wyder, D., Friedman, R.J., Perren, S.M., 1989. Experimental method for the in vitro testing of the initial stability of cementless hip prostheses. Journal of Biomechanics 22 (6-7), 735-744.

[53] Schwartz, JT. Jr, Mayer, J.G., Engh, C.A., 1989. Femoral fracture during non-cemented total hip arthroplasty. Journal of Bone Joint Surgery [Am] 71(8), 1135-42.

[54] Senapati, S.K., Pal, S., 2002. UHMWPE-Aluminia ceramic composite, an improved prosthesis materials for an artificial cemented hip joint. Trends Biomaterial Artificial Organs 16(1), 5-7.

[55] Simões, J.A, Marques, A.T., 2005. Design of a composite hip femoral prostheis. Material and Design 26, 391-401.

[56] Søballe, K., Hansen E.S. et al., 1991a. Gap healing enhanced by hydroxyapatite coating in dogs. Clinical Orthopaedic , 300-307.

[57] Søballe, K., Hansen E.S. et al., 1991b. Fixation of titanium and hydroxyapatite-coated implants in arthritic osteopenic bone. Journal of Arthroplasty 6, 307-316.

[58] Søballe K., Brockstedt_Rasmussen H. et al., 1992a. Hydroxyapatite coating modifies implant membrane formation. Controlled micromotion studied in dogs. Acta Orthopaedica Scandinavica 63(2), 128-40.

[59] Søballe K., Hansen E.S. et al., 1992b. Tissue ingrowth into titanium and hydroxyapatite-coated implants during stable and unstable mechanical conditions. J Orthop Res 10, 285-299.

[60] Søballe, K., Hansen, E.S., Brockstedt-Rasmussen, H., Bunger, C., 1993. Hydroxyapatite coating converts fibrous tissue to bone around loaded implants. Journal of Bone and Joint Surgery 75(2), 270-278.

[61] Søballe K., Hansen E.S. et al., 1994. Hydoxyapatite coating enhances fixation of porous coated implants. Acta Orthopaedics research 61: 299-306.

[62] Spears, I.R., Pfleiderer, M., Schneider, E., Hille, E., Morlock, M.M., 2001. The effect of interfacial parameters on cup-bone relative micromotions. A finite element investigation. Journal of Biomechanics 34(1), 113-120.

[63] Stea, S., Bordini, B., Sudanese, A., Toni, A., 2002. Registration of hip prostheses at the Rizzoli Institute. 11 years' experience. Acta Orthopaedica Scandinavica Supplement 73(305), 40-44(5).

[64] Sugiyama, H., Whiteside, L. A., Kaiser, A.D., 1989. Examination of rotational fixation of the femoral component in total hip arthroplasty. A mechanical study of micromovement and acoustic emission. Clinical Orthopaedics and Related Research 249, 122-128.

[65] Taddei, F., Viceconti, M., Manfrini, M., Toni, A., 2003. Mechanical strength of a femoral reconstruction in paediatric oncology: a finite element study. Proceedings of the Institution of Mechanical Engineers. Part H, Journal of engineering in medicine 217(2), 111-119.

[66] Taddei, F., Pancanti, A., Viceconti, M., 2004. An improved method for the automatic mapping of computed tomography numbers onto finite element models. Journal of Medical Engineering & Physics 26, 61-69.

[67] Taddei, F., Martelli, S., Reggiani, B., Cristofolini, L., Viceconti, M., 2006. Finite-Element Modeling of Bones From CT Data: Sensitivity to Geometry and Material Uncertainties. IEEE Transactions on Biomedical Engineering 53 (11).

[68] Taylor, M.M., Meyers, M.H., Harvey, J.P. Jr, 1978. Intraoperative femur fractures during total hip replacement. Clinical Orthopaedics and Related Research 137, 96-103.

[69] Testi, D., Zannoni, C., Cappello, A., Viceconti, M., 2001. Border-tracing algorithm implementation for the femoral geometry reconstruction. Computer Methods and Programs in Biomedicine 65, 175-182.

[70] Testi, D., Simeoni, M., Zannoni, C., Viceconti, M., 2004. Validation of two algorithms to evaluate the interface between bone and orthopaedic implants. Computer Methods and Programs in Biomedicine 74(2), 143-150.

[71] Tissakht, M., Eskandari, H., Ahmed, A. M., 1995. Micromotion analysis of the fixation of total knee tibial component. Computers & Structures 56, 365-375.

[72] Varini, E., Cristofolini, L., Cappello, A., Toni, A., 2004. Primary stability of cementless hip stems: intraoperatively recorded micomotions. In Proceedings of the 14th Annual Meeting of the European Society of Biomechanics, s' Hertogenbosch, the Netherlands, July 4-7, Poster # 229.

[73] Various authors, 2004. Annual Report 2004. The Swedish National Hip Arthroplasty Register. (http://www.jru.orthop.gu.se/)

[74] Various authors, 2005. Annual Report 2005a. Registro dell'Implantologia Protesica Ortopedica. (http://ripo.cineca.it/pdf/049_2005.pdf)

[75] Various authors, 2005. Annual Report 2005b. The Norwegian Arthroplasty Register. (http://www.haukeland.no/nrl/Report2005.pdf)

[76] Viceconti, M., Zannoni, C., Testi, D., Cappello, A., 1999. A new method for the automatic mesh generation of bone segments from CT data. Journal of Medical Engineering Technology 23, 77-81.

[77] Viceconti, M., Muccini, R., Bernakiewicz, M., Baleani, M., Cristofolini, L., 2000. Large-sliding contact elements accurately predict levels of bone-implant micromotion relevant to osseointegration. Journal of Biomechanics 33, 1611-1618.

[78] Viceconti, M., Cristofolini, L., Baleani, M., Toni, A., 2001. Pre-clinical validation of a new partially cemented femoral prosthesis by synergetic use of numerical and experimental methods. Journal of Biomechanics 34, 723-731.

[79] Viceconti, M., Lattanzi, R., Antonietti, B., Paderni, S., Olmi, R., Sudanese, A., Toni, A., 2003. CT-based surgical planning software improves the accuracy of total hip replacement preoperative planning. Medical Engineering & Physics 25(5), 371-377.

[80] Viceconti, M., Davinelli, M., Taddei, F., Cappello, A., 2004a. Automatic generation of accurate subject-specific bone finite element models to be used in clinical studies. Journal of Biomechanics 37, 1597-1605.

[81] Viceconti, M., Chiarini, A., Testi, D., Taddei, F., Bordini, B., Traina, F., Toni, A., 2004b. New aspects and approaches in pre-operative planning of hip reconstruction: a computer simulation. Langenbecks Archives of Surgery 389(5), 400-404.

[82] Viceconti, M., 2004c. Essay: The use of finite element analysis to produce recommendations for clinical practice.

[83] Viceconti, M., Pancanti, A., Brusi, G., Cristofolini, L., 2005. Primary stability of an anatomical cementless hip stem: a statistical analysis. In press on Journal of Biomechanics.

[84] Zienkiewicz , O.C., Zhu, J.Z., 1987. A simple error estimator and adaptive procedure for practical engineering analysis. International Journal for numerical methods in engineering 24, 337-357.

Chapter 3

Surveying on the flexural stiffness of a close-wound coiled spring for a novel joint of robotic hands by means of the Finite Element Method

Indagine sulla rigidezza flessionale
di una molla in configurazione a pacco
per un nuovo giunto di mani robotiche attraverso il
Metodo agli Elementi Finiti

Chapter 3.1

Introduction

The present work is part of a wider study aimed to design and analyse new solutions of robotic hands. The content of innovation of the last generations of robotic hands is mostly tied to a new concept of articulated fingers: the compliant joints. On this direction, a promising solution was found considering the use of an helical steel element (close-wound spring) as basic unit of the hinge.

Analytical models from literature are inadequate to describe the kinematical and structural behaviour of such kind of springs; this leads towards new methodologies of surveying for the close-wound spring configuration. In particular, in the present work, the flexural stiffness of a close-wound helicoidal spring is investigated by means of the Finite Element (FE) method.

An historical overview on the evolution of robotic hands and of the concept of compliant mechanisms is firstly presented.

Afterwards, experimental measurements and analytical results on close-wound springs in the same geometrical configurations are used as benchmark to compare predictions of the developed FE models.

A good agreement was found between data obtained from experimental tests and a purposely-developed analytical model for close-wound springs and the FE predictions with mean relative percentage errors of 11% and 8% respectively.

Finally, a synthesis of the study is suggested comparing the stiffness for both the close-wound and the open-coil helical springs.

Il presente lavoro è parte di un più ampio studio finalizzato alla progettazione ed analisi di nuove soluzioni per mani robotiche. Il contenuto di innovazione dell'ultima generazione di mani robotiche è principalmente legato a nuovi concetti di articolazioni delle dita: i meccanismi compliant. Muovendosi in questa direzione, è emersa una promettente soluzione considerando, come unità base del giunto, elementi a molla elicoidali, nello specifico molle in configurazione a pacco.

I modelli analitici disponibili in letteratura sono inadeguati a descrivere il comportamento cinematico e strutturale di questo tipo di molle spingendo così verso l'impiego di nuove metodologie di indagine. In particolare, nel presente lavoro, viene investigata la rigidezza flessione di una molla in configurazione a

pacco tramite il metodo agli Elementi Finiti (FE).

Si presenta inizialmente una sintesi dell'evoluzione storica delle mani robotiche e del concetto dei meccanismi compliant.

Successivamente, le predizioni del modello FE vengono confrontate con misure sperimentali e con risultati di un modello analitico specificatamente sviluppato per molle a pacco ottenuti nelle stesse configurazioni geometriche.

Si osserva un buon accordo tra i dati ottenuti dalle diverse metodiche di indagine con errore medi percentuali massimi dell'11%, tra FE e sperimentale, e dell'8% tra FE e modello analitico.

In ultimo, una sintesi del lavoro viene suggerita dal confronto tra la rigidezza delle molle in configurazione a pacco e molle a spire aperte.

Chapter 3.2

The state of the art

In this section, an overview to the historical evolution of robotic hands and of the concept of compliant mechanisms till the novel design of articulated finger made with close-wound helical springs is presented.

In questa sezione vengono in breve presentati l'evoluzione storica delle mani robotiche e del concetto di meccanismi compliant fino ad arrivare al nuovo progetto di dita articolate costituite da molle elicoidali in configurazione a pacco.

3.2.1. Historical evolution of robotic hands

The idea of robotic hands took place since 1960s (Godden, 1968). Examples of robotic hands with several working fingers can be found in the studies of Hanafusa, Asadas and Okada in 1980s (Hafanusa et al., 1982; Okada, 1986) (Figure 3.1).

Figure 3.1: Okada robotic hand prototype (Okada, 1986)

With the growth of interest towards humanoid robots, anthropomorphism of robotic hands becomes a necessary design goal, that has been purposely addressed by the most recent research projects. A detailed literature analysis is reported in (Lotti, 2005b).

Anthropomorphism is the device capability to mimic human hand as to size, shape, dexterity and internal mobility.

A wide range of design solutions has been proposed in literature for robotic hands according to different criteria (Lotti et al., 2002a,b,c).

The first classification concerns the modularity, distinguishing between modular and integrated robotic hands. The former can be inserted into whichever type of robotic arm; in the latter, arm and hand cannot be carried out as separated subsystems (examples in Figure 3.2).

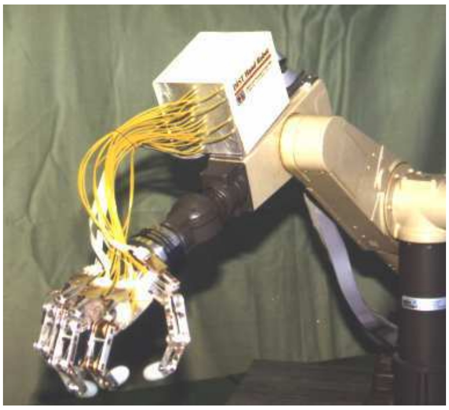

Barret Hand

DIST Hand

Examples of modular Robotic hands

SHADOW Hand

UB Hand

Examples of integrated Robotic hands

Figure 3.2: Modular versus Integrated Robotic Hands: two different constructive approaches

Looking at the choice of the mechanical structure for articulated fingers, most of design solutions were inspired to the exoskeletal model. This consists of a rigid and hollow structure holding inside the organs for the motion transmission as tendons, pulleys, gears or small actuators. Biomorphic models of the human hand were introduced with endoskeletal structures, where actuation, sensors and wiring are placed around an inner stiff framework. This clearly better cope with the human hand structure where bones and ligaments are set in action by muscles and tendons disposed around them (Figure 3.2).

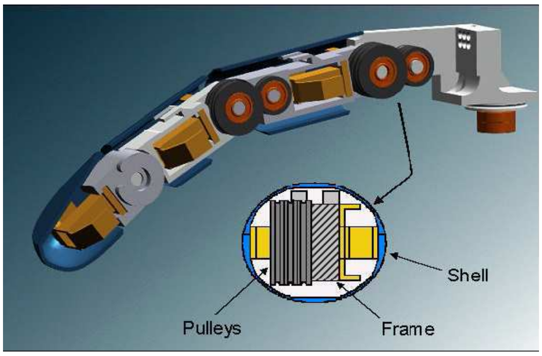

Exoskeletal model

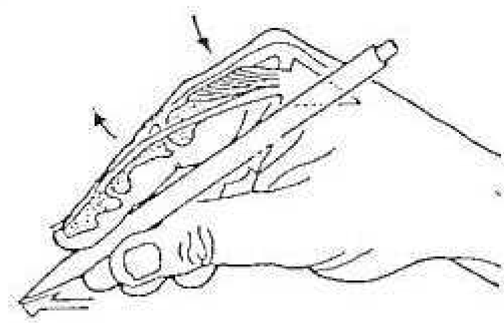
Endoskeletal model

Figure 3.3: Examples of mechanical structures for articulated fingers

An additional classification concerns the system of motion transmission by means of flexible organs. In many robotic hands, pulleys route actuators and joints without friction effects (e.g. UB Hand II (Melchiorri and Vassura, 1995)) whilst, in biological models, tendons are transmitted within lubricated sheathes (Figure 3.4). Pulley help to overcame design problems in developing technological solutions of low friction sheathes, but drastically penalize the advantages of motion transmission with flexible organs.


UB Hand II

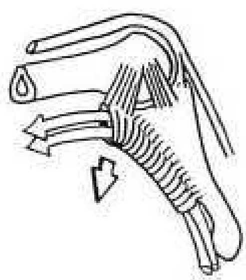
Biological human finger

Figure 3.4: Two different mechanisms of motion transmission

Two main classes of solutions can be identified for the articulated finger structures (Lotti, 2002a) (Figure 3.5):

- joints in which the relative motion between adjacent rigid links is obtained by means of kinematical pairs (that means contact surfaces between the two links and a discontinuity of material),
- compliant mechanism (section 3.2.2.).
-

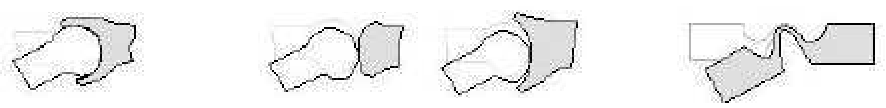
Sliding-contact pair *Rolling-contact pair*
Joints with kinematical pairs *Compliant mechanism*

Figure 3.5: Design solutions for articulated fingers

3.2.2. Compliant mechanisms

A *compliant hinge* (Lobontiu, 2002; Howell, 2001) consists of a flexible, slender region between two rigid parts that can undergo relative displacement due to the deformation of this flexible region under the action of applied loads. The allowed displacements are mainly rotations due to bending about one ore more axes that are called *sensitive axes*. Hinges where bending effects are prevalent are also named *flexure hinges*. Undesired displacements along axes different from the sensitive ones are usually called *parasitic effects* and can represent a severe limitation of the hinge performance.

Rotational precision of a flexure hinge is the capacity to reproduce the kinematical behaviour of an ideal revolute joint placed in the middle of two connected links.

Compliant hinges can profitably substitute revolute or more complex joints inside articulated mechanisms, providing great structural simplification, mass and bulk reduction, ease of assembly and overall reliability improvement. Many different shapes of monolithic hinges (e.g. Figure 3.6) have been proposed and characterized and a vast literature is available about their modelling and design. In particular, systematic work on flexure hinges with mono or multi sensitive axes was made by Lobontiu (Lobontiu, 2002) who provided detailed tools for practical design of many types of flexure hinges. Special design hinges (e.g. Figure 3.7) have been developed for better rotational precision and/or capacity.

Flexure hinges can be used both in planar and in spatial mechanisms: their application is usually limited to cases where the required joint displacement is relatively small, in order to satisfactorily prevent strain and fatigue problems.

The introduction of elastic hinges in robotic articulated structures seems very attractive. Besides some general advantages (simplified design, reduced complexity, elimination of backlash and frictional losses) they can allow a significant reduction of the joint size, generating very slender and light articulated structures, that better cope with the goal of a close reproduction of the biological endo-skeletal models.

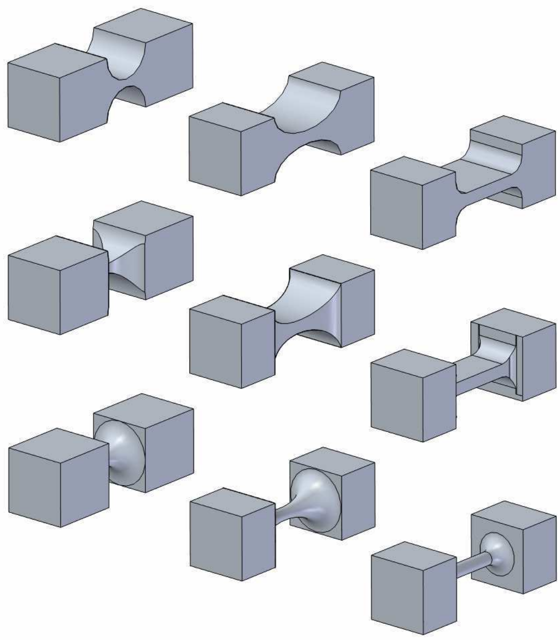

Figure 3.6: Different shapes of elastic hinges

The small displacements allowed by normal flexure hinges can be fully compatible with functional specifications of devices devoted to micromanipulation, but represent an obstacle for the adoption of compliant joints in robotic devices where large displacements may be required, as in the fingers of a robotic hand.

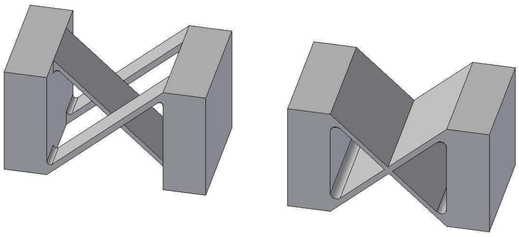

Figure 3.7: Special-design hinges

An increase in the flexibility of flexure hinges should be achieved without increasing the parasitic effects, that can dramatically compromise the performance of the robotic device. As sketched in Figure 3.8, two fingers with elastic joints holding an object in fingertip grasp, could undergo severe problems of grasp stability due to parasitic effects in their compliant joints.

In conclusion, a compliant hinge suitable for application in robotic hands should be purposely designed for some important properties, that are:

- capability of large displacement, while maintaining high reliability, in particular with respect to fatigue failure;
- selective compliance, which means low stiffness about the sensitive axis, high stiffness about all the others (reduction of parasitic effects);
- small size with respect to the length of the connected links and good rotational precision, very useful in defining the kinematical model of the structure.

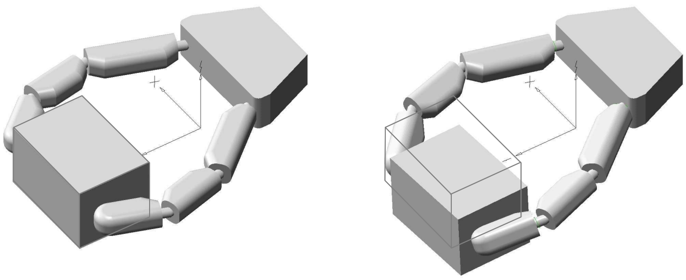

Figure 3.8: Effects of parasitic displacements in a robotic gripper

In a first attempt, a robotic finger with flexure hinges has been developed (Lotti and Vassura, 2002a) (Figure 3.9).

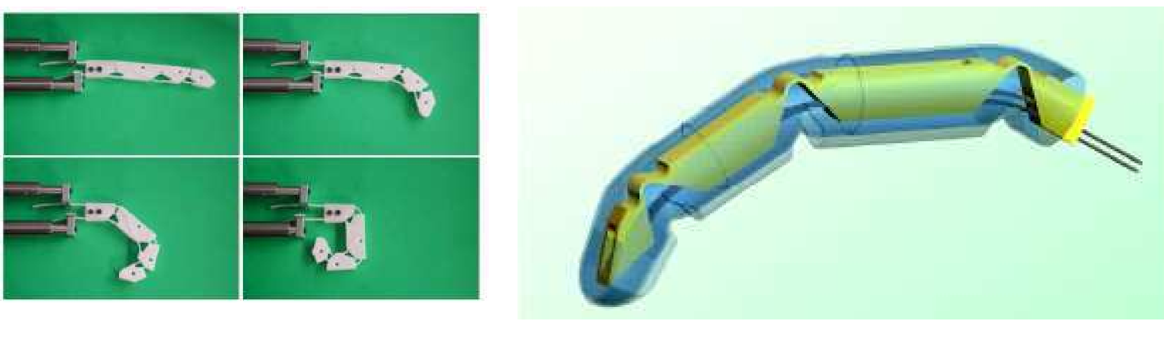

Figure 3.9: Sketches of the finger with flexure hinges

A detailed comparative analysis of different design solutions for flexure hinges (Figure 3.10) has been performed by means of FE analysis (Battaglia, 2002; Zucchelli et al., 2003) (Figure 3.11) mainly focused on kinematical behaviour and the resultant stiffness related to the hinge shape.

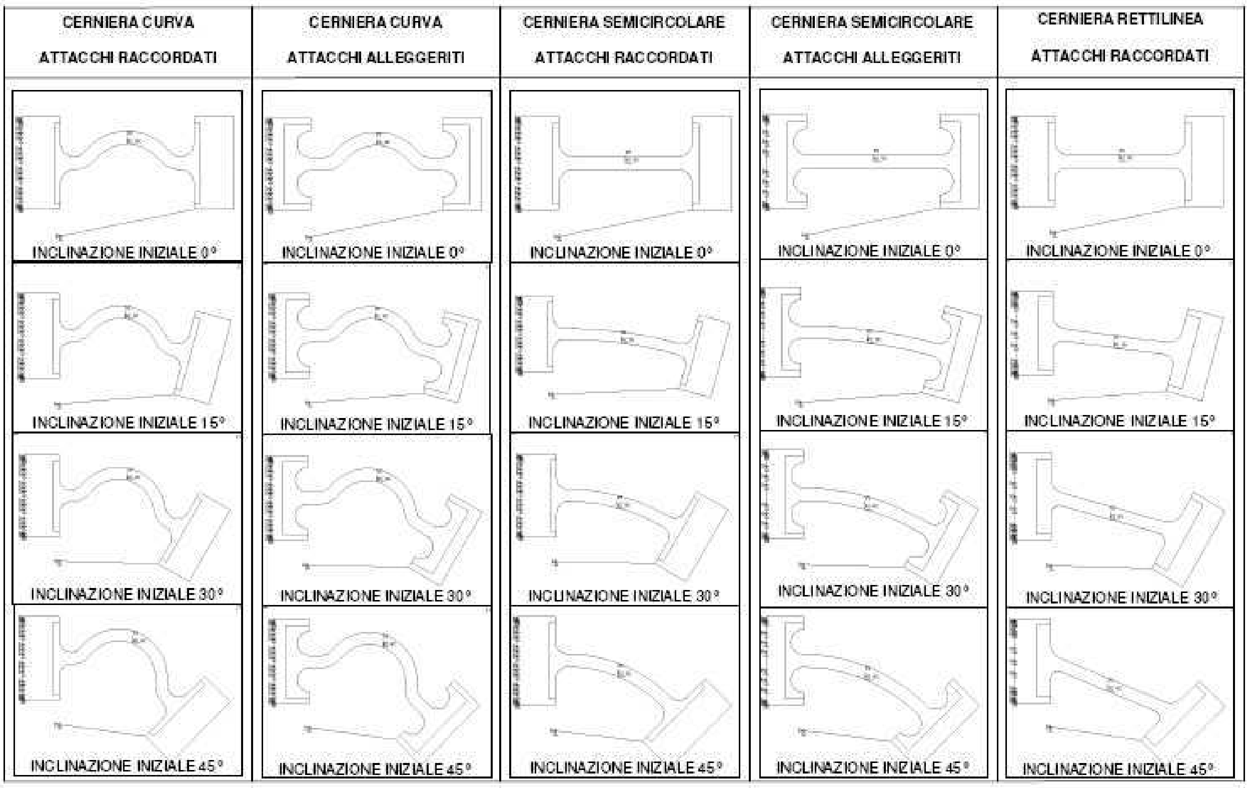

Figure 3.10: Design solutions for flexure hinges

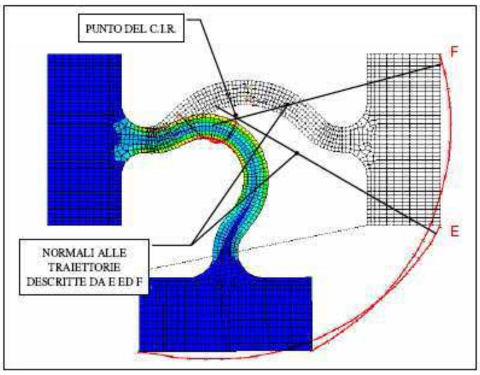

Figure 3.11: Kinematical analysis of the Instantaneous Centre of Rotation by means of FE results

However, although robotic finger with flexure hinges exhibits good kinematical behaviour, it shows unsatisfactory reliability and non-negligible parasitic effects.

Thus, efforts were focused towards the conceptual design of novel types of compliant hinges (section 3.2.2). A promising solution was found considering the use of an helical steel element (close-wound spring) as basic unit of the hinge. Close-wound springs can be manufactured with very small size and individually exhibit a very good bending behaviour when loaded in different directions (multi-axial sensitivity). Furthermore, they can be placed in parallel configuration constituting an elastic hinge with interesting mechanical properties (mono-axial sensitivity).

3.2.3. A novel design of the robotic hand joints by means of springs

A robotic anthropomorphic hand with fingers having spring-based elastic hinges has been developed since 2004 at the University of Bologna (Lotti et al., 2005c; Biagiotti et al., 2004) and is now serving as test bed of such design solution. Figure 3.12 shows the hand performing early manipulation experiments, while Figure 3.13 shows the skeleton of the hand, where multi-spring hinges have been used in all the finger joints, except the thumb proximal joint, where a single-spring hinge has been adopted. The most remarkable feature of this hand is the adoption of a fully endo-skeletal design, with the internal structure covered by a thick compliant layer distributed all over the hand surface. This surface compliance is very useful to get high adaptability of the finger pads over object surface, thus increasing contact area and stability and smoothing oscillations and shocks. This result was possible thanks to the simplification of the internal articulated structure due to the adoption of the compliant hinges.

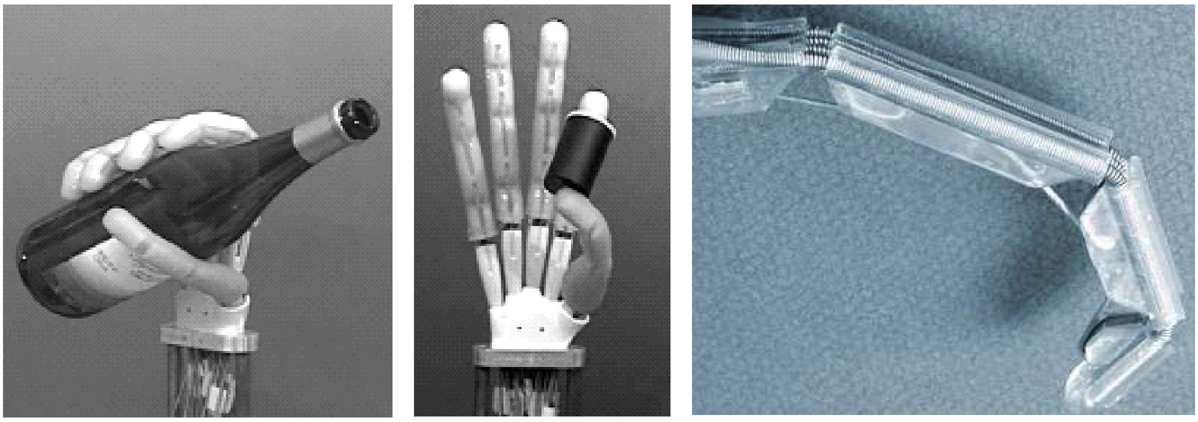

Figure 3.12: The U.B.Hand III during grasping and manipulation experiments

The hinges were sized according to a trial-and-error procedure. After two years of tests the following considerations can be made:

- the compliant hinges have quite satisfactorily substituted a more complex mechanical design, allowing to obtain a one-piece low-cost finger skeleton that has been the base of a modular hand architecture (four equal upper fingers and a special design thumb joined to a tarsal link);
- the reliability of such design solution is very good both in terms of hinge life cycle (no appreciable fatigue effect was noticed) and in terms of the whole finger structure (the compliance of the structure can easily support shocks that could damage conventional structures);
- the kinematical behaviour of spring based hinges is very close to that of a revolute joint, due to the small size of the hinge and to its bending behaviour, so that elastic joints can be approximated to a pin joint and the finger kinematics can be easily computed;
- by placing four or five springs in parallel a good trade-off between bending and torsional stiffness of each hinge has been achieved, (selective compliance), obtaining reduced bending stiffness in the finger plane and avoiding actuator over-sizing;
- in spite of the exhibited transverse compliance (mainly torsional) most grasping operations can be performed with success on objects of mass up to 2 Kg, without grasp loss but with non negligible changes in the hand configuration.

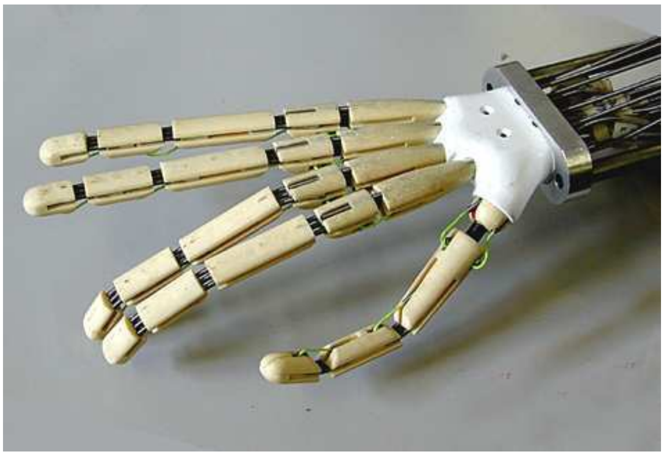

Figure 3.13: The articulated skeleton of the UB Hand

As above said, the development of the spring-based hinges was successful thanks to the intuition of the designer rather than to the availability of satisfactory design tools or optimization criteria; an effort towards a systematic investigation on the behaviour of the proposed hinge configuration seems necessary in order to fully exploit the potential they have, understanding which are the limits on one side, optimizing their performance on the other.

Close-wound helical springs have coils touching each other, due to the fact that the coil pitch p (see Figure 3.14) equals the diameter d of the steel wire. Usually adopted as elastic elements working under axial load, they can however be applied as elastic beams working under any other type of external load. In particular, they exhibit a relatively low flexural stiffness and can easily reach high values of angular displacement under the action of low bending moments. A point of force of this compliant structure is the capability to distribute deformation all along the helical beam, so that a limited number of coils can generate large displacements at the end, while presenting very reduced external size. At the same time parasitic effects are reduced thanks to higher stiffness respect to other load components, so that the spring can be considered a sort of elastic beam with prevalent bending compliance. Common helical springs, that are not close-wound and have $p>>d$, can also be used to this purpose (Yang et al., 2004), but exhibit higher compliance under axial and transverse loads, which is not compatible with the requirement of selective compliance above discussed.

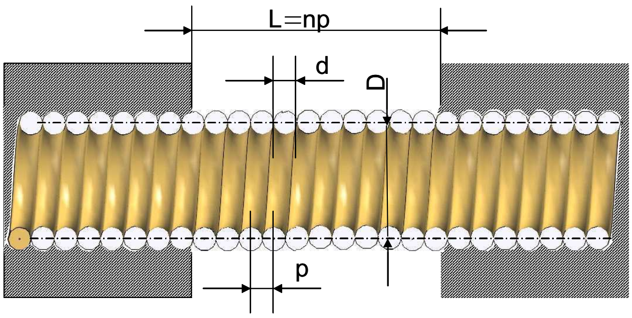

Figure 3.14: Close-wound spring hinge: basic parameters

Different types of compliant hinges made with close-wound springs can be proposed, made of a single spring or of multiple springs differently placed. In any case, each spring is assumed to be rigidly joined at both ends to the links of the articulated structure. This condition can be obtained including a portion of spring of proper length (Figure 3.15) inside the rigid body (e.g. molding the link made of plastic material over the steel spring). The simplest type of hinge, sketched in Figure 3.15, has a single spring, thus allowing bending mobility in any direction.

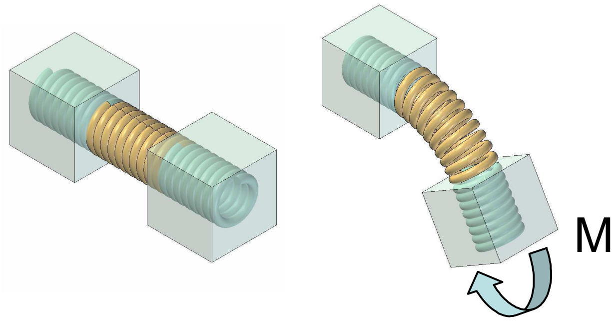

Figure 3.15: Single-spring hinge

This joint presents multi-axial sensitivity and can be useful for robotic structures where multiple degrees of freedom are required (e.g. around normal intersecting rotational axes) and can be of great potential interest in robotic structures mimicking biological joints, like shoulder or thumb proximal articulations.

Preliminary experimental investigation performed on the spring hinges of a robotic finger actuated by tendons (Lotti, 2005b) showed that the position of the centre of rotation (C.o.R.) of one link with respect to the other changes depending on the value of the imposed angular displacement, so that the C.o.R. position is not fixed, but describes a trajectory. The extension of this trajectory is however so small compared with the hinge size, that a C.o.R. position independent of the value of the actual angular displacement can be defined with acceptable approximation. Figure 3.16 represents the repeatability of this C.o.R. position resulting from a series of experiments. It can be noticed that the repeatability is fairly good, but a significant position offset with respect to the ideal joint C.o.R. position must be taken into account. The reported experiments cannot be considered exhaustive and need further investigation, however they show a rotational precision worse than that of classical types of flexure hinges. Anyway it seems compatible with application on robotic devices where other compliant elements are present (e.g. soft pads) and purposely developed sensor-based control techniques, suitable to compensate for uncertainty must be applied.

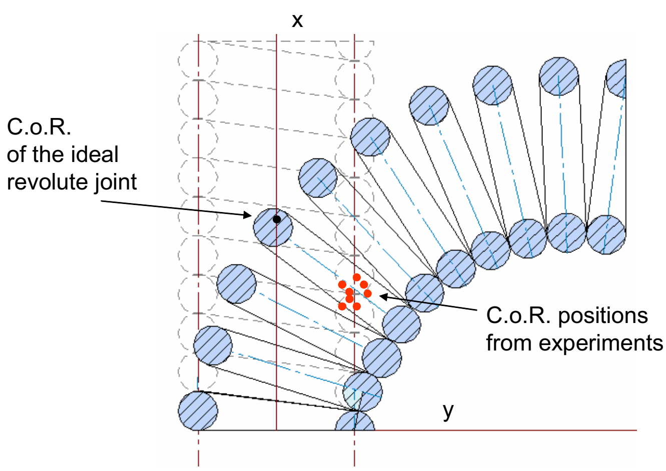

Figure 3.16: Rotary precision of a spring hinge

A second type of hinge adopts a plurality of springs placed in parallel, as sketched in Figure 3.17. By inserting a proper number of springs, it is possible to obtain only one sensitive axis and progressively reduce the parasitic effects.

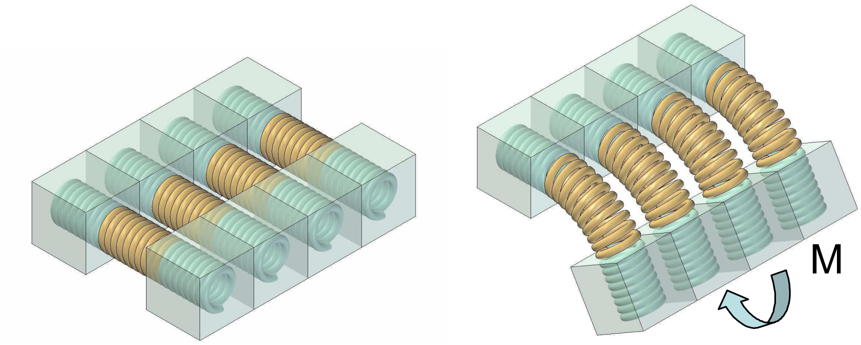

Figure 3.17: Multiple-spring hinge

The achievement of a really selective compliance, that is a good reduction of parasitic effects, mainly depends on the intrinsic properties of each spring, on their number and on their relative placement inside the hinge. A great number of parameters influence the resultant mechanical properties, so that the development of purposely oriented design procedures seems strongly recommendable.

Chapter 3.3

Analytical models available in literature for springs design

Analytical models taken from the literature to compute the flexural rigidity of helicoidal springs are presented. The purposely-developed model for close-wound helical springs under a bending moment is also shown.

Vengono di seguito mostrati i modelli analitici disponibili in letteratura per il calcolo della rigidezza flessione di molle elicoidali. Si presenta inoltre il modello analitico sviluppato specificatamente per molle in configurazione a pacco.

The investigation of analytical models from the literature is restricted to lateral bending, the fundamental loading configuration for the study of the compliant hinges.

The following list of symbols is adopted:

D	Spring helix diameter	[mm]
d	Wire diameter	[mm]
$R = (D\text{-}d)/2$	Mean spring helix radius	[mm]
r	Wire radius	[mm]
ε_o	Helix angle	[rad]
p_o	Helix pitch	[mm]
l	Overall length of the wire	[mm]
L_0	Free length of the spring	[mm]
n	Number of active coils	
E	Young's modulus	[MPa]
G	Shear modulus	[MPa]
ν	Poisson's coefficient	
M	Value of applied moment M	[Nm]

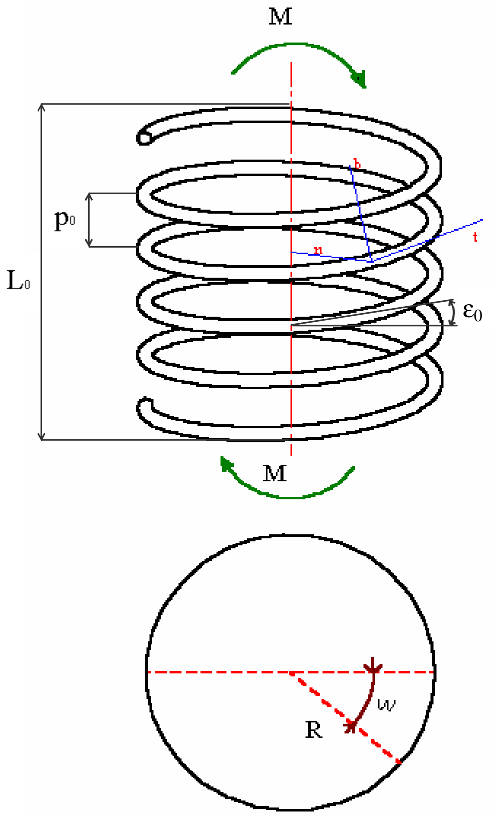

Figure 3.18: Symbols and notations adopted

3.3.1. Analytical models from the theory of elasticity

Analytical models developed for helicoildal springs from the theory of elasticity (Belluzzi, 1947; Timoschenko, 1976) are valid only for small deflections that do not imply mutual contact between coils and a large enhancement of the helix angle. The effect of large deflections (i.e. deflection per turn less than half the coil radius) is accounted, in terms of stresses and deflection, only for open-coil springs under axial load (Wahl, 1978). For close-wound helical springs (i.e. helix angle less than 10 degrees) more exact methods are provided merely under the hypothesis of small deflections and axial loading (Timoschenko, 1976; Wahl, 1978). In case of lateral bending, in all these formulations, the analytical solution for the flexural rigidity is provided only for small deflection where the close-wound configuration is simply accounted by a null helix angle without any other additional consideration.

A discussion on the applicability of these models for the analysis of the close-wound spring configuration is illustrated in chapter 3.6.

Belluzzi, 1947

It is possible to express the loads acting in a cross-section of the helical spring subjected to a bending torque, located by ω angle, according to the coordinate local system defined in the Figure 3.18:

$$\begin{cases} M_t = M\cos(\varepsilon_0)\cos(\omega) \\ M_n = Msen(\omega) \\ M_b = -Msen(\varepsilon_0)\cos(\omega) \end{cases} \tag{3.1}$$

Moments M_b and M_n generate a bending torque, M_t a torsional torque in the cross-section.
The total angular twist for a complete turn is computed by the Principle of Virtual Work (P.V.W.) applying a unit virtual torque M=1 to the overall length of the wire:

$$\Phi = \frac{1}{EJ_n}\int_0^l M\sin^2(\omega)\cdot dl + \frac{1}{EJ_b}\int_0^l M\sin^2(\varepsilon_0)\cos^2(\omega)\cdot dl + \frac{1}{G2J_t}\int_0^l M\cos^2(\varepsilon_0)\cos^2(\omega)\cdot dl \tag{3.2}$$

where *dl* could be found according to this geometrical consideration:

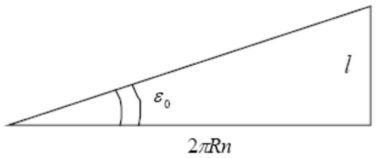

$$l = \frac{2\pi Rn}{\cos(\varepsilon_0)} \rightarrow dl = \frac{R\cdot d\omega}{\cos(\varepsilon_0)} \tag{3.3}$$

Figure 3.19

Integrals in (3.2) can be solved for a single coil then multiplying the result for the number of active coils *n* since loads in equation (3.1) vary in the same way in all coils. Thus, from (3.2) and (3.3) it results:

$$\vartheta = \frac{n}{EJ_n}\int_0^{2\pi} M\sin^2(\omega)\frac{Rd\omega}{\cos(\varepsilon_0)} + \frac{n}{EJ_b}\int_0^{2\pi} M\sin^2(\varepsilon_0)\cos^2(\omega)\frac{Rd\omega}{\cos(\varepsilon_0)} + \frac{n}{G2J_t}\int_0^{2\pi} M\cos^2(\varepsilon_0)\cos^2(\omega)\frac{Rd\omega}{\cos(\varepsilon_0)} \tag{3.4}$$

Solving, being:

$$\int_0^{2\pi}\sin^2(\omega)\cdot d\omega = \int_0^{2\pi}\cos^2(\omega)\cdot d\omega = \pi \tag{3.5}$$

it results:

$$\Phi = \frac{nMR}{\cos(\varepsilon_0)}\pi\left(\frac{1}{EJ_n} + \frac{sen^2(\varepsilon_0)}{EJ_b} + \frac{\cos^2(\varepsilon_0)}{G2J_t}\right) \tag{3.6}$$

Since the wire diameter is circular:

$$J_n = J_b = J_t = \frac{\pi d^4}{64}; G = \frac{E}{2(1+\upsilon)} \tag{3.7}$$

and then:

$$\Phi = \frac{nMR}{\cos(\varepsilon_0)}\pi\left(\frac{2+\upsilon\cdot\cos^2(\varepsilon_0)}{E\cdot J}\right) \tag{3.8}$$

Finally, the flexural rigidity, K, computed as the ratio of bending moment M and the angular twist Φ, results:

$$K = \frac{M}{\Phi} = \frac{EJ}{2 + \upsilon \cdot \cos^2(\varepsilon_0)} \frac{\cos(\varepsilon_0)}{n\pi R} = E \frac{\cos(\varepsilon_0)}{\left(2 + \upsilon \cdot \cos^2(\varepsilon_0)\right)} \frac{1}{n} \frac{\pi d^4 / 64}{\pi R} = E \frac{\cos(\varepsilon_0)}{4 \cdot \left(2 + \upsilon \cdot \cos^2(\varepsilon_0)\right)} \frac{1}{n} \frac{r^4}{R} \tag{3.9}$$

The helix angle ε_0 is defined by

$$\varepsilon_0 = arctg\left(\frac{p_0}{2\pi R}\right) \tag{3.10}$$

For a null value of the helix angle (p_0 << (D-d)), the equation (3.9) becomes:

$$\boxed{K = E \frac{1}{4 \cdot (2 + \upsilon)} \frac{1}{n} \frac{r^4}{R}} \tag{3.11}$$

Wahl, 1978

Wahl (1978) models the spring as a column composed by a number of unclosed circular rings connected by rigid elements. This assumption was proved, by the same author, to be enough accurate when the pitch is half or less the spring helix diameter D. As a direct consequence of this hypothesis, the helix angle is assumed null.

The total angular twist Φ is computed multiplying the number of active coils n for the angular twist of a quarter of coil subjected to a moment M at its end. According to the local coordinate system in Figure 3.18, the loads at the cross-section at an angle ω are:

$$\begin{cases} M_t = M \cos(\omega) \\ M_n = Msen(\omega) \end{cases} \tag{3.12}$$

It immediately can be observed that equation (3.12), compared to (3.1), lacks of the bending term M_b.

The angular twist for the quarter of a coil is computed by the static equilibrium of moments under bending moment M as:

$$\theta_{1/4} = \int_0^{\pi/2} \left(\frac{M \cos^2(\omega)}{EJ_n} + \frac{M \sin^2(\omega)}{G2J_t} \right) \cdot R d\omega \tag{3.13}$$

For a coil, the angular twist results four times that one from equation (3.13)

$$\theta = \frac{\pi MR}{EJ_n} \left(1 + \frac{EJ_n}{G2J_t} \right) \tag{3.14}$$

and, for the whole spring, the angular twist of a coil is multiplied by the number of active coils *n*:

$$\Phi = n \cdot \theta = \frac{\pi n MR}{EJ_n} \left(1 + \frac{EJ_n}{G2J_t} \right) \tag{3.15}$$

The author computes the flexural rigidity both as the ratio of the bending moment M and the angular twist Φ (K) and as the ratio of the bending moment M and the curvature 1/ρ (β_0). According to the former definition, it results, for a circular cross-section (see equation (3.7)):

$$\boxed{K = \frac{M}{\Phi} = E\frac{1}{4\cdot(2+\upsilon)}\frac{1}{n}\frac{r^4}{R}} \tag{3.16}$$

This corresponds to equation (3.11) from (Belluzzi, 1947) under the hypothesis of a null helix angle.

According to the latter definition, being the angular deflection per unit axial length, i.e. the curvature 1/ρ,

$$\frac{1}{\rho} = \frac{\Phi}{L_0} \tag{3.17}$$

the flexural rigidity β_0 is defined, for a cross-circular section (equation (3.7), as:

$$\boxed{\beta_0 = \frac{M}{1/\rho} = \frac{M\cdot L_0}{\Phi} = \frac{2L_0EJG}{n\pi R(2G+E)}} \tag{3.18}$$

Timoschenko, 1976

The bending torque M acting on a cross-section of the helical spring can be expressed as the sum of three contributions: two bending moments and a torsional moment. The elastic energy results:

$$U = \frac{\pi nR}{\cos(\varepsilon_0)}\cdot\left[\frac{M^2\cdot\left(1+\sin^2(\varepsilon_0)\right)}{2EJ} + \frac{M^2\cos^2(\varepsilon_0)}{4GJ}\right] \tag{3.19}$$

Under the hypothesis of a null value of the helix angle:

$$U = \pi nR\cdot\left[\frac{M^2}{2EJ} + \frac{M^2}{4GJ}\right] \tag{3.20}$$

The angular deflection of one end of the spring with respect to the other is:

$$\frac{L_0}{\rho} \tag{3.21}$$

where ρ is the curvature radius of the elastic line. The curvature 1/ρ can be estimated equalling the work of the bending moment M to the elastic energy in (3.19):

$$\frac{M}{2}\frac{L_0}{\rho} = U \tag{3.22}$$

From (3.20) and (3.22) it results:

$$\frac{1}{\rho} = \frac{n\pi RM}{L_0EJ}\left[1+\frac{E}{2G}\right] \tag{3.23}$$

As Wahl (1978), Timoshenko computes the flexural rigidity as the ratio between the bending moment M and the curvature $1/\rho$ (β_0):

$$\boxed{\beta_0 = \frac{M}{1/\rho} = \frac{2L_0 EJG}{n\pi R(2G+E)}} \tag{3.24}$$

It results the same expression of (3.18) from Wahl.

Other formulations

A number of other formulations have been proposed in literature to investigate the mechanical behaviour of helical springs (i.e. Cook and Young, 1985; Belingardi, 1988; Haringx, 1949). Nevertheless, all these analytical models are not suitable to cope with the kinematical and structural behaviour of close-wound helical springs under large deflections, neither for a preliminary investigation.

3.3.2. A mathematical model for the close-wound helical spring

An analytical model able to take into account both the contact occurring between adjacent coils during the deflection and the non-linearity due to the large displacements has been purposely developed (Ciocca, 2003; Lotti, 2005b). This model represents an extension of models previously analysed (see sections 3.3.1.).

Similarly to the analysis of non close-wound springs, the overall spring angular displacement (Φ) is assumed as the sum of the elementary contributions provided by the single coils (θ) (see Figure 3.20).

$$\Phi = n \cdot \theta \tag{3.25}$$

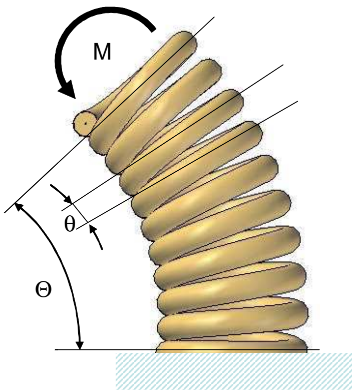

Figure 3.20: Close-wound spring subjected to lateral bending

Furthermore, the same approach is used to correlate the external loads acting on the spring to the loads acting on a generic cross section in the local coordinate system (n, t, b) (Figures 3.18 and 3.21).

The peculiarity of the proposed model, that makes it suitable to analyze close-wound springs, is the assumption that the initial and terminal sections A, B of each coil (see Fig. 3.21) remain in contact during the deformation and that friction is negligible.

From this consideration it's reasonable to model the single coil constrained as the hyperstatic curved beam.

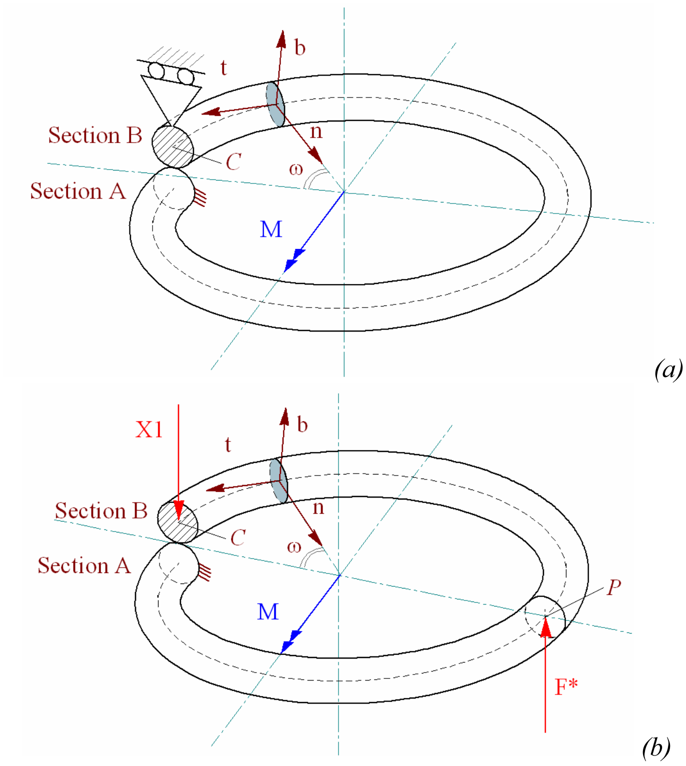

Figure 3.21: Constraint configuration of the single coil

Assuming that the contact friction is negligible, the constraint reaction X1 acting on the section B is normal (Figure 3.21b) and the internal actions on a generic cross section (defined by angular position ω) expressed in the local coordinate system are:

$$\begin{cases} M_t = M \cdot \cos(\omega) \cdot \cos(\varepsilon_o) - X1 \cdot R \cdot (1 - \cos(\omega)) \cdot \cos(\varepsilon_o) \\ M_n = M \cdot sin(\omega) + X1 \cdot R \cdot sin(\omega) \\ M_b = -M \cdot \cos(\omega) \cdot sin(\varepsilon_o) + X1 \cdot R \cdot (1 - \cos(\omega)) \cdot sin(\varepsilon_o) \end{cases} \tag{3.26}$$

In this formulation the effects of normal and shear loads, according to the considerations expressed in literature (Belluzzi, 1947), are neglected.

It's possible to obtain X1 as function of the applied moment M posing the congruency equation (3.27), where the displacement of point C, δ_C, can be calculated by means of Castigliano's Theorem (3.28).

$$\delta_C = 0 \tag{3.27}$$

$$\delta_C = \frac{\partial(L)}{\partial X1} = 0 \tag{3.28}$$

where L is the strain energy:

$$L = \frac{1}{2}\int_0^l \left[\frac{M_t^2}{GJ_p} + \frac{M_n^2}{EJ_n} + \frac{M_b^2}{EJ_b} \right] dl$$

$$\text{with} \quad J_n = J_b = \frac{\pi d^4}{64} \quad and \quad J_p = 2 \cdot J_n \tag{3.29}$$

Finally, X1 results:

$X1 = \frac{Z}{A}$; where

$$Z = -MR^2\pi \left[\frac{\cos(\varepsilon_o)}{G \cdot J_p} + \frac{sin^2(\varepsilon_o)}{E \cdot J_b \cdot \cos(\varepsilon_o)} + \frac{1}{E \cdot J_n \cdot \cos(\varepsilon_o)} \right] \tag{3.30}$$

$$A = \pi R^3 \left[\frac{3\cos(\varepsilon_o)}{G \cdot J_p} + \frac{1}{E \cdot J_n \cdot \cos(\varepsilon_o)} + \frac{3sin^2(\varepsilon_o)}{E \cdot J_b \cdot \cos(\varepsilon_o)} \right]$$

Once known the X1 reaction, according to the scheme of Figure 3.21b, it's possible to correlate the external torque M with the displacements of the P middle point of the coil by means of the Principle of Virtual Work (P.V.W.), introducing the virtual force F*, according to the following notation:

$$\delta_p = \frac{\lim}{F^* \to 0} \left(\frac{\partial(L)}{\partial(F^*)} \right); \tag{3.31}$$

where L is expressed as function of M_n, M_t, M_b and is calculated as follows:

$$\begin{cases} M_t = M \cdot \cos(\omega) \cdot \cos(\varepsilon_o) - X1 \cdot R \cdot (1 - \cos(\omega)) \cdot \cos(\varepsilon_o) + \\ +F^* \cdot R \cdot (1 + \cos(\omega)) \cdot \cos(\varepsilon_o); \\ M_n = M \cdot sin(\omega) + X1 \cdot R \cdot sin(\omega) + F^* \cdot R \cdot sin(\omega); \\ M_b = -M \cdot \cos(\omega) \cdot sin(\varepsilon_o) + X1 \cdot R \cdot (1 - \cos(\omega)) \cdot sin(\varepsilon_o) + \\ -F^* \cdot R \cdot (1 + \cos(\omega)) \cdot sin(\varepsilon_o). \end{cases} \tag{3.32}$$

The development of above equations provides:

$$\delta_p = \frac{1}{B \cdot \cos(\varepsilon_o)} \cdot \begin{Bmatrix} M \cdot R^2 \cdot \pi \cdot \left[(1+\nu) \cdot \cos^2(\varepsilon_o) + 1 + sin^2(\varepsilon_o) \right] + \\ +X1 \cdot R^3 \cdot \pi \cdot \left[-(1+\nu) \cdot \cos^2(\varepsilon_o) + 1 - sin^2(\varepsilon_o) \right] \end{Bmatrix} \tag{3.33}$$

where:

$$E \cdot J_n = E \cdot J_b = B \qquad G \cdot J_p = \frac{B}{(1+\nu)}; \tag{3.34}$$

The following geometrical considerations, concerning the kinematical behaviour of the coil during the deformation, allow to obtain the rotation of a single coil from the displacement δ_P. Note that in order to take into account the non-linearity due to large displacements, the model is computed by a recursive procedure. For each step, the input torque is increased of an incremental quantity (ΔM) and θ_i is calculated as function of the previous value θ_{i-1}. The process ends when the overall rotation (Φ) occurring between the free ends of the spring reaches a value (Φ_{End}) imposed by the user. Called *m* the number of the steps of the recursive procedure, it results:

$$\theta = \sum_{i=0}^{m} \theta_i \quad and \quad \theta_{i-1} = \sum_{k=0}^{i-1} \theta_k \tag{3.35}$$

As explained in the Figure 3.22, θ_i can be calculated once known the displacement δ_P at the step *i* as follows:

$$\theta_i = \frac{\sqrt{\delta_{pi}^2 + \eta_{pi}^2}}{D} \tag{3.36}$$

where η_{pi} is obtained as function of the angle in θ_{i-1} known at the previous step, according to this expression:

$$\eta_{pi} = \delta_{pi} \cdot \tan(\theta_{i-1}) \tag{3.37}$$

It's assumed that $\theta_0 = 0$:

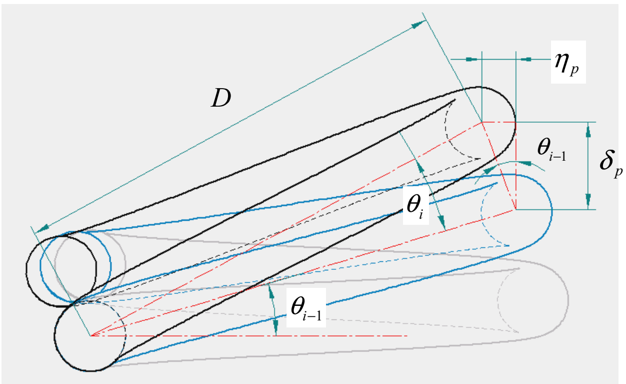

Figure 3.22: Geometrical scheme for calculation of θ_i known δ_P

The Figure 3.23 shows the results obtained by the proposed model. The first plot (3.23 (a)) describes the relationship between torque and imposed rotation for three springs different only for the wire diameter. Note that this relationship appears strongly linear.

The surface, shown in the Figure 3.23 (b), defines a color-map representation that outlines the influence of two basic spring parameters: the wire diameter *d* and the spring external diameter *D*, on the torque necessary to obtain 90° deflection of a single spring.

This last plot shows how the model may represent a useful tool for the joint design. The points highlighted on the diagram indicate the combination of values for which both experimental validation (Lotti, 2005b) and numerical analysis (see chapter 3.4) were performed.

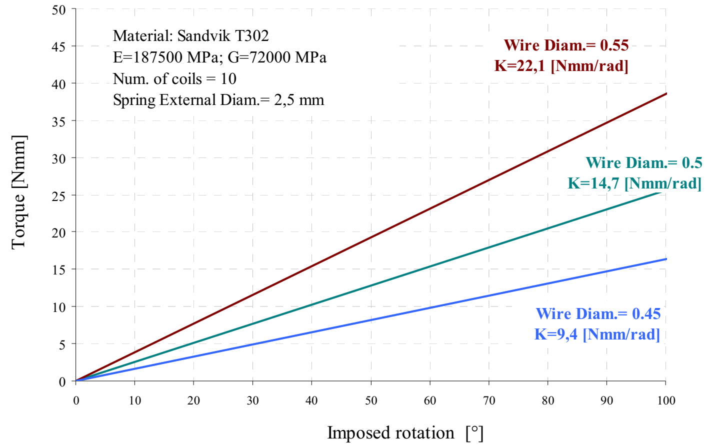

(a)

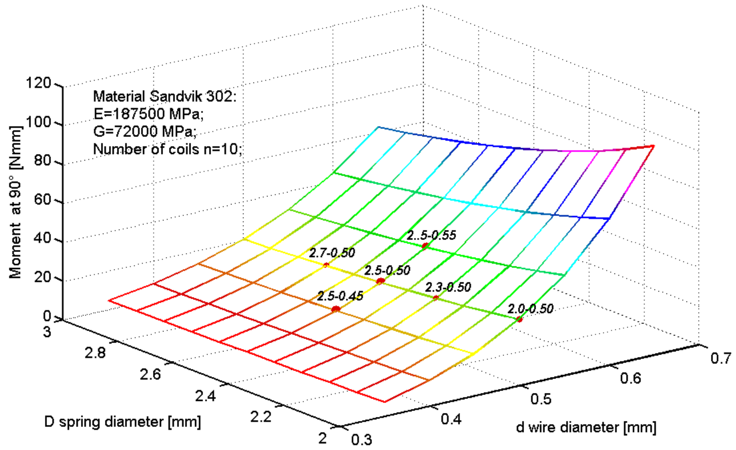

(b)

Figure 3.23: (a) Torque vs. imposed rotation computed by the analytical model; (b) Color map representation of the proposed model output

Chapter 3.4

Finite Element model of a close-wound coiled helicoidal spring

This session presents the methodology applied to generate the FE model of a close-wound coiled helical spring for different geometrical configurations of the wire and the spring diameters.

Questa sezione presenta la metodologia sviluppata per generare il modello agli Elementi Finiti di una molla elicoidale a pacco per diverse configurazioni geometriche dei diametri dello spira e della molla.

The problematical enforceability of the analytical models led towards the application of various methodologies of surveying for the close-wound spring configuration. In the present work, a numerical analysis of the close-wound cylindrical spring under a bending moment M has been performed by means of FE method. The following steps were followed:

- Geometrical modelling of the close-wound spring;
- Mesh definition and selection of the proper mesh refinement, with development of a comprehensive numerical model;
- Realistic representation of the boundary conditions;
- Test scheduling;
- Setting of the solution parameters and execution.

The investigation has been restricted to a limited number of coils, accounting for the fact that in the case of pure bending the resultant angular displacement can be considered the sum of equal contributions due to the single coils under the same bending moment (Belluzzi, 1947; Timoschenko, 1976; Whal, 1978).

Thus a four-coil model was considered (Figure 3.24); two end-coils were introduced to apply suitable boundary conditions while two central coils were considered active, that means contributing to the spring deformation. In order to solve convergence problems it was necessary to add to each end coil an additional coil portion of about 36 degrees.

This model represents the minimum significant structure in order to describe the mechanical behaviour of a spring since it allows both to account for mutual rotation and for contact between two adjacent coils and to correctly consider the boundary effects.

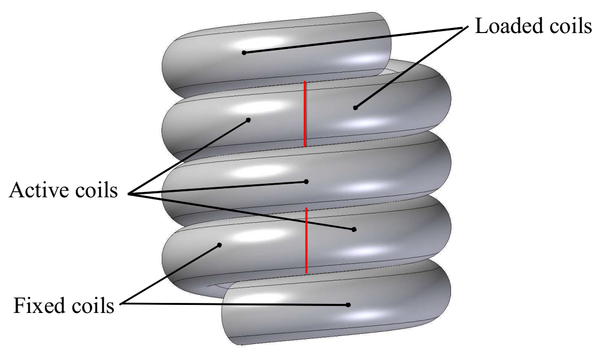

Figure 3.24: The geometrical model of the four coils spring

In order to generate distinct target-surface and contact-surface, required by the adopted FE code to implement the face-to-face contact, the geometrical model of each coil (Figure 3.25 (c)) was obtained combining an internal helical core (Figure 3.25 (a)) and two external helical volumes with lunette-shaped cross section (Figure 3.25 (b)). The tolerance of the helical pitch was set in both cases to the minimum positive value (0.004 mm).

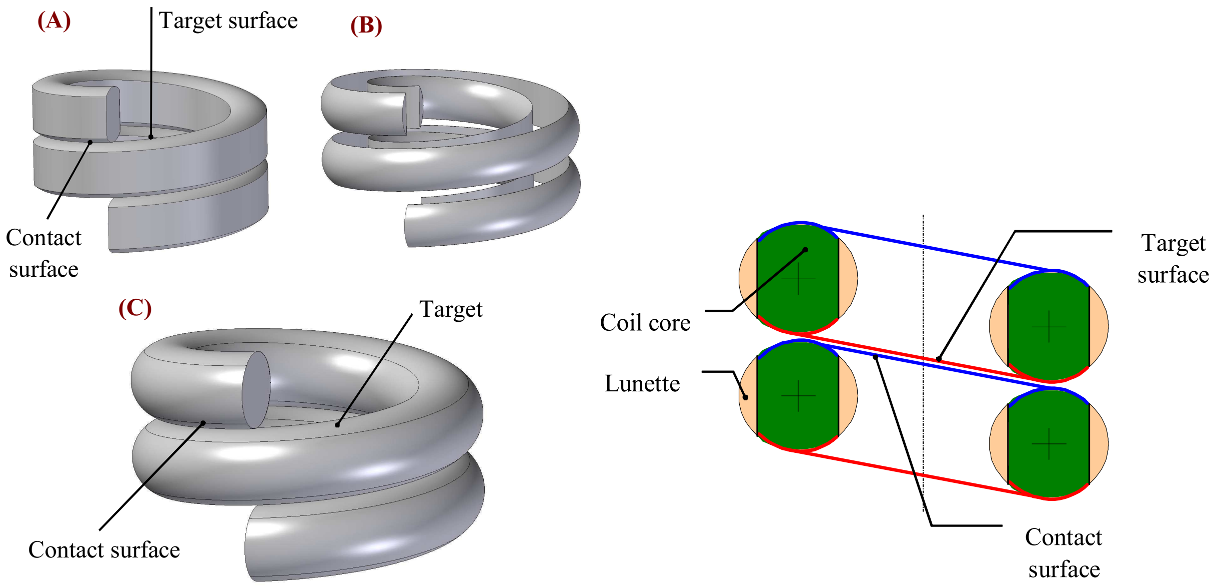

Figure 3.25: Subsequent steps in the contact surfaces generation(left): (a) coil core; (b) lunette volumes (c) overall model; (right) 2-D representation of the volume divisions

As second step, a linear (h-type) convergence test was performed on five unstructured meshes with increasing refinement levels, consisting of 10-noded parabolic tetrahedral elements (Forrester, 2001; Ansys Theory Reference), in order to ensure the numerical accuracy of the model. The average element length was set to 0.15 mm.

Unilateral frictionless contact was assumed between two adjacent coils. With the aim of obtaining a minimum time-consuming FE model, the contact region was defined including only the areas of likely compenetration (Figure 3.26).

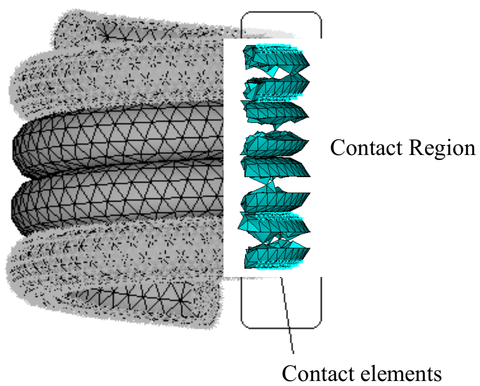

Figure 3.26: Definition of the contact region

The pilot node technique has been adopted for the realistic representation of the boundary conditions (Ansys Theory Reference). Two additional external nodes with both rotational and translational degrees of freedom, that is the so-called pilot node, were defined and rigidly linked to both opposite end coils allowing a rigid transmission of body motion to the nodes of the meshed structure (Figure 3.27).

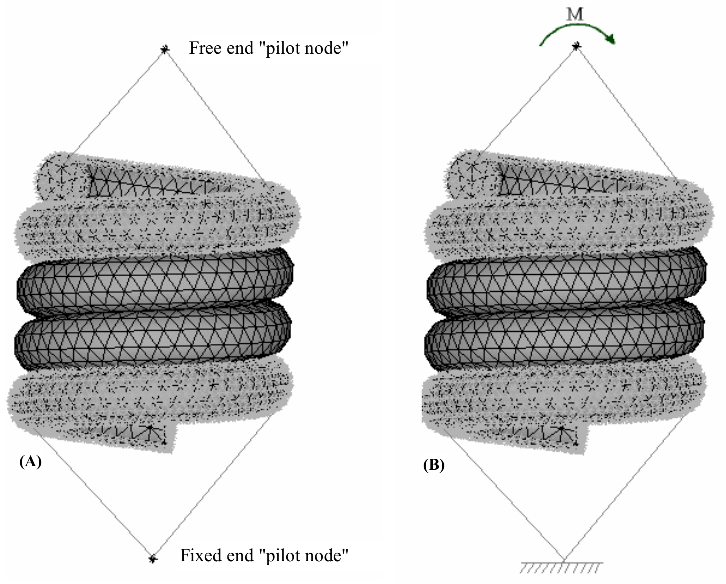

Figure 3.27: Definition of the contact region

One of the pilot nodes was fixed, the opposite one was allowed to rotate around the sensitive axis under the action of the bending moment.

The test schedule has been defined in order to be congruent with the program of experimental tests (Lotti, 2005b; see Figure 3.23 (b)), that means adopting the same geometrical parameters of the available springs (*d, D*) and the same values of displacement imposed to each coil unit (Table 3.1).

Spring Diameter *D*	2.0			2.3			2.5			2.7		
Wire diameter *d*	0.45	0.50	0.55	0.45	0.50	0.55	0.45	0.50	0.55	0.45	0.50	0.55

Table 3.1: Geometrical configuration replicated with the FE models

The value of the applied moment M was chosen so that the resultant angular displacement was in the range of values obtained from corresponding experiments.

The FE models were solved performing a non-linear analysis due to relatively large deflections. The load history was subdivided into a number of substeps that guarantee the solution convergence. An augmented Lagrangian approach with a full Newton-Raphson iterative scheme on residual force, combined with line search technique, was chosen to solve the contact problem. For force convergence, 1% tolerance based on Euclidean L_2 norm was used. The peak compenetration was monitored, since it must be very small to get a good level of numerical accuracy. The default contact normal stiffness factor involved a negligible peak compenetration (maximum value 0.002 μm).

Chapter 3.5

Results

In this section, the main results of the numerical simulations are presented. The FE model predictions of the flexural rigidity are compared to experimental data and analytical results of the purposely-developed model for close-wound springs.

Sono di seguito riportati i principali risultati delle simulazioni numeriche effettuate. Le predizioni del modello FE in termini di rigidezza flessionale della molla, sono comparati con dati sperimentali e con i risultati di un modello analitico specificatamente sviluppato per molle in configurazione a pacco.

In Figure 3.28 it is shown an example of the FE model kinematics for a specific geometric configuration (*D*=2.5 mm, *d*=0.5 mm).

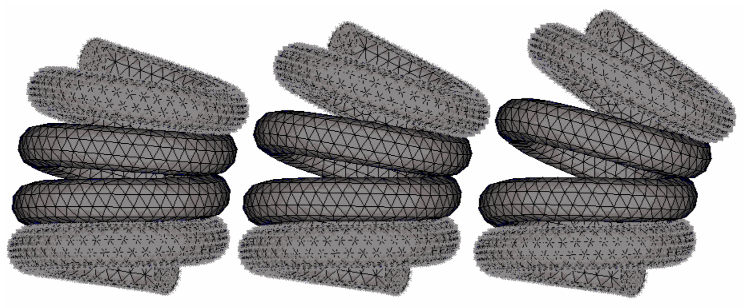

Figure 3.28: Kinematics of the developed FE model for three subsequent increments of the applied torque

The flexural rigidity has been computed according to the definition of (Belluzzi, 1947) as the ratio between the moment and the angular deflection, i.e. the rotation.

The Figure below shows the results obtained by the numerical simulation. This plot describes the relationship between torque and imposed rotation for three springs that differ only for the wire diameter. The linear regressions fit the results of single substeps.

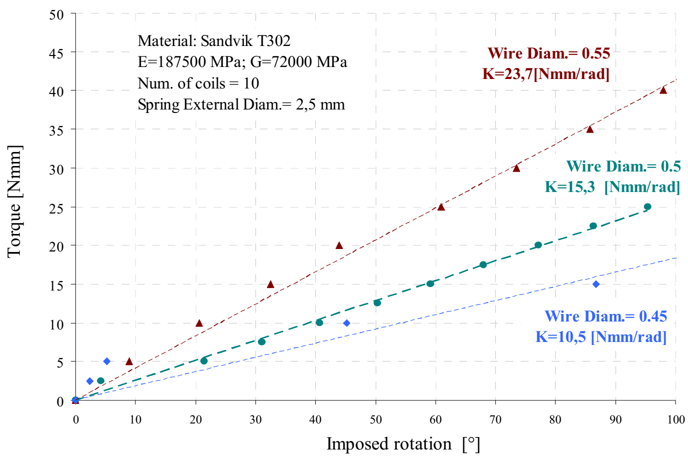

Figure 3 29: Torque vs. imposed rotation computed by the numerical model

The flexural rigidity (Nmm/rad) obtained from numerical simulations has been compared to that one from experimental tests (Ciocca, 2003; Lotti, 2005b) and from the analytical model purposely developed for close-wound springs (see section 3.3.2).

Fixed the number of the coils (*n* =10) and the maximum imposed rotation (90 degrees), in Table 3.2 the values plotted in Figure 3.30 for the geometrical configurations reported in Table 3.1 are listed.

External diameter (D) [mm]	Wire diameter (d) [mm]	Spring bending stiffness [Nmm/rad]		
		Experimental	**Analytical**	**FEM**
2	0.45	N.A.	12.40	13.09
	0.5	18.90	19.60	19.69
	0.55	N.A	29.60	28.85
2.3	0.45	N.A.	10.40	10.38
	0.5	15.07	16.30	18.12
	0.55	N.A.	24.60	25.26
2.5	0.45	11.25	9.40	10.47
	0.5	14.66	14.70	15.35
	0.55	22.08	22.10	23.68
2.7	0.45	N.A.	8.60	10.11
	0.5	13.04	13.40	14.54
	0.55	N.A.	20.00	21.28

Table 3.2: Comparison between numerical, analytical and experimental data for different geometrical configurations of the close-wound coiled helical spring (N.A.=Not Attained).

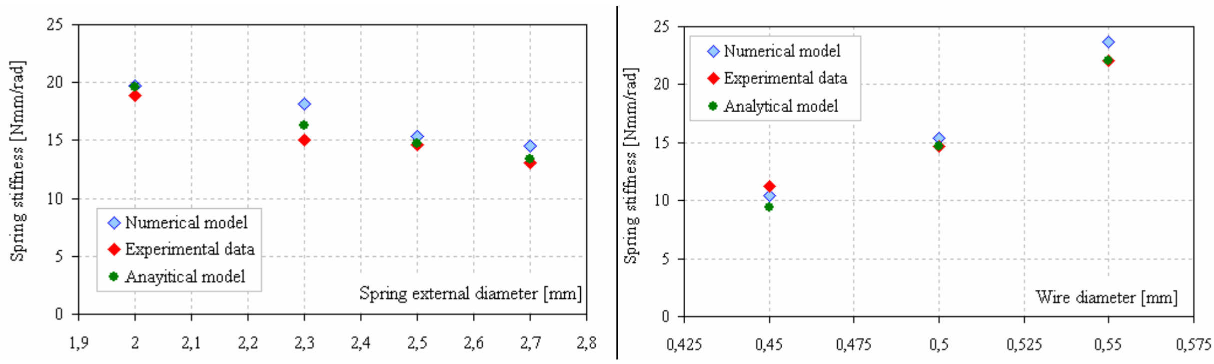

Figure 3.30: Comparison between experimental data and the results from analytical and numerical (FEM) models:
(left) wire diameter fixed (d=0.5 mm);(right) spring diameter fixed (D=2.5 mm).

A fairly good agreement was found between numerical and analytical results and experimental data. Figure 3.30 shows that the numerical models developed for the analysed geometrical configurations provide only slight overestimations of experimental data and analytical results with a peak mean percentage error of 11% and 8% respectively.

A graphical comparison of the results from the various analysed methodologies is shown in Figure 3.31 in terms of flexural rigidity as function of the wire and the spring external diameters.

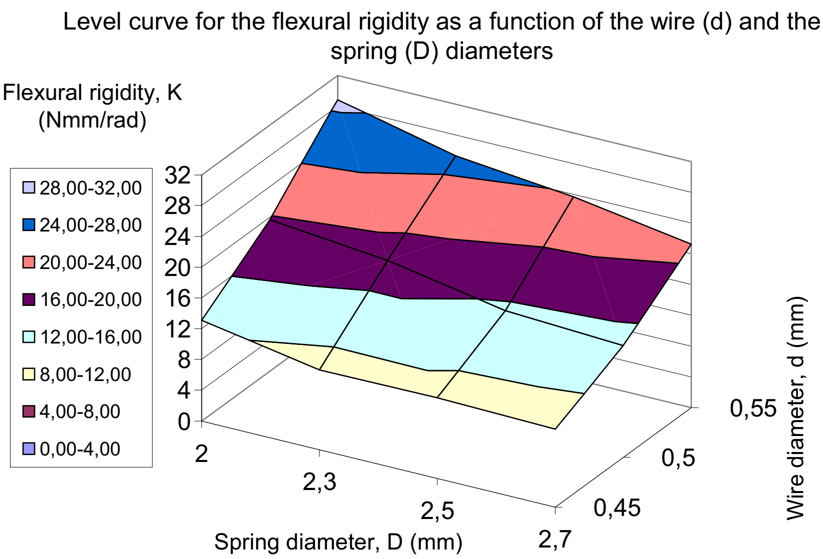

Figure 3.31: 3-D representation of the flexural rigidity over the geometrical parameters

From the above Figure two main considerations emerge:

1. The flexural rigidity exhibits a marked non linear tendency over the spring diameter, *D*, and less emphasized but however present one, over the wire diameter *d*;
2. The peak value of flexural rigidity corresponds to the minimal value of the spring diameter and the maximum of the wire diameter.

An example of the results achieved by FE analysis is reported in Figure 3.32 that shows the four-coil model deformation and the Von Mises stress values corresponding to the case of a ten-coil spring subjected to 90° overall rotation. It can be observed that the maximum stress of 1760 MPa is below the yield stress limit of 1950 MPa, well fitting with theoretical results.

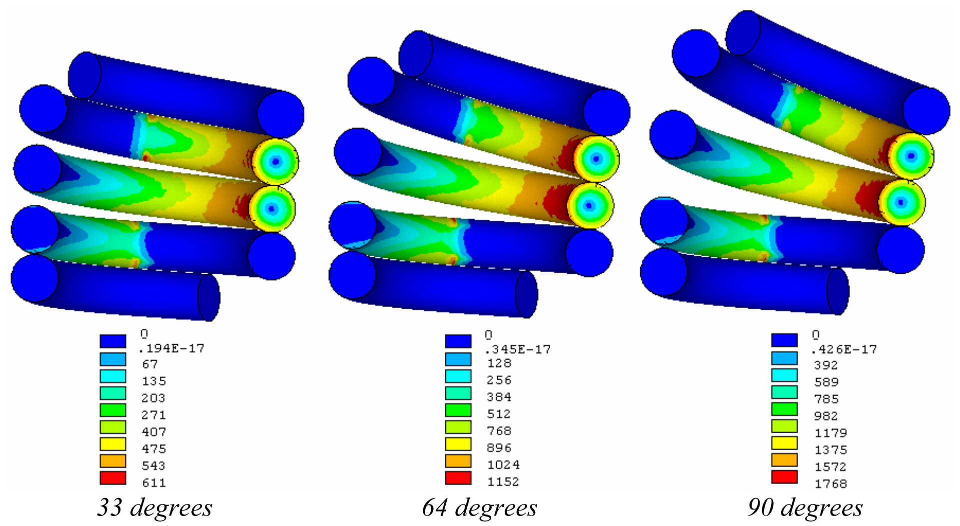

2 coils subjected to 18° of free ends rotation corresponding to 90° for 10 coils spring.

Spring parameters: d=0,45, D=2,7;

Material: Sandvik 11R51;

Figure 3.32: Von Mises stress distribution (MPa) over the transerval cross-section (D=2.7; d=0.45)

Chapter 3.6

Discussion

A discussion of the developed work is here suggested by the comparison of the flexural rigidity for both the close-wound helical springs and the open-coiled helical springs.

Viene di seguito suggerita una discussione del lavoro svolto attraverso il confronto della rigidezza flessione delle molle in configurazione a pacco e delle molle a spire aperte.

Based on the strength of material theory (Belluzzi, 1947; Timoschenko, 1976; Wahl, 1978) (see section 3.3.1.), the stiffness of open-coiled helical springs can be calculated by means of the following relation:

$$K_{1,\theta_z - M_z}^{OC} = \underbrace{\frac{E\cos(\varepsilon_0)}{4\left(2 + \upsilon \cdot \cos^2(\varepsilon_0)\right)}}_{a} \cdot \underbrace{\frac{1}{n}}_{b} \cdot \underbrace{\frac{r^4}{R}}_{c} \tag{3.38}$$

where ε_0 is the helix angle, r the wire radius, n the number of coils and R the mean spring radius. This relation contains three contributions:

- the first, (*a*), depends on the material and the helix configuration;
- the second (*b*) on the number of coils;
- and the third (c) is a function of the main design parameter *R* and *r*.

It is important to observe that, in the case of close-wound helical springs, the helix angle is strictly depending by the parameters *r* and *R* as follows:

$$\text{tang}(\varepsilon_0) = \frac{p_0}{2\pi R} = \frac{r}{\pi R} \tag{3.39}$$

where p_0 is the pitch. For the cases here studied the helix angle is little ($\varepsilon_0 \in [3.64°; 6.88°]$) and the corresponding values for the $cos(\varepsilon_0) \in [9.93\times10^{-1}, 9.98\times10^{-1}]$. So it is possible to assume $cos(\varepsilon_0) \approx 1$ and then simplify the equation (3.39) as follows:

$$K_{1,\theta_z - M_z}^{OC} \approx \frac{E}{4(2+\upsilon)} \frac{1}{n} \frac{r^4}{R} \tag{3.40}$$

The stiffness values of an open-coiled helical springs can be calculated by (3.40) in the same configuration considered for close-wound springs. Since the analysed springs differ each other for the wire *(r)* and the spring mean radius *(R)*, in order to perform the comparison between open-coil and close-wound helical springs, the auxiliary variable:

$$\lambda = \frac{r^4}{R} \; [mm^3] \tag{3.41}$$

has been introduced. In Figure 3.33 the flexural stiffness of the close-wound as predicted by analytical models, numerical simulations and experimental data, and that of the open-coil helical springs are plotted.

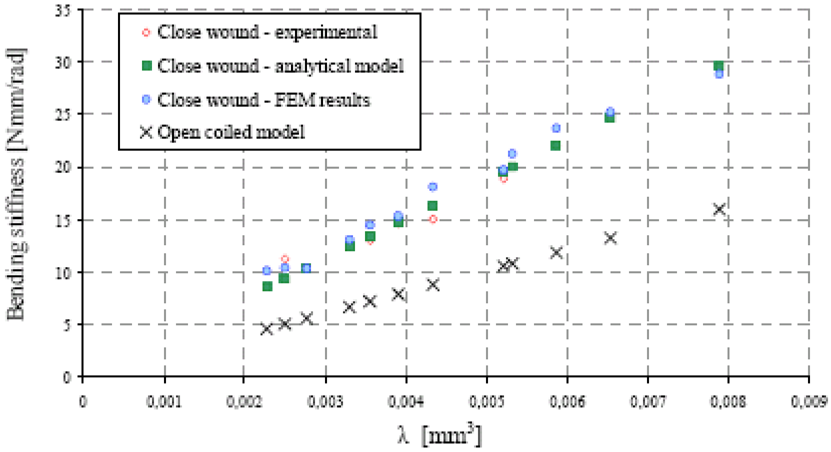

Figure 3.33: Comparison of the flexural stiffness vs. the auxiliary parameter λ

From Figure 3.33 it emerges that the open-coil theoretical models predict flexural stiffness values lower than the ones of close-wound helical springs.

Beside, from the stiffness values comparison, it is also interesting to notice that the predicted results for close-wound springs have a linear tendency (Figure 3.34); thus it is possible to hypothesize also in the case of the close-wound helical springs a direct proportionality between its flexural stiffness and the geometrical factor λ.

As consequence, the flexural stiffness of close-wound helical springs (K^{OC}_{1,θ_z-M_z}) can be assumed proportional to λ:

$$K^{OC}_{1,\theta_z-M_z} \propto \lambda \tag{3.42}$$

Moreover, the ratio between K^{OC}_{1,θ_z-M_z} and K^{CW}_{1,θ_z-M_z} results approximately constant for all λ values as shown in Figure 3.34 (mean value and standard deviation of the ratio $K^{OC}_{1,\theta_z-M_z} / K^{CW}_{1,\theta_z-M_z}$ equal to 1.9 and 0.1 respectively):

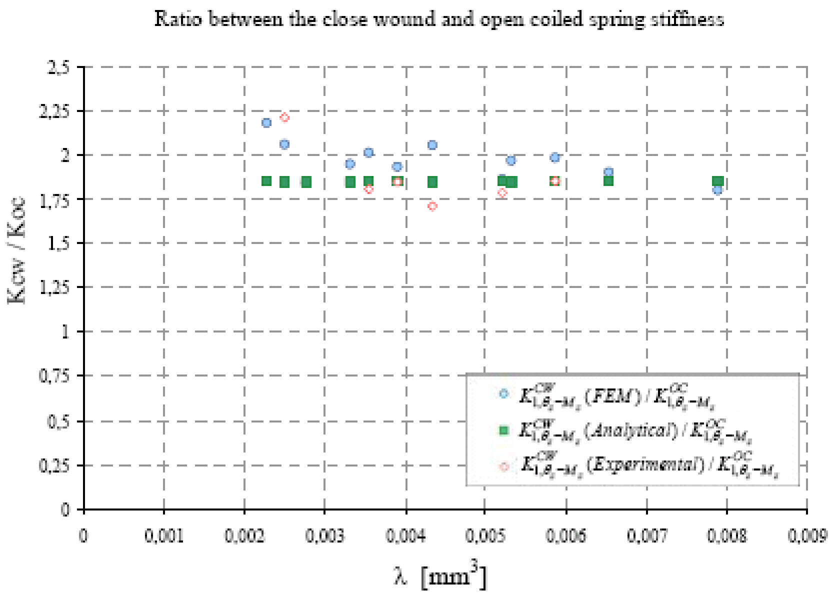

Figure 3.34: Ratio between the close-wound (CW) and the open-coiled (OC) flexural stiffness as function of the auxiliary parameter λ..

A possible interpretation of this discrepancy relates to spring geometrical configuration. For close-wound helical springs there is a non uniform working status of coils: all the loaded coils have a limited mutual contact area and the rest of the coil has no displacement restriction. As a consequence of this internal boundary non linearity, the coil stress appears non uniform along the length and the presence of a contact area between adjacent coils leads to an increasing of the overall spring stiffness. As can be seen in Figure 3.35 that shows the stress distributions for a specific geometrical configuration (D=2.5 mm, d=0.45) over four increases of the overall rotation, active coils may be considered under pure rotation in the contact region (3.35 (a)) whilst far from this area (3.35 (b)) the stress distribution is ascribable both to flexural and torsional stress components.

In Figure 3.35 (c) the flexural stress over the cross-section orthogonal to the contact area is shown. It can be seen the sign inversion of the flexural stress from the two sides of the contact area that could indicates the flexural contribution discharging on the contact zone.

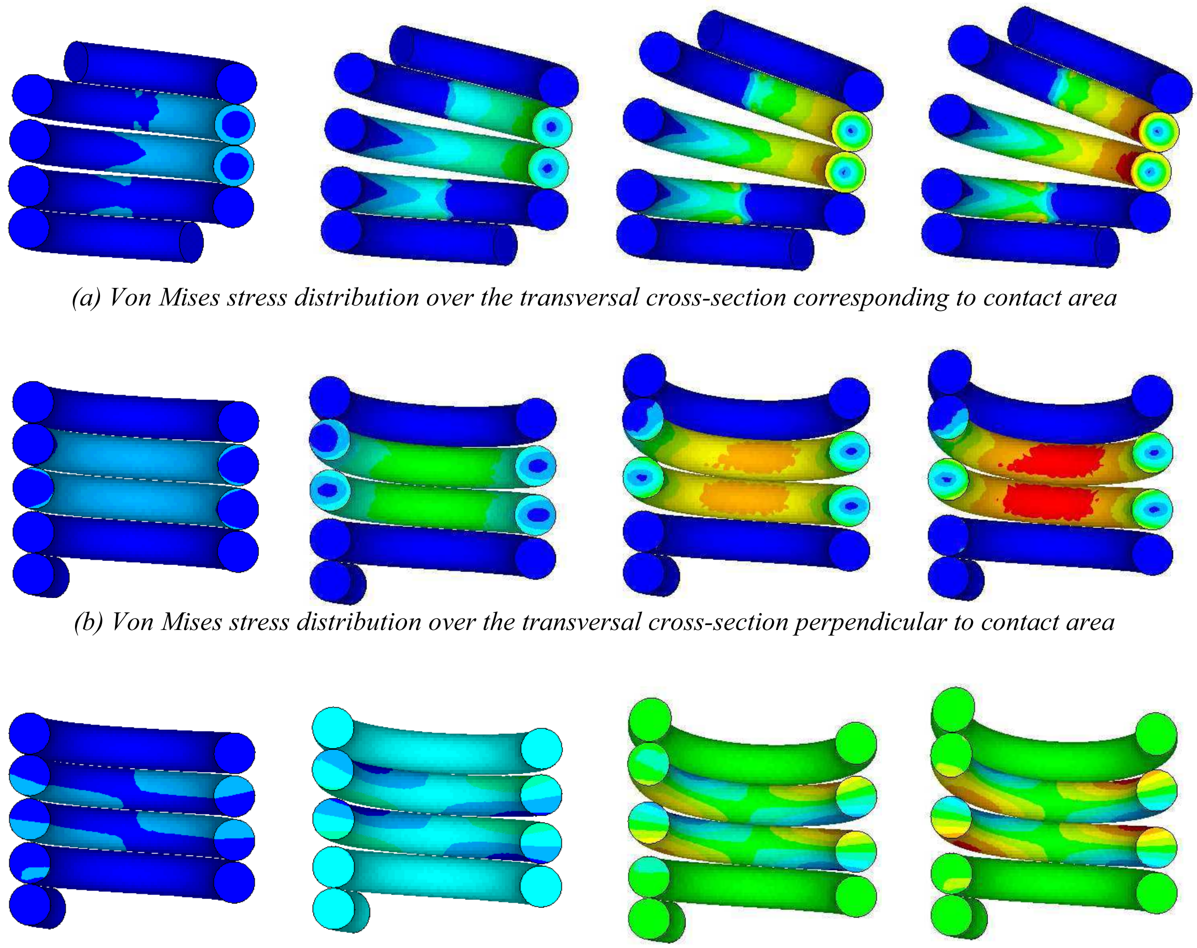

(a) Von Mises stress distribution over the transversal cross-section corresponding to contact area

(b) Von Mises stress distribution over the transversal cross-section perpendicular to contact area

(c) Flexural stresses on the transversal cross-section perpendicular to contact area

16 degrees 48 degrees 78 degrees 90 degrees

Figure 3.35: Stress distributions over two cross-sections (D=2.7, d=0.45)

A plausible consequence of this interpretation is that the analytical model proposed for open-coil springs (equation (3.40)), accounting for the flexural contribution without regards for the coils contact, introduces twisting components that involve a slackening of the spring (see Figure 3.33). In other words, the mutual contact of coils stiffens the spring through a dampening of the bending twisting component.

If the flexural contribution is removed from equation (3.40), it results:

$$K_{1,\theta_z - M_z}^{OC} \approx \frac{E}{4(1+\upsilon)} \frac{1}{n} \frac{r^4}{R} \tag{3.43}$$

that differs from (3.40) for a term 2 in the denominator.

In Figure 3.36 the flexural stiffness of close-wound springs as function of the auxiliary variable λ is reported as predicted by numerical simulations and experimental data and by the analytical model from equation (3.43).

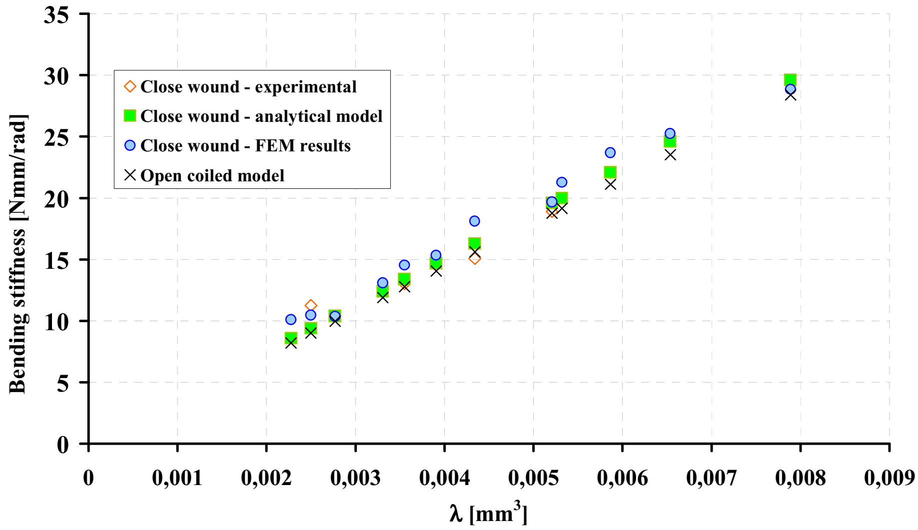

Figure 3.36: Comparison of the flexural stiffness vs. the auxiliary parameter λ

As expected, analytical model from (3.43) well fits the experimental and numerical data. These observations could justify the discrepancy of a factor nearly 2 found in Figure 3.34 and help to describe the mechanical behavior of close-wound springs. Nevertheless, the good fitting of the analytical model from equation (3.43) with experimental and numerical data does not have an absolute validity. With an increase of the spring index *D/d*, i.e. of the spring slenderness, the analytical model predictions tend to drastically stray from experimental data since this model does not account for large deflection and mutual contact of coils in the close-wound spring configuration. In Figure 3.37 the relative percentage error between the FE predictions, assumed as exact value due to a limited number of available experimental data, and the analytical model results from (3.43) is reported over the spring index *D/d*.

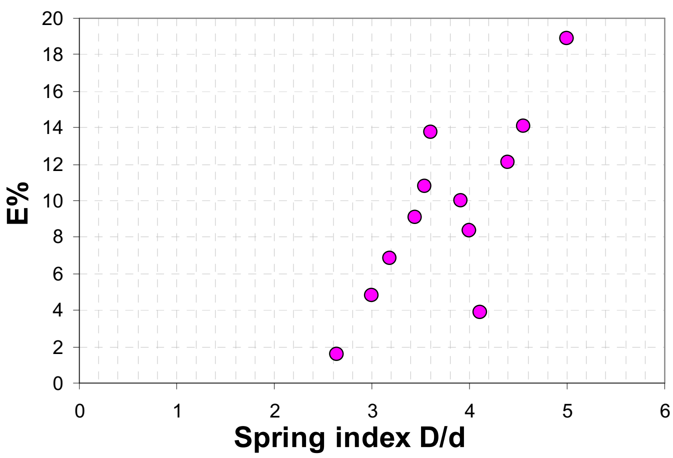

Figure 3.37: Percentage error (E%) between the analytical (equation (3.43)) and the FE model predictions over the spring index D/d

Chapter 3.7

Conclusions

The study, which the present work is part of, was aimed to identify criteria for the design of articulated finger made with novel types of compliant hinges, i.e. close-wound helical springs, specifically oriented to application on robotic devices, like desterous hands, where large joint displacements, reduced parasitic effects and good rotary precision are required.

After general considerations on the possible procedure for the characterization of the hinge stiffness, the flexural behaviour around the principal sensistive axis has been investigated.

For the numerical analysis, main purpose of the present work, a finite element model of the close-wound spring configuration, not previously reported, to the author knowledge, in literature has been developed.

The FE model predictions have been compared with the ones from a purposely-developed analytical model for close-wound springs and with experimental data. The achieved results, in terms of flexural rigidity (ratio between the applied bending moment and the imposed rotation) for various geometric configurations showed a fairly good convergence between data obtained from the different sources and substantially confirmed a linear relationship between the applied bending torque and the achieved rotation.

Numerical results have been also compared to the flexural rigidity predicted by an analytical model from the theory of beams developed for open-coil springs. A possible interpretation of the predictions discrepancy between this model and the ones from the other analyzed methodologies (experimental, FE, analytical model for close-wound springs) may indicate that the close-wound configuration should not be studied with the acquired knowledge for springs in different configuration. The mutual contact of coils involves an internal loading transmission such that a non uniform working status of coils emerges.

The methodology applied to generate the numerical model has been found accurate, flexible and not-time consuming. This is the first step towards an extension to further geometric configurations and loading conditions (e.g. torsion, shear, bending in the secondary plane). The so gained data could therefore be used as a basis for the determination of design curves that will allow to correlate the rigidity to the angular excursion as function of the geometric characteristics of the articulation.

Lo studio, nel quale è stato inquadrato il presente lavoro, aveva come obiettivo l'identificazione di criteri per la progettazione di dita articolate realizzate mediante un nuovo tipo di giunti elastici, ovvero molle elicoidali in configurazione a pacco. Tali giunti sono orientati ad applicazioni robotiche dove vengono richiesti grandi spostamenti, ridotti effetti parassiti ed una grande precisione rotativa.

Dopo considerazioni generali sulle possibili procedure per la caratterizzazione della rigidezza del giunto, è stato investigato il comportamento flessionale attorno al principale asse sensibile.

Per l'analisi numerica, scopo principale del presente lavoro, è stato sviluppato il modello agli Elementi Finiti di una molla in configurazione a pacco non riportata, a conoscenza degli autori, in precedenza in letteratura.

Le predizioni del modello FE sono state confrontate con i risultati di un modello analitico specificatamente sviluppato per molle a pacco e con dati sperimentali. I risultati ottenuti, in termini di rigidezza flessionale (intesa come rapporto tra momento flettente applicato e rotazione imposta), per diverse configurazioni geometriche, hanno mostrato una buona convergenza delle diverse metodiche d'analisi comparate, confermando sostanzialmente una relazione lineare tra coppia applicata e rotazione ottenuta.

I risultati numerici sono stati inoltre confrontati con la rigidezza flessionale predetta da modelli analitici, derivanti dalla teoria delle travi, sviluppati per molle a spire aperte. Una possibile interpretazione delle discrepanze tra le predizioni di questi ultimi modelli e quelle delle altre metodiche considerate (sperimentale, FE, modello analitico per molle a pacco) suggerisce l'impossibilità di studiare le molle a pacco con le conoscenze acquisite, e presenti in letteratura, per molle in diversa configurazione. Il mutuo contatto tra le spire sembrerebbe infatti comportare una trasmissione interna di carico tale da generare uno stato di sollecitazione fortemente non uniforme delle spire.

La metodologia applicata per sviluppare il modello numerico si è dimostrata accurata, flessibile e veloce. Questo lavoro deve essere inteso come primo passo verso l'estensione dell'analisi ad ulteriori configurazioni geometriche e di carico (esempio torsione, taglio, flessione nel piano secondario). I dati così ottenibili potrebbero pertanto essere utilizzati come base per la determinazione di curve di progettazione atte a correlare la rigidezza con l'escursione angolare in funzione delle caratteristiche geometriche dell'articolazione.

References

[1] Ansys Theory Reference Manual. Ansys 8.0.

[2] Battaglia, M., 2002. Ottimizzazione strutturale di cerniere elastiche per "compliant mechanism". Tesi di Laurea in Macchine Automatiche e Robot presso l'Università degli Studi di Bologna.

[3] Belingardi, G.I., 1989. On the lateral deflection of cylindrical helical springs", Wire, I parte n.3 maggio 1989, II parte n.4 luglio 1989, III parte n.5 settembre 1989.

[4] Belluzzi, O., "Scienza delle Costruzioni". Zanichelli Editore, Bologna, Vol. II, pp.525-532.

[5] Biagiotti, L., Melchiorri, C., Lotti, F., Tiezzi, P., Vassura, G., Palli, G., 2004. UBH 3: A Biologically Inspired Robotic Hand. IMG'04, International Conference on Intelligent Manipulation and Grasping, Genova, Italia, 1-2 Luglio.

[6] Ciocca, G., 2003. Impiego di molle elicoidali come elementi cedevoli in strutture robotiche. Tesi di Laurea in Macchine Automatiche e Robot svolta presso l'Università di Bologna.

[7] Cook, R.D., Young, W.C., 1985. Advanced Mechanics of Materials. Macmillian Publishing Company, New York.

[8] Ding, Xilun, Selig, Jon M., 2004. On the compliance of coiled springs. International Journal of Mechanical Sciences, v 46, n 5, p 703-727.

[9] Forrester M. K.; "Stiffness Model of a Die Spring"; Master's Thesis, Master of Science, Mechanical Engineering; Faculty of the Virginia Polytechnic Institute & State University.

[10] Godden, A.K., 1968. Some factors in the design of an adaptive artificial hand. Proc. Inst. Mech. Eng. 183, Pt. 3J,. pp. 50-53.

[11] Haringx, J.A., 1949. On Highly Compressible Helical springs and Rubber rods, and their application for Vibration-Free Mountings. Part 1 and 2, Philips Research Reports, Vol. 3, pp. 401-449 and Vol. 4, pp. 49-80.

[12] Howell L., 2001, "Compliant Mechanisms", John Wiley & Sons, New York. ISBN: 0-471-38478-X.

[13] Lobontiu, N., 2002. Compliant Mechanisms. CRC Press, Florida, ISBN: 0849313678.

[14] Lotti F., Vassura G., 2002a. A novel approach to mechanical design of articulated finger for robotic hands. International conference on intelligent robot and systems IEEE/RSJ IROS, Lausanne, Switzerland.

[15] Lotti, F., Tiezzi, P., Vassura, G., Zucchelli, A., 2002b. Mechanical structures for robotic hands based on the "compliant mechanism" concept. ASTRA, Nordvejk, NL.

[16] Lotti F., Vassura G., 2002c. Sviluppo di soluzioni innovative per la struttura meccanica di dita articolate per mani robotiche. Associazione Italiana per l'Analisi delle Sollecitazioni (AIAS) XXXI Convegno Nazionale–18-21 Settembre, Parma.

[17] Lotti, F., Vassura, G., 2005a Analisi di cerniere elastiche costituite da molle elicoidali con spire a pacco soggette a inflessione laterale. XXXI Convegno Nazionale AIAS Associazione Italiana per l'Analisi delle Sollecitazioni, Milano.

[18] Lotti, F., 2005b. Design of anthropomorphic robot hands based on the 'Compliant Mechanism' concept. Tesi di Dottorato di Ricerca in Meccanica Applicata, Università di Bologna.

[19] Lotti, F., Tiezzi, P., Vassura, G., Biagiotti, L., Palli, G., Melchiorri, C., 2005c. Development of UB Hand 3: Early Results. Robotics and Automation IEEE International Conference, ICRA.

[20] Lotti. F., Zucchelli, A., Reggiani, B., Vassura, G., 2006. Evaluating the Flexural Stiffness of Compliant Hinges Made with Close-wound Helical Springs. ASME 2006 Design Engineering Technical Conferences and Computers and Information in Engineering Conference. September 10-13. Philadelphia, Pennsylvania, USA.

[21] Melchiorri, C., Vassura, G., 1995. Implementation of Whole Hand Manipulation Capability in the U.B. Hand System Design. Journal of Advanced Robotics 9 (5), pp. 547-560.

[22] Musiani, F., 2004. Indagine sul comportamento di cerniere elastiche costituite da molle elicoidali. Tesi di Laurea in Macchine Automatiche e Robot presso l'Università degli studi di Bologna.

[23] Okada, T., 1986. Computer control of multijointed finger system for precise object handling. International Trends in Manufacturing Technology - Robot Grippers, pp.391-417.

[24] Whal, A.M., 1978. Mechanical Springs. 2a Edizione, McGraw-Hill, Inc. New York.

[25] www.sandvik.com

[26] Yang, J., Peña, E., Abdel-Malek, K., Patrick, A., and Lindkvist, L. "A Multi-Fingered Hand Prosthesis," Mechanism and Machine Theory, Vol.39, 2004 555–581.

[27] Reggiani, B., Zucchelli, A., Vassura, G., 1005. Modellazione numerica di giunzioni a molla per dita articolate di mani robotiche. XXXI Convegno Nazionale AIAS Associazione Italiana per l'Analisi delle Sollecitazioni, Milano.

[28] Timoshenko, S., 1976. Strength of Materials. 2nd Vol. Krieger Pub Co; 3rd Edition. ISBN: 0882754203.

[29] Zucchelli, A, Battaglia, M., Vassura G., 2003, "Studio ed analisi di cerniere elastiche per dita articolate di mani robotiche", Associazione Italiana per l'Analisi delle Sollecitazioni (AIAS) XXXII Convegno Nazionale, 3-6 Settembre 2003, Salerno.

Chapter 4

A contribution to the method of the fatigue life prediction in components by local stress concept

Un contributo al metodo della predizione della vita a fatica in componenti basato sul concetto di tensione locale

Chapter 4.1

Introduction

The ultimate goal of this work was to assess a novel formulation proposed in literature to predict the local fatigue life of components with uneven stress distribution by means of Finite Element Analysis. The basic idea of this theory is that the relative stress gradient in the highly stressed region is the fundamental parameter governing the fatigue life phenomenon.

A new method to compute the relative stress gradient by FE results has been proposed. Comparison with known analytical solutions proved that the method is robust and accurate enough to allow a reliable measurement of the relative stress gradient.

The equations used to compute the slope of the S-N curves and the local fatigue limit have been proved against data from literature. Whilst the formulation for the fatigue limit showed a good agreement with experimental data (mean percentage error of 7%), the slope k was overestimated by the used formulation. Thus, a novel formula was presented that attained a mean percentage error of 24%.

Scopo ultimo del presente lavoro era la valutazione di una formulazione proposta in letteratura per predire la vita a fatica locale di componenti con qualunque distribuzione irregolare di tensione tramite l'analisi agli Elementi Finiti. Il concetto base di questa nuova teoria è che il fenomeno della vita a fatica sia dominato dal gradiente relativo di tensione nella zona maggiormente sollecitata del componente.

In questo capitolo viene presentato un nuovo metodo per il calcolo del gradiente relativo di tensione per mezzo degli Elementi Finiti. Il confronto con soluzioni analitiche note mostra che il metodo proposto è robusto ed accurato, permettendo quindi una misura affidabile del gradiente relativo.

Le equazioni proposte dalla nuova teoria per il calcolo della pendenza delle curve S-N e del limite di fatica sono state verificate su dati sperimentali da letteratura. Mentre la formulazione per il calcolo del limite di fatica ha mostrato un buon accordo con i dati sperimentali (errore medio percentuale del 7%), la pendenza k è risultata sovrastimata dall'equazione proposta. E' stata quindi presentata una nuova formulazione che ha permesso di ottenere un errore medio percentuale del 24%.

Chapter 4.2

On the fatigue life prediction by local stress concept

In this section, an overview to the most meaningful theories of the German school of thought is presented having laid the basis for the local stress concepts in the fatigue life prediction.

A summary of the main geometrical and material parameters that affect the fatigue life founded on the relative stress gradient is also presented.

Finally, the theory proposed by Prof. Eichlseder to predict the local fatigue life of components with uneven stress distributions by means of Finite Element analysis is illustrated.

In questa sezione vengono presentate le teorie più significative per la predizione della vita a fatica della scuola di pensiero tedesca, fondate sul concetto di tensione locale.

Viene proposto un sunto dei principali parametri geometrici e del materiale che influenzano la resistenza a fatica sulla base del gradiente relativo di tensione.

Viene infine illustrata la teoria proposta dal Prof. Eichlseder per predire la vita a fatica locale di componenti con distribuzione irregolare di tensione tramite il metodo agli Elementi Finiti.

The following main symbols, where not differently made explicit, will be adopted:

σ_B	Static tensile strength
$\sigma_{0.2}$	Yield limit at 0.2% of deformation
K_t	Stress concentration factor
K_f	Fatigue notch factor
q	Notch sensitivity factor
χ	Relative stress gradient
N	Number of cycles to failure
N_D	Number of cycles at the fatigue limit
$\sigma_{D(\chi=0)}$	Fatigue limit for a uniform stress distribution
$\sigma_{D(\chi\neq0)}$	Fatigue limit for a uneven stress distribution
$\sigma_{D\ local\ (\chi\neq0)}$	Local fatigue limit for a uneven stress distribution
σ_{ai}	Stress level at a generic endurable number of cycles N_i
n	Support effect number
k	Slope of the S-N curve

4.2.1. Approaches to the fatigue life design and prediction

The term "Fatigue" was introduced in 1860s when several investigations showed that bridges and railroads components fail under repeated loading. With progress in the use of metals in machines, an ever increasing number of failures was recorded due to cycling loading. The research activity within the fatigue topics was intensive since the mid of 1800s and is still undertake today (ASM Handbook, 1996). Nevertheless, fatigue of materials is still controversial and its physical basis is not well understood although it has been identified as the most common cause of the mechanical failure (Stephens et al., 2001). This can be ascribable to the host factors affecting the fatigue life: entity and type of acting loads, geometry, conditions of material, roughness of surface, heat and mechanical treatments, test conditions and so on. This means that a further great deal of work has to be done.

The analytical models that have evolved to deal with cyclic loads in design can be reduced to the following (Stephens et al., 2001):

1. The stress-life approach
2. The strain-life approach
3. The fatigue-crack propagation approach
4. The two-stage model

The last less renowned model basically consists of a combination of the strain –life and the fatigue-crack propagation approaches to incorporate both macroscopic fatigue crack formation (nucleation) and growth.

Each of the fatigue life prediction models has areas of best applicability based also on the purpose of the design (infinite-life, safe-life, fail-safe, damage-tolerance) (Bannantine et al., 1988; Lee et al., 2005; Stephens et al., 2001). Nevertheless, generally speaking, the stress-life approach is used to model the fatigue life in the range of the high-cycle fatigue (approximately $>10^4$ cycles) whilst the strain-life approach covers the range of the low-cycle fatigue ($<10^4$ cycles) (Freddi, 2005; Lee et al., 2005; Vergani, 2006). In Figure 4.1, based on this criterion, the two ranges are shown both in the S-N diagram, used in the stress-life approach, and in the Manson-Coffin curve, used in the strain-life approach.

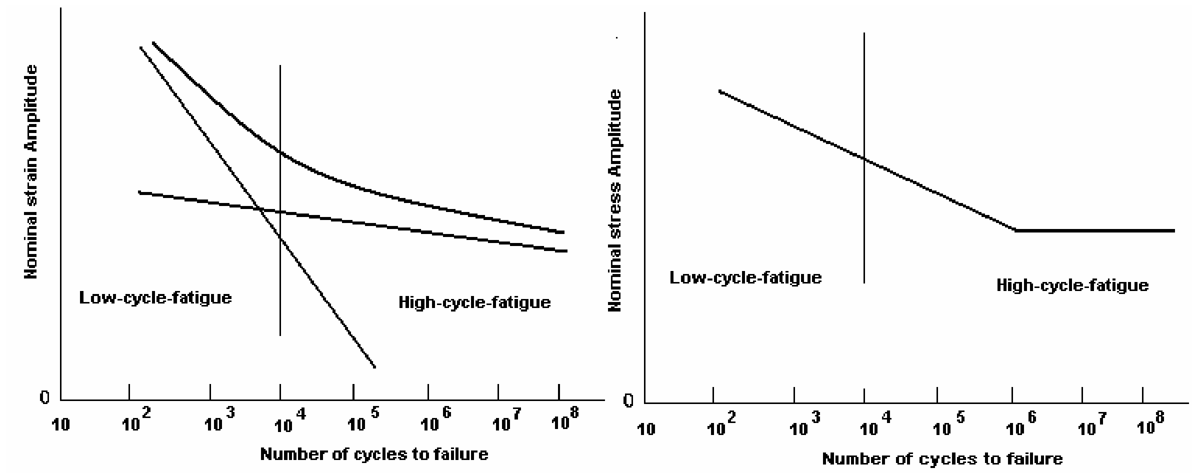

Manson-Coffin curve *S-N diagram*

Figure 4.1: Low and High cycle fatigue ranges

In the region of the high-cycle-fatigue most of the fatigue life is spent on crack nucleation, in the low-cycle-fatigue on crack propagation. Likewise, the other significant distinction that leads to substantial different formulations, is that only little local plastic deformations occurring due to cyclic loading in the high-cycle-fatigue region.

Since fatigue attempts are usually very expensive and time-consuming, they should have only a completeness meaning. For many years researchers of materials have been attempting to find out a theory for the fatigue life assessment based on simple tests. Since the mid-1900s, the researches dealt with the common effort to overcome pure mathematical notions for more practical formulations to be addressed to real mechanical components so that a novel approach has become known as “the component test model approach” (ASM Handbook, 1996). This was also feasible by means of sophisticated tools of computational surveying as the finite element method (FEM).

On this direction, the present work was intended as a thorough analysis of a novel formulation proposed in literature to predict the local fatigue life of complex components in the high-cycle-fatigue region by FE results. The investigation started from the study of the works of the German school of thought that, since the first mid-1900s, has laid the basis of this new formulation.

4.2.2. Historical contribution of the German school of thought

With specific reference to the German school of thought, since 1850s with the Wöhler studies, many works, specially between 1930s and 1960s, have contributed to the current knowledge of the materials fatigue. The attention paid by the early studies to the analysis of the notches effects on the fatigue strength (Moore et al., 1930; Morkovin et al., 1944; Neuber, 1937; Peterson, 1938; Philipp, 1942; Thum et al., 1939) lead to the mathematical and physical formalization that the fatigue strength of components ups not only to the peak stress but also, and mainly, to the relative stress gradient, i.e. the slope of the stress at the point of maximum stress (Siebel and Pfender, 1947) (Figure 4.2).

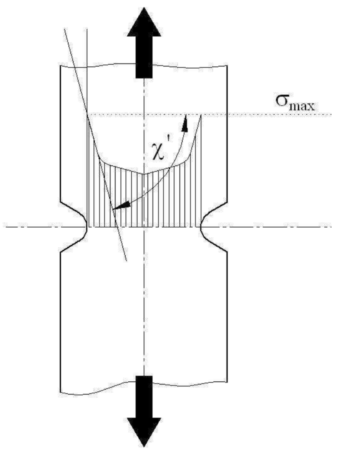

$$\chi = \frac{1}{\sigma_{\max}}\left(\frac{d\sigma}{dx}\right)$$

x = normal distance form the notch root;
σ = theoretically calculated elastic stress distribution.

Figure 4.2 :Definition of the relative stress gradient χ

Theoretically, the nominal strength of a smooth component, based on the same maximum stress that creates a cracking in notched and unnotched members, should be higher than that of a notched component by a factor K_t (elastic stress concentration factor). However, several tests showed (examples in Figure 4.3 and 4.4) that, at the fatigue limit, the presence of a notch on a component under cyclic nominal stresses reduces the fatigue strength of the smooth component by a factor K_f (fatigue notch factor) and not K_t.

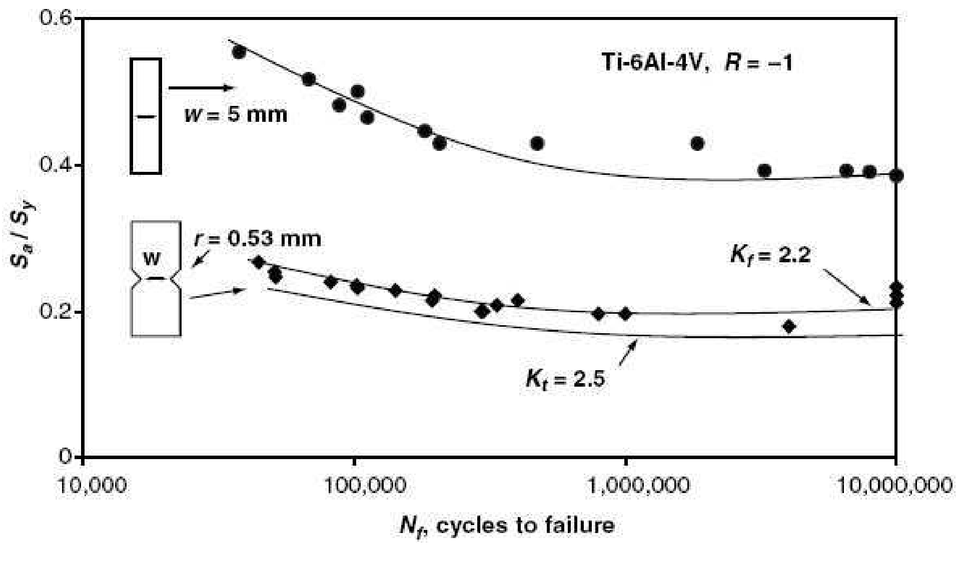

Figure 4.3:Fatigue data of notched und unnotched samples (taken form Lee et al., 2005)

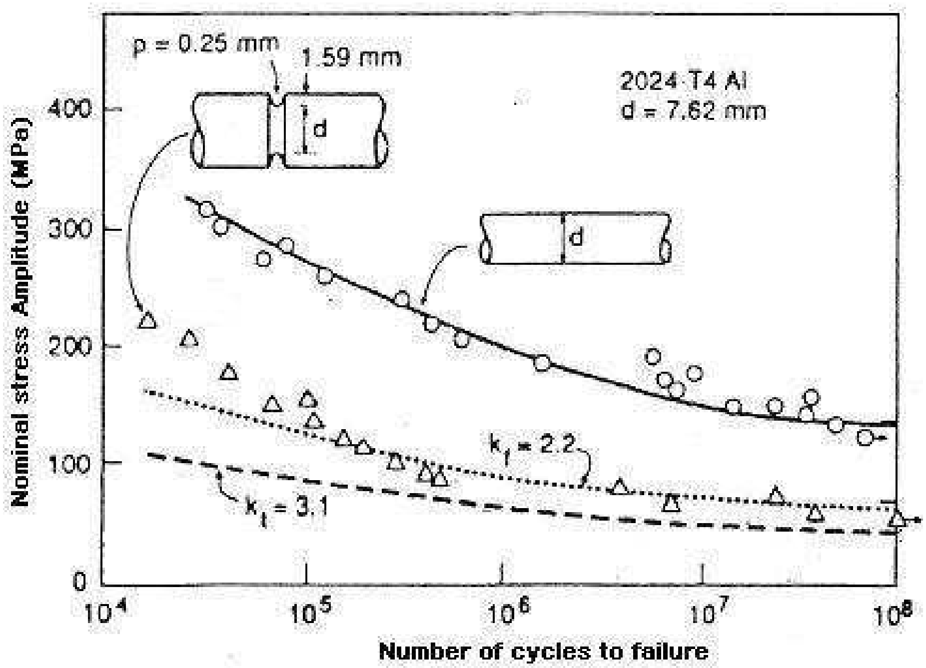

Figure 4.4: Fatigue data of notched und unnotched samples (taken from Various author, 2004)

Moreover, experimental tests showed that in the low and intermediate life region, i.e. when the applied stresses are over the fatigue limit ($N < 10^6 \div 10^7$), the strength of smooth components is reduced by the presence of notch less than what predicted by K_f (Figure 4.5).

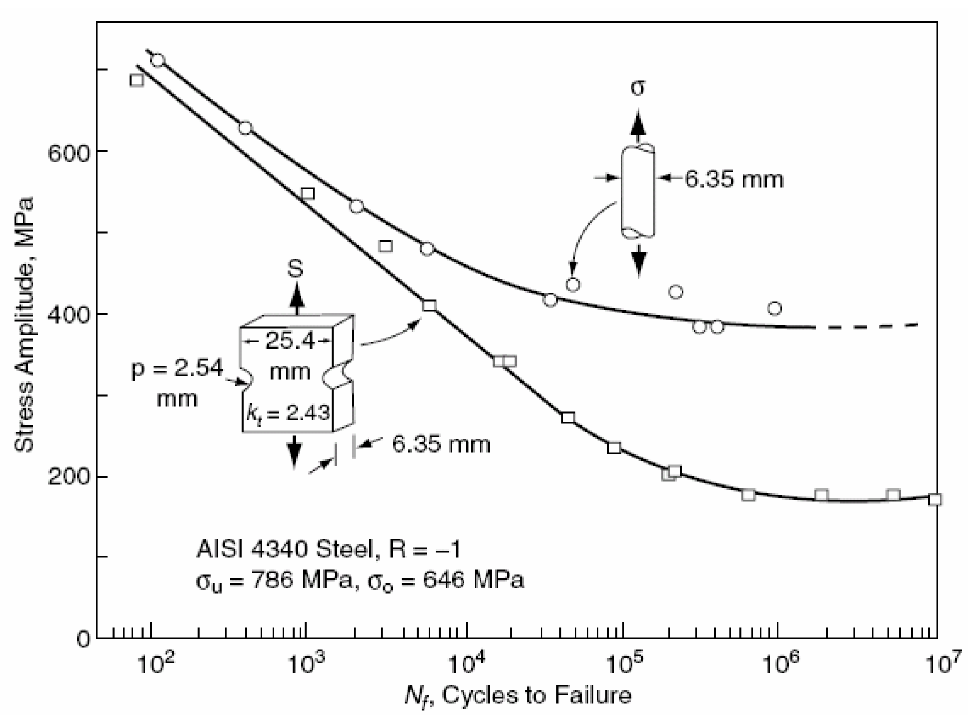

Figure 4.5: Strength of notched and unnotched samples in the low-intermediate fatigue life region (taken form Lee et al., 2005)

The difference between K_t and K_f is ascribable to both geometrical and material factors that interact affecting distinctly the high and the low-intermediate life region, as described in detail in section 4.2.3.

For a correct interpretation of the basic concepts and parameters that will be introduced, a specification is required. With respect to the classic point of view where the S-N curves are compared under the same nominal stress, thus resulting in a reduced strength of notched components, the formulation proposed by the German school of thought carries out comparisons in terms of maximum stress. This point of view defines the so called **local** or **synthetic** S-N curves since the maximum stress is located, for notched components, at the notch root (Figure 4.6).

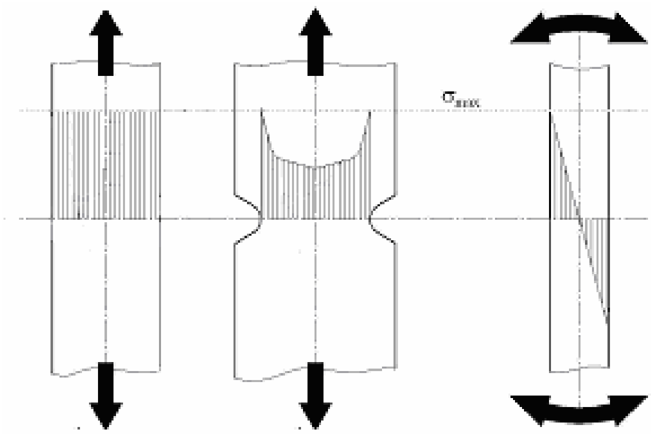

Figure 4.6: Comparison of the stress distribution for different geometrical and loading configurations.

Under this novel perspective a clear correlation between the stress-life and the strain-life criterions can then be recognized since both methods correctly interpret the fatigue as a *localized* phenomenon that occurs in a limited area or volume of components.

The previous observation has therefore to be re-interpreted in sense that the *local* fatigue life of a smooth component, with a null value of the relative stress gradient, is increased by the presence of a notch, or more generally, by the presence of a stress gradient and this increase is proportional to the elastic stress concentration factor K_t but dampened by the fatigue notch factor K_f, also called the fatigue strength reduction factor.

On this basis, the central idea of the *support effect* as the **beneficial** consequence of a stress gradient, i.e. of an uneven stress distribution, on the fatigue life was introduced.

The support effect was therefore defined (Stieler and Siebel, 1954) as the ratio between the linear stress concentration factor K_t and the fatigue notch factor K_f.

Starting from the original definition of K_f as the ratio of the nominal endurance limits of smooth and notched components, it results:

$$K_f = \frac{\sigma_{D(x=0)}}{\sigma_{D(x\neq 0)}} \Rightarrow \sigma_{D(x\neq 0)} = \frac{\sigma_{D(x=0)}}{K_f} \Rightarrow \sigma_{D(x\neq 0)} \cdot K_t = \left(\frac{\sigma_{D(x=0)}}{K_f}\right) \cdot K_t \Rightarrow \sigma_{DLocal(x\neq 0)} = \left(\frac{\sigma_{D(x=0)}}{K_f}\right) \cdot K_t \qquad (4.1)$$

$$\Downarrow$$

Support effect $\boxed{n = \frac{K_t}{K_f}}$ (4.2)

$$\Downarrow$$

$$\boxed{n = \frac{K_t}{K_f} = \frac{\sigma_{DLocal(\chi\neq 0)}}{\sigma_{D(\chi=0)}}} \qquad (4.3)$$

As later shown, all the proposed theories of the German school correlate the fatigue life prediction, by means of support effect, both to a material constant (typically the static tensile strength R_m, the yield strength $R_{p0.2}$ or a characteristic material length ρ*) and to a geometrical parameter, i.e. the notch radius (Bollenrath, 1952; Dietmann, 1985; Heywood, 1947) or the relative stress gradient (Eichlseder, 2002a,b; Huck, 1981; Neuber, 1968; Petersen, 1951, 1952; Siebel and Stieler, 1954, 1955).

The meaning of relative stress gradient and support effect is to overcome the limits of the classic definitions of stress concentration factor, K_t, fatigue notch factor, K_f, and the material notch sensitivity, q, not definable for generally complex shaped components for which the idea of net section and therefore of a nominal stress are not identifiable.

Here the most meaningful proposed theories are synthetically stated and analysed.

4.2.2.1. Siebel et al. (1947-1955)

In 1947 Siebel e Pfender (Siebel e Pfender, 1947) analysed the influence of an irregular stress distribution over the fatigue strength. With respect to traditional models proposed to analyse the fatigue behaviour of a material, they observed that not only the peak stress is required, but the curve of the fatigue strength as a function of the relative stress gradient. Bending and torsional loads were intended as particular cases of an uneven stress distribution leading to the idea that the conclusions found for these loading conditions can be extended to account for more general cases of not null value of stress gradient.

Experimental tests showed that values of stress gradient up to 1 mm^{-1} correspond to a small increasing of the fatigue strength, whilst under this value the fatigue strength rapidly decreases to the fatigue strength of an uniform stress distribution.

Based on the observation that the bending load is only a special case of an irregular stress distribution, an unifying definition of the stress concentration factor was proposed by Siebel and Meuth (1949) defining K_t in bending, as well as in axial loading, as the ratio between the peak stress and the average stress and not the nominal one as usually used, as showed in Figure 4.7.

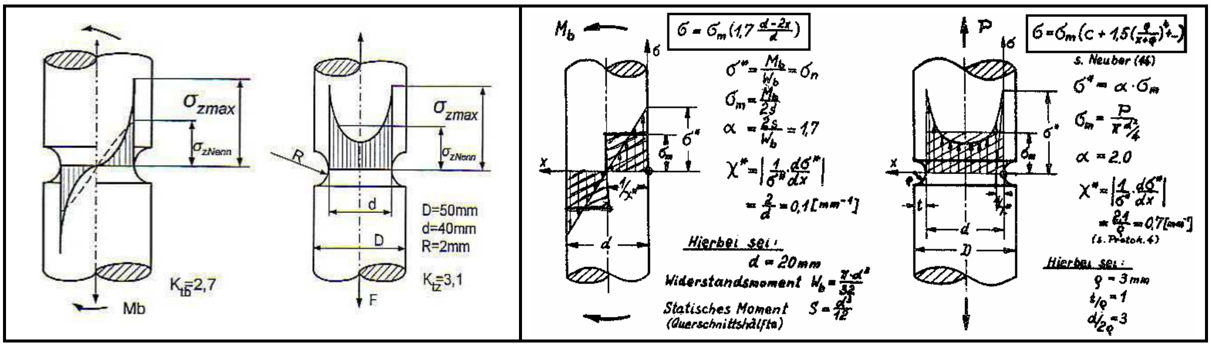

(Taken from Eichlseder, Instalment) (Taken from Stieler et al.., 1954)

Figure 4.7: Comparison of the traditional (left) and the novel (right) definition of K_t

The average stress σ_m is defined as the stress homogeneously distributed on the examined section that balances moments and forces.

In such a way the stress concentration factor K_t is a measure of the stress irregular distribution. The K_t values obtained with this novel definition thus differ from the computed ones according to the Neuber theory (Neuber, 1946).

These theories were assessed by further experimental tests on specimens with different notch shapes (Siebel and Bussmann, 1948; Siebel e Meuth, 1949; Siebel and Stieler, 1954, 1955). The proposed theory to compute the fatigue strength

$$\sigma_{DLocal} = \frac{f(\chi)}{\sigma_B} \cdot K_t \quad \text{(Siebel and Bussman, 1948)} \tag{4.4}$$

allows to account for the influence of dimensions, type of load and material notch sensitivity in a correct way. A possible approach to provide a direct measure of the material sensibility to the stress gradient is given by the history of the ratio between the fatigue strength of component under a non uniform stress distribution and an uniform stress distribution, $\sigma_{DLocal(\chi \neq 0)} / \sigma_{D(\chi = 0)}$, over the relative stress gradient (Siebel and Meuth, 1949). It was therefore observed that for materials with low notch sensibility even a small value of the relative stress gradient leads to a significant improvement of the fatigue strength.

Siebel and Stieler, in 1954-1955, further developed this basic idea coming to the definition of the support effect as the ratio between the stress concentration factor K_t and the notch factor K_f as a measure of the beneficial effect of a stress gradient on the local fatigue strength. They expressed the material effect on the fatigue life of notched components by means of a material constant function of the yield stress $\sigma_{0.2}$.

Siebel and Stieler observed that the empirical approximated relations of the fatigue life with the tensile strength σ_B work satisfactorily in many situations but fail however when materials exhibit very different yield limit values $\sigma_{0.2}$ with approximately the same σ_B, since the hardening effect is neglected. From experimental investigations, they concluded that the beginning of fatigue failure corresponds, for monocrystals, to the reaching of a critical shear stress. The alternating slips cause then the progressive damage of the metal structure. Also for polycrystals the fatigue cracking cannot be merely explained by the sum of the alternating slips (note 1). On the basis of these findings, Siebel and Stieler then tried to extend the previous approximation relations with the tensile strength to account for the hardening effect, coming to the following formulation:

$\sigma_{D(\chi=0)} = K \cdot \sqrt{\sigma_{0.2}}$ (Siebel and Stieler, 1954) (4.5)

where $\sigma_{D(\chi=0)}$ is the fatigue strength of a smooth specimen under alternating tensile stress (uniform stress distribution) and K is a material constant.

The idea of the sliding procedure in metallic materials led to the statement that for the introduction of a plastic deformation (i.e. for the reaching of the yield limit $\sigma_{0.2}$) a critical shear stress value $\tau_F = \sigma_{0.2}/2$ must be exceeded over a certain finite structure volume. Thus, if with any uneven stress distribution, the peak shear stress τ^* is less than the critical value τ_F falling within this layer, specified as *sliding layer* with the width S_g, then here no plastic deformation occurs.

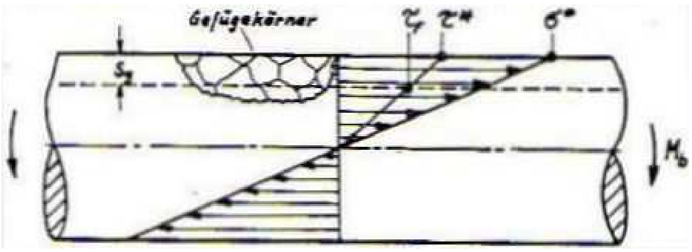

Figure 4.8: Definition of the sliding layer according to Stieler et al., 1954.

From these observations, Siebel and Stieler came to the following formulation for the support effect:

$n = 1 + \sqrt{S_g \cdot \chi}$ (Siebel and Stieler, 1954) (4.6)

Comparison with experimental value showed that the sliding layer S_g has the same order of magnitude of the grain diameter (Siebel and Stieler, 1954).

In Table 4.1, the values of S_g derived by Siebel and Stieler are shown:

Material	σ_B [MPa]	$\sigma_{0.2}$ [MPa]	S_g [µm]
Armco-Stainless Steel	290	95	150
C45 normalized	605	335	50
C45 hardened	665	475	10
Spring steel 70 Si 7	1320	1185	< 1

Table 4.1: Values of the sliding layer S_g as reported in (Siebel and Stieler, 1954)

(note 1) To date it is known that the reason could be found in the accumulation of the dislocations pile-up (ASM Handbook)

The strength gradient of the equivalent Von Mises stress has to be computed with multiaxial loads (Siebel and Bussman, 1948; Siebel and Meuth, 1949). Likewise, a multiaxial stress state acts at the notch root since not only longitudinal stresses are present but also circumferential ones and, in case of cylindrical specimens, also radial stresses. The difference between the peak longitudinal stress and the peak equivalent Von Mises stress was found of 12% at the notch root (Figure 4.9); this meant a difference of 22% between the relative gradient computed by means of the only longitudinal stress and the equivalent Von Mises stress (Siebel and Meuth, 1949).

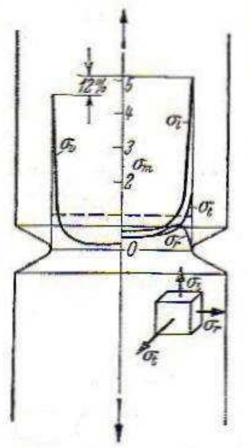

Figure 4.9: Difference between longitudinal stress and Von Mises equivalent stress (taken from Siebel and Meuth., 1949).

The following values are reported in literature for the sliding layer S_g as a function of the tensile strength σ_B (Niemann, 1981):

Tensile strength σ_B [MPa]	**Sliding layer S_g** [mm]
300	0.054
400	0.046
500	0.038
600	0.032
700	0.026
800	0.020
900	0.015
1000	0.010
1100	0.006

Table 4.2: S_g values as function of the static tensile strength (Niemann, 1981)

4.2.2.2. Heywood (1947-1962)

In 1947 Heywood discussed the meaning of the notch sensitivity index q observing that, in the following formulation:

$$q=\frac{K_f-1}{K_t-1}=\frac{\left(\dfrac{\sigma_{D,smooth}-\sigma_{D,notched}}{\sigma_{D,notched}}\right)}{\left(\dfrac{\sigma_{\max}-\sigma_{no\min al}}{\sigma_{no\min la}}\right)} \tag{4.7}$$

it expresses the "*ratio of the proportional reduction in the fatigue strength due to notch to that of the proportional increase in the elastic stress due to notch*" (Heywood, 1947). He noted that it would have been more meaningful to divide the reduction in the fatigue strength by the endurance limit of the unnotched specimen instead of the one of the notched specimen concluding that the meaning of the factor q is a little bit obscure.

Moreover, experimental tests by other authors showed that q is not a material constant but depends on type of notch or, more generally, on the extension of the highly stressed region.

From these observations, Heywood moved towards a novel formulation to account for the notch effect in the fatigue life prediction

$$\frac{K_t}{K_f}=1+\frac{c}{\sqrt{b\cdot\rho}} \tag{4.8}$$

c= augmented factor depending only on the material
b= constant depending only on the type of notch
ρ= notch radius

that was later modified in the following equation:

$$\frac{K_t}{K_f}=1+2\sqrt{\left(\frac{a}{\rho}\right)} \tag{4.9}$$

where "a" is a material constant indicated as "material notch alleviation factor" (Heywood, 1947) because the notch fatigue strength increases as it increases. This constant incorporates the influence of both the type of notch and the material, in the equation (4.8) accounted with two different constants. The quantity on the left side of the equation represents the gain in the fatigue life to the limited extend of the region of maximum stress.

Heywood (1962) related this constant to the inhomogeneity of materials that contain inclusions, cavities, surface discontinuities, etc. producing microscopic stress distribution. The notch alleviation factor was therefore correlated to the length of equivalent inherent flaws and computed by the tensile strength σ_B (expressed in MPa) in the following way for steels (Heywood, 1962):

Type of notch in circular specimen	**Notch alleviation factor "a" [mm]**
Transverse hole	$\left[\dfrac{5}{(\sigma_B/6.894757)}\right]^2\cdot 25.4$
Shoulder	$\left[\dfrac{4}{(\sigma_B/6.894757)}\right]^2\cdot 25.4$
Groove	$\left[\dfrac{3}{(\sigma_B/6.894757)}\right]^2\cdot 25.4$

Table 4.3: Alleviation factor "a" for various types of notches (Heywood, 1962)

A refinement of the previous formula was proposed by Heywood to satisfy the limit case when the stress concentration factor K_t approaches the unity:

$$\frac{K_t}{K_f} = 1 + 2\left(\frac{K_t - 1}{K_t}\right)\sqrt{\left(\frac{a}{\rho}\right)} \tag{4.10}$$

Nevertheless, this formula does not account for the impossibility of a definition of the stress concentration factor for complex geometry, like in real components.

Additionally, Heywood was, to the knowledge of the authors, a pioneer in dealing with the problem of the fatigue life prediction in the region of finite life (Heywood, 1962). He observed the progressive reduction of the fatigue notch factor K_f from the fatigue limit to static failure and divided the S-N curve into three regions where different mechanisms occur:

(a) the region near the fatigue limit where the size effect is predominant;
(b) the intermediate region where the stress redistribution caused by plastic flow is predominant;
(c) the region near the static failure where the triaxiality stress state of the notch root or the necking of the smooth specimens are additional complicating features.

The following formulation has been proposed to compute the fatigue notch factor K_f' for any value of the number of cycles N (see Figure 4.18):

$$K_f' = K_{static} + \frac{N^4}{b + N^4}\left(K_f - K_{static}\right) \tag{4.11}$$

where K_{static}, defined as

$$K_{static} = \frac{\text{Tensile strength of plain specimen}}{\text{Nominal stress (maximum) at static failure of notched specimen}} \tag{4.12}$$

it expresses the basic idea that, at static loading, the notch sensitivity is increased by the reduction of the ductility and so by the increasing of the static strength. As a limit case, $K_{static} = K_t$ for brittle materials. Some values of K_{static} are reported in the table below for steels as a function of the notch type:

Type of notch	K_{static}
Transverse hole, unloaded	0.95
Transverse hole, loaded through hole	1.00-1.70
Shoulder in plate	1.00
Shoulder in bar	1.00
Groove in plate	0.95
Groove in bar	0.75

Table 4.4: K_{static} for various types of notches (Heywood, 1962)

The term “b” is a constant dependent only on the material computed, for steel, by:

$$b = \left(\frac{1750}{\sigma_B} \right)^2 \tag{4.13}$$

4.2.2.3. Petersen (1951-1952)

Petersen started from the analysis of the results of previous studies on the notch effect on the fatigue life that led to the introduction of the fatigue notch factor K_f. In particular, he proposed a novel formulation for the fatigue life prediction of notched components moving from some basic ideas previously developed by other authors:

(1) Moore and Ver, (1930), Neuber (1937), Thum and Federn (1939), Philipp (1942), Peterson (1944) showed that the fatigue life depends on the dimension of the grain material, thus on the stress level that acts on a critical volume;
(2) Morkovin and Moore (1944) proposed a method to deal both with smooth and notched specimens; they assumed that smooth specimens are only particular cases of notched specimens due to the inhomogeneity of structure (effect of inner notches); in this way the notched specimens are thought as governed by a double notch effect: microstructural (inner micro notches) and macrostructural (external macro notches).
(3) Siebel et al (1947, 1948) introduced the relative stress gradient to explain the difference in terms of fatigue strength for specimens with various geometrical and loading configurations.
(4) Heywood (1947) presented the formulation (4.8) for notched specimens (see section 4.2.2.2.) in good agreement with the general trend of experimental data.

Petersen proposed a method to account for internal material flaws introducing a so-called “substitution-notch” thought as a single internal notch that causes the same damage to component produced by inner defects. He thus modified the formula proposed by Heywood in order to

a) extend its applicability also to smooth specimens;
b) account for this “substitution-notch” and, specifically, for the fact that, as for a macro-notch, also the stress concentration factor of the “substitution-notch” depends on the stress gradient

in the following equation:

$$n = \frac{K_t}{K_f} = \frac{\sigma_{DLocal(\chi \neq 0)}}{\sigma_{D(\chi = 0)}} = \left(1 + \sqrt{\rho^* \chi} \right) \tag{4.14}$$

where χ is the relative stress gradient of the specimen with the macro-external notch and ρ^* is the radius of the internal “substitution-notch”.

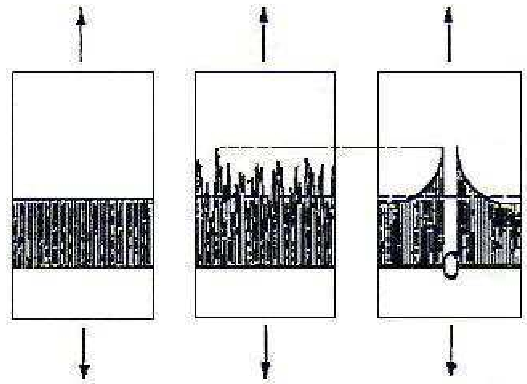

Theoretical *Real* *"substitution-notch"*

Figure 4.10: Definition of the internal "substitution-notch"(taken from Petersen, 1952).

The shape of the "substitution-notch" was selected on the basis of the following considerations:

(1) the peak stress occurs almost in all cases on the external surface of the material that may be the external surface of a hole;
(2) the "substitution-notch" is chosen so that the global stress concentration factor of a "substitution-notch" carried out in a macrocospic notch is simply equal to the product of the two single stress concentration factors.

A hole satisfies the aforementioned conditions. Moreover, an elliptic hole allows to represent "substitution-notches" with various stress concentration factors.

Petersen observed that for materials with internal flaws the static tensile strength is not appropriate to represent the type of structure being reduced by their presence even if it should be independent. He therefore suggested to use the Brinnell or Vickers hardness, H, as basic characteristic to practically compute the radius ρ* as:

$$\rho^* = \left(\frac{H_0}{H}\right)^2 \text{ with } H_0 = 40\ \text{Kg/mm}^2 \approx 400\text{MPa mm} \tag{4.15}$$

Nevertheless, H can be estimated by the static tensile strength as $H=\sigma_B/0.35\div0.36$.

Furthermore, Peterson suggested to deal the problem of the influence of the superficial roughness in the same way of the inner notches.

4.2.2.4. Neuber (1968)

Neuber (1961) and Peterson (1959) presented two similar formulations of the fatigue notch sensitivity factor q accounting for the fact that, as stated by Kuhn and Hardraht (1952), the fatigue failure occurs when the average stress at a specific distance from the notch root is equal to the fatigue limit of a smooth specimen.

Whilst the Neuber method is renamed as "the length method", since it fixed a specific length from the notch root

$$q = \frac{1}{1+\sqrt{\rho^{**}/\rho}}$$ (Neuber, 1961) ρ^{**} = microstructural length (see eq. (4.18)-(4.19) ρ = notch radius (4.16)

Peterson assumed that the fatigue failure occurs when the stress over some distance from the notch root reaches the fatigue limit of a smooth specimen. So, it is called the point method.

Thus, the Peterson model can be considered a special case of the length method:

$$q = \frac{1}{1+(\rho^{***}/\rho)}$$ (Peterson, 1959) $\rho^{***} = \left(\frac{140}{\sigma_B}\right)^2$ = material constant ρ = notch radius (4.17)

This method is more generally named "Stress averaging approach" since it assumes that the fatigue failure is controlled by the stress averaged over a small material volume at the maximum notch stress site.

In 1968, Neuber further developed this theory moving towards a novel formulation in which the relative stress gradient is introduced. He presented a differentiation between a micro and a macrosupport effect. The former concerns the support effect that the central part of the volume, in which the fatigue life is concentrated, exerts on the region highly stressed in reason of the fact that the material is not a continuous but it is characterized by a crystalline structure. Therefore the fatigue life can be correlated not to the peak stress acting on the notch root but to the average stress on a fictitious length that describes the critical volume. This was the basic idea of the formulations (4.16) and (4.17).

On the other side, the macrosupport described the support effect related to the redistribution of the stresses due to an overcoming of the elastic limit. In others terms, the macrosupport regards the support supplied to highly stressed fibers by the plasticization of the material.

Nevertheless, Neuber neglected the effect of the macrosupport accounting for the fact that the fatigue limit is generally lower than the yield stress (Neuber, 1968).

In the novel formulation the fatigue notch factor K_f is defined as the ratio between the average maximum notch stress $\overline{\sigma}_{\max}$ and the nominal stress; thus:

$$n = \frac{K_t}{K_f} = \frac{\dfrac{\sigma_{\max}}{\sigma_{no\min al}}}{\dfrac{\overline{\sigma}_{\max}}{\sigma_{no\min al}}} = \frac{\sigma_{\max}}{\overline{\sigma}_{\max}} \tag{4.18}$$

The average maximum notch stress $\overline{\sigma}_{\max}$ is determined by a fictitious radius ρ_f (Figure 4.11) defined as:

$$\rho_f = \rho + s \cdot \rho^{**} = \rho \cdot \left(1 + \frac{s}{\rho}\rho^{**}\right) = \rho \cdot \left(1 + \chi\rho^{**}\right) \tag{4.19}$$

where ρ^{**} is the microstructural length that allows to account for the microsupport effect. ρ^{**} depends on the chemical composition of the material, on the working process, on the load history, etc. and is comparable to the structural grain dimension (Neuber, 1968). The factor "s" results from the multiaxiality of the notch stress state in combination with the strength criterion to be applied.

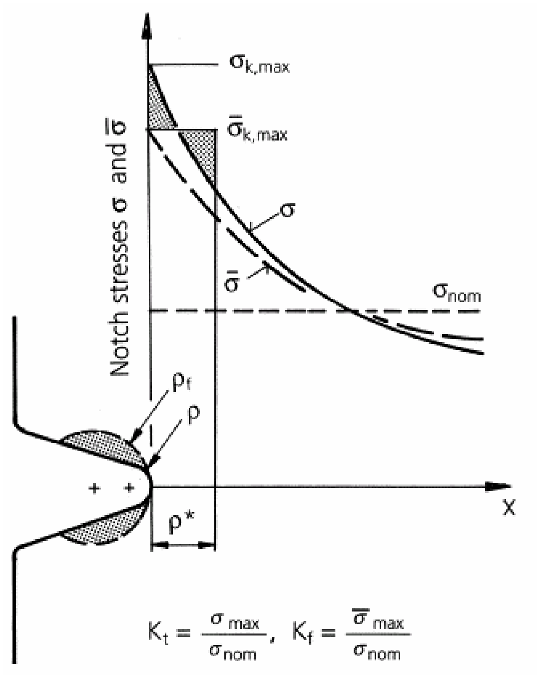

Figure 4.11: Definition of the fictitious microstructural length according to Neuber (taken from Sonsino et al., 1999)

From (4.18) it can be inferred

$$\frac{\bar{\sigma}_{\max}}{\sigma_{\max}}=\frac{K_{t,\rho}\cdot\sigma_{no\min al}}{K_{t,\rho_f}\cdot\sigma_{no\min al}}=\frac{K_{t,\rho}}{K_{t,\rho_f}}=\frac{K_{t,\rho}}{K_{t,\rho}\cdot\sqrt{\dfrac{\rho}{\rho_f}}}=\frac{1}{\sqrt{\dfrac{\rho}{\rho\cdot\left(1+\dfrac{s}{\rho}\cdot\rho^{**}\right)}}}=\sqrt{1+\frac{s}{\rho}\cdot\rho^{**}}=\sqrt{1+\chi\cdot\rho^{**}} \tag{4.20}$$

4.2.2.5. Bollenrath and Troost (1951-1952)

Bollenrath and Troost, starting from the observation that the plastic deformation is a function, being more or less prevented, of the stress and strain gradients, interpreted the fatigue strength as a limit of tolerable portions of plastic strain (shortly named deformation limit) that occurs within a grain of multicrystalline materials. With cyclic loading, for the critical plastic deformation that leads to a propagating crack, the most important factor is the greatest specific sliding, that is the greatest sliding along the single planes of sliding. Thus, according to this theory, to get the same total deformation, the product of the number of acting sliding planes and of the medium specific sliding one must be the same.

The fatigue strength is therefore a limit of strain characterized by a critical specific sliding in crystals edge. The considerations in the work developed by Bollenrath and Troost in 1950-1952 led to simple formulations on the influence of an uneven stress and strain distribution on the impediment of plastic deformation for different loading conditions like bending and torsion for prismatic specimens. In their examination they have been included various and simple shapes of sections. For a specified material, the parameters required to compute the fatigue strength are obtained by means of a limited number of experimental attempts, i.e. a tensile or compressive test and two further tests with geometrically similar members of various measures loaded in bending or torsion.

Through a complex elaboration of the developed method, Bollenrath and Troost finally proposed the following formulation for the support number n:

$$\frac{K_t}{K_f} = \frac{1}{1 - \dfrac{154/\sigma_B}{\dfrac{1}{1+\sigma_B/1370} + \dfrac{\rho}{10}}} \qquad \begin{array}{l} \sigma_B \text{ in [MPa]} \\ \rho \text{ in [mm]} \end{array} \tag{4.21}$$

that applies to steels with a static tensile strength σ_B from 440 to 1000 MPa.

4.2.2.6. Hück (1981)

A significant work has been done by Hück in 1981 for the prediction of the complete S-N curve of components by empirical formulas for the fatigue limit σ_D, the slope in the finite life region k and the number of cycles at the fatigue limit N_D. These “fatigue parameters” were related to measurable parameters as the static tensile strength σ_B, the yield stress $\sigma_{0.2}$, the stress ratio R and the stress concentration factor K_t on the basis of statistics considerations on a wide number of Wöhler curves taken from literature (beyond 600 analyzed curves). Hück presented a protocol for three different types of materials (steel, cast steel and grey cast iron) that, accounting for:

- stress concentrations
- type of loading
- stress ratio
- dimension of components
- superficial roughness
- hardening degree,

allows to compute σ_D, k and N_D as functions of the relative stress gradient χ.

With zero average stress (R=-1) and polished surfaces, the following relations were proposed:

		Local fatigue limit τ_D or σ_D ($\sigma_D=\sigma_{DLocal(\chi\neq0)}$; $\tau_D=\tau_{DLocal(\chi\neq0)}$;)	Slope k	Number of cycles at the fatigue limit N_D
Steel	Axial\ bending	$\sigma_D=\sigma_{D(\chi=0)}\cdot\left(1+0.45\cdot\chi^{0.3}\right)=\sigma_{D(\chi=0)}\cdot n$	$k=n^2\dfrac{12}{K_t^2}+3$	$LogN_D=6.4-\dfrac{2.5}{k}$
($\sigma_B\leq1200$MPa)	Torsion	$\tau_D=\sigma_D\cdot\left[0.42\cdot\left(\dfrac{\sigma_{0.2}}{\sigma_B}\right)^5+\dfrac{1}{\sqrt{3}}\right]$		$LogN_D=7.0-\dfrac{2.5}{k}$
Cast steel	Axial\ bending	$\sigma_D=\sigma_{D(\chi=0)}\cdot\left(1+0.33\cdot\chi^{0.65}\right)=\sigma_{D(\chi=0)}\cdot n$	$k=n^4\dfrac{5.5}{K_t^4}+6$	$LogN_D=6.8-\dfrac{3.6}{k}$
	Torsion	$\tau_D=\sigma_D\cdot\left[0.42\cdot\left(\dfrac{\sigma_{0.2}}{\sigma_B}\right)^5+\dfrac{1}{\sqrt{3}}\right]$		$LogN_D=7.2-\dfrac{3.6}{k}$
Grey cast iron	Axial\ bending	$\sigma_D=\sigma_{D(\chi=0)}\cdot\left(1+0.43\cdot\chi^{0.68}\right)=\sigma_{D(\chi=0)}\cdot n$	$k=n^2\dfrac{7.5}{K_t^2}+2.5$	$LogN_D=6.4-\dfrac{2.5}{k}$
($\sigma_B\leq300$ MPa)	Torsion	$\tau_D=\sigma_D\cdot\left[0.42\cdot\left(\dfrac{\sigma_{0.2}}{\sigma_B}\right)^5+\dfrac{1}{\sqrt{3}}\right]$		$LogN_D=7.0-\dfrac{2.5}{k}$

Table 4.5: Relations proposed by Hück to compute the fatigue limit, the slope and the number of cycles at the fatigue limit for three types of material under various loading conditions.

For ductile material $\sigma_{0.2}<<\sigma_B$; thus the first term in brackets to evaluate τ_D from σ_D is negligible and results $\tau_D=\dfrac{\sigma_D}{\sqrt{3}}$ (Von Mises hypotheses).

For brittle material $\left(\dfrac{\sigma_{0.2}}{\sigma_B}\right)\rightarrow1$ thus $\left[0.42\cdot\left(\dfrac{\sigma_{0.2}}{\sigma_B}\right)^5+\dfrac{1}{\sqrt{3}}\right]\rightarrow1$ and $\tau_D\approx\sigma_D$ (Rankine - hypotheses).

4.2.2.7. Dietmann (1985)

Dietmann (1985) proposed a novel equation for the calculation of the support effect starting from the analysis of the formulations previously developed by Siebel (see section 4.2.2.1.) and Petersen (see section 4.2.2.3.). Observing that these authors had elaborated two formulas with the same structure, he proposed the following generalized formula:

$$\frac{K_t}{K_f}=n=1+\left(\frac{C_1}{K}\right)^m\sqrt{\chi} \tag{4.22}$$

where C_1 and *m* are characteristic constants of the class of the material and K is a static parameter, i.e. the static tensile strength σ_B or the yield stress $\sigma_{0.2}$.

The relative stress gradient χ is the sum of two contributions:

$$\chi=\chi_0+\chi_k \tag{4.23}$$

where χ_0 relates to the type of the applied load and χ_k to the notch geometry. In bending $\chi_0 = 2/d$ and $\chi_k = 2/\rho$; in torsion $\chi_0 = 2/d$ and $\chi_k = 1/\rho$. Dietmann observed that the ratio $\chi_0/\chi_k = \rho/d$ in bending and $\chi_0/\chi_k = 2\rho/d$ in torsion for real components or subcomponents with functional notches cyclical loaded is always very small, typically 0.03-0.06. Thus, for almost all cases, he considered χ_0 negligible.

The previous relation was therefore rewritten as:

$$\frac{K_t}{K_f} = n = 1 + \left(\frac{C_1}{K}\right)^m \sqrt{\frac{C_2}{\rho}} \tag{4.24}$$

Typical values for C_1 and *m* for steel are 12 and 0.2 respectively with $K=R_m$.
Values for C_2 are reported in the Table below:

	Push-Pull	*Bending*	*Torsion*
C_2	2	2	1

Table 4.6: Values of the constant C_2 as function of the applied load.

4.2.3. Micro and macroscopic aspects of the fatigue life phenomenon: a summary of the main geometrical and material parameters that affect the fatigue life based on the relative stress gradient

On the basis of the presented theories, it will be now attempted to make a synthesis of the problem of notches in the fatigue life assessment.

As previously mentioned, a distinction between the fatigue behaviour of components in the region of *finite* (i.e., the leaning portion of the Wöhler curve) and *infinite* life (the horizontal line of the Wöhler curve), correlated with a different physical mechanism to the support effect, needs to be done.

Whilst the latter range, through the fatigue or endurance limit, σ_D, estimation, has been widely analysed in literature, only a few works, to the knowledge of the authors, attempted to describe the complete S-N curve by the further assessment of the slope k and of the number of cycles at the fatigue limit, N_D (Collins, 1993; Eichlseder in 2002a,b; Heywood, 1962; Hück, 1981).

Infinite life region

The fatigue limit, that delineates the region of infinite life, is the maximum operating cyclic stress that has not to be overcome to avoid further propagation of the crack. At this stress level, the microcrack nucleates within a grain of material, than growths to the size of about the order of the grain until it is arrested by the first grain boundary or by a dominant, strong, microstructural barrier (Lee et al., 2005).

The reference fatigue conditions for fatigue S-N data are usually fully reversed (R=-1) bending or axial load by using small, unnotched, mirror-polished surface specimens. Nevertheless, in the mechanical components fatigue failure generally occurs where a notch is present, due to the increasing of the stress level, and the dimensions and the surface finishing differ from those of the reference specimens one. It is therefore necessary to understand the influence of these factors on the fatigue strength of components.

The fatigue strength of notched components thus depends, among others factors, on the stress concentration factor as well as on the material:

$$\text{Fatigue strength} = f(K_t;\ \text{material}) \tag{4.25}$$

Like the stress concentration factor K_t, the relative stress gradient χ is related both to the geometry of the component (for simple specimens is a function of the diameter d and the notch radius ρ) and to the type of loading. Thus, accounting for the fact that the fatigue strength of a notched component can be represented by means of the support effect number, n (see 4.2.2.), the previous relation is rewritable as:

$$n = f(\chi;\ \text{material}) \tag{4.26}$$

The contribution of the term "material" can be made explicit through various main effects. The effect of a localized plastic deformation at the notch root needs to be accounted for.

To understand the other effects, the definition of term notch has to be given: *notch* is defined as a geometric discontinuity that may be introduced either by design, such as a hole, (*macroscopic notch*), or by the manufacturing process in the form of material or/and fabrication defects such as inclusion, voids/porosity, carbides, casting defect, machining marks, etc (*microscopic notch*). So it can be stated that the fatigue strength of a (macro) notched component depends on the relationship both between the stress distribution caused by the macroscopic notch and the grain dimension and between the stress distributions due to macroscopic and microscopic notch, the latter strictly correlated to the material microstructure. Thus:

$$n = f\left(\chi ;\, \text{local plasticity};\, \begin{array}{c} \text{macroscopic stress distribution} \\ \text{related to} \\ \text{grain dimension} \end{array} ;\, \begin{array}{c} \text{macroscopic stress distribution} \\ \text{related to} \\ \text{macroscopic stress distribution} \end{array} \right) \tag{4.27}$$

1. χ

The favourable effect of the relative stress gradient is reflected in a reduced number of material fibres that are loaded at high stress level. This phenomenon can be clearly understood looking at Figure 4.12 where three specimens with increasing diameter under the same value of σ_{max} are compared in terms of number of fibres (red zone) stressed over the threshold of 90% of the maximum stress, $\overline{\sigma}$ (= 0.9 σ_{max}):

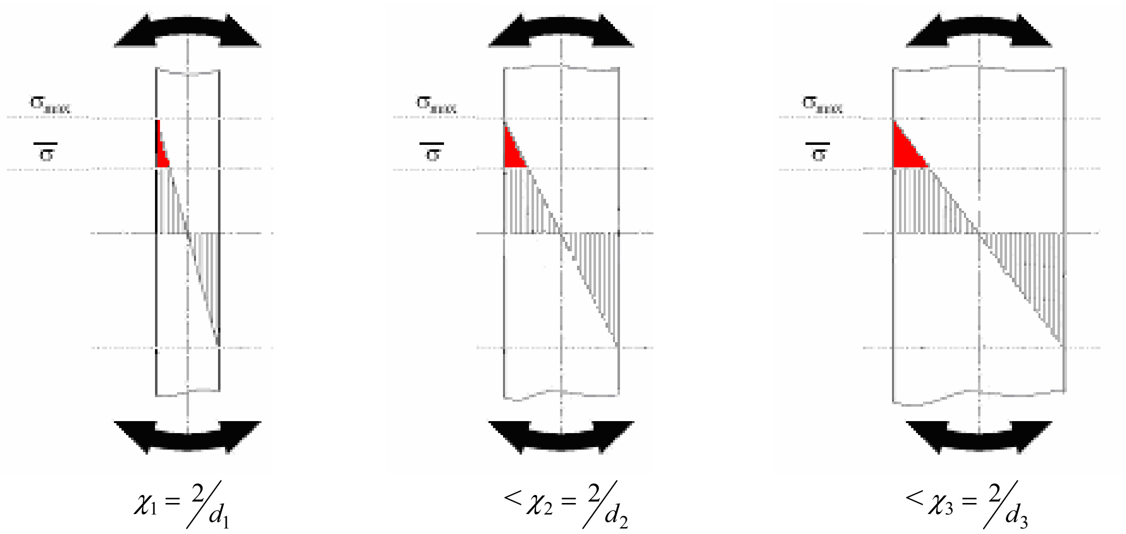

Figure 4.12: Relative stress gradient in specimens with different diameters under bending

This observation allows to understand the lower fatigue strength of a component loaded in rotating bending than the fatigue strength in alternating bending, under the same test conditions. In the former case all the external fibres of the section are loaded to the maximum value of the stress whereas in the latter just a single point of the external surface is loaded to the maximum stress level.

Thus:

$$n = f\left(\begin{array}{c} \chi \\ \text{related to} \\ \text{volume of critical stress range} \end{array} ;\, \text{local plasticity};\, \begin{array}{c} \text{macroscopic stress distribution} \\ \text{related to} \\ \text{grain dimension} \end{array} ;\, \begin{array}{c} \text{macroscopic stress distribution} \\ \text{related to} \\ \text{macroscopic stress distribution} \end{array} \right) \tag{4.28}$$

2. Local plasticity

The cyclic yielding that leads to a localized plastic deformation at the notch root reduces the peak stress amplitude. The beneficial effect of the stress gradient is achieved by a less number of plasticized fibres (Figure 4.13).

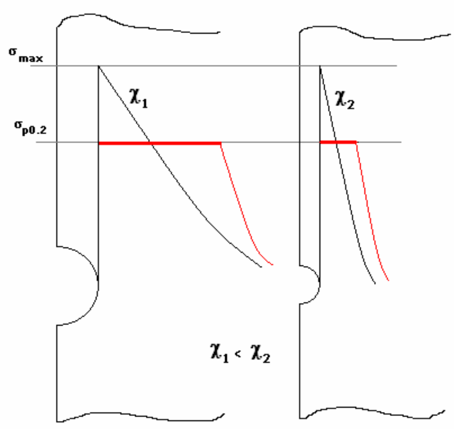

Figure 4.13: Schematic representation of the relative stress gradient effect in presence of a plastic deformation

3. Macroscopic stress distribution/ grain dimension

The effect of the ratio between the stress distribution caused by the macroscopic notch and the grain dimension can be understood observing that the level of stress acting on material grains is responsible of fatigue failure.

As schematically shown in the Figure below for five different notches with the same material and the same peak stress, as notch radius decreases, the stress gradient becomes steeper and steeper resulting in a lower average stress level.

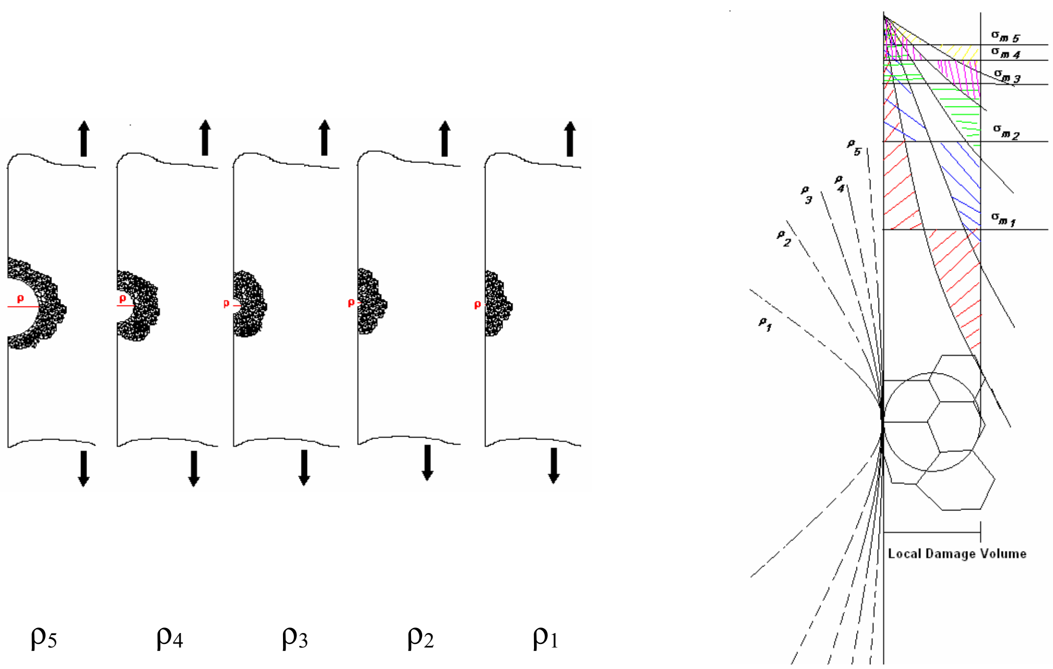

Figure 4.14: Effect of different relative stress gradient on the average stress that acts on structural grains

The Figure below illustrates, on the contrary, the same notched component with different material tensile strength values, i.e. with different grain dimension.

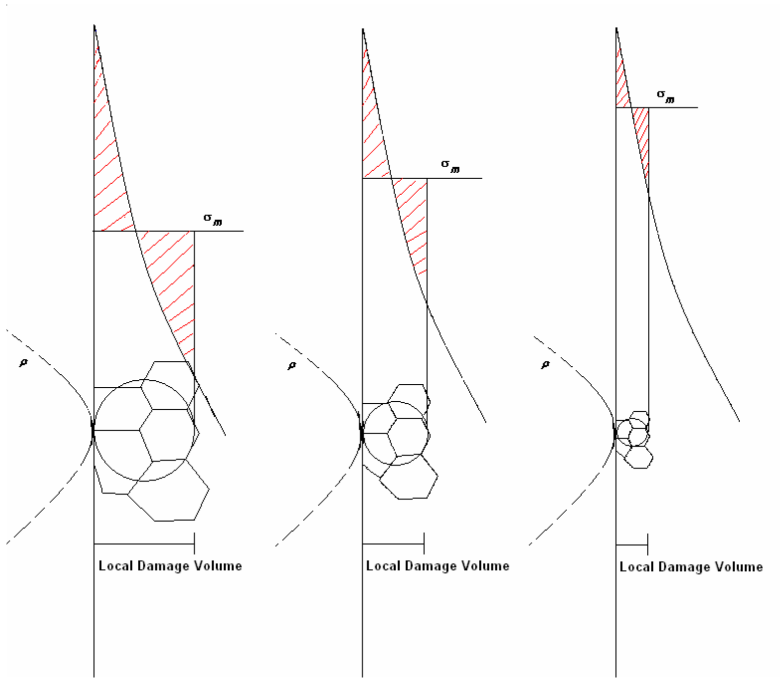

Figure 4.15: Effect of the grain dimension on the average stress that acts on structural grains

4. Macroscopic stress distribution/ Microscopic stress distribution

The fatigue strength depends also on the ratio between the stress distribution due to the presence of a macroscopic notch (like a hole, thread, etc.) and the stress distribution generated by an internal flaw. If the stress gradient is similar, that means a notch radius of the same order of magnitude of the characteristic dimension of the flaw, the material is almost insensible to the presence of a macroscopic notch since the internal flaws act as internal notches and significantly reduce the effect of external notches.

Thus, mid and high strength steels, and, more generally, uniform fine grained-materials, where the flaws and the inhomogeneity are smaller than the grain size, are very sensitive to the presence of an external notches; on the contrary, the grey cast iron has a very low sensitivity due to the graphite flakes.

These observations should also explain why the surface finishing is usually more critical for high-strength steels since surface conditions can be characterized as notch-like surface irregularities.

The trade-off between the mechanical static and dynamic properties of a material can be thus understood. On one side the static strength increases with a fine-grained regular structure; on the other the fatigue strength improves with the increasing grain dimensions that reduce the average stress level on the local damage zone and the notch sensitivity effect.

So, even if from a low-static strength steel to an higher-static strength and hardness steel the fatigue resistance usually improves, such an increase is not as attended due to the increased notch sensitivity.

In other terms, the difference between the stress concentration factor K_t and the fatigue notch factor K_f, that accounts for material effects, increases with a decrease in both the notch root radius, i.e. with an increase of the relative stress gradient, and the ultimate static tensile strength.

With the same material (the same static tensile strength) the effect of the stress gradient on the fatigue strength, can be clearly seen in Figure 4.16 through the support effect number expressing this difference as a ratio between K_t and K_f, n=K_t/K_f.

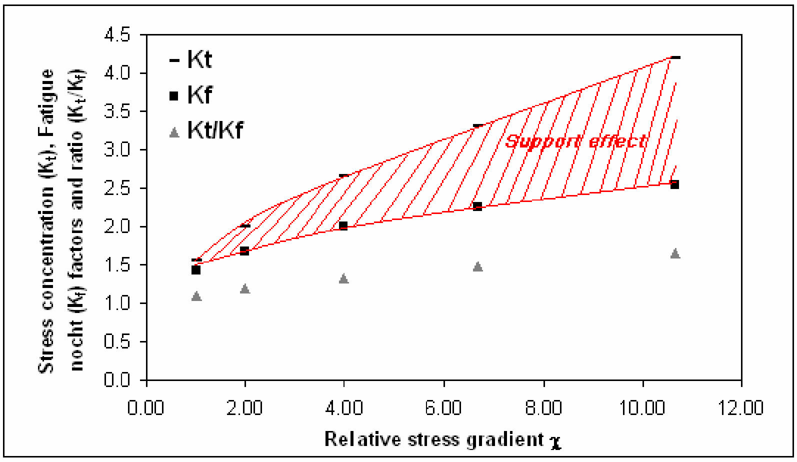

Figure 4.16: Support effect over the relative stress gradient

The red region in the Figure above represents the beneficial effect of an increased relative stress gradient in the fatigue strength but appropriately damped by the effect of material that account for the notch sensitivity.

Low-intermediate life region (Finite life)

In the low and intermediate life region (N =10^3÷10^6) an increasing cyclic yielding occurs at the notch root reducing the sensibility to the one notch to that predicted by K_f at the fatigue limit.

This means that the various formulations proposed to modify the fatigue life in the infinite life region to account for notches can not be extended to this region.

Two models have been proposed in literature to adapt the S-N curve in the low-intermediate life region for the notch effect, one by Heywood in 1962, the other by Collins in 1993. Whilst the former has been described in section 4.2.2.2., in the Collins model the S-N curve for a notched component is defined by a straight line that connect the fatigue limit of the notched component with the fatigue strength at one cycle. The two models are schematically represented in the Figure below:

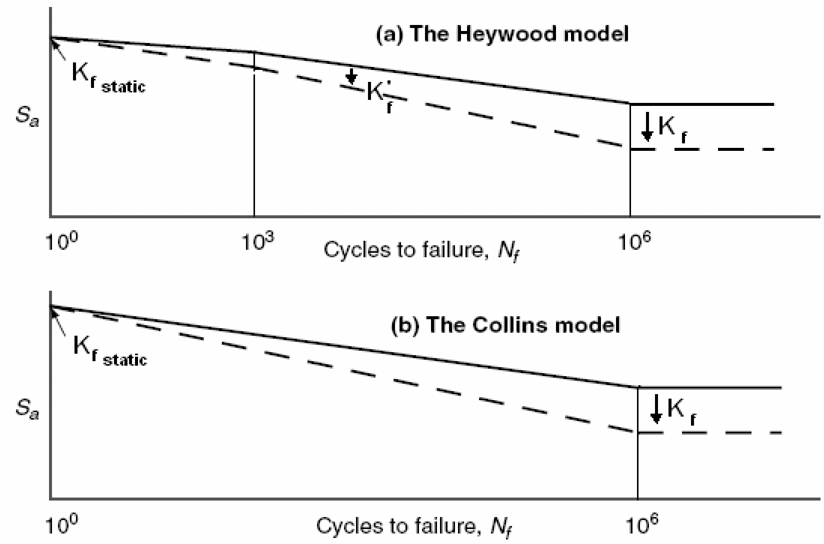

Figure 4.17: Schematic representation of the model proposed by Heywood (a) and Collins (b) to compute the fatigue life in the low-intermediate region

Nevertheless, these formulations can not be extended to components being based on the definition of the fatigue notch factor K_f. Empirical models have been proposed by Hück (1981) (section 4.2.2.6.) and Eichlseder (2002a,b) (section 4.2.4.) that not account for K_f or K_t.

In general, if the fatigue behaviour is dominated by the crack propagation mechanism (i.e. for sharp notched component) the S-N curve often has a steep slope; if the fatigue behaviour is controlled by the crack initiation mode (i.e. smooth or blunt notched components), the S-N-curve has a flatter slope (Lee et al., 2005).

If this phenomenon is observed in terms of local S-N curve instead of nominal S-N curve, according with the previous analysis in the finite life region, it can be stated that, under the same imposed local stress, the specimen with the highest gradient (χ_3) has expected to fail after a greater number of cycles than the specimens with χ_1 and χ_2 (Figure 4.18).

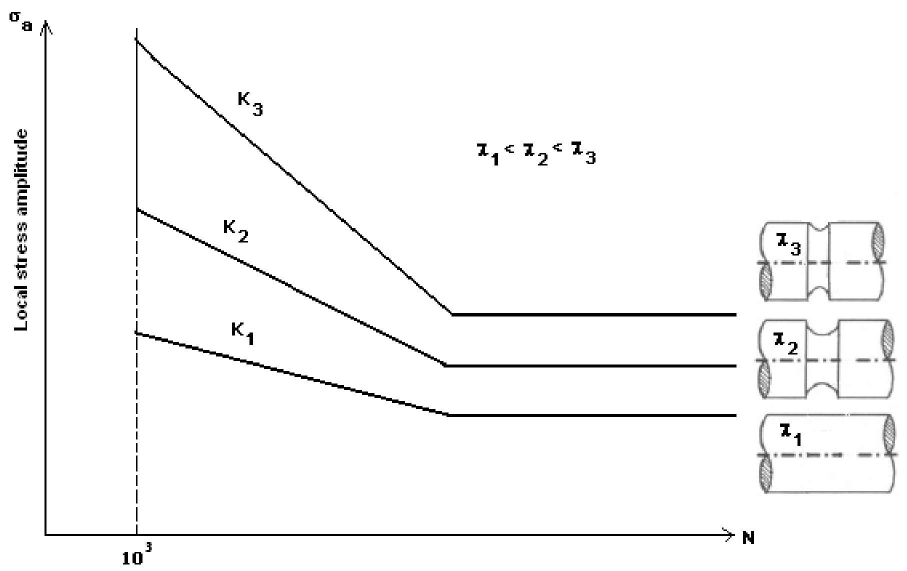

Figure 4.18: Comparison among the slopes of three samples with different values of the relative stress gradient

4.2.4. A recent comprehensive formulation proposed by Prof. Eichlseder

A very recent formulation has been proposed by Prof. Eichlseder that moved towards a most comprehensive formulation of the S-N curves for generally complex shaped components by means of Finite Element Method (Eichlseder, 2002a, 2002b). The major effort of this theory concerns the possibility to compute the fatigue life in each node of the meshed structure by the knowledge of only two S-N curves of the material.

On the basis of the theories previously reported, Eichlseder proposes novel empirical formulations for the fatigue limit, the slope k and the number of cycles at the fatigue limit based on the support effect n **:**

$$n = \left(1 + \left(\frac{\sigma_{bf}}{\sigma_{tf}} - 1\right) \cdot \left(\frac{\chi^*}{(2/b)}\right)^{K_D}\right) \tag{4.29}$$

$$\sigma_{DLocal(\chi \neq 0)} = \sigma_{D(\chi = 0)} \cdot n \tag{4.30}$$

$$k = k_{\min} + \frac{k_{\max} - k_{\min}}{n^{K_k}} \tag{4.31}$$

$$\log(N_D) = \log(N_{D\min}) + \frac{\log(N_{D\max}) - \log(N_{D\min})}{n^{K_n}} \tag{4.32}$$

where

$\sigma_{DLocal\,(\chi \neq 0)}$	Local fatigue limit of the *component*
σ_{bf}	Fatigue limit of the *material* under rotating bending load ($\chi = 2/d$)
σ_{tf}	Fatigue limit of the *material* under axial load ($\chi = 0$)
$(2/b)$	Relative stress gradient of the specimen under rotating bending
χ^*	Relative stress gradient of the *component*
K_D	Damping coefficient for the fatigue limit
$k_{\min}$	Slope of unnotched specimen under rotating bending load
$k_{\max}$	Slope of unnotched specimen under axial load
k	Slope of the S-N curve of the *component*
K_k	Damping coefficient for the slope k
N_D	Number of cycles at the fatigue limit for the *component*
$N_{D\min}$	Number of cycles at the fatigue limit for the specimen under rotating bending load
$N_{D\max}$	Number of cycles at the fatigue limit for the specimen under axial load
K_n	Damping coefficient for the number of cycles at the fatigue limit

The parameters are correlated by the well-known equation:

$$N_i = N_D \left(\frac{\sigma_D}{\sigma_{ai}} \right)^k \tag{4.33}$$

According to the basic idea of Bollenrath and Troost (1950-1951) of limiting the number of required attempts, for equations (4.29-4.30), (4.31) and (4.32) to define σ_D, k and N_D respectively, two data sets are needed: generally, an S-N curve of the material for a specimen with a zero or low relative stress gradient value, corresponding to N_{max} and k_{max}, and an S-N curve of the material for a specimen with an high value of χ, corresponding to N_{min} and k_{min}. In the formula (4.29), the former condition refers to the general term σ_{tf}, intended as the fatigue limit of an unnotched specimen under push-pull loading with a stress gradient equal to 0, while the latter refers to the term σ_{bf} of a bending specimen with a gradient of χ=2/b.

Nevertheless, a more general formulation can be rewritten as follow:

$$n = \left(1 + \left(\frac{\sigma_{D(\chi \neq 0)}}{\sigma_{D(\chi = 0)}} - 1 \right) \cdot \left(\frac{\chi^*}{\chi \neq 0} \right)^{K_D} \right) \tag{4.34}$$

from which emerges that the interpolation is carried out between a fatigue limit correspondent to null gradient and a fatigue limit correspondent to a not null gradient, thus releasing the formulation from the push-pull or the bending tests. In fact a null gradient, or close to zero value, can, for example, be obtained also with thin thickness hollow specimens under torsion loading. Likewise, a not null gradient could be obtained for a lot of geometric and loading configurations.

Thus, the proposed formulation has the advantage to relate the local S-N curve of the component to the knowledge of only two S-N curves of the material in rotating bending and axial loads. These are usually already known for a wide variety of materials and allow to determine the fatigue life in each stressed area of the component according to the proposed theory. The Finite Element Method lets to calculate the relative stress gradient in each point of interest of the structure computing the derivative of the stress distribution according to

$$\chi' = \frac{1}{\sigma_{\max}} \left(\frac{d\sigma}{dx} \right)$$

The exponent K_D in the formula (4.29) proposed by Eichlseder to compute the fatigue limit allows to account for the history of the support effect over the stress gradient according to what observed in sections 4.2.2. and 4.2.3. (see Figure 4.16).

As reported in section 4.2.3., the correlation between the fatigue life of smooth and notched components in the low-intermediate life region does not follow the same rules that in the infinite life region, owing to an increasing cyclic plastic yielding. For this, Eichlseder proposed a different damping coefficient value for the fatigue limit and the slope k, K_D and K_k respectively.

K_D, K_k and K_n are characteristic exponents of the class of material. For steel, the following values were proposed:

	K_D	K_k	K_n
Steel	0.3	6.3	2.9

Table 4.7: Values of the characteristic exponents for the formulas (4.29)-(4.32)

In the Figures below the histories of the fatigue limit and the slope k over the relative stress gradient, taken from Eichlseder 2000a, are reported.

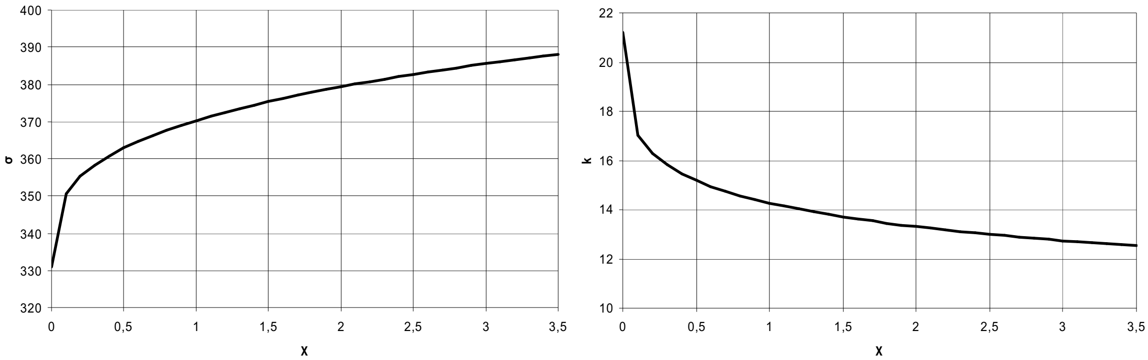

Figure 4.19:General trend of the fatigue limit and the slope k over the relative stress gradient (taken form Eichlseder, 2002a)

Chapter 4.3

Estimation of the relative stress gradient by means of FE Analysis

In this chapter a novel method developed for the computation of the relative stress gradient by means of the Finite Element Method is presented with geometries and procedures used. The main results are shown and compared with known analytical solutions.

Nel seguente capitolo viene introdotto e presentato un nuovo metodo sviluppato per il calcolo del gradiente relative di tensione per mezzo dell'analisi agli Elementi Finiti. Vengono mostrate le geometrie e le procedure di modellazione utilizzate per il confronto dei valori predetti con soluzioni analitiche note.

The paramount importance of the stress gradient for assessing the fatigue strength in components. clearly emerges from the analysis of the literature made in the previous paragraph. The stress gradient actually allows to know and describe the uneven stress field due to the geometry and/or to the type of acting loading.

The sole available Table for stress gradient formulations is provided by Siebel and Stieler (Siebel and Stieler, 1954, 1955):

Notch geometry	Relative stress gradient χ		
	Type of load		
	Axial	Bending	Torsion
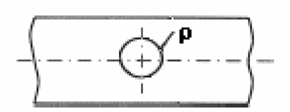	$\chi = \frac{2}{\rho}$	—	—
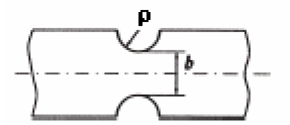	$\chi = \frac{2}{\rho}$	$\chi = \frac{2}{\rho} + \frac{2}{b}$	—
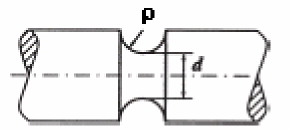	$\chi = \frac{2}{\rho}$	$\chi = \frac{2}{\rho} + \frac{2}{d}$	$\chi = \frac{2}{d} + \frac{1}{\rho}$
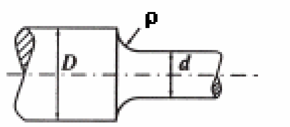	$\chi = \frac{2}{\rho}$	$\chi = \frac{2}{D+d} + \frac{2}{\rho}$	$\chi = \frac{2}{D+d} + \frac{1}{\rho}$
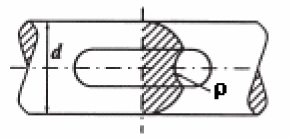	—	—	$\chi = \frac{2}{\rho}$
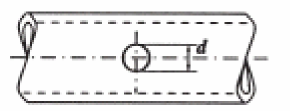	—	$\chi = \frac{2}{D} + \frac{8}{\rho}$	$\chi = \frac{2}{D} + \frac{6}{\rho}$

Table 4.8: Relative stress gradient as given by Siebel and Stieler (Siebel and Stieler, 1954, 1955)

The expressions reported in the Table 4.8 are approximated formulas since they do not take into account the finite dimensions of components. These forms are valid for the components for which the absolute dimensions of notch are small compared with all other dimensions. As an example, the relative stress gradient for a flat bar with a central circular hole under axial load was derived form the analytical solution proposed by Neuber (Neuber, 1958) for a flat infinite bar with circular hole under tension:

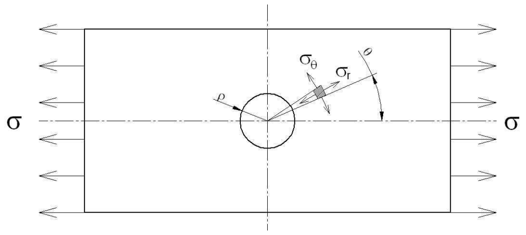

Figure 4.20: Schematic problem for the analytical solution of a flat bar with a circular hole under tension according to Neuber

$$\begin{aligned}
\sigma_r(r,\theta) &= \frac{\sigma}{2}\left(1-\frac{\rho^2}{r^2}\right)+\frac{\sigma}{2}\left(1-\frac{4\rho^2}{r^2}+\frac{3\rho^4}{r^4}\right)\cos 2\theta \\
\sigma_\theta(r,\theta) &= \frac{\sigma}{2}\left(1+\frac{\rho^2}{r^2}\right)-\frac{\sigma}{2}\left(1+\frac{3\rho^4}{r^4}\right)\cos 2\theta \\
\tau_{r\theta}(r,\sigma) &= -\frac{\sigma}{2}\left(1+\frac{2\rho^2}{r^2}-\frac{3\rho^4}{r^4}\right)\sin 2\theta
\end{aligned} \tag{4.35}$$

The peak stress occurs at $r=\rho$, $\theta=90°$ or $\theta=270°$, where $\sigma_r=0$ e $\tau_{r\theta}=0$. Thus, the relative stress gradient along the direction (x) perpendicular to the applied load (y) ($\theta=90°$) is (Zambonelli, 2006):

$$\sigma_y(x)=\frac{\sigma}{2}\left(2+\frac{\rho^2}{x^2}+\frac{3\rho^4}{x^4}\right) \tag{4.36}$$

$$\chi'=\left|\frac{1}{\sigma_y(\rho)}\left(\left.\frac{d\sigma_y}{dx}\right|_{x=\rho}\right)\right|=\frac{7}{3\rho} \tag{4.37}$$

Although the importance of an exact solution of the relative stress gradient has been emphasized and various analytical solutions have been proposed in literature (Filippini, 2000), the aim of the present work was to propose a method for the computation of the stress gradient by means of Finite Element Method. It was intrinsically accepted, in first approximation, to compare FE results with the forms in Table 4.8. However, the values in Table 4.8 can be considered as conservative approximations (Dietmann, 1985); they actually provide the lowest value of the relative stress gradient implying the lowest support effect and, consequently, a reduced predicted fatigue life.

The Finite Element models of the cases reported in Table 4.8 and the related main results are here shown.

Flat bar with circular central hole

(a1) Axial load

The following geometrical parameters have been simulated:

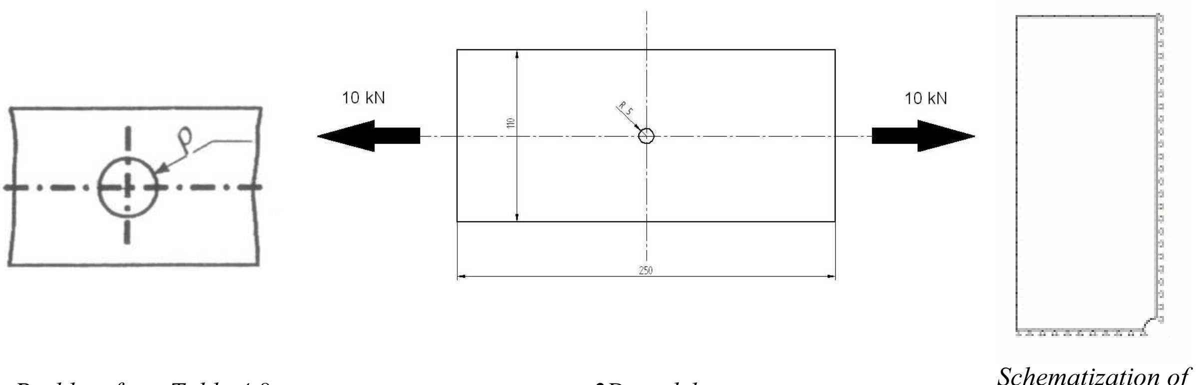

Problem from Table 4.8 *2D model* *Schematization of the constrains*

Figure 4.21: Models for the FE calculation of the flat bar with circular central hole under axial load

From the analytical solution proposed by Neuber (equation (4.37)), for the specific dimensions reported in Figure 4.21, it is expected a value of the relative stress gradient $\chi = 7/3\rho = 0.467 mm^{-1}$.

This geometry presents two perpendicular symmetry axes; thus only a quarter of model has been simulated. The model has been studied under the hypothesis of plane stress state and bidimensional isoparametric elements chosen for meshing: triangular 6-noded or quadrangular 8-noded elements.

Different methods of meshing have been taken into account and compared with increasing number of element in terms of peak stress and predicted relative stress gradient:

- Mapped mesh with quadrangular 8-noded elements (a)
- Free mesh with quadrangular 8-noded elements (only near the notch root) (b)
- Free mesh with triangular 6-noded elements (c)

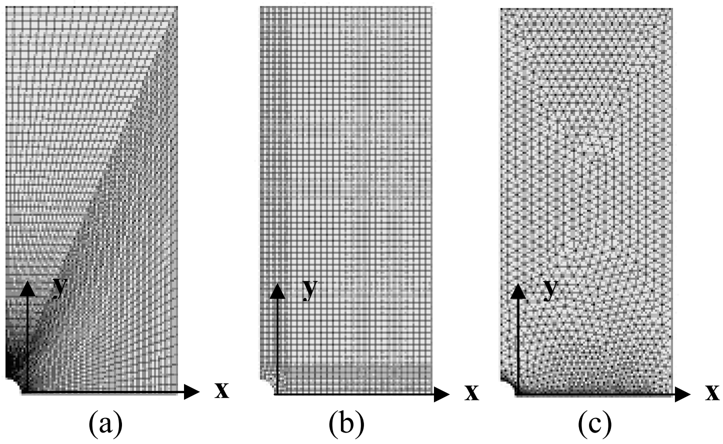

Figure 4.22: Meshes evaluated in the simulation: (a) mapped; (b) free only near the notch root; (c) free

A preliminary convergence test with increasing mesh refinement level was developed to ensure the numerical accuracy of the models. The element dimension is governed by the number of divisions of the side fitting the x-axis. In the Table below, the peak stress (σ_{max}) and the relative stress gradient (χ), calculated as linear interpolation between the first two adjacent nodes from the notch root, are reported over the number of divisions of this side.

The relative stress gradient was calculated on the basis of the stress at the node at the notch root (node i) and the adjacent node along the x-axis (node j):

$$\chi = \frac{\sigma_i - \sigma_j}{x_i - x_j} \cdot \frac{1}{\sigma_i} \tag{4.38}$$

where x_i and x_j are the x-coordinates of the node i and j respectively.

Number of divisions	Theoretical values		Mesh type					
			(a)		(b)		(c)	
	σ_{max}	χ	σ_{max}	χ	σ_{max}	χ	σ_{max}	χ
50	276	0.467	257	0.297	266	0.309	262	0.301
100			262	0.362	264	0.362	262	0.358
150			263	0.389	264	0.386	263	0.390
200			263	0.403	264	0.401	263	0.404

Table 4.9. Convergence test of the peak stress and the relative stress gradient over different types of meshes.

As can be observed, the three meshing methods give almost the same results. It was chosen to use the mapped mesh with quadrangular 8-noded elements.

Two methods of load application were subsequently simulated: concentrated and distributed, monitoring the peak stress and the relative stress gradient.

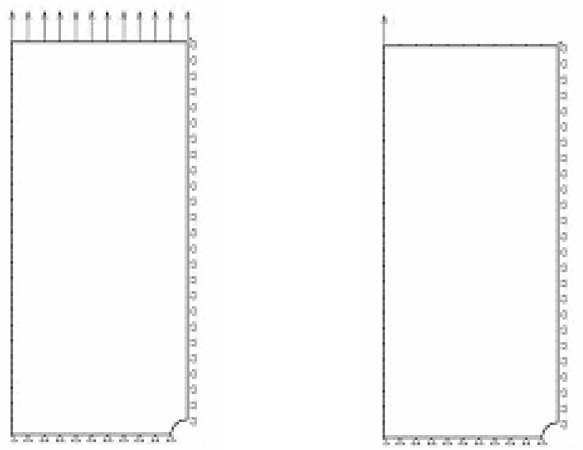

Distributed load *Concentrated load*

Figure 4.23: Simulated methods of load applying

The results are reported in the Table below.

Number of divsions	Theoretical values		Type of load			
			Distribuited		Concentrated	
	σ_{max}	χ	σ_{max}	χ	σ_{max}	χ
50	276	0.467	269	0.306	257	0.297
100			273	0.374	262	0.362
150			275	0.402	263	0.389
200			275	0.417	263	0.403

Table 4.10. Convergence test of the peak stress and the relative stress gradient over different types of load application.

As expected, the distributed load gave a more accurate convergence to theoretical values than the concentrated one, since the former better simulates the real loading conditions.

The relative stress gradient, being defined as a derivative, is, for its nature, a punctual measure. The analysis with the Finite Element Method can on the contrary provide only discreet measures in form of nodal or element solutions.

In order to overcome this problem, it has been proposed to interpolate a number of consecutive nodal or element solutions and to compute the relative stress gradient as the ratio between the derivative of the interpolation and the interpolation itself at the peak stress.

The most accurate result was achieved by the polynomial interpolation of 4 or more than 4 nodal adjacent nodal solutions analytically computing the derivate ($d\sigma/dx$) at the point of σ_{max}.

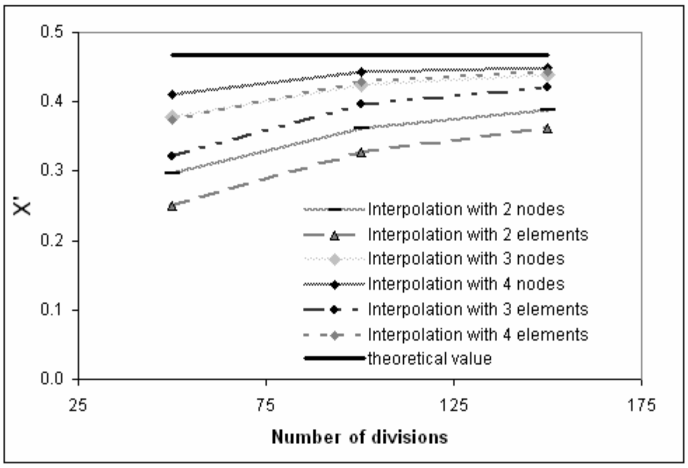

Figure 4.24: Comparison of the convergence of the relative stress gradient for various interpolations of nodal or element solutions

More than cubic polynomial interpolation did not give a significant improvement to convergence.

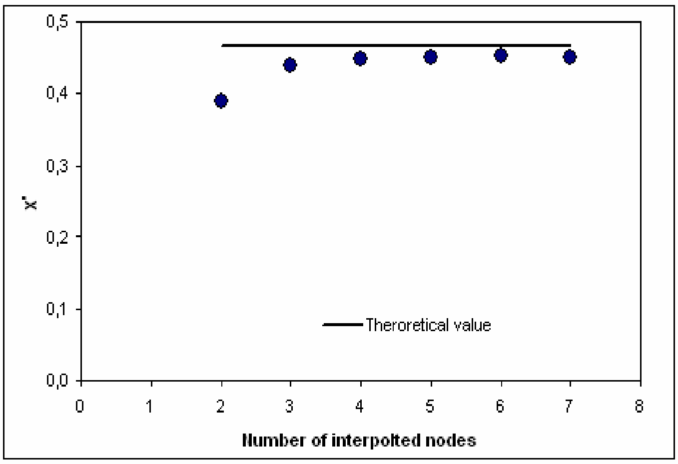

Figure 4.25: Comparison of the increasing number of interpolated nodes in term of relative stress gradient

Obviously, the same result would have been achieved with a greater number of divisions, i.e. lower element dimensions. However, the aim was to develop "an operating" method allowing robust and accurate calculation of the relative stress gradient in reasonable time.

An additional faced problem was the choice of the stress used for the calculation. As reported in literature (Siebel and Gaier, 1956), if the percentage difference between one of the principal stresses and the equivalent Von Mises stress is less than 12% the relative stress gradient has to be computed through the peak principal stress. A 12% difference leads to overestimate the relative stress gradient of an order of 22%, using the Von Mises equivalent stress (Siebel and Gaier, 1956).

For the analysed case it was obtained:

Number of divisions	χ		**% Err**
	σ_y	σ_{id}	
50	0.426	0.504	18 %
100	0.458	0.552	21 %
150	0.464	0.562	21 %
200	0.466	0.565	21 %

Table 4.11: Comparison of the convergence of the relative stress gradient computed by the longitudinal stress σ_y and the Von Mises stress σ_{id}.

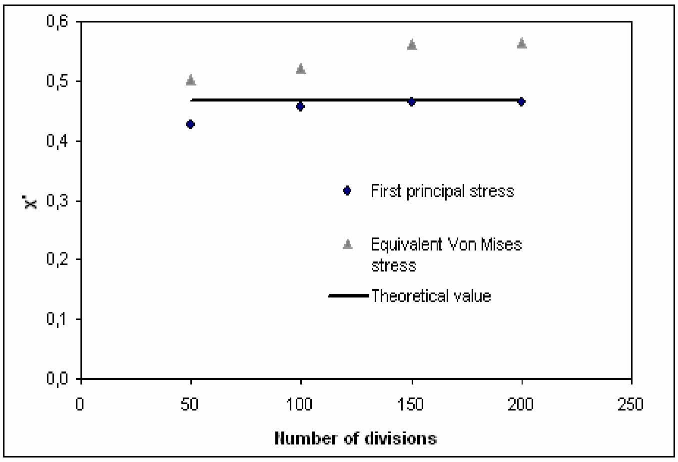

Figure 4.26: Comparison of the relative stress gradient computed by the longitudinal stress σ_y and the Von Mises stress σ_{id} with the theoretical solution.

Resulting computed and theoretical relative stress gradients for this geometry were therefore:

$$\chi_{computed} = 0.466\, mm^{-1}$$
$$\chi_{theoretical} = 0.467\, mm^{-1} \tag{4.39}$$

The computation of the relative stress gradient for the remaining cases reported in Table 4.8 was therefore carried out by means of cubical interpolation of nodal solutions, mapped meshes and distributed loads. The equivalent Von Mises stress was used in the cases where it was not possible to characterize a prevalent stress direction for the stress distribution.

Flat bar with lateral notches

(b1) Axial load

The FE model is identical to the one of case (a1) except for the longitudinal symmetry axes.

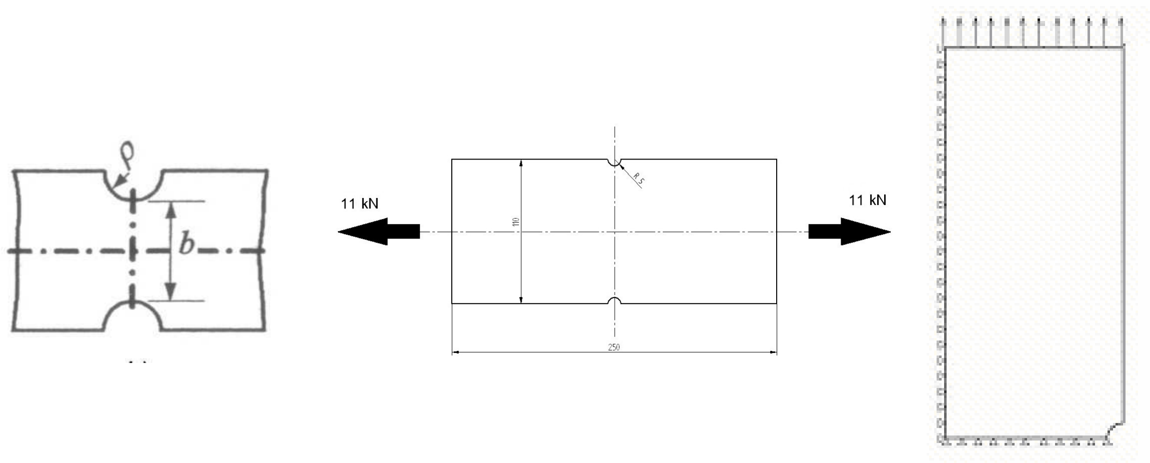

Problem from Table 4.8 *2D model* *Schematization of the constrains*

Figure 4.27: Models for the FE calculation of the flat bar with lateral notches under axial load

Using the same procedure previously described, computed and theoretical relative stress gradients were:

$$\chi_{computed} = 0.448\, mm^{-1}$$
$$\chi_{theoretical} = 0.460\, mm^{-1} \tag{4.40}$$

(b2) Bending load

For this type of load, an antisymmetric constraint was imposed to the neutral axes. The bending load (M_b=202 Nm) was distributed with constant triangular law.

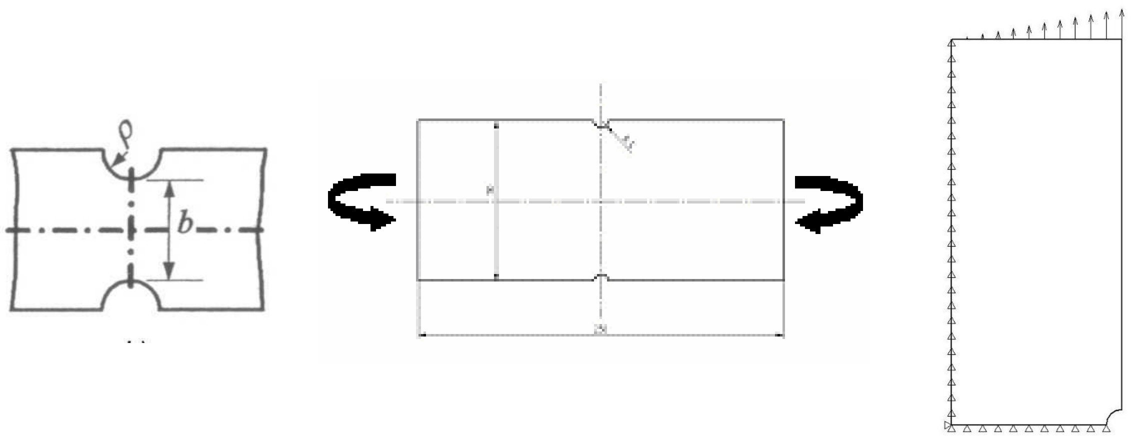

Problem from Table 4.8 *2D model* *Schematization of the constrains*

Figure 4.28: Models for the FE calculation of the flat bar with lateral notches under bending load

Computed and theoretical relative stress gradients were

$$\chi_{computed} = 0.453\,mm^{-1}$$
$$\chi_{theoretical} = 0.450\,mm^{-1} \tag{4.41}$$

Cylindrical specimen with circular groove

(c1) Axial load

The problem is axis-symmetric, both in terms of geometry and loading conditions. Thus, only the plane figure whose revolution generates the specimen geometry was modelled. This led to the same schematization of case (b1).

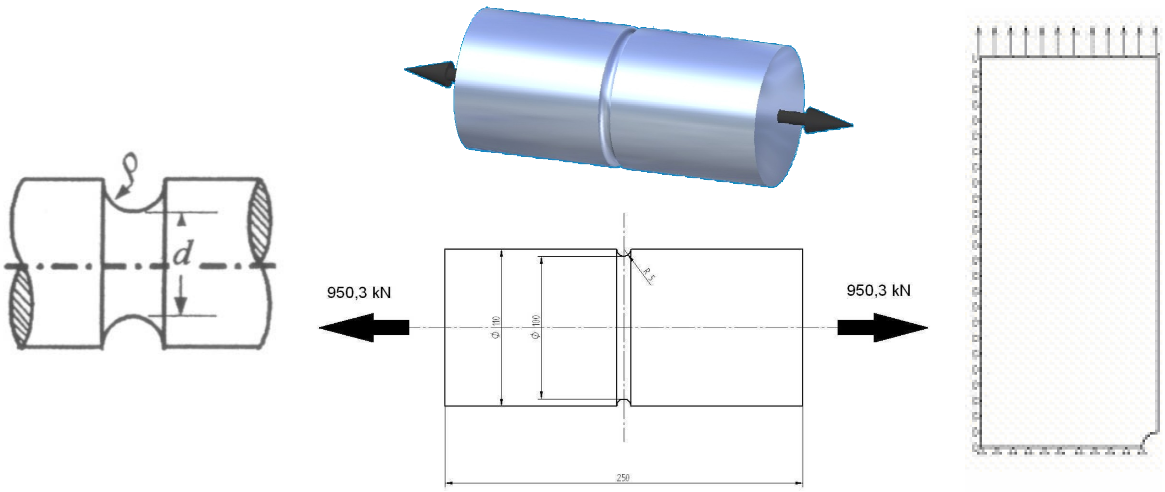

Problem from Table 4.8 *2D model* *Schematization of the constrains*

Figure 4.29: Models for the FE calculation of the cylindrical specimen with circular groove under axial load

Computed and theoretical relative stress gradients were:

$$\chi_{computed} = 0.445\,mm^{-1}$$
$$\chi_{theoretical} = 0.460\,mm^{-1} \tag{4.42}$$

(c2) Bending load

The bending loading conditions make the problem not axis-symmetric. Harmonic elements were used allowing bidimensional modelling but accounting, in each node, for 3 degrees of freedom. At least a point was fixed, i.e. all the constrained degrees of freedom, in order to get the problem isostatic. The bending load (13.1 KNm) was applied with harmonic law in respect of the circumferential coordinate.

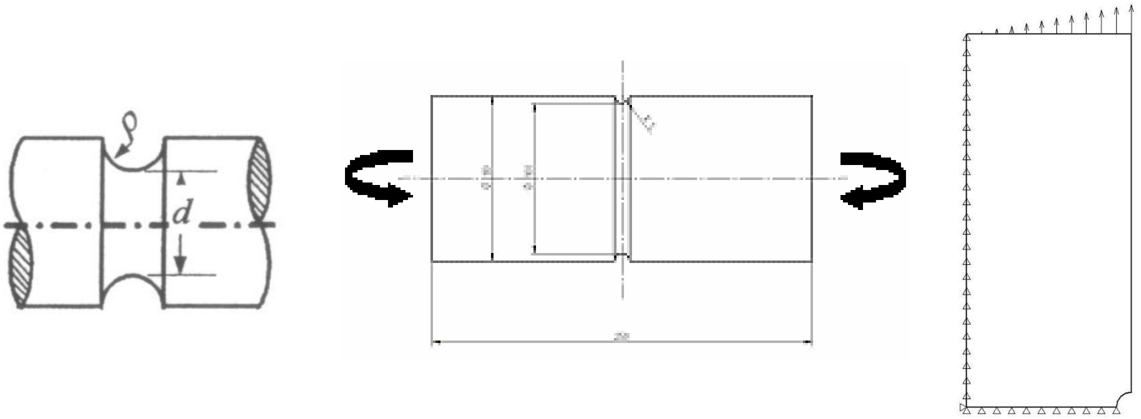

Problem from Table 4.8 *2D model* *Schematization of the constrains*

Figure 4.30: Models for the FE calculation of the cylindrical specimen with circular groove under bending load

Computed and theoretical relative stress gradients were:

$$\begin{aligned} \chi_{computed} &= 0.450\, mm^{-1} \\ \chi_{theoretical} &= 0.450\, mm^{-1} \end{aligned} \tag{4.43}$$

(c3) Torsional load

Like bending, torsional loading makes the problem not axis-symmetric. As in (c2), harmonic elements were used. The points on the rotating axis were constrained in both perpendicular directions to the axis itself, while those ones on the symmetry plane were constrained in the direction parallel to the rotating axis and in the direction perpendicular to the model plane.

The torque (3.95 KNm) was applied with harmonic law in respect of the circumferential coordinate.

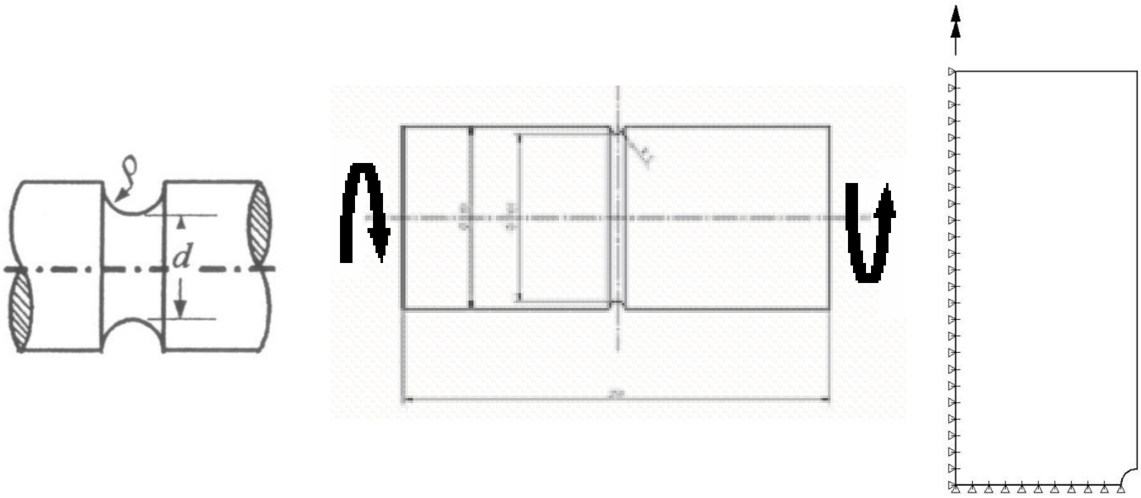

Problem from Table 4.8 *2D model* *Schematization of the constrains*

Figure 4.31: Models for the FE calculation of the cylindrical specimen with circular groove under torsional load

The relative stress gradient was calculated by means of tangential stresses. Computed and theoretical relative stress gradients were:

$$\chi_{computed} = 0.220\, mm^{-1}$$
$$\chi_{theoretical} = 0.220\, mm^{-1} \tag{4.44}$$

Cylindrical specimen with shoulder

(d1) Axial load

The same modelling conditions of (c1) were applied. Thw model was meshed using a mapped mesh in proximity of the connection and a free mesh in the rest of the model.

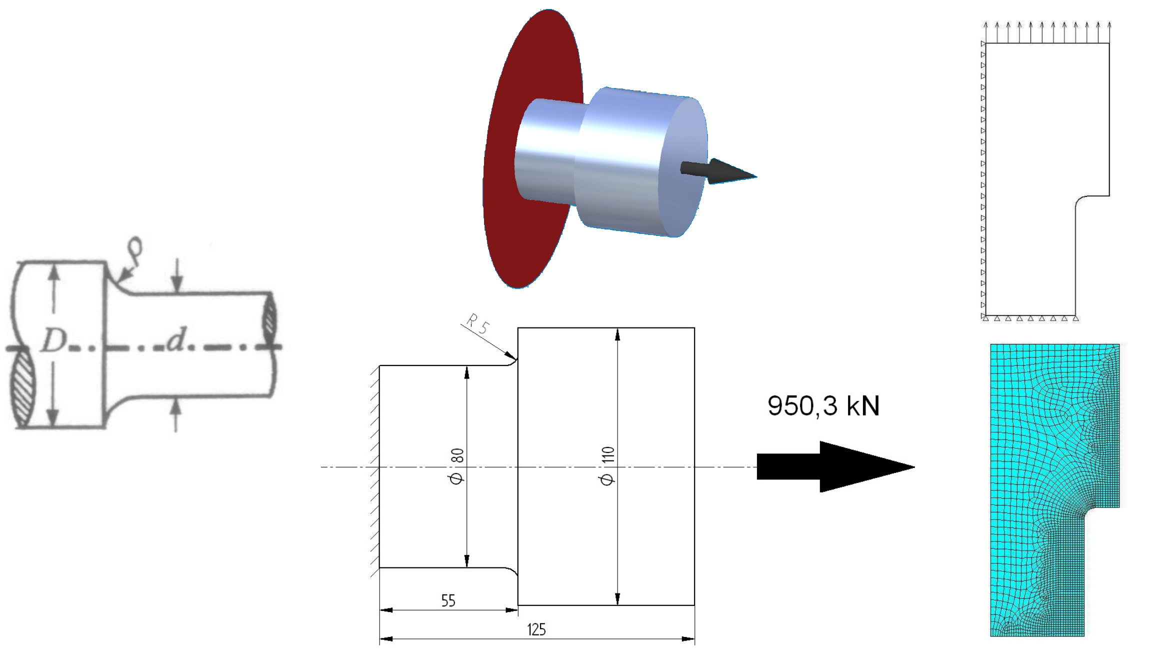

Problem from Table 4.8 *2D model* *Schematization of the constrains*

Figure 4.32: Models for the FE calculation of the cylindrical specimen with shoulder under axial load

Computed and theoretical relative stress gradients were:

$$\chi_{computed} = 0.494\, mm^{-1}$$
$$\chi_{theoretical} = 0.460\, mm^{-1} \tag{4.45}$$

(d2) Bending load

The same modelling conditions of (c2) were applied. A bending moment of 13.1 KNm was applied.

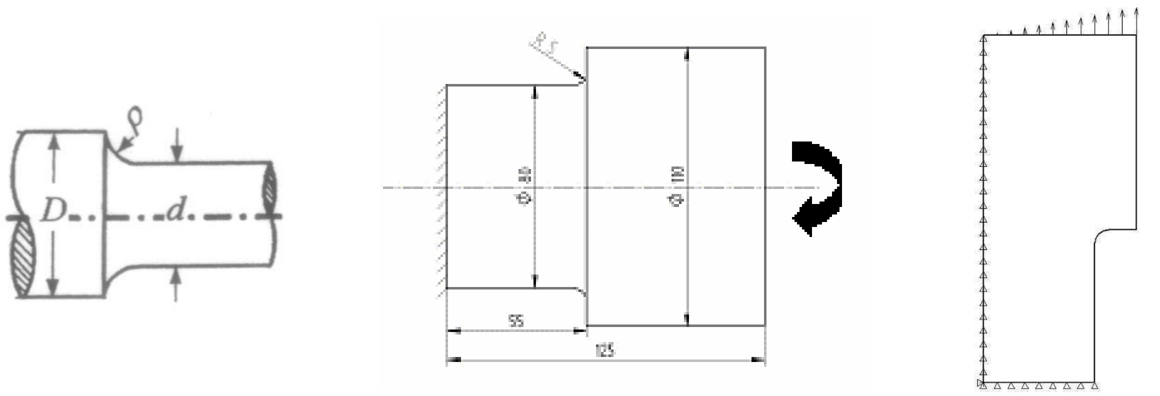

Problem from Table 4.8 *2D model* *Schematization of the constrains*

Figure 4.33: Models for the FE calculation of the cylindrical specimen with shoulder under bending load

Computed and theoretical relative stress gradients were:

$$\chi_{computed} = 0.500\,mm^{-1}$$
$$\chi_{theoretical} = 0.487\,mm^{-1} \tag{4.46}$$

(d3) Torsional load

The same modelling conditions of (c3) were applied. A torque of 3.95 KNm was applied.

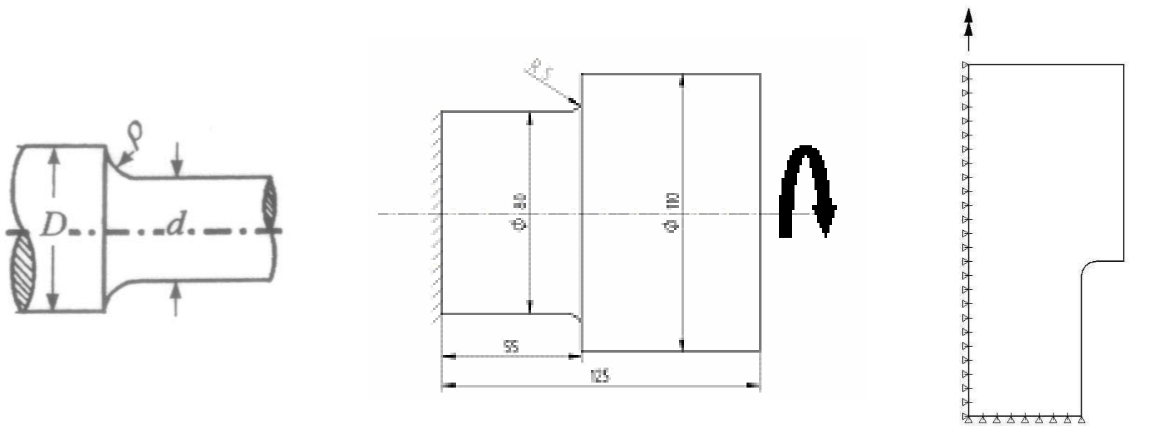

Problem from Table 4.8 *2D model* *Schematization of the constrains*

Figure 4.34: Models for the FE calculation of the cylindrical specimen with shoulder under torsional load

Computed and theoretical relative stress gradients were:

$$\chi_{computed} = 0.253\,mm^{-1}$$
$$\chi_{theoretical} = 0.221\,mm^{-1} \tag{4.47}$$

Cylindrical specimen with parallel key

(e1) Torsional load

The problem is not axis-symmetric; a 3D FE model was thus solved.

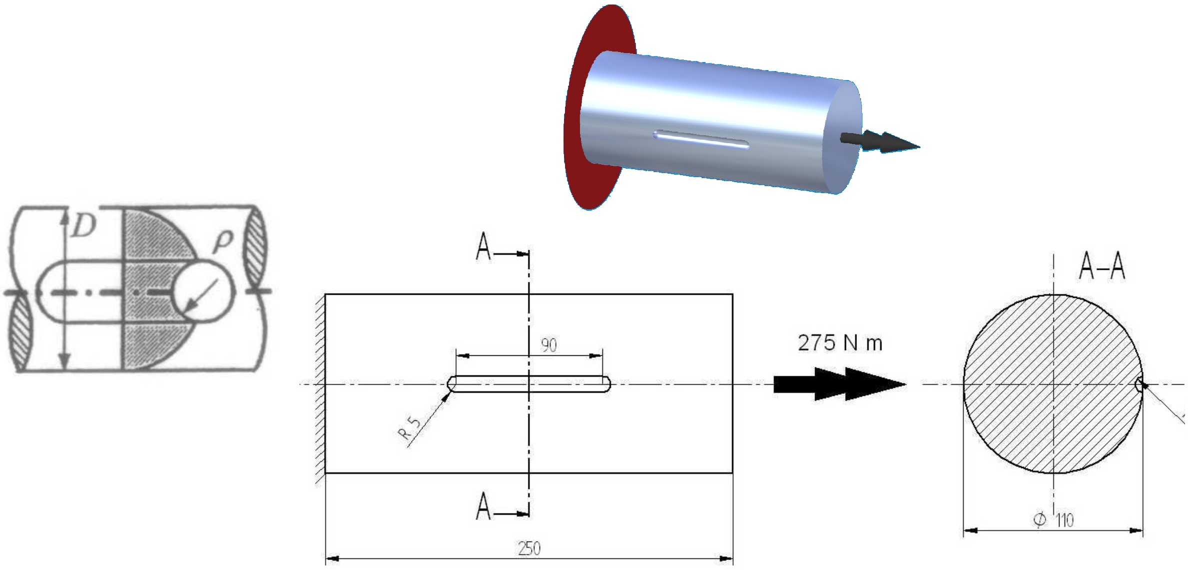

Problem from Table 4.8 *2D model*

Figure 4.35: Models for the FE calculation of the cylindrical specimen with parallel key under torsional load

A fine mapped mesh with hexahedral elements was used near the parallel key, whereas a coarse free mesh with tetrahedral elements was used in the rest of the model.

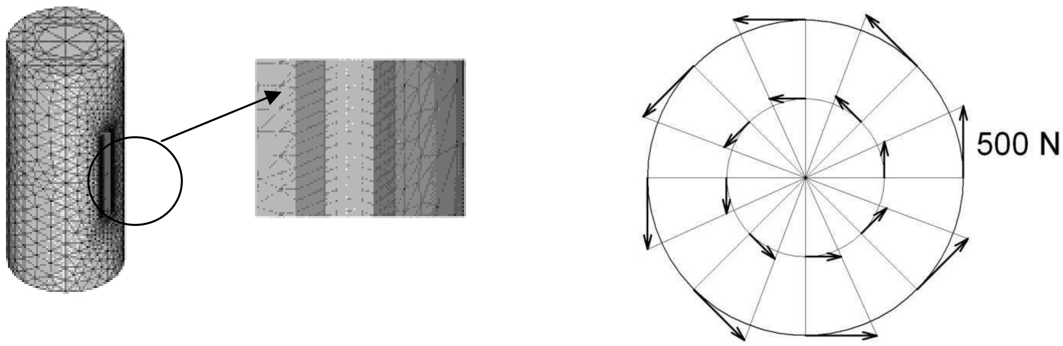

Figure 4.36: FE model of the cylindrical specimen with parallel key (right) and schematic representation of the applied load (left)

The FE model was fixed at one end. In order to better simulate the distributed torsional load, a constant force was applied in many nodes of the model free end.

The stress state near the parallel key is strongly multiaxial. The relative stress gradient was therefore calculated by means of the equivalent Von Mises stress. Computed and theoretical relative stress gradients were:

$$\begin{aligned} \chi_{computed} &= 0.223\, mm^{-1} \\ \chi_{theoretical} &= 0.218\, mm^{-1} \end{aligned} \qquad (4.48)$$

Hollow cylindrical specimen with transversal hole

(f1) Torsional load

Like (e1), the 3D FE solid model was solved using a fine mapped mesh with hexahedral elements near the hole and a coarse free mesh with tetrahedral elements in the rest of the model. The FE model was fixed at one end and loaded at the free end with a constant force applied in many nodes.

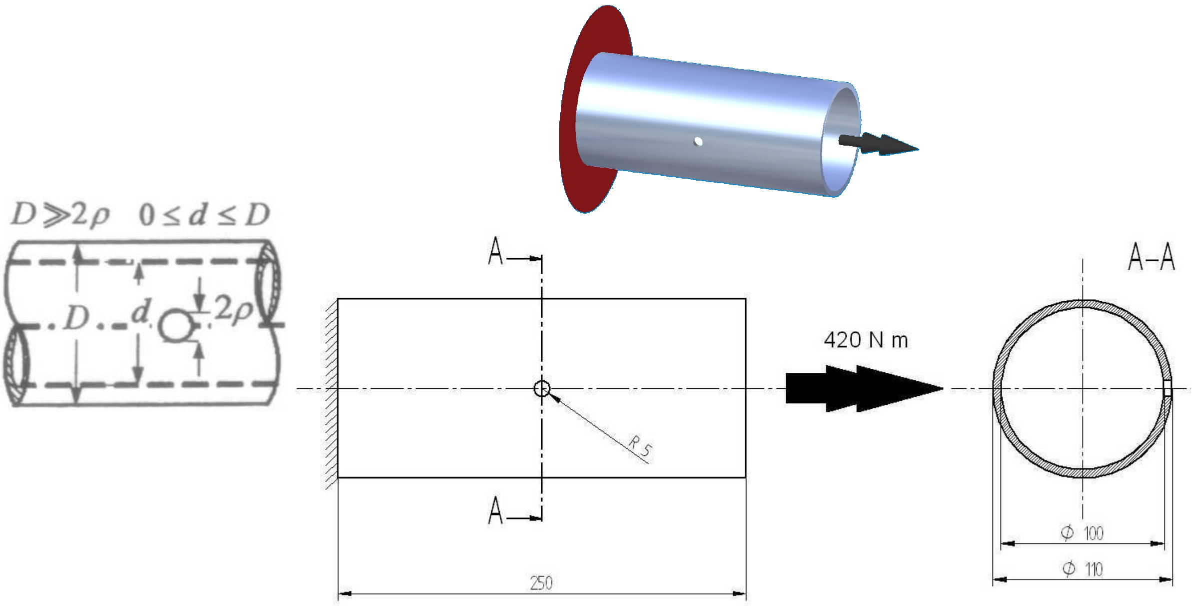

Problem from Table 4.8 *2D model*

Figure 4.37: Models for the FE calculation of the hollow cylindrical specimen with transversal hole under torsional load

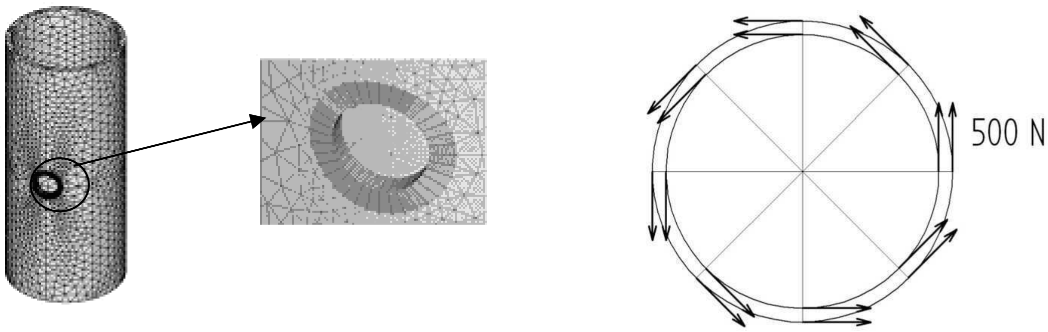

Figure 4.38: FE model of the hollow cylindrical specimen with transversal hole (right) and schematic representation of the applied load (left)

Computed, by means of Von Mises stress, and theoretical relative stress gradients were:

$$\chi_{computed} = 0.318\,mm^{-1}$$
$$\chi_{theoretical} = 0.318\,mm^{-1} \tag{4.49}$$

(f2) Bending load

The same FE model developed for (f1) was used in case of bending load (M=40 KNm).

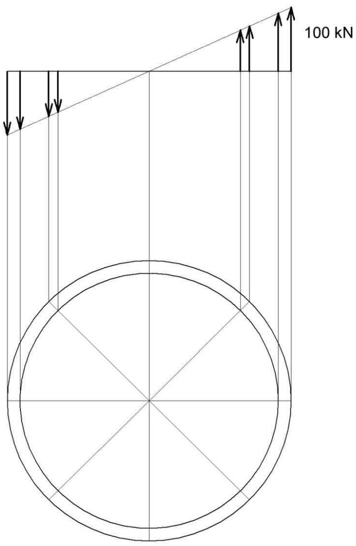

Figure 4.39: Schematic representation of the bending load applied to the hollow cylindrical specimen with transversal hole

Computed, by means of Von Mises stress, and theoretical relative stress gradient were:

$$\chi_{computed} = 0.436\,mm^{-1}$$
$$\chi_{theoretical} = 0.418\,mm^{-1} \qquad (4.50)$$

In the Table below the computed relative stress gradients are shown and compared with theoretical solutions. The percentage errors are also reported.

Notch geometry	**Load**	**χ**		**% Err**
		Theoretical	Computed	
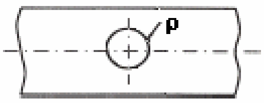	Axial (a1)	0.467	0.466	0.2 %
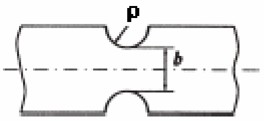	Axial (b1)	0.460	0.448	2.6 %
	Bending (b2)	0.450	0.453	0.7 %
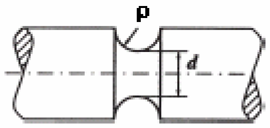	Axial (c1)	0.460	0.445	3.3 %
	Bending (c2)	0.450	0.450	0.0 %
	Torsion (c3)	0.220	0.220	0.0 %
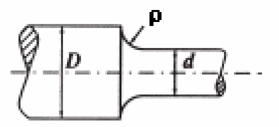	Axial (d1)	0.460	0.494	7.4 %
	Bending (d2)	0.487	0.500	2.7 %
	Torsion (d3)	0.221	0.253	14.5 %
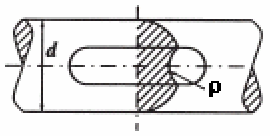	Axial (e1)	0.218	0.223	2.3 %
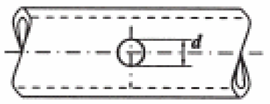	Axial (f1)	0.318	0.318	0.0
	Bending (f2)	0.418	0.436	4.3

Table 4.12: Comparison of computed versus theoretical values of the relative stress gradient

As it can be observed, the developed method leads to percentage errors less than 8% with only one case of 14%. It can therefore be considered enough accurate, robust and reliable to compute χ in more complex FE models of components or subcomponents.

Chapter 4.4

Verification of the theory proposed by Prof. Eichlseder against experimental data from literature: fatigue limit and slope

The proposed theory to compute the local S-N curve has been assessed against experimental data from the literature.

In this section experimental fatigue limits and slopes of the S-N curves are compared with the values predicted by the theories presented in chapter 4.2, based on the local stress and relative stress gradient concepts.

La teoria proposta per calcolare la curva S-N locale viene verificata tramite il confronto con dati sperimentali da letteratura.

Nella presente sessione, i limiti di fatica e le pendenze delle curve S-N sperimentali vengono comparati con i valori predetti dalle diverse teorie presentate nel capitolo 4.2, basate sui concetti della tensione locale e del gradiente relativo di tensione.

4.4.1. Data from the literature

A great amount of data in literature is available on various types of steels. Nevertheless, in order to validate the proposed theory on the local S-N curves, it was necessary to collect data with following characteristics:

(1) Groups of data with at least three tests with different relative stress gradient values but with exactly the same other test conditions (e.g. static properties, material state, etc.);

(2) Tests performed on specimens in standard conditions (stress ratio R=-1, room temperature, etc.).

The former condition arises from the need, as explained in section 4.2.4., of two data sets to estimate the local S-N curves of additional data sets with different values of the relative stress gradient by means of the theory proposed by Prof. Eichlseder. The latter clause relates to the fact that the proposed formulation aims to estimate the effect of a relative stress gradient on the fatigue life without accounting for other effects.

Under these criterions, a total of 51 groups of data for steels have been collected from the literature (Freddi et al., 1989; Heywood, 1962; Siebel and Stieler, 1954; Various authors, 2005). The complete S-N curves were available and the slope k was derived for 14 of these data sets. The collected experimental fatigue data from the literature are summarized in Appendix A.

4.4.2. Estimation of the fatigue limit

Over the range of 51 different steels for which the fatigue limit was available from the literature, the experimental value was compared against the value predicted by formulations proposed by authors cited in section 4.2.

In Appendix A there are reported the material constants values computed according to each theory and used, through the relative stress gradient or the notch root, to calculate the fatigue limit through the support effect *n*, as summarized in Table 4.12.

The characteristic material constants, S_g and ρ^{**}, of the theories proposed by Siebel and Neuber respectively, were available from the literature for a limited number of static tensile strength values. Thus, in order to allow an estimation of these constants for each analysed material, the best approximating interpolation of available data, i.e. the one with the R^2 value closest to 1, was chosen and the resulted regression equations (Figure 4.41) were used to compute S_g and ρ^{**} as function of the static tensile strength σ_B.

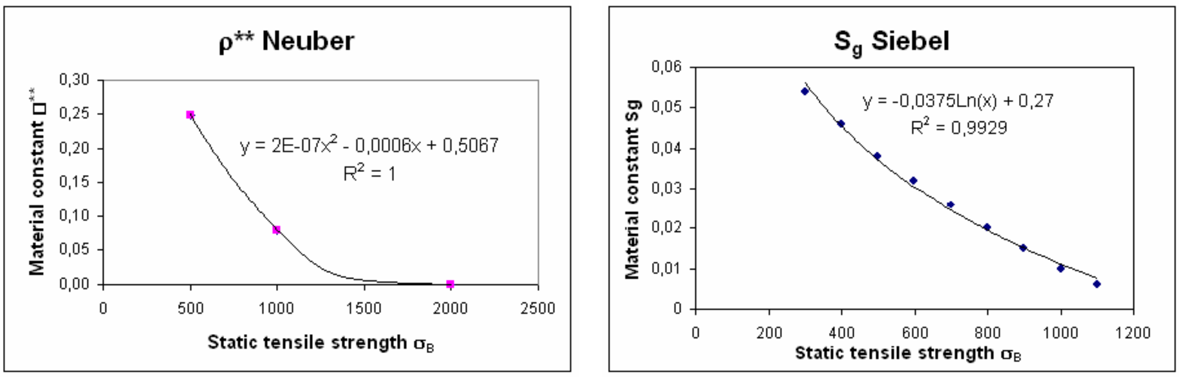

Figure 4.41:Regression equations used to compute the characteristic material constants of the theories proposed by Neuber and Siebel

Author	Support effect	Required constant	
Eichlseder	$n=\left(1+\left(\frac{\sigma_{D(\chi\neq 0)}}{\sigma_{D(\chi=0)}}-1\right)\cdot\left(\frac{\chi}{\chi\neq 0}\right)^{K_D}\right)$	K_D	0.3
		$\sigma_{D(\chi\neq 0)}$	Fatigue limit corresponding to the highest χ in Appendix A
		$\sigma_{\chi=0}$	Fatigue limit corresponding to the lowest χ in Appendix A
		$\chi\neq 0$	Highest χ in Appendix A
		χ	Appendix A
Siebel	$n=1+\sqrt{S_g\cdot\chi}$	S_g	Figure 4.41
		χ	Appendix A
Neuber	$n=\sqrt{1+\chi\cdot\rho^{**}}$	ρ**	Figure 4.41
		χ	Appendix A
Petersen	$n=1+\sqrt{\rho^{*}\chi}$	ρ*	Appendix A
		χ	Appendix A
Bollenrath and Troost	$n=\frac{1}{1-\frac{154/\sigma_B}{\frac{1}{1+\sigma_B/1370}+\frac{\rho}{10}}}$	σ_B	Appendix A
		ρ	Appendix A
Heywood	$n=1+2\sqrt{\left(\frac{a}{\rho}\right)}$	a	Appendix A
		ρ	Appendix A
Dietmann	$n=1+\left(\frac{C_1}{K}\right)^m\sqrt{\frac{C_2}{\rho}}$	C_1	Appendix A
		C_2	Appendix A
		ρ	Appendix A
		K	$=\sigma_B$

Table 4.13. Formulas and constants used to compute the support effect number according to the theories presented in section 4.2.2.

For each material, in Appendix B the comparison between the fatigue limits computed according to the proposed formulations in Table 4.12 and experimental values is shown. The percentage error ("%Err") is also reported:

$$\%Err=\left(\frac{\sigma_{D_{Experimental}}-\sigma_{D_{predicted}}}{\sigma_{D_{Experimental}}}\right)\cdot 100 \tag{4.51}$$

Experimental local fatigue limit (column "Exp") was computed, according to what discussed in section 4.2, by multiplying the nominal fatigue limit for the stress concentration factor K_t (Appendix A). The predicted local fatigue limit (column "σ_{Dlocal}") was derived by multiplying the experimental fatigue limit at zero stress gradient for the support effect (column" n"). In the cases for which data at exact zero stress gradient were not available, a small error was accepted to be committed, considering however the relative stress gradient closest to zero as benchmark.

As regards materials for which the static tensile strength σ_B was not available, the computation of support was allowed only according to Eichlseder's formulation. Moreover, the calculation of the support effect according to Bollenrath, Heywood and Dietmann was not feasible in case of smooth specimens requiring a not null value of the notch radius ρ.

As explained in details in section 4.2.4., the theory proposed by Prof. Eichlseder computes the fatigue limit corresponding to the stress gradient χ interpolating two values: the fatigue limit corresponding to a null value of the relative stress gradient and the one corresponding to a not null value of the relative stress gradient. This means that percentage errors (%Err) corresponding to this two benchmarks data are null in each case. Likewise, in the theories of Siebel, Neuber and Petersen, a null value of the relative stress gradient exactly corresponds to the experimental value of the fatigue limit. Thus, in order to correctly estimate the global percentage error of each theory, these data were not counted in the global error calculation in Table 4.13. This justifies also the different counted number of tests.

In the following Table the main results are reported:

	Eichlseder	**Siebel**	**Neuber**	**Petersen**	**Bollenrath**	**Heywood**	**Dietmann**
Number of tests	157	194	194	194	80	83	104
Mean %Err	**7**	**11**	**11**	**12**	**18**	**24**	**40**
St.dev.	8	15	31	17	11	28	61
95% Confidence interval	**1**	**2**	**4**	**2**	**2**	**6**	**9**

Table 4.14: Predicted versus experimental values of the fatigue limits in terms of percentage errors

The 95% confidence interval was computed in order to filter the calculations from potential error esteem of particular cases. An example for C45 normalized steel is shown in the Figure below.

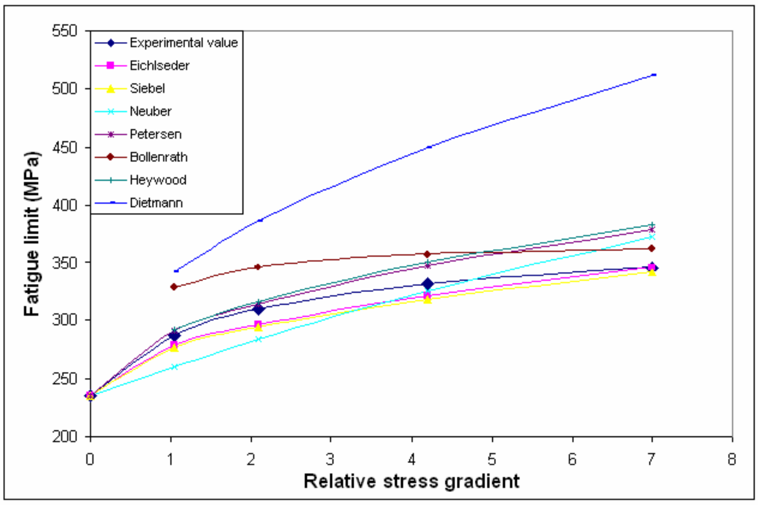

Figure 4.42: Predicted versus experimental values of the fatigue limits over the relative stress gradient

The Eichlseder's formulation provides the best approximation of experimental values with a mean percentage error of 7% ± 1% with a significant level α=0.05. A good approximation is also provided, even if with greater mean percentage errors, by Siebel, Neuber and Petersen formulations. Nevertheless, whilst the former theory required only two experimental data sets, the other proposed formulations should be attended by a great experimental effort in order to exactly compute the material constants for the analysed material.

On the contrary, not accounting for the effect of the relative stress gradient, Bollenrath, Heywood and Dietmman showed greater percentage errors.

4.4.3. A novel formulation for the slope calculation of local S-N curves

Fourteen groups of collected data for steels were analysed in terms of the slope k. Three formulas were taken into account and compared to experimental data:

(1) The value of slope k derived from the proposed formula by Prof. Eichlseder

$$k = k_{\min} + \frac{k_{\max} - k_{\min}}{n^{K_k}} \tag{4.31}$$

where K_k=6.9.

Nevertheless, this formulation provides a sensible overestimation of experimental values of the slope k. This is ascribable to a not exact interpolation of data according to formula (4.31); actually, whereas for the null value of the relative gradient (4.31) confirms the k_{max} values, for the case with the highest gradient k_{min} value is overestimated.

Thus, a novel calculation of the slope based on a logarithmic interpolation of the error between the experimental and the predicted value of k as calculated by (4.31) has been initially proposed.

(2) Logarithmic correction of (4.31) as a function of χ.

$$k_{correction} = k + A\ln(B \cdot \chi + 1) \tag{4.52}$$

where A and B are the coefficients of the logarithmic interpolation. The developed algorithm (Matlab) to compute A and B is reported in Appendix C.

The main disadvantage of this novel formulation is that it requires at least three values of the absolute error to extrapolate a logarithmic regression whilst the one proposed by Prof. Eichlseder requires only two values of k to estimate the slope of the fatigue curve of the component, one relates to a specimen with zero relative stress gradient and the other to a specimen with an high value of the gradient. Based on this observation, the present work moved to a new formulation to improve the prediction:

(3) An interpolating novel formulation:

$$k_{estimated} = k_K \cdot \left[1 + \left(\frac{k_i}{k_K} - 1 \right) \cdot \left(\frac{\chi}{\chi_i} \right)^{0.05} \right] \tag{4.53}$$

where

k_K	Slope of the S-N curve of the specimen with null value of the relative stress gradient
k_i	Slope of the S-N curve of the specimen with *not* null value of the relative stress gradient
χ	Stress gradient of the component
χ_i	Stress gradient of the component of the specimen with *not* null value of the relative stress gradient

The structure of the new equation is similar to the one presented by Prof. Eichlseder for the calculation of the fatigue limit but it presents a different empirical value of the exponent and requires the knowledge of only two k values. In order to achieve the best results, a protocol (Appendix D) has been developed to compute the slope k of the S-N curves of the components by means of (4.53).

This protocol accounts for the necessity to base the interpolation on statistically significant data. For this, the clause that the reference data, the benchmark slopes, must be derived from linear regression of experimental data with an R^2 value at least to 0.85 has been introduced. Otherwise, the possibility to derive meaningful considerations is rejected.

If more than two slopes are available from experiments with an R^2 value higher than 0.85, and these values differ more than 2%, the data set with the highest value of the slope k is taken as second benchmark; the first benchmark is the corresponding one to the null value of the relative stress gradient. This can be interpreted as a conservative hypothesis since an high value of the slope, under the same other conditions, i.e. the number of cycles at the fatigue limit and the fatigue limit, underestimates the number of cycles to failure.

Following these criterions, the number of analysed data sets was reduced to 13 since the R^2 value corresponding to the null value of the relative stress gradient for the spring steel 37MnSi5 was less than 0.85. In Appendix E experimental data, the Eichlseder formulation (4.31), the logarithmic correction (4.52) and the proposed modified interpolating formula (4.53) for k are reported as functions of the relative stress gradient. Values indicated in blue are used as benchmarks in order to compute the slope k following the developed protocol.

For the groups of data without indications of the R^2 value, the general criterion to use the slopes of data with the highest and the lowest values of the relative stress gradient was followed.

In Figure 4.43 the comparisons of experimental versus predicted values for two analysed steels are plotted. It can be seen the improved estimation of experimental data by using the novel proposed interpolating formula (4.53).

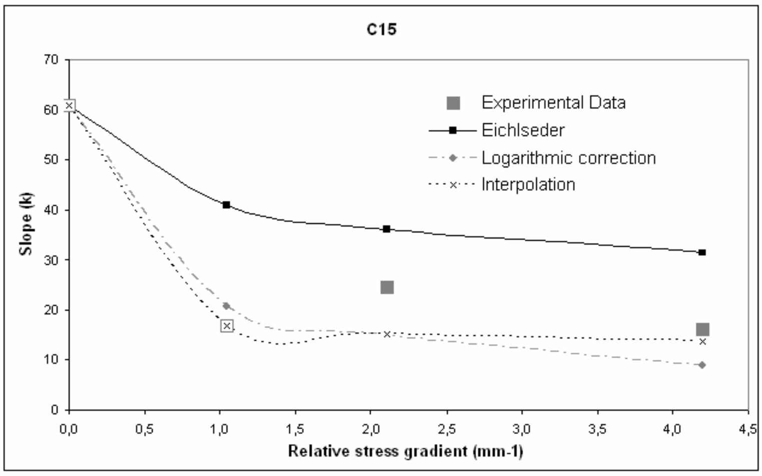

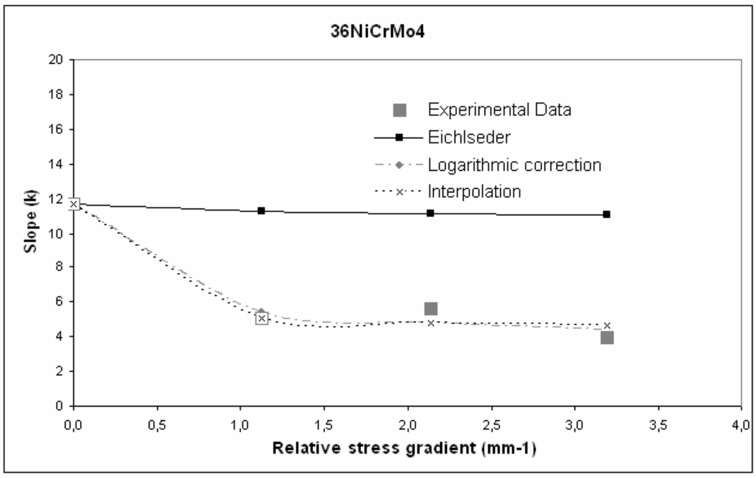

Figure 4.43: Predicted versus Experimental values of the slope k over the relative stress gradient for two analysed steels

An average percentage error of 24%±7%, with a significant level α=0.05, is attained with the novel equation. This is still an high value; however it should account for the wide experimental scattering of fatigue data in the low-intermediate region.

An additional condition was applied to the protocol due to the experimental observation (Siebel and Pfender, 1947; Siebel and Bussmann, 1948) that the asymptotic conditions, i.e. the levelling down of the curves over the relative stress gradient, are reached for values of the stress gradient greater than 1 mm^{-1}. As shown in Figure 4.44, for values between 0 and 1 mm^{-1}, a rapid decreasing of the slope is observed, not captured by the proposed formulations.

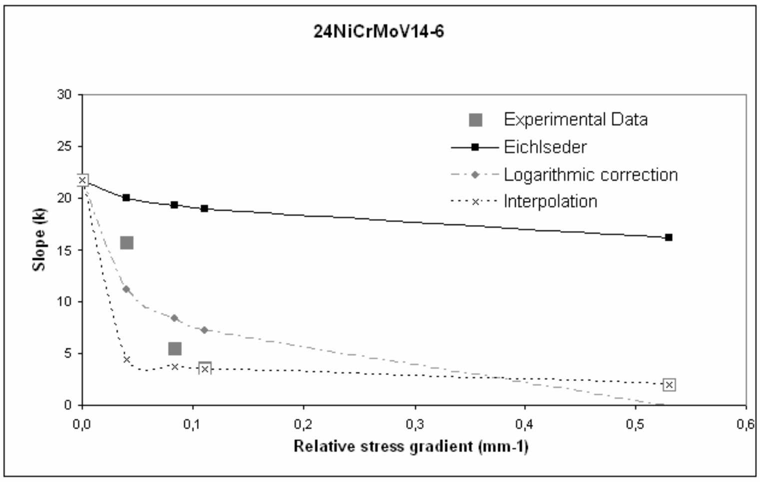

Figure 4.44: Predicted versus experimental values of the slope k over relative stress gradients lower than 1 mm^{-1} for an analysed steel

The following correction was therefore proposed:

$$k^* = k_{estimated} + \left[k_{estimated} \cdot \frac{\left(4.3 \cdot \chi^{-0.85}\right)}{100 - \left(4.3 \cdot \chi^{-0.85}\right)} \right] \qquad \left(0 < \chi < 1\right) \tag{4.54}$$

However, further tests are necessary to corroborate this additional formulation.

Chapter 4.5

Experimental tests

In this chapter the experimental tests performed on a Ni-Cr-Mo-V steel are shown. Main results are also reported.

In questo capitolo vengono descritte le prove sperimentali eseguite su un acciaio Ni-Cr-Mo-V ed i principali risultati ottenuti.

Experimental tests were performed on steel 28NiCrMoV chosen for the construction of a low-pressure turbine disc. The thermal treatment conditions of the material are reported in Table 4.15. The specimens were manufactured from CT specimens previously used for fracture mechanics tests (Curioni et al., 1986).

Thermal treatments	Temperature	Time	Depth
Austenizing	845 °C	1 h	25 mm
Tempering	845 °C	1 h	25 mm
Relieving	845 °C	1 h	25 mm

Table 4.15:Thermal treatment conditions of the steel 28NiCrMoV

The selection of CT specimens from the same sector and radius of the turbine disc made certain that individual specimens had constant material composition and thermal treatment conditions. Moreover, in order to guarantee that the plastic deformation that occurred during the fracture mechanics tests did not interest the region of the CT specimens from which the samples were extracted, these were taken from the external section.

The specimens were dimensioned accounting for

(1) Standards
(2) Test machine specifications
(3) Expected predicted values of the fatigue life in the range of the low-intermediate region

(1) Standard

The standard ISO 1143 ("Metals - Rotating bar bending fatigue testing") specifies the geometrical conditions to prepare the samples to carry out rotating bending fatigue tests:

- nominal specimen diameter between 5 ÷ 12.5 mm;
- for cylindrical specimens: transition fillet radius r≥3d; for hourglasses specimens r≥ 5d
- dimensional tolerance on nominal diameter: ± 0.05 mm

(2) Test machine specifications

The following specifications were defined by the test machine:

- total specimen length = 90mm
- testing length ≤ 40 mm
- diameter of the gripped end of the test specimen D = 12 mm

(3) Expected predicted values of the fatigue life in the range of the low-intermediate region

Data from literature for materials with a chemical composition similar to the analysed one have been collected in order to estimate the static tensile strength σ_B. They are summarized in the Table below:

Material	Chemical composition										Mechanical properties					Reference
	C	Si	S	P	Mn	Cr	Ni	Mo	V	Sn	$R_{p0.2}$	Rm	Re	A	Z	
	%	≤	≤	≤	%	%	%	%	%	≤		N/mm^2 ≤		%	%	
28NiCrMoV	0.22-0.26	0.10	0.015	0.015	0.25-0.35	1.40-1.60	2.60-2.80	0.45-0.55	0.08-0.13	0.02	600			19	57	(Curioni et al., 1986)
24NiCrMoV16-4	0.28	0.07	0.004	0.008	0.23	1.63	3.59		0.09			$807^{(\phi 12)}$		20	64	(Curioni et al., 1986)
28NiCrMo4	0.24-0.34	0.40	0.035	0.035	0.30-0.60	1.00-1.30	1.00-1.30	0.20-0.30				$930^{(\phi 101-160)}$	590	13	60	(Wegst et al., 2004)
28NiCrMoV8-5	0.24-0.32	0.40	0.035	0.035	0.15-0.40	1.00-1.50	1.80-2.10	0.35-0.55	0.05-0.15			$950^{(\phi 101-160)}$	630	14		(Wegst et al., 2004)
33NiCrMoV14-5	0.28-0.38	0.40	0.035	0.035	0.15-0.40	1.00-1.70	2.90-3.80	0.30-0.60	0.08-0.25			$1320^{(\phi 101-160)}$		8	45	(Wegst et al., 2004)

Table 4.16. Steels with chemical composition and mechanical properties similar to the 28NiCrMoV

In order to avoid an under-dimensioning of samples, 950 MPa has been assumed as reference value for the static tensile strength; the 28NiCrMoV8-5 steel moreover shows the most similar chemical compositions to the 28NiCrMoV one.

A 26% more than this value was considered (Table 4.17) to account for the reduced specimens dimensions to be tested. In fact, the only indicated value of σ_B for this material in literature relates samples diameters between 101 and 160 mm. Therefore a static tensile strength of 1200 MPa has been considered.

Material	$R_m^{(\phi 101-160)}$	$R_m^{(\le \phi 16)}$	$R_m^{(\le \phi 16)}/R_m^{(\phi 101-160)}$
	N/mm^2		
36NiCrMo4	950	1300	1.37
30NiCrMo8	1200	1450	1.21
34NiCrMo6	1100	1400	1.27
36NiCrMo16	1200	1450	1.21
		average	**1.26**

Table 4.17. Increment of the static tensile strength with the decreasing of specimen diameter

From the literature (Niemann, 1981), the fatigue limit for smooth specimens under rotating bending is 0.43 times the static tensile strength; thus, a value of 0.43*1200=516 MPa is estimated. This means that a nominal stress amplitude up to 516 MPa must be applied to investigate the ordinary high-cycle fatigue range of three decades of cycles, i.e. from 10^4 to 10^6 cycles (ISO 12107).

With these specifications, the following specimen geometries have been designed:

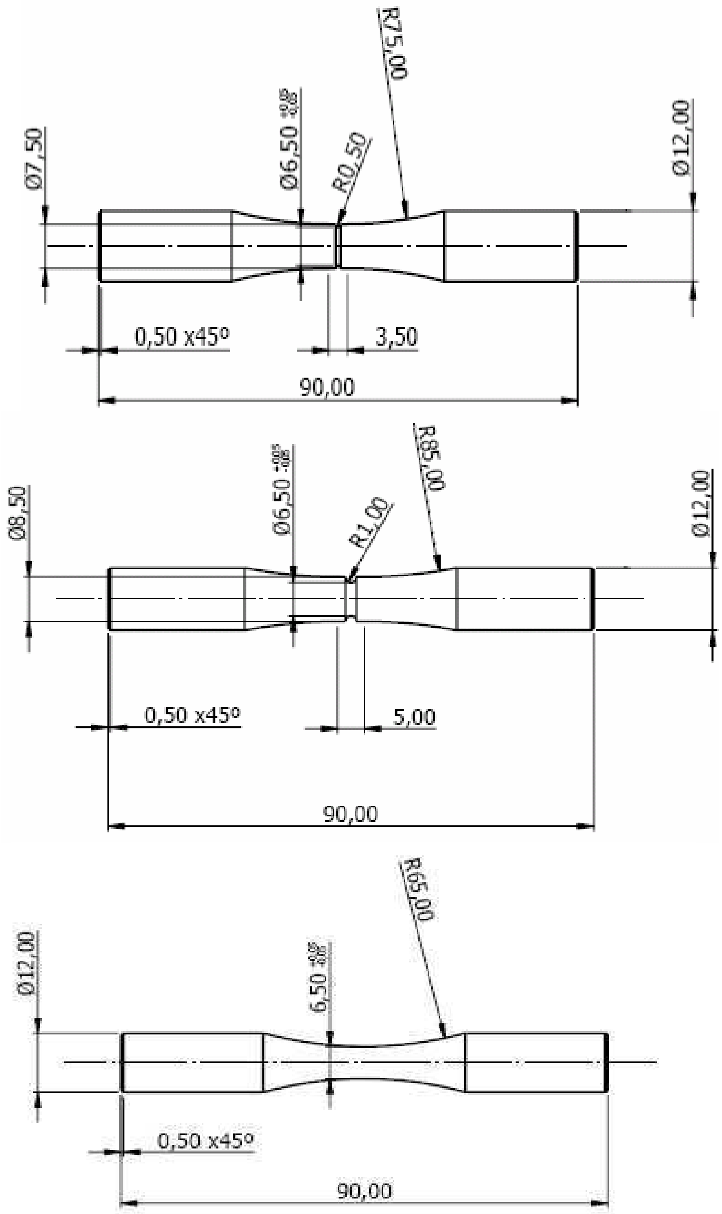

Figure 4.45: Specimen geometries used for experimental tests

Relative stress gradients χ and stress concentration factors K_t for each geometry are reported in Appendix F.

The standards ASTM E739-91 (2004) and ISO 12107 (2003) report the guidelines for the generation of statistical S-N curves. In first analysis the median S-N curve is derived, that's the S-N curve with a reliability of 50% using the minimum sample size.

ASTM standard recommends a sample size between 6-12 for preliminary and research and development tests; the ISO standard indicates to use eight specimens to determine the low-intermediate fatigue life region.

Thus 10 specimens for each sample type were designed: two samples at four different levels of stress amplitude (ISO 12107) and two more specimens for preliminary investigations.

The specimens were machined on the turning lathe. All smooth samples were polished by hand in the longitudinal direction, as indicated by the ISO standard 1143, with sandpaper up to the finest granulation (2000 grade in oil) until a superficial roughness was reached of approx. 0.1 microns. Notched specimens were polished with sandpaper only in the notch; however the notch should act as a stress concentrator without accounting for the superficial roughness. The reached roughness of the smooth specimens has been controlled by using a tactile rugosimetry whose operating parameters are reported in the Table below.

Touch probe	Filter	LT	LC	VT
TK300	RC 75%	1.5 mm	0.25 mm	0.15 mm/s

Table 4.18. Operating parameters of the rugosimetry

Three repetitions for each sample were performed. The R_a values are reported in Appendix F.

The achieved final geometry was examined with the projector profile (Figure 4.46) to guarantee the correspondence with the geometrical nominal tolerance (± 0.05 mm). Nominal and real dimensions of specimens, with relative percentage errors, are reported in Appendix F.

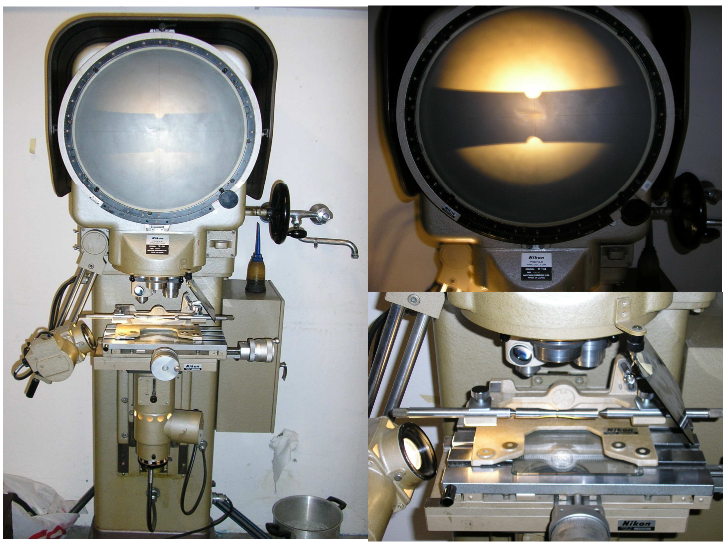

Figure 4.46: Project profile

In order to restrain the statistics dispersion that however affect fatigue data, the two repetitions for each stress amplitude level were performed on specimens with approximately the same value of the percentage error on the nominal diameter, for the smooth samples, or on the notch root for the notched specimens.

Specimens material homogeneity was verified by testing the Rockwell Hardness (HR) (C scale). An order of maximum 1÷2 experimental dispersion points was shown (Appendix F).

The attempts for the determination of the fatigue life in the low-intermediate life region were accomplished on a rotating bending machine of the Laboratory (Figure 4.47).

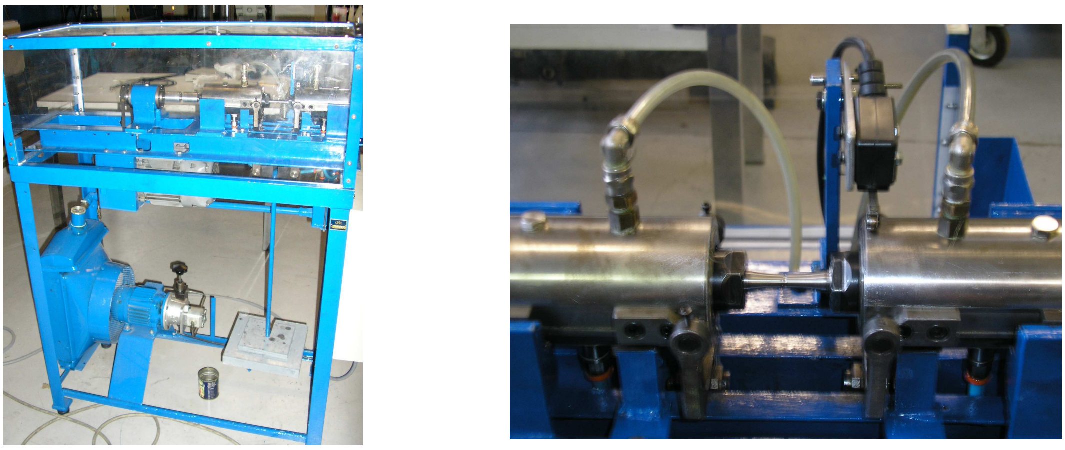

Figure 4.47: Rotating bending machine of the Laboratory

A four-points bending loading was applied. A schematic representation of the test machine is reported in Figure

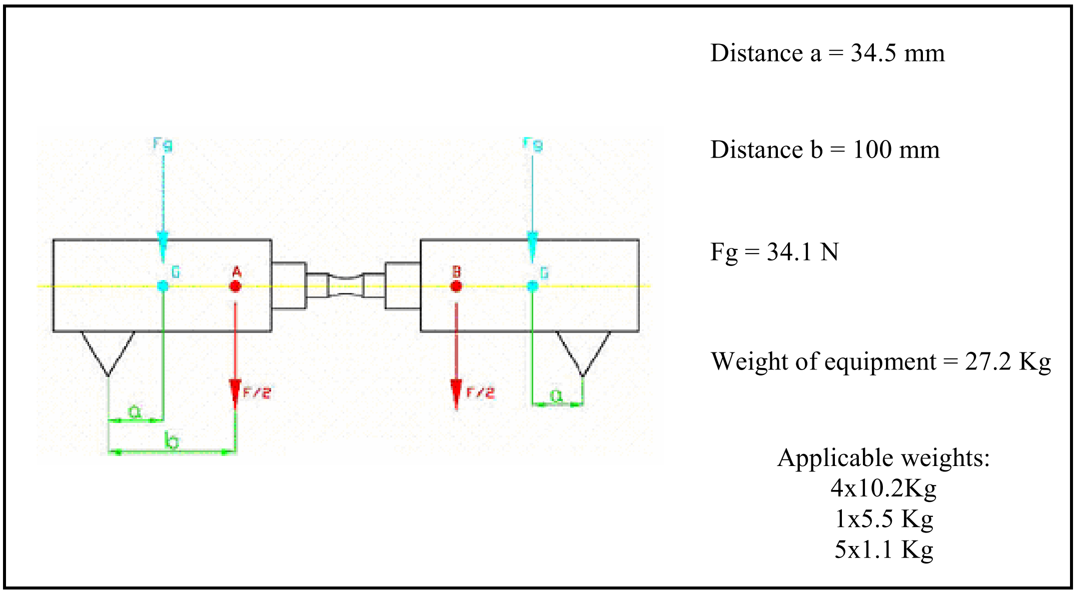

Figure 4.48: Scheme of the Rotating Bending Machine Test

The nominal stress amplitude was therefore computed as:

$$\sigma_{nominal} = \frac{32}{\pi \cdot d^3} \cdot \left[\left(F_g \cdot b \right) + \frac{(27.2 + m) \cdot g}{2} \right] \tag{4.55}$$

where m [Kg] is the mass that has to be applied. Nevertheless, this theoretical value was corrected accounting for the real value of the applied bending moment experimentally proved:

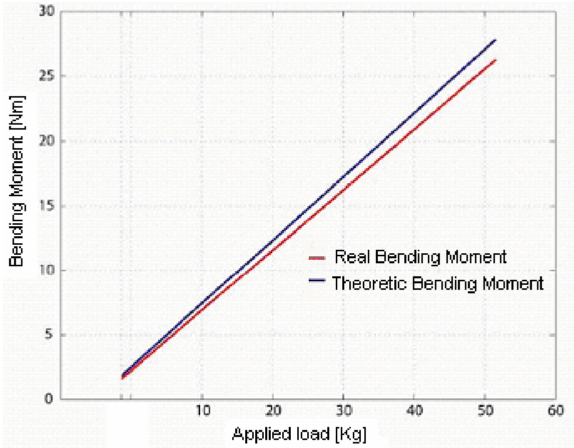

Figure 4.49: Real versus theoretical value of bending moment over the applied load

The test machine is described in details elsewhere (Calanca, 2006).

A rough esteem of the fatigue limit for notched specimens was made by dividing the fatigue limit of smooth sample for the fatigue notch factor K_f computed according to Peterson's formulations and reported in Appendix F.

The attempts were accomplished at 50 Hz.

4.5.1. Results

The results of experimental tests are reported in details in Appendix G. The stereographic illustrations of the fracture surfaces taken with a stereo microscope are shown in Appendix H. The comparison of two fracture surfaces with the well-known scheme (Figure below) shows a good agreement.

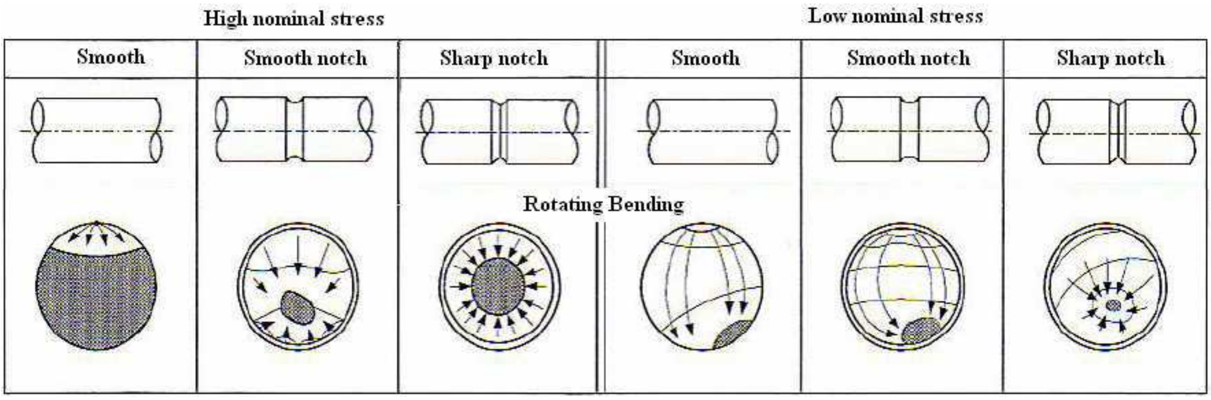

Figure 4.50: Fracture surfaces for smooth and notched specimens from high to low nominal stress

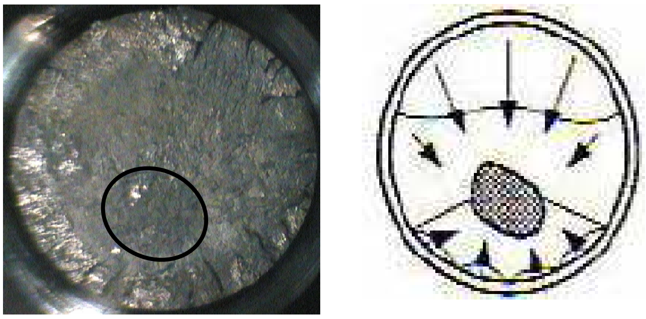

ε2: Notched R1

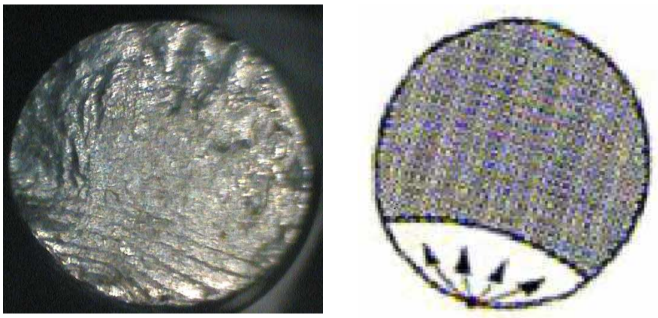

B1: Smooth

Figure 4.51: Experimental fracture surfaces

The following observations have to be done on some specimens:

- *G1* (smooth) was tested over the yield stress at 100 Hz by applying a nominal stress amplitude of 730 MPa. The sample overheated yielding after a few cycles.
- *H2* (smooth) and *T1* (notched R0.5) failed 9 million cycles before the specimens tested at the same stress amplitude. The presence of superficial flaw emerged from a metallographic analysis to the Scanning Electron Microscope (SEM, Zeiss EVO 50) (Figure 4.52):

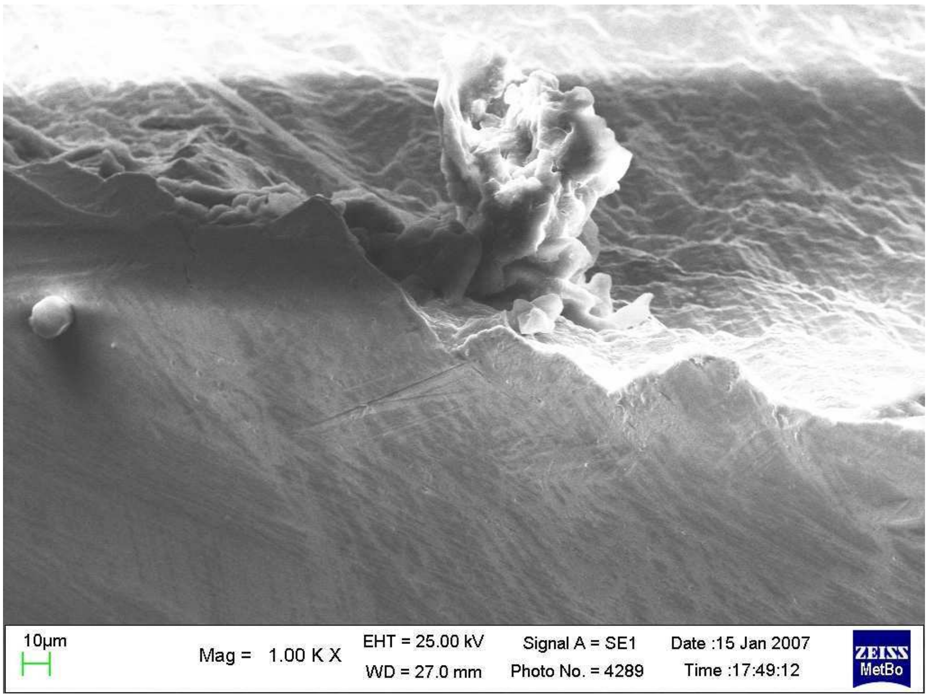

H2 smooth specimen

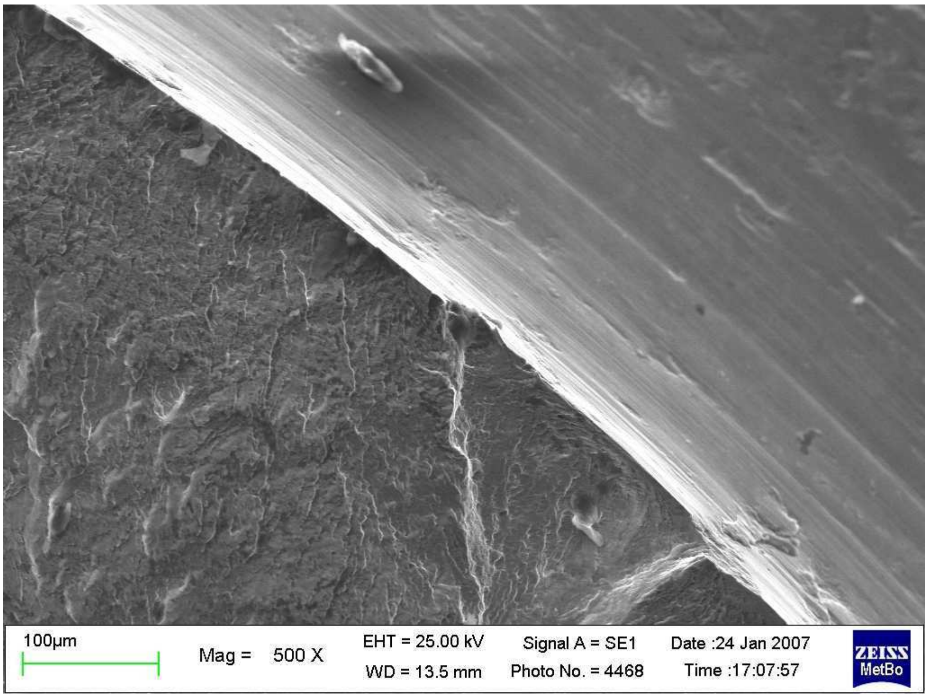

T1 notched specimen (R0.5)

Figure 4.52: Images from SEM

Actually, H2 was the specimen with the highest value of the superficial roughness (see Appendix F).

- *V1*and ε2 (notched R1), producing vibrations, made elevated noisiness during the test, so revealing an anomaly of the testing conditions. Consequently, they failed an order of 300000-400000 cycles before the samples tested at the same stress amplitude. A more accurate analysis by means of SEM showed, for these samples, a not perfectly continuous material due to the presence of some internal flaws.

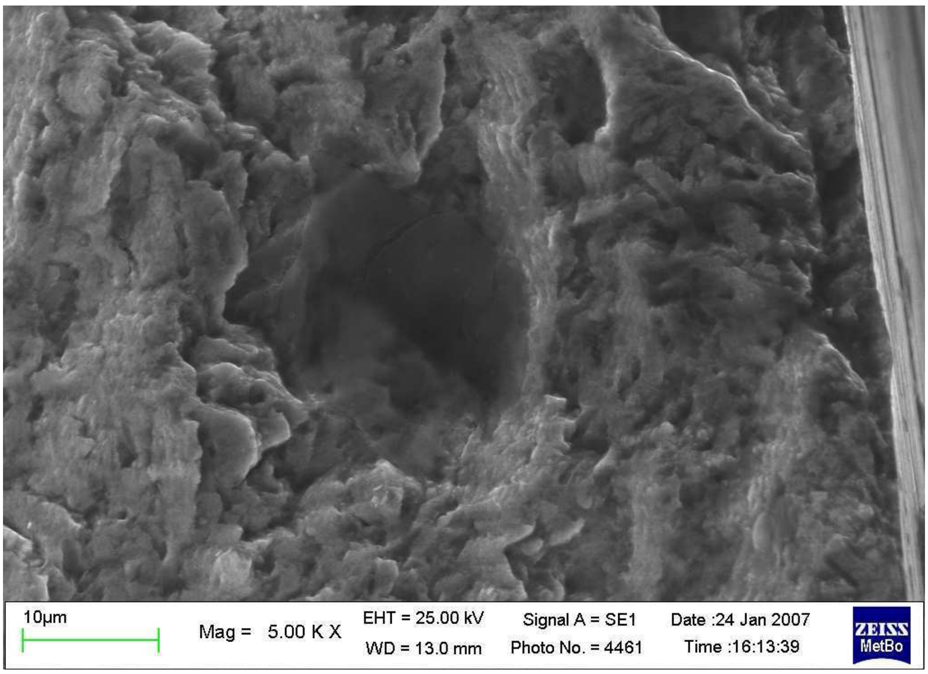

V1 notched specimen (R1)

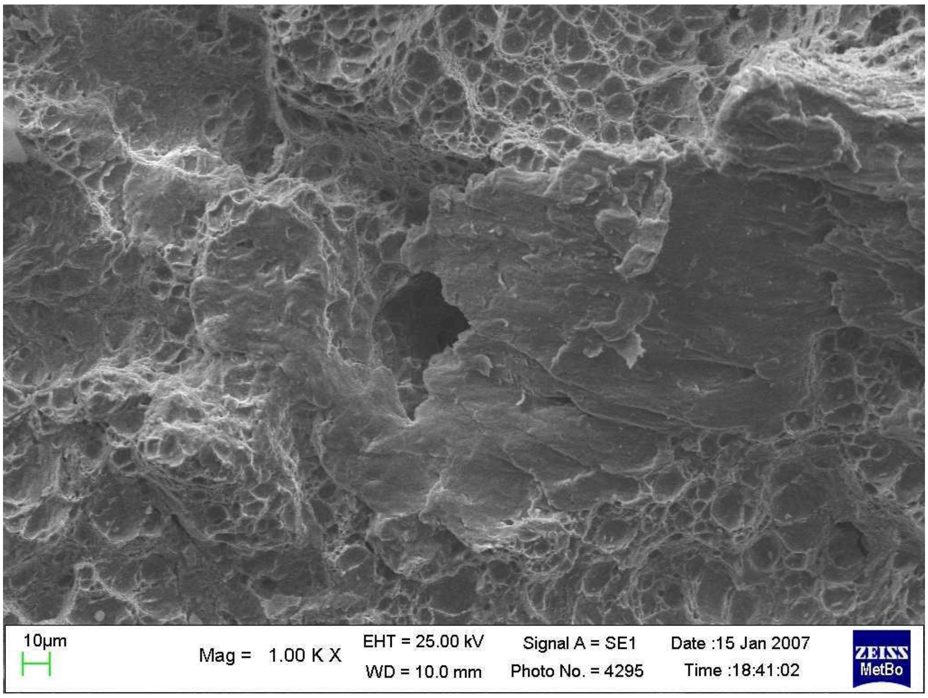

ε2 notched specimen (R1)

Figure 4.53: Images from SEM

- *U2* (notched R0.5) produced such machine vibrations as to cause the weights to fall down from the stirrup. The test was therefore judged not reliable.

For the aforementioned reasons, the results of those samples were not included in the fatigue life estimation.

The obtained S-N curves in double-logarithmic scale are shown in the Figure below.

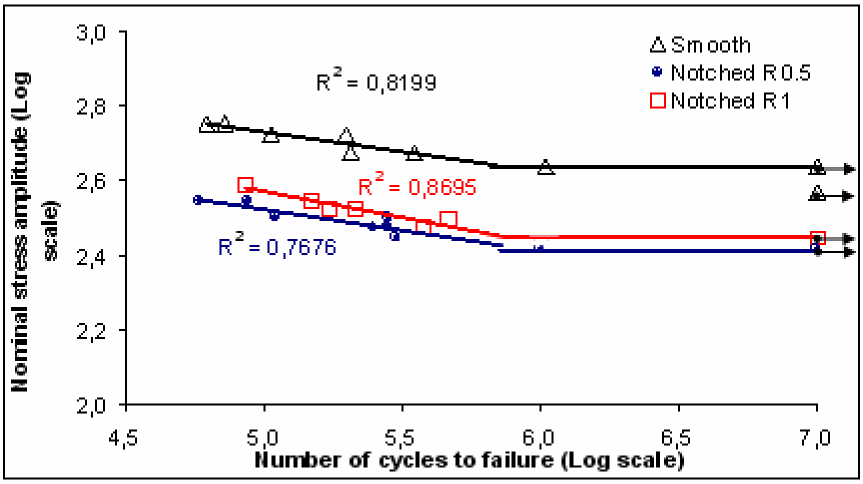

Figure 4.54: Experimental test results

The finite life region data is assumed linear in the log-log coordinates and data analysed by the least square method.

	Gradient χ	K_t	Slope k	R^2	Fatigue limit	
					nominal	local
Smooth	0.31	1.00	7.7	0.8268	436	436
Notched R1	2.29	1.78	6.3	0.8689	279	497
Notched R0.5	4.34	2.07	6.8	0.7785	260	538

Table 4.19: Experimental test results

As indicated in Appendix F, the relative stress gradient reported in Table 4.19 is the average value over the tested specimens accounting for the real achieved dimensions.

Comparisons of experimental slopes and fatigue limits with theoretical predictions are reported in Table 4.20 and 4.21 respectively:

	Exp. Slope	Eichlseder		Log-correction		Novel formulation	
		k	%Err	k	%Err	k	% Err
Smooth	7.7	7.4	4 %	7.3	5 %	6.4	16 %
Notched R1	6.3	7.2	14 %	6.8	7 %	6.3	0 %
Notched R0.5	6.8	7.1	3 %	6.5	5 %	6.3	9 %

Table 4.20: Comparison of experimental and predicted values of the slope k (equations (4.31) - column Eichlseder; (4.52) - column Log-correction; (4.53) – column Novel formulation).

All the proposed theories give a good approximation of the experimental values for the slope k. Furthermore, experimental data show a good agreement with the observed general trend of the slope over the relative stress gradient, i.e. k decreases with an χ increasing. For the novel calculation, besides slope of the smooth specimens, the slope of the notched R1 specimens, associated with an higher value of the goodness of fit R^2 than the one of the notched R0.5 specimens, has been taken as benchmark.

	Exp. Local fatigue limit	Eichlseder		
		n	Local fatigue limit	%Err
Smooth	436	1.0594	467	5.9 %
Notched R1	497	1.1614	511	3.0 %
Notched R0.5	538	1.2222	538	0.0 %

Table 4.21: Comparison of experimental and predicted (see Table 4.12) values of the fatigue limits

Eichlseder formulation predicts experimental local fatigue limit with a good approximation.

The median S-N curve is however not sufficient for fatigue analysis and design due to the statistical nature of the fatigue and, thus, to the inevitable variation of fatigue data.

To account for the uncertainties in the regression analyses, the *design* S-N curves, i.e. the lower bound of the median S-N curves, are computed (ISO 12107). The design curve characterizes the minimum fatigue life at a given stress amplitude level so that the majority of the fatigue data fall into the lower bound value (Lee et al., 2005). The R90C95 lower-bound curve was computed to ensure a 90% possibility of survival (R90) with a 95% confidence level for a fatigue life at a specified stress amplitude (Figure 4.55).

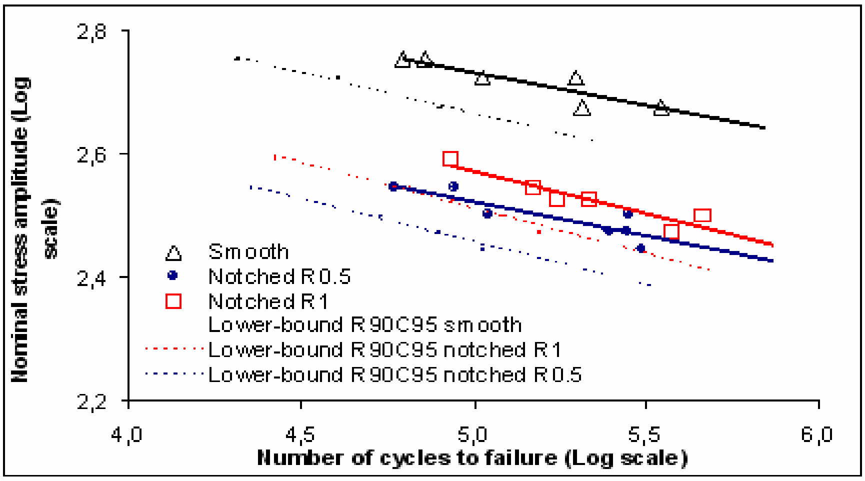

Figure 4.55: Design and median experimental S-N curves

Moreover, according to the ISO standard (12107), the hypothesis of linearity was verified:

	$\frac{\sum_i m_i\left[(b-ay_i)-\overline{x}_i\right]^2 (l-2)}{\sum_i\sum_j (x_{ij}-\overline{x}_i)^2 (n-l)}$	$F(1-\alpha,\upsilon_1,\upsilon_2)$	$\frac{\sum_i m_i\left[(b-ay_i)-\overline{x}_i\right]^2 (l-2)}{\sum_i\sum_j (x_{ij}-\overline{x}_i)^2 (n-l)} > F(1-\alpha,\upsilon_1,\upsilon_2)$
Smooth	0.04360	6.61	NO
Notched R1	0.40873	6.61	NO
Notched R0.5	0.04627	5.99	NO

Table 4.22: Parameters for the verification of the adequacy of the linear model according to the ISO standard 12107

The hypothesis of linearity is therefore accepted in all cases.

Chapter 4.6

Discussion and conclusions

The aim of this section was to assess a novel formulation proposed by Prof. Eichlseder to predict the local fatigue life of components with uneven stress distributions in the high-cycle fatigue region by means of Finite Element Analysis. The final purpose is to overcome, or at least to limit, the need of costly, time-consuming and complicated experimental tests towards different predictive methods of the fatigue life.

The proposed theory allows to estimate the fatigue life in terms of fatigue limit, slope of the S-N curve and number of cycles at the fatigue limit as function of the relative stress gradient in each node of the meshed structures. The fundamental idea at the basis of this theory is that the relative stress gradient seems to govern, under the same other conditions, the fatigue life phenomenon.

Through an in-depth study of the works of the German school that, since the first mid-1900s, have led to the formalization of the fatigue life depending on the relative stress gradient, the present work suggests a comprehensive formulation of the main geometrical and material parameters that affect the fatigue life based on the relative stress gradient.

A novel method to compute the relative stress gradient by means of Finite Element Analysis has been proposed: it was calculated as the derivative of a polynomial interpolation of nodal solutions in the point of peak stress normalized on the peak stress itself. The comparison of the results of this calculation with analytical known solutions for simple specimen geometries showed percentage errors less than 8% with only one case of 14%. The proposed method is therefore robust and accurate enough to allow a reliable measurement of the relative stress gradient.

Over a range of 51 groups of data for steels, collected from the literature, the experimental fatigue limits were compared with the predicted ones by various proposed formulations. It was found that Eichlseder's formulation provides the best approximation with a mean percentage error of 7% ± 1% with a significant level of 95%. This theory requires the knowledge of only two S-N curves of the material to estimate the fatigue life of a component.

The slope of S-N curves is a more infrequent datum than the fatigue limit. Only 13 groups of collected data were liable to be analyse in terms of the slope. Observing that the equation proposed by Eichlseder provided a significant overestimation of experimental data, a novel formulation has been proposed. In order to achieve the best approximation, a protocol was developed accounting for statistical considerations and experimental observations. A mean percentage error of 24% was attained with the novel equation. It can be acknowledged that this is a still high value; however it should account for the wide experimental scattering of fatigue data in the low-intermediate life region (finite life).

Finally, experimental tests on a 28NiCrMoV steel used in a low pressure turbine disc were performed on a rotating bending machine of the Laboratory. Three specimen typologies were manufactured with an increasing value of the relative stress gradient. The experimental data confirmed the general trend observed for the slope of the S-N curve and the fatigue limit over the relative stress gradient, i.e. a decrease and an increase respectively with the increasing of the relative stress gradient. Experimental data and theoretical predictions showed a good agreement with a low value of the relative percentage error.

As a general inference, the valid theoretical and physical ground of the formulation proposed by Prof. Eichlseder to compute the fatigue life of components as function of the relative stress gradient has been assessed.

Discussioni e conclusioni

Scopo di questa parte del lavoro era la verifica di una nuova formulazione proposta dal Prof. Eichlseder per predire la vita a fatica locale di componenti con una qualsiasi distribuzione irregolare di tensione nella regione della fatica ad alto numero di cicli per mezzo del metodo agli Elementi Finiti.

Obiettivo ultimo delle ricerche nelle quali si inquadra questo studio è superare, o almeno limitare, la necessità di complicate e costose prove sperimentali a favore di altri metodi predittivi della vita a fatica.

La teoria proposta in letteratura permette di stimare la vita a fatica, in termini di limite di fatica, pendenza della curva S-N e numero di cicli al limite di fatica, in funzione del gradiente relativo di tensione, χ, in ogni nodo della struttura discretizzata. L'idea fondamentale alla base di questa teoria è che il gradiente relativo di tensione governi, a parità di ogni altra condizione, il comportamento sotto carichi affaticanti.

Attraverso un approfondito studio dei lavori della scuola tedesca che, a partire dalla metà del 1900, hanno portato alla formalizzazione della dipendenza della vita a fatica da χ, il presente lavoro suggerisce un sunto dei principali parametri geometrici e del materiale che influenzano la vita a fatica interpretati proprio sulla base del concetto del gradiente relativo di tensione.

Viene presentato un nuovo metodo di calcolo del gradiente relativo di tensione tramite il metodo agli Elementi Finiti definendolo come la derivata di un'interpolante polinomiale di soluzioni nodali adiacenti calcolata nel punto di massima tensione e normalizzata sulla stessa tensione massima. Il confronto dei valori così calcolati con soluzioni analitiche note per semplici geometrie ha mostrato errori percentuali inferiori all'8%, con solo un caso del 14%. Il metodo proposto si è quindi dimostrato robusto ed accurato, permettendo una misurazione affidabile del gradiente relativo di tensione.

Su un campione di 51 gruppi di dati per diversi acciai raccolti dalla letteratura, i limiti di fatica sperimentali sono stati confrontati con quelli predetti dalle principali formulazioni proposte dalla scuola di pensiero tedesca. Si è verificato che la formulazione proposta dal Prof. Eichlseder fornisce la migliore approssimazione con un errore medio percentuale del / % ± 1% ad un livello di significatività del 95 %. Questa teoria richiede, per la stima del limite di fatica, la conoscenza di solo due curve S-N del materiale.

La pendenza delle curve S-N è un dato meno frequentemente fornito. Solo per 13 gruppi dei 51 dati raccolti era fornita anche questa informazione. A partire dall'osservazione che l'equazione fornita dal Prof. Eichlseder per il calcolo della pendenza sovrastimava significativamente i dati sperimentali, è stata proposta una nuova formulazione. Per fornire la migliore approssimazione, è stato sviluppato un protocollo di calcolo che tenesse conto anche di considerazioni statistiche ed osservazioni sperimentali. Con questa nuova espressione si è ottenuto un errore medio percentuale del 24 %. Pur essendo quest'ultimo *ancora un valore elevato, occorre tuttavia considerare la grande dispersione dei dati di fatica sperimentali nella regione della vita a fatica finita.*

In ultimo, sono state condotte delle prove di fatica sulla macchina a flessione rotante del laboratorio sull'acciaio 28NiCrMoV utilizzato per realizzare un disco di turbina a bassa pressione. Sono state utilizzate tre diverse geometrie di provini con diverso valore del gradiente relativo di tensione. I dati sperimentali hanno confermato l'andamento generale atteso per la pendenza della curva S-N ed il limite di fatica in funzione di χ*, ovvero una diminuzione ed un aumento rispettivamente con l'incremento del gradiente relativo. Dati sperimentali e previsioni analitiche hanno mostrato un buon accordo con bassi valori dell'errore percentuale.*

Concludendo, si può affermare che è stato verificato il fondamento teorico e fisico della formulazione proposta dal Prof. Eichlseder per calcolare la vita a fatica di componenti come funzione del gradiente relativo di tensione.

References

[1] ASM Handbook, 1996. Volume 19: Fatigue and Fracture.

[2] ASTM E739-91. Standards practice for statistical analysis of linear or linearized stress-life (S-N) and strain-life (e-N) fatigue data. West Conshohocken, PA, 2004.

[3] Bannantine, J., Comer, J., Handrock, J., 1987. Fundamentals of metal fatigue analysis

[4] Bollenrath, F., Troost, A., 1950. Wechselbeziehungen zwischen Spannungs-und Verformungsgradient. Teil 1. Arch. Eisenhuttenwesen 21, 11/12, p. 431-436

[5] Bollenrath, F., Troost, A., 1951. Wechselbeziehungen zwischen Spannungs-und Verformungsgradient. Teil 2. Arch. Eisenhuttenwesen 22, 9/10, p. 327-335

[6] Bollenrath, F., Troost, A., 1952. Wechselbeziehungen zwischen Spannungs-und Verformungsgradient. Teil 3. Arch. Eisenhuttenwesen 23, 5/6, p. 193-201-

[7] Calanca, A., 2006. Messa a punto di macchina per prove di fatica a flessione rotante. Università degli studi di Bologna.

[8] Campa, G., 2006. Il metodo del gradiente delle tensioni per la determinazione delle curve di fatica locali. Tesi di Laurea. Università degli studi di Bologna

[9] Cesari, F., 1996. Introduzione al metodo degli elementi finiti. Pitagora, Seconda edizione.

[10] Cesari, F., 1997. Calcolo matriciale delle strutture. Pitagora, Seconda edizione.

[11] Collins, J.A., 1993. Failure of Materials in Mechanical Design – Analysis, Prediction and Prevention. 2nd Edition, Wiley, New York.

[12] Curioni, S., Dal Re, V., Freddi. A., 1986. Fracture Mechanics Analysis of a Ni-Cr-Mo-V steel for a Turbine disc. OIAZ. 131. Jg., Heft 8. pp. 320-323.

[13] Dietmann, H., 1985. Zur Berechnung von Kerbwirkungszahlen, Konstruktion 37(2), pp. 67-71.

[14] Eichlseder, W.. Betriebsfestigkeit I. Instalment.

[15] Eichlseder, W., Leitner, H., 2002a. Influence of Stress Gradient on S/N-Curve, New Trends in Fatigue and Fracture.

[16] Eichlseder, W., 2002b. Fatigue analysis by local stress concept based on finite elements results, Computers and Structures 80, pp. 2109-13.

[17] Eichlseder, W.. Comparison of Test results with concepts for the simulation of the stress gradient and size effect under fatigue loading.

[18] Eichlseder, W., 2000. Synthetic S/N curves. Computational Techniques for Materials, Composites and Composite Structures. Civil-Comp Press, Edinburgh., pp. 161-164.

[19] Eichlseder, W., Leitner, H., 2002. Fatigue life prediction based on gradient S/N-curves of Al-alloy-components. In proceeding of Fatigue Congress in Stockholm 2002.

[20] Filippini, M. 2000. Stress gradient calculations at notches. International Journal of Fatigue 22. p. 397-409.

[21] Freddi, A., Curioni, S., Caligiana, G., 1989. La vita a fatica torsionale negli alberi dei turbo gruppi. La collaborazione ENEA industria nel settore termo-elettromeccanico, 22 giugno 1989.

[22] Freddi, A., 2005. Dispense di Analisi Sperimentale delle tensioni: il ruolo della sperimentazione nell'evoluzione progettuale della meccanica delle strutture.

[23] Giovannozzi, R., 1980. Costruzione di macchine. Pàtron editore, Terza edizione. Vol. I, Vol. II

[24] Heywood, R.B., 1947. The relationship between fatigue and stress concentration, Aircraft Engineering 19, pp. 81-84.

[25] Heywood, R.B., 1962. Designing against fatigue, London, Chapman and Hall.

[26] Howard, E. Boyer, 2005. Atlas of fatigue curves. American Society for Metals

[27] Hück, M., Thrainer, L., Schütz, W., 1981. Berechnung von Wöhlerlinien für Bauteile aus Stahl, Stahlguss und Grauguss – Synthetische Wöhlerlinien.

[28] ISO 1143, "Metals - Rotating bar bending fatigue testing", First edition, 1975.

[29] ISO 12107, "Metallic materials - Fatigue testing - Statistical planning and analysis of data", First edition, 2003.

[30] Juvinall, R.C., Marshek, K.M., 2001. Fondamenti della progettazione dei componenti di macchine. Edizioni ETS.

[31] Lee, Y.I., Pan, J., Hathaway, R.B., Barkey, M.E., 2005. Fatigue Testing and Analysis. Elsevier Butterworth-Heinemann.

[32] Manfè, G., Pozza, R., Scarato, G., 1992. Disegno meccanico. Principato Editore, Quarta edizione.

[33] Moore, H.F., Ver, T., 1930. Univ. Illinois, Bulk 27, Nr. 208.

[34] Morkovin, D., Moore, H.F., 1944. Proc. ASTM 44, 137 (Diskuss. 156).

[35] Neuber, H., 1937. Kerbspannungslehre. 1nd Edition. Springer-Verlang, Berlin.

[36] Neuber, H., 1946. Theory of Notch Stress. J.W. Edwards, Ann Arbor, MI.

[37] Neuber, H., 1958. Kerbspannungslehre. 2nd Edition. Springer-Verlang, Berlin.

[38] Neuber, H., 1961. J. Appl. Mech. ASME 28.

[39] Neuber, H., 1968. Über die Berücksichtigung der Spannungskonzentration bei Festigkeitsberechnungen, Konstruktion 20(7), pp. 245-251.

[40] Niemann, G., 1981. Elementi delle macchine, Vol. I: Progettazione e calcolo di accoppiamenti, supporti, alberi. Edizioni di Scienza e Tecnica Milano. Springer-Verlag berlin Heidelberg New York.

[41] Petersen, C., 1951. Die Vorgange im zugig und wechselnd beanspruchten Metallgefüge. Teil 3. Z. Metallkunde 42, H.6, pp. 161-170.

[42] Petersen, C., 1952. Die Vorgange im zugig und wechselnd beanspruchten Metallgefüge. Teil 4. Z. Metallkunde 43, H.12, pp. 429-433.

[43] Peterson., R.E., 1938. Timoschenko-Festschr.

[44] Peterson, R.E., 1959. Notch Sensitivity. Metal Fatigue, G. Sines and J.L. Waisman, eds., McGraw-Hill Book Co., New York.

[45] Peterson, R.E., 1959. Analytical approach to stress concentration effects in aircraft materials. Technical report 59-507. U.S. Air Force – WADC Symposium on Fatigue Metals, Dayton, Ohio.

[46] Peterson, R.E., 1974. Stress concentration factors. John Wiley & Sons, Inc., New York.

[47] Pfender e Siebel, 1947. Weiterentwicklung der Festigkeitsrechnung bei Wechselbeanspruchung. Die Technik 2, pp. 117-121.

[48] Philipp, H.A., 1942. Forsch. Ing.-Wes. 13, 99.

[49] Siebel, E., Bussmann K.H., 1948. Das Kerbproblem bei schwingender Beanspruchung, Technik 3 , pp. 249-252.

[50] Siebel, E., Meuth, H.O., 1949. Die Wirkung von Kerben bei schwingender Beanspruchung, VDI Journal 91, pp. 319-323.

[51] Stieler, M., 1954. Untersuchungen über die Dauerschwingfestigkeit metallischer Bauteile bei Raumtemeratur, Dissertation, TU Stuttgart.

[52] Siebel, E., Stieler M., 1955. Ungleichformige Spannungsverteilung bei schwingender Beanspruchung, VDI-Z 97, pp. 121-126.

[53] Siebel, E., Gaier, M., 1956. Untersuchungen über Einflub der Oberflächen-Beschaffenheit auf die Dauerschwingfestigkeit metallischer Bauteile, VDI-Journal 98, pp. 1751-1774.

[54] Stephens, R. I., Fatemi, A., Stephens, R. R., and Fuchs, H. O., 2001. Metal Fatigue in Engineering, 2nd ed., Wiley, New York.

[55] Strozzi, A., 1998. Costruzione di Macchine", Pitagora, Bologna.

[56] Thum, A., Federn, K., 1939. Spannungszustand und Bruchausbildung. Springer-Verlag. Berlin

[57] Various authors, 2004. Diseno Y Càlculo de elementos de màquinas. Universidad Politècnica de Valencia. Departamento de Ingenierìa Mecànica y de Materiales. Area de conocimiento de Ingenierìa Mecànica.

[58] Various authors, 2005. Tesi di laurea. Università degli studi di Pisa.

[59] Vergani, L., 2006. Meccanica dei materiali. Seconda edizione. McGraw-Hill

[60] Wegst, C., Wegst, M., 2004. Stahlschlüssel. Herausgabe und vertreib. Verlag Stahlschlüssel Wegst GmbH. pp. 37-39.

[61] Ansys Theory reference, www.ansys.com

[62] Kuhn, P. and Hardraht, H.F. An Engineering Method for Estimating the Notch-Size Effect in Fatigue test on Steel. NACA TN2805, Langlet Aeronautical Laboratory, Washington, 1952.

[63] Zambonelli, L., 2006. Analisi di fatica basta sul concetto di tensione locale. Tesi di laurea. Università degli studi di Bologna

Appendix A

Data collected from the literature

Table caption

State	*Material state*
σ_B	*Static tensile strength*
Sg Siebel *ρ** Neuber* *ρ* Petersen* *"a" Heywood* *C1 m C2 Dietmann*	*Material characteristic constant computed as reported in section 4.2.2*
K_t	*Elastic stress concentration factor*
σ_D	*Nominal fatigue limit*
$\sigma_{D\ local}$	*Local fatigue limit*
k	*Slope of the S-N curve*
R^2	*The statistical goodness of fit indicator*
Number of tests	*Number of performed experimental tests*
Notch radius	*Nominal notch radius*
χ	*Relative stress gradient computed according to Table 4.8*
Type of load	*Type of load applied*
Reference	*Reference from which data has been taken*

Material	State	σ_B [MPa]	S_g Siebel	ρ** Neuber	ρ* Petersen	"a" Heywood	C1 (Dietmann)	m (Dietmann)	C2 (Dietmann)	K_t	Fatigue Limit σ_D [MPa]	Fatigue Limit $\sigma_{D\,LOCAL}$ [MPa]	k	R^2	Number of test	notch radius [mm]	χ [1/mm]	Type of load	Reference
C15	normalized	370	0,048	0,312	0,143	-	12	0,2	2	1,00	185	185	61	0,85	5	-	0,00	Push-Pull	(Stieler, 1954)
										2,05	110	226	17	0,99	5	2,00	1,05	Push-Pull	
										2,10	120	252	24	0,86	5	1,00	2,10	Push-Pull	
										2,15	125	269	16	0,93	4	0,50	4,20	Push-Pull	
C10	normalized	345	0,051	0,323	0,165	-	12	0,2	1	1,00	115	115	54	0,95	5	-	0,00	Torsion	(Stieler, 1954)
										2,30	58	132	10	0,93	5	3,25	0,90	Torsion	
										2,30	80	184	16	0,99	5	1,00	3,00	Torsion	
										2,30	98	224	18	0,97	5	0,50	6,00	Torsion	
13CrMo44	normalized	555	0,033	0,235	0,064	-	12	0,2	1	1,00	150	150	43	0,99	4	-	0,00	Torsion	(Stieler, 1954)
										2,30	70	161	13	0,99	4	3,25	0,90	Torsion	
										2,30	100	230	17	0,70	4	1,00	3,00	Torsion	
										2,30	120	276	13	0,97	5	0,50	6,00	Torsion	
Stg 45	glowed	540	0,034	0,241	0,067	0,037	12	0,2	2	1,00	160	160	42	0,90	5	-	0,00	Push-Pull	(Stieler, 1954)
										1,00	185	185	25	0,92	6	-	0,30	Bending	
										1,55	145	225	21	0,99	4	2,00	1,05	Push-Pull	
										2,65	130	345	20	0,97	5	0,50	4,20	Push-Pull	
C45	normalized	605	0,029	0,217	0,054	0,030	12	0,2	2	1,00	235	235	30	0,94	7	-	0,00	Push-Pull	(Stieler, 1954)
										1,55	185	287	13	0,90	5	2,00	1,05	Push-Pull	
										2,00	155	310	11	0,95	4	1,00	2,10	Push-Pull	
										2,65	125	331	13	1,00	4	0,50	4,20	Push-Pull	
										3,30	105	347	17	0,93	5	0,30	7,00	Push-Pull	
C45	hardened	665	0,026	0,196	0,044	0,025	12	0,2	2	1,00	290	290	31	0,69	6	-	0,00	Push-Pull	(Stieler, 1954)
										1,00	310	310	30	0,71	6	-	0,30	Bending	
										1,55	200	310	22	0,95	5	2,00	1,05	Push-Pull	
										2,65	140	371	17	0,99	5	0,50	4,20	Push-Pull	
37MnSi5	hardened	1175	0,005	0,078	0,014	-	12	0,2	2	1,00	520	520	71	0,38	5	-	0,00	Push-Pull	(Stieler, 1954)
										1,85	280	518	18	0,95	6	4,00	0,55	Push-Pull	
										2,05	255	523	56	0,82	4	2,00	1,05	Push-Pull	
										2,15	240	516	33	0,91	4	0,50	4,20	Push-Pull	
V2A	glowed (austenitic)	715	0,024	0,179	0,038	-	12	0,2	1	1,00	150	150	-	-	5	-	0,00	Torsion	(Stieler, 1954)
										2,30	85	196	-	-	3	3,25	0,90	Torsion	
										2,30	120	276	-	-	3	1,00	3,00	Torsion	
										2,30	140	322	-	-	4	0,50	6,00	Torsion	

Material	State	σ_B [MPa]	S_g Siebel	ρ** Neuber	ρ* Petersen	"a" Heywood	C1 (Dietmann)	m (Dietmann)	C2 (Dietmann)	K_t	Fatigue Limit σ_D [MPa]	Fatigue Limit $\sigma_{D\ LOCAL}$ [MPa]	k	R^2	Number of test	notch radius [mm]	χ [1/mm]	Type of load	Reference
Armco Eisen	normalized	290	0,057	0,349	0,233	0,129	12	0,2	2	1,00	125	125	-	-	7	-	0,00	Push-Pull	(Stieler, 1954)
										1,00	145	145	-	-	6	-	0,30	Bending	
										1,55	110	171	-	-	5	2,00	1,05	Push-Pull	
										2,65	90	239	-	-	5	0,50	4,20	Push-Pull	
24NiCrMoV14-6		807	0,026	0,152	0,030	-	12	0,2	2	1,00	-	-	22	1,00	-	-	0,00	Push-Pull	(Freddi, 1989)
										1,00	-	-	16	0,95	8	-	0,04	Torsion	
									1	1,00	-	-	5	0,97	16	-	0,08	Torsion	
										1,00	-	-	4	0,97	-	-	0,11	Torsion	
										1,74	-	-	2	0,97	14	-	0,53	Torsion	
36NiCrMo4		1010	0,011	0,105	0,019	0,010	12	0,2	2	1,00	416	416	12	0,89	12	-	0,00	Push-Pull	(Various authors, 2005)
										1,78	233	415	5	0,98	10	2,00	1,13	Push-Pull	
										2,23	204	455	6	0,95	11	1,00	2,14	Push-Pull	
										2,60	165	429	4	0,95	16	0,70	3,19	Push-Pull	
Mo-steel-1		807	0,026	0,152	0,030	-	12	0,2	2	1,00	338	338	18	-	-	-	0,00	Push-Pull	(Huck,1981)
										2,00	172	344	8	-	-	38,00	0,05	Push-Pull	
										1,50	248	372	6	-	-	19,00	0,11	Push-Pull	
										2,00	186	372	9	-	-	8,00	0,25	Push-Pull	
										4,00	97	388	5	-	-	1,50	1,33	Push-Pull	
										5,00	76	380	4	-	-	0,80	2,50	Push-Pull	
										4,00	117	468	5	-	-	0,50	4,00	Push-Pull	
Mo-steel-2		979	0,012	0,111	0,020	0,011	12	0,2	2	1,00	448	448	20	-	-	-	0,00	Push-Pull	(Huck,1981)
										2,00	214	428	7	-	-	0,41	4,88	Push-Pull	
										2,00	221	442	6	-	-	0,25	8,00	Push-Pull	
S-816		1014	0,010	0,103	0,019	0,011	12	0,2	2	1,00	393	393	13	-	9	-	0,00	Push-Pull	(Huck,1981)
										2,40	186	446	6	-	5	0,56	3,57	Push-Pull	
										3,40	165	561	4	-	7	0,25	8,00	Push-Pull	
34niCrMo6-H1		725	0,023	0,177	0,037	0,021	12	0,2	2	1,00	530	530	14	-	16	-	0,00	Push-Pull	(Huck,1981)
										1,60	383	613	5	-	16	8,00	0,25	Push-Pull	
										2,40	265	636	3	-	16	2,00	1,00	Push-Pull	
										5,20	118	614	3	-	16	0,25	8,00	Push-Pull	
										8,10	79	640	3	-	16	0,01	200,00	Push-Pull	
34niCrMo6-H2		1120	0,007	0,085	0,016	0,009	12	0,2	2	1,00	314	314	11	-	16	-	0,00	Push-Pull	(Huck,1981)
										1,60	245	392	7	-	16	8,00	0,25	Push-Pull	
										2,40	177	425	4	-	16	2,00	1,00	Push-Pull	
										5,20	78	406	4	-	16	0,25	8,00	Push-Pull	
										8,10	54	437	4	-	16	0,01	200,00	Push-Pull	

Material	State	σ_B [MPa]	S_g Siebel	ρ^{**} Neuber	ρ^* Petersen	"a" Heywood	C1 (Dietmann)	m (Dietmann)	C2 (Dietmann)	K_t	Fatigue Limit σ_D [MPa]	Fatigue Limit $\sigma_{D\,LOCAL}$ [MPa]	k	R^2	Number of test	notch radius [mm]	χ [1/mm]	Type of load	Reference
0.04% C		380	0,047	0,308	0,136	-	12	0,2	2	1,00	182	182	-	-	-	-	0,00	Push-Pull	(Heywood,1962)
										1,00	276	276	-	-	-	-	0,25	Bending	
										1,00	276	276	-	-	-	-	0,49	Bending	
										1,00	272	272	-	-	-	-	0,98	Bending	
										1,00	299	299	-	-	-	-	1,97	Bending	
0.41% C		449	0,041	0,277	0,097	-	12	0,2	2	1,00	137	137	-	-	-	-	0,00	Push-Pull	(Heywood,1962)
										1,00	187	187	-	-	-	-	0,25	Bending	
										1,00	187	187	-	-	-	-	0,49	Bending	
										1,00	187	187	-	-	-	-	0,98	Bending	
										1,00	211	211	-	-	-	-	1,97	Bending	
0.35% C	mechanically polished	611	0,029	0,215	0,053	-	12	0,2	2	1,00	235	235	-	-	-	-	0,00	Push-Pull	(Heywood,1962)
										1,00	226	226	-	-	-	-	0,04	Bending	
										1,00	220	220	-	-	-	-	0,06	Bending	
										1,00	243	243	-	-	-	-	0,12	Bending	
										1,00	257	257	-	-	-	-	0,25	Bending	
										1,00	265	265	-	-	-	-	0,49	Bending	
										1,00	281	281	-	-	-	-	0,98	Bending	
0.35% C	electrolitically polished	611	0,029	0,215	0,053	-	12	0,2	2	1,00	202	202	-	-	-	-	0,00	Push-Pull	(Heywood,1962)
										1,00	217	217	-	-	-	-	0,06	Bending	
										1,00	203	203	-	-	-	-	0,12	Bending	
										1,00	208	208	-	-	-	-	0,25	Bending	
										1,00	221	221	-	-	-	-	0,49	Bending	
										1,00	230	230	-	-	-	-	0,98	Bending	
0.17%C, 0.7%Mn, 0.2% Si	normalized	463	0,039	0,272	0,091	-	12	0,2	2	1,00	218	218	-	-	-	-	0,00	Push-Pull	(Heywood,1962)
										1,00	245	245	-	-	-	-	0,16	Bending	
										1,00	266	266	-	-	-	-	0,31	Bending	
										1,00	266	266	-	-	-	-	0,49	Bending	
										1,00	266	266	-	-	-	-	0,79	Bending	
0.08%C, 0.4% Mn, 0.7% Ni, 0.07% Mo	rolled	459	0,040	0,273	0,093	-	12	0,2	2	1,00	276	276	-	-	-	-	0,00	Push-Pull	(Heywood,1962)
										1,00	290	290	-	-	-	-	0,17	Bending	
										1,00	316	316	-	-	-	-	0,26	Bending	
										1,00	319	319	-	-	-	-	0,66	Bending	
										1,00	304	304	-	-	-	-	0,79	Bending	
SAE 4340	hot treated	1039	0,009	0,099	0,018	-	12	0,2	2	1,00	556	556	-	-	-	-	0,00	Push-Pull	(Heywood,1962)
										1,00	522	522	-	-	-	-	0,16	Bending	
										1,00	560	560	-	-	-	-	0,31	Bending	
										1,00	553	553	-	-	-	-	0,49	Bending	
										1,00	587	587	-	-	-	-	0,79	Bending	

Material	State	σ_B [MPa]	S_g Siebel	ρ^{**} Neuber	ρ^{*} Petersen	"a" Heywood	C1 (Dietmann)	m (Dietmann)	C2 (Dietmann)	K_t	Fatigue Limit σ_D [MPa]	Fatigue Limit $\sigma_{D\,LOCAL}$ [MPa]	k	R^2	Number of test	notch radius [mm]	χ [1/mm]	Type of load	Reference
0.14%C, 0.5% Mn, 3.1% Ni, 0.9% Cr	hot treated	820	0,018	0,149	0,029	-	12	0,2	2	1,00	372	372	-	-	-	-	0,00	Push-Pull	(Heywood,1962)
										1,00	402	402	-	-	-	-	0,28	Bending	
										1,00	480	480	-	-	-	-	0,56	Bending	
0.07%C, 0.2% Mn, 0.2% Si	normalized	387	0,046	0,305	0,131	0,202	12	0,2	2	1,00	204	204	-	-	-	-	0,00	Push-Pull	(Heywood,1962)
										2,81	95	266	-	-	-	3,57	0,65	Push-Pull	
										2,81	104	291	-	-	-	1,98	1,18	Push-Pull	
										2,81	122	344	-	-	-	1,19	1,95	Push-Pull	
										2,81	130	365	-	-	-	0,70	3,34	Push-Pull	
										2,81	116	326	-	-	-	0,60	3,90	Push-Pull	
										2,97	110	326	-	-	-	0,39	5,92	Push-Pull	
										2,96	133	395	-	-	-	0,17	14,11	Push-Pull	
										2,97	172	511	-	-	-	0,10	22,93	Push-Pull	
0.43% C, 2.64% Ni, 0.75% Cr, 0.65% Mn, 0.32% Si, 0.58% Mo, 0.05%V	hot treated	974	0,012	0,112	0,021	0,032	12	0,2	2	1,00	596	596	-	-	-	-	0,00	Push-Pull	(Heywood,1962)
										2,81	216	606	-	-	-	3,57	0,65	Push-Pull	
										2,81	216	606	-	-	-	1,98	1,18	Push-Pull	
										2,81	248	697	-	-	-	1,19	1,95	Push-Pull	
										2,81	265	744	-	-	-	0,70	3,34	Push-Pull	
										2,81	232	652	-	-	-	0,39	5,92	Push-Pull	
0.44% C, 0.6%Mn		564	0,032	0,232	0,062	-	12	0,2	2	1,00	219	219	-	-	-	-	0,04	Bending	(Heywood,1962)
										1,00	217	217	-	-	-	-	0,08	Bending	
										1,00	230	230	-	-	-	-	0,17	Bending	
										1,00	247	247	-	-	-	-	0,29	Bending	
										1,00	241	241	-	-	-	-	1,57	Bending	
0.42% C, 0.6%Mn, 0,.25% Si	hot rolled	510	0,036	0,253	0,075	-	12	0,2	2	1,00	231	231	-	-	-	-	0,08	Bending	(Heywood,1962)
										1,00	225	225	-	-	-	-	0,17	Bending	
										1,00	221	221	-	-	-	-	0,29	Bending	
										1,00	230	230	-	-	-	-	1,57	Bending	
0.45% C		-	-	-	-	-	12	0,2		1,00	225	225	-	-	-	-	0,04	Bending	(Heywood,1962)
										1,00	221	221	-	-	-	-	0,16	Bending	
										1,00	218	218	-	-	-	-	1,57	Bending	
0.19% C		-	-	-	-	-	12	0,2	2	1,00	169	169	-	-	-	-	0,04	Bending	(Heywood,1962)
										1,00	191	191	-	-	-	-	0,16	Bending	
										1,00	180	180	-	-	-	-	1,57	Bending	
SAE 2345	hot treated	867	0,016	0,137	0,026	-	12	0,2	2	1,00	459	459	-	-	-	-	0,05	Bending	(Heywood,1962)
										1,00	442	442	-	-	-	-	0,09	Bending	
										1,00	459	459	-	-	-	-	0,16	Bending	
										1,00	484	484	-	-	-	-	0,26	Bending	
										1,00	461	461	-	-	-	-	0,31	Bending	
										1,00	488	488	-	-	-	-	0,49	Bending	
										1,00	485	485	-	-	-	-	0,63	Bending	

Material	State	σ_B [MPa]	S_g Siebel	ρ^{**} Neuber	ρ^{*} Petersen	"a" Heywood	C1 (Dietmann)	m (Dietmann)	C2 (Dietmann)	K_t	Fatigue Limit σ_D [MPa]	Fatigue Limit $\sigma_{D\,LOCAL}$ [MPa]	k	R^2	Number of test	notch radius [mm]	χ [1/mm]	Type of load	Reference
SAE 1020	strain relieved	414	0,044	0,293	0,114	-	12	0,2	2	1,00	193	193	-	-	-	-	0,04	Bending	(Heywood,1962)
										1,00	193	193	-	-	-	-	0,08	Bending	
										1,00	193	193	-	-	-	-	0,16	Bending	
										1,00	200	200	-	-	-	-	0,31	Bending	
										1,00	200	200	-	-	-	-	0,49	Bending	
SAE X4130	hot treated	980	0,012	0,111	0,020	-	12	0,2	2	1,00	449	449	-	-	-	-	0,05	Bending	(Heywood,1962)
										1,00	449	449	-	-	-	-	0,09	Bending	
										1,00	449	449	-	-	-	-	0,16	Bending	
										1,00	482	482	-	-	-	-	0,31	Bending	
										1,00	515	515	-	-	-	-	0,66	Bending	
SAE 1020	rolled	428	0,043	0,287	0,107	-	12	0,2	2	1,00	193	193	-	-	-	-	0,04	Bending	(Heywood,1962)
										1,00	193	193	-	-	-	-	0,08	Bending	
										1,00	187	187	-	-	-	-	0,16	Bending	
										1,00	218	218	-	-	-	-	0,31	Bending	
										1,00	228	228	-	-	-	-	0,66	Bending	
SAE 1035	rolled	605	0,030	0,217	0,054	-	12	0,2	2	1,00	238	238	-	-	-	-	0,04	Bending	(Heywood,1962)
										1,00	245	245	-	-	-	-	0,08	Bending	
										1,00	245	245	-	-	-	-	0,16	Bending	
										1,00	269	269	-	-	-	-	0,31	Bending	
										1,00	269	269	-	-	-	-	0,66	Bending	
SAE 1035	polished and annealed in vacuo	536	0,034	0,243	0,068	-	12	0,2	2	1,00	218	218	-	-	-	-	0,16	Bending	(Heywood,1962)
										1,00	235	235	-	-	-	-	0,31	Bending	
										1,00	242	242	-	-	-	-	0,66	Bending	
0.46% C, 0.7%Mn, 0,.2% Si, 0.12% Mo		618	0,029	0,212	0,051	-	12	0,2	2	1,00	238	238	-	-	-	-	0,04	Bending	(Heywood,1962)
										1,00	249	249	-	-	-	-	0,08	Bending	
										1,00	275	275	-	-	-	-	0,26	Bending	
										1,00	267	267	-	-	-	-	0,98	Bending	
SAE X4340-A		-	-	-	-	-	12	0,2	2	1,00	497	497	-	-	-	-	0,04	Bending	(Heywood,1962)
										1,00	497	497	-	-	-	-	0,08	Bending	
										1,00	553	553	-	-	-	-	0,26	Bending	
SAE 4340	hot treated	1131	0,006	0,084	0,015	-	12	0,2	2	1,00	511	511	-	-	-	-	0,04	Bending	(Heywood,1962)
										1,00	511	511	-	-	-	-	0,08	Bending	
										1,00	539	539	-	-	-	-	0,16	Bending	
										1,00	560	560	-	-	-	-	0,31	Bending	
										1,00	570	570	-	-	-	-	0,66	Bending	

Material	State	σ_B [MPa]	S_g Siebel	ρ^{**} Neuber	ρ^{*} Petersen	"a" Heywood	C1 (Dietmann)	m (Dietmann)	C2 (Dietmann)	K_t	Fatigue Limit σ_D [MPa]	Fatigue Limit $\sigma_{D\,LOCAL}$ [MPa]	k	R^2	Number of test	notch radius [mm]	χ [1/mm]	Type of load	Reference
0.1% C		408	0,045	0,295	0,118	-	12	0,2	2	1,00	245	245	-	-	-	-	0,07	Bending	(Heywood,1962)
										1,00	256	256	-	-	-	-	0,12	Bending	
										1,00	260	260	-	-	-	-	0,26	Bending	
0.3% C		555	0,033	0,235	0,064	-	12	0,2	2	1,00	270	270	-	-	-	-	0,07	Bending	(Heywood,1962)
										1,00	285	285	-	-	-	-	0,12	Bending	
										1,00	289	289	-	-	-	-	0,26	Bending	
0.45% C, 0.79% Mn, 0.18% Si	normalized	525	0,035	0,247	0,071	0,110	12	0,2	2	1,96	146	287	-	-	-	9,53	0,28	Bending	(Heywood,1962)
										1,96	160	313	-	-	-	3,18	0,84	Bending	
										2,51	120	300	-	-	-	2,40	1,00	Bending	
										1,96	164	321	-	-	-	1,59	1,68	Bending	
										1,96	171	334	-	-	-	0,92	2,89	Bending	
										2,51	143	359	-	-	-	0,80	3,00	Bending	
										2,51	167	420	-	-	-	0,40	5,99	Bending	
										2,51	200	391	-	-	-	0,32	8,39	Bending	
										2,51	200	501	-	-	-	0,23	10,32	Bending	
0.42% C, 2.96% Ni, 0.68% Mn, 0.19% Si, 0.38% Mo		670	0,195	0,247	0,044	0,067	12	0,2	2	1,96	188	368	-	-	-	6,35	0,42	Bending	(Heywood,1962)
										2,37	170	403	-	-	-	2,29	1,06	Bending	
										1,96	205	402	-	-	-	1,59	1,68	Bending	
										2,37	198	470	-	-	-	0,57	4,25	Bending	
										1,96	229	448	-	-	-	0,57	4,71	Bending	
										1,96	248	486	-	-	-	0,32	8,39	Bending	
										2,37	236	558	-	-	-	0,20	11,95	Bending	
0.45% C, 0.79% Mn, 0.18% Si	normalized	525	0,035	0,247	0,071	0,070	12	0,2	2	1,40	180	252	-	-	-	10,16	0,26	Bending	(Heywood,1962)
										2,29	121	277	-	-	-	2,54	0,95	Bending	
										1,41	188	265	-	-	-	2,60	1,02	Bending	
										1,40	193	270	-	-	-	1,59	1,68	Bending	
										2,31	147	340	-	-	-	0,65	3,71	Bending	
										2,29	155	354	-	-	-	0,40	6,09	Bending	
0.42% C, 2.96% Ni, 0.68% Mn, 0.19% Si, 0.38% Mo	normalized	670	0,026	0,195	0,044	0,043	12	0,2	2	1,54	240	370	-	-	-	8,13	0,32	Bending	(Heywood,1962)
										1,61	252	406	-	-	-	1,56	1,62	Bending	
										1,55	275	426	-	-	-	1,08	2,37	Bending	
0.44% C, 1.75% Ni, 0.75% Cr, 0.8% Mn, 0.26% Si, 0.25% Mo	hot treated	1002	0,011	0,106	0,020	0,019	12	0,2	2	1,20	449	539	-	-	-	19,05	0,16	Bending	(Heywood,1962)
										1,47	408	599	-	-	-	7,14	0,37	Bending	
										2,19	276	605	-	-	-	2,39	1,02	Bending	
0.43% C, 0.54% Ni, 0.51% Cr, 0.84% Mn, 0.24% Si, 0.24% Mo	hot treated	947	0,013	0,118	0,022	0,022	12	0,2	2	1,20	415	497	-	-	-	19,05	0,16	Bending	(Heywood,1962)
										1,47	276	406	-	-	-	7,14	0,37	Bending	
										2,19	221	484	-	-	-	2,39	1,02	Bending	

Material	State	σ_B [MPa]	S_g Siebel	ρ** Neuber	ρ* Petersen	"a" Heywood	C1 (Dietmann)	m (Dietmann)	C2 (Dietmann)	K_t	Fatigue Limit σ_D [MPa]	Fatigue Limit $\sigma_{D\,LOCAL}$ [MPa]	k	R^2	Number of test	notch radius [mm]	χ [1/mm]	Type of load	Reference
0.46% C, 0.57% Ni, 0.56% Cr, 1.06% Mn, 0.26% Si, 0.33% Mo	hot treated	1036	0,010	0,100	0,018	0,018	12	0,2	2	1,20	421	506	-	-	-	19,05	0,16	Bending	(Heywood,1962)
										1,47	345	508	-	-	-	7,14	0,37	Bending	
										2,19	249	545	-	-	-	2,39	1,02	Bending	
0.44% C, 0.52% Ni, 0.33% Cr, 1.18% Mn, 0.46% Si, 0.12% Mo	hot treated	850	0,017	0,141	0,027	0,027	12	0,2	2	1,20	366	439	-	-	-	19,05	0,16	Bending	(Heywood,1962)
										1,47	311	457	-	-	-	7,14	0,37	Bending	
										2,19	221	484	-	-	-	2,39	1,02	Bending	
0.28% C, 0.79% Mn, 0.23% Si, 0.06% Cu		614	0,029	0,214	0,052	0,051	12	0,2	2	1,11	274	304	-	-	-	8,00	0,47	Bending	(Heywood,1962)
										1,20	266	319	-	-	-	4,29	0,72	Bending	
										1,37	234	320	-	-	-	2,01	1,34	Bending	
										5,83	147	858	-	-	-	0,10	23,70	Bending	
0.32% C, 0.41% Ni, 1.2% Cr, 0.52% Mn, 0.3% Si, 1W	hot treated	1188	0,007	0,090	0,014	0,014	12	0,2	2	1,09	672	732	-	-	-	10,01	0,41	Bending	(Heywood,1962)
										1,23	629	773	-	-	-	3,61	0,82	Bending	
										1,52	480	730	-	-	-	1,30	1,98	Bending	
										3,65	258	943	-	-	-	0,20	11,79	Bending	

Appendix B

Comparison of experimental versus predicted values of the fatigue limit

Table caption

χ	*Relative stress gradient computing according to Table 4.7*
$\sigma_{D\ local}$	*Local fatigue limit*
Exp.	*Experimental value of the local fatigue limit from Appendix A*
n	*Support effect number according to Table 4.12*
% Err	*Percentage error of the experimental versus predicted values of the fatigue limit*
Load	*Type of load applied*

χ	σ_{Dlocal}	EICHLSEDER			SIEBEL			NEUBER			PETERSEN			BOLLENRATH			HEYWOOD			DIETMANN			Load
mm-1	Mpa																						
C15-normalized (Stieler et al., 1954)																							
	Exp.	n	σ_{Dlocal}	%Err	n	σ_{Dlocal}	%Err	n	σ_{Dlocal}	%Err	n	σ_{Dlocal}	%Err	n	σ_{Dlocal}	%Err	n	σ_{Dlocal}	%Err	n	σ_{Dlocal}	%Err	
0,00	185	1,0000	185	**0**	1,0000	185	**0**	1,0000	185	**0**	1,0000	185	**0**	-	-	-	-	-	-	-	-	-	Push-Pull
1,05	226	1,2264	227	**1**	1,2251	227	**1**	1,1523	213	**5**	1,3875	257	**14**	-	-	-	-	-	-	1,5037	278	**23**	Push-Pull
2,10	252	1,3201	244	**3**	1,3183	244	**3**	1,2866	238	**6**	1,5480	286	**14**	-	-	-	-	-	-	1,7124	317	**26**	Push-Pull
4,20	269	1,4527	269	**0**	1,4501	268	**0**	1,5201	281	**5**	1,7750	328	**22**	-	-	-	-	-	-	2,0075	371	**38**	Push-Pull
37MnSi5 (Stieler et al., 1954)																							
	Exp.	n	σ_{Dlocal}	%Err	n	σ_{Dlocal}	%Err	n	σ_{Dlocal}	%Err	n	σ_{Dlocal}	%Err	n	σ_{Dlocal}	%Err	n	σ_{Dlocal}	%Err	n	σ_{Dlocal}	%Err	
0,00	520	1,0000	520	**0**	1,0000	520	**0**	1,0000	520	**0**	1,0000	520	**0**	-	-	-	-	-	-	-	-	-	Push-Pull
0,55	518	0,9990	519	**0**	1,0520	547	**6**	1,0212	531	**3**	1,0877	566	**9**	1,1624	604	**17**	-	-	-	1,2827	667	**29**	Push-Pull
1,05	523	0,9986	519	**1**	1,0718	557	**7**	1,0401	541	**3**	1,1212	583	**12**	1,2158	632	**21**	-	-	-	1,3998	728	**39**	Push-Pull
4,20	516	0,9973	519	**0**	1,1436	595	**15**	1,1519	599	**16**	1,2425	646	**25**	1,2866	669	**30**	-	-	-	1,7996	936	**81**	Push-Pull
13 CrMo44 (Stieler et al., 1954)																							
	Exp.	n	σ_{Dlocal}	%Err	n	σ_{Dlocal}	%Err	n	σ_{Dlocal}	%Err	n	σ_{Dlocal}	%Err	n	σ_{Dlocal}	%Err	n	σ_{Dlocal}	%Err	n	σ_{Dlocal}	%Err	
0,00	150	1,0000	150	**0**	1,0000	150	**0**	1,0000	150	**0**	1,0000	150	**0**	-	-	-	-	-	-	-	-	-	Torsion
0,90	161	1,3253	199	**23**	1,1724	176	**9**	1,1008	165	**3**	1,2400	186	**16**	1,3655	205	**27**	-	-	-	1,2577	189	**17**	Torsion
3,00	230	1,5940	239	**4**	1,3148	197	**14**	1,3061	196	**15**	1,4382	216	**6**	1,5194	228	**1**	-	-	-	1,4645	220	**4**	Torsion
6,00	276	1,8400	276	**0**	1,4452	217	**21**	1,5530	233	**16**	1,6197	243	**12**	1,5731	236	**15**	-	-	-	1,6569	249	**10**	Torsion
C10 (carburized steel) (Stieler et al., 1954)																							
	Exp.	n	σ_{Dlocal}	%Err	n	σ_{Dlocal}	%Err	n	σ_{Dlocal}	%Err	n	σ_{Dlocal}	%Err	n	σ_{Dlocal}	%Err	n	σ_{Dlocal}	%Err	n	σ_{Dlocal}	%Err	
0,00	115	1,0000	115	**0**	1,0000	115	**0**	1,0000	115	**0**	1,0000	115	**0**	-	-	-	-	-	-	-	-	-	Torsion
0,90	132	1,3679	157	**19**	1,2140	140	**6**	1,1363	131	**1**	1,3854	159	**20**	-	-	-	-	-	-	1,2834	148	**12**	Torsion
3,00	184	1,6718	192	**4**	1,3906	160	**13**	1,4038	161	**12**	1,7036	196	**6**	-	-	-	-	-	-	1,5108	174	**6**	Torsion
6,00	224	1,9500	224	**0**	1,5525	179	**20**	1,7149	197	**12**	1,9950	229	**2**	-	-	-	-	-	-	1,7224	198	**12**	Torsion
V2A (Stieler et al., 1954)																							
	Exp.	n	σ_{Dlocal}	%Err	n	σ_{Dlocal}	%Err	n	σ_{Dlocal}	%Err	n	σ_{Dlocal}	%Err	n	σ_{Dlocal}	%Err	n	σ_{Dlocal}	%Err	n	σ_{Dlocal}	%Err	
0,00	150	1,0000	150	**0**	1,0000	150	**0**	1,0000	150	**0**	1,0000	150	**0**	-	-	-	-	-	-	-	-	-	Torsion
0,90	196	1,4441	217	**11**	1,1456	172	**12**	1,0779	162	**17**	1,1849	178	**9**	1,2809	192	**2**	-	-	-	1,2449	187	**4**	Torsion
3,00	276	1,8108	272	**2**	1,2657	190	**31**	1,2409	186	**33**	1,3376	201	**27**	1,3976	210	**24**	-	-	-	1,4415	216	**22**	Torsion
6,00	322	2,1467	322	**0**	1,3758	206	**36**	1,4421	216	**33**	1,4775	222	**31**	1,4380	216	**33**	-	-	-	1,6244	244	**24**	Torsion
Armco-Eisen (Stieler et al., 1954)																							
	Exp.	n	σ_{Dlocal}	%Err	n	σ_{Dlocal}	%Err	n	σ_{Dlocal}	%Err	n	σ_{Dlocal}	%Err	n	σ_{Dlocal}	%Err	n	σ_{Dlocal}	%Err	n	σ_{Dlocal}	%Err	
0,00	125	1,0000	125	**0**	1,0000	125	**0**	1,0000	125	**0**	1,0000	125	**0**	-	-	-	-	-	-	-	-	-	Push-Pull
0,30	145	1,2427	155	**7**	1,1312	141	**2**	1,0511	131	**9**	1,2644	158	**9**	-	-	-	-	-	-	-	-	-	Bending
1,05	171	1,4540	182	**7**	1,2455	156	**9**	1,1692	146	**14**	1,4946	187	**10**	-	-	-	1,5079	188	**11**	1,5289	191	**12**	Push-Pull
4,20	239	1,9080	239	**0**	1,4909	186	**22**	1,5710	196	**18**	1,9892	249	**4**	-	-	-	2,0159	252	**6**	2,0578	257	**8**	Push-Pull

χ	σ_{Dlocal}	EICHLSEDER			SIEBEL			NEUBER			PETERSEN			BOLLENRATH			HEYWOOD			DIETMANN			Load
mm-1	Mpa																						
Stg 45 (Stieler et al., 1954)																							
	Exp.	n	σ_{Dlocal}	%Err	n	σ_{Dlocal}	%Err	n	σ_{Dlocal}	%Err	n	σ_{Dlocal}	%Err	n	σ_{Dlocal}	%Err	n	σ_{Dlocal}	%Err	n	σ_{Dlocal}	%Err	
0,00	160	1,0000	160	**0**	1,0000	160	**0**	1,0000	160	**0**	1,0000	160	**0**	-	-	-	-	-	-	-	-	-	Push-Pull
0,30	185	1,3082	209	**13**	1,1011	176	**5**	1,0355	166	**10**	1,1418	183	**1**	-	-	-	-	-	-	-	-	-	Bending
1,05	225	1,5766	252	**12**	1,1891	190	**15**	1,1194	179	**20**	1,2652	202	**10**	1,4512	232	**3**	1,2720	204	**9**	1,4670	235	**4**	Push-Pull
4,20	345	2,1531	345	**0**	1,3783	221	**36**	1,4185	227	**34**	1,5305	245	**29**	1,5916	255	**26**	1,5441	247	**28**	1,9341	309	**10**	Push-Pull
C45-normalized (Stieler et al., 1954)																							
	Exp.	n	σ_{Dlocal}	%Err	n	σ_{Dlocal}	%Err	n	σ_{Dlocal}	%Err	n	σ_{Dlocal}	%Err	n	σ_{Dlocal}	%Err	n	σ_{Dlocal}	%Err	n	σ_{Dlocal}	%Err	
0,00	235	1,0000	235	**0**	1,0000	235	**0**	1,0000	235	**0**	1,0000	235	**0**	-	-	-	-	-	-	-	-	-	Push-Pull
1,05	287	1,1838	278	**3**	1,1769	277	**4**	1,1080	260	**9**	1,2381	291	**1**	1,3983	329	**15**	1,2449	293	**2**	1,4565	342	**19**	Push-Pull
2,10	310	1,2599	296	**4**	1,2502	294	**5**	1,2064	284	**9**	1,3367	314	**1**	1,4721	346	**12**	1,3464	316	**2**	1,6457	387	**25**	Push-Pull
4,20	331	1,3675	321	**3**	1,3538	318	**4**	1,3824	325	**2**	1,4762	347	**5**	1,5204	357	**8**	1,4899	350	**6**	1,9131	450	**36**	Push-Pull
7,00	347	1,4745	347	**0**	1,4568	342	**1**	1,5869	373	**8**	1,6148	379	**10**	1,5426	363	**5**	1,6325	384	**11**	2,1788	512	**48**	Push-Pull
C45-hardened (Stieler et al., 1954)																							
	Exp.	n	σ_{Dlocal}	%Err	n	σ_{Dlocal}	%Err	n	σ_{Dlocal}	%Err	n	σ_{Dlocal}	%Err	n	σ_{Dlocal}	%Err	n	σ_{Dlocal}	%Err	n	σ_{Dlocal}	%Err	
0,00	290	1,0000	290	**0**	1,0000	290	**0**	1,0000	290	**0**	1,0000	290	**0**	-	-	-	-	-	-	-	-	-	Push-Pull
0,30	310	1,0746	312	**1**	1,0888	316	**1**	1,0290	298	**4**	1,1149	323	**4**	-	-	-	-	-	-	-	-	-	Bending
1,05	310	1,1397	331	**7**	1,1660	338	**9**	1,0982	318	**3**	1,2149	352	**14**	1,3609	395	**27**	1,2236	355	**14**	1,4480	420	**35**	Push-Pull
4,20	371	1,2793	371	**0**	1,3321	386	**4**	1,3505	392	**6**	1,4299	415	**12**	1,4710	427	**15**	1,4472	420	**13**	1,8960	550	**48**	Push-Pull
36NiCrMo4 (Thesis Pisa)																							
	Exp.	n	σ_{Dlocal}	%Err	n	σ_{Dlocal}	%Err	n	σ_{Dlocal}	%Err	n	σ_{Dlocal}	%Err	n	σ_{Dlocal}	%Err	n	σ_{Dlocal}	%Err	n	σ_{Dlocal}	%Err	
0,00	416	1,0000	416	**0**	1,0000	416	**0**	1,0000	416	**0**	1,0000	416	**0**	-	-	-	-	-	-	-	-	-	Push-Pull
1,13	415	1,0186	424	**2**	1,1092	461	**11**	1,0573	440	**6**	1,1463	477	**15**	1,2447	518	**25**	1,1414	475	**14**	1,4121	587	**42**	Push-Pull
2,14	455	1,0256	427	**6**	1,1504	479	**5**	1,1062	460	**1**	1,2015	500	**10**	1,2915	537	**18**	1,2000	499	**10**	1,5828	658	**45**	Push-Pull
3,19	429	1,0313	429	**0**	1,1838	492	**15**	1,1551	481	**12**	1,2462	518	**21**	1,3092	545	**27**	1,2390	515	**20**	1,6965	706	**65**	Push-Pull
0.04% C (Heywood, 1962)																							
	Exp.	n	σ_{Dlocal}	%Err	n	σ_{Dlocal}	%Err	n	σ_{Dlocal}	%Err	n	σ_{Dlocal}	%Err	n	σ_{Dlocal}	%Err	n	σ_{Dlocal}	%Err	n	σ_{Dlocal}	%Err	
0,00	182	1,0000	182	**0**	1,0000	182	**0**	1,0000	182	**0**	1,0000	182	**0**	-	-	-	-	-	-	-	-	-	Push-Pull
0,25	276	1,2322	224	**19**	1,1093	202	**27**	1,0383	189	**32**	1,1859	215	**22**	-	-	-	-	-	-	-	-	-	Bending
0,49	276	1,3232	240	**13**	1,1521	209	**24**	1,0730	195	**29**	1,2587	229	**17**	-	-	-	-	-	-	-	-	-	Bending
0,98	272	1,4571	265	**3**	1,2151	221	**19**	1,1414	207	**24**	1,3659	248	**9**	-	-	-	-	-	-	-	-	-	Bending
1,97	299	1,6464	299	**0**	1,3042	237	**21**	1,2671	230	**23**	1,5174	276	**8**	-	-	-	-	-	-	-	-	-	Bending
0.41% C (Heywood, 1962)																							
	Exp.	n	σ_{Dlocal}	%Err	n	σ_{Dlocal}	%Err	n	σ_{Dlocal}	%Err	n	σ_{Dlocal}	%Err	n	σ_{Dlocal}	%Err	n	σ_{Dlocal}	%Err	n	σ_{Dlocal}	%Err	
0,00	137	1,0000	137	**0**	1,0000	137	**0**	1,0000	137	**0**	1,0000	137	**0**	-	-	-	-	-	-	-	-	-	Push-Pull
0,25	187	1,1913	164	**12**	1,1019	152	**19**	1,0346	142	**24**	1,1570	159	**15**	-	-	-	-	-	-	-	-	-	Bending
0,49	187	1,2663	174	**7**	1,1419	157	**16**	1,0660	147	**21**	1,2185	168	**10**	-	-	-	-	-	-	-	-	-	Bending
0,98	187	1,3766	189	**1**	1,2006	165	**12**	1,1282	155	**17**	1,3090	180	**4**	-	-	-	-	-	-	-	-	-	Bending
1,97	211	1,5327	211	**0**	1,2838	177	**16**	1,2432	171	**19**	1,4370	198	**6**	-	-	-	-	-	-	-	-	-	Bending

χ	σ_{Dlocal}	EICHLSEDER			SIEBEL			NEUBER			PETERSEN			BOLLENRATH			HEYWOOD			DIETMANN			Load
mm-1	Mpa																						
0.35% C mechanically polished (Heywood, 1962)																							
	Exp.	n	σ_{Dlocal}	%Err	n	σ_{Dlocal}	%Err	n	σ_{Dlocal}	%Err	n	σ_{Dlocal}	%Err	n	σ_{Dlocal}	%Err	n	σ_{Dlocal}	%Err	n	σ_{Dlocal}	%Err	
0,00	235	1,0000	235	0	1,0000	235	0	1,0000	235	0	1,0000	235	0	-	-	-	-	-	-	-	-	-	Push-Pull
0,04	226	1,0375	244	8	1,0324	243	7	1,0038	236	4	1,0435	245	8	-	-	-	-	-	-	-	-	-	Bending
0,06	220	1,0497	247	12	1,0429	245	12	1,0067	236	8	1,0576	248	13	-	-	-	-	-	-	-	-	-	Bending
0,12	243	1,0702	251	4	1,0607	249	3	1,0133	238	2	1,0814	254	5	-	-	-	-	-	-	-	-	-	Bending
0,25	257	1,1001	258	1	1,0865	255	1	1,0269	241	6	1,1160	262	2	-	-	-	-	-	-	-	-	-	Bending
0,49	265	1,1393	268	1	1,1204	263	1	1,0515	247	7	1,1615	273	3	-	-	-	-	-	-	-	-	-	Bending
0,98	281	1,1971	281	0	1,1702	275	2	1,1006	259	8	1,2284	289	3	-	-	-	-	-	-	-	-	-	Bending
0.35% C electroytically polished (Heywood, 1962)																							
	Exp.	n	σ_{Dlocal}	%Err	n	σ_{Dlocal}	%Err	n	σ_{Dlocal}	%Err	n	σ_{Dlocal}	%Err	n	σ_{Dlocal}	%Err	n	σ_{Dlocal}	%Err	n	σ_{Dlocal}	%Err	
0,00	202	1,0000	202	0	1,0000	202	0	1,0000	202	0	1,0000	202	0	-	-	-	-	-	-	-	-	-	Push-Pull
0,06	217	1,0344	209	3	1,0429	211	3	1,0067	204	6	1,0576	214	1	-	-	-	-	-	-	-	-	-	Bending
0,12	203	1,0486	212	5	1,0607	215	6	1,0133	205	1	1,0814	219	8	-	-	-	-	-	-	-	-	-	Bending
0,25	208	1,0694	216	4	1,0865	220	6	1,0269	208	0	1,1160	226	9	-	-	-	-	-	-	-	-	-	Bending
0,49	221	1,0965	222	0	1,1204	227	3	1,0515	213	4	1,1615	235	6	-	-	-	-	-	-	-	-	-	Bending
0,98	230	1,1365	230	0	1,1702	237	3	1,1006	223	3	1,2284	249	8	-	-	-	-	-	-	-	-	-	Bending
0.17% C, 0.7%Mn, 0.2% Si normalized (Heywood, 1962)																							
	Exp.	n	σ_{Dlocal}	%Err	n	σ_{Dlocal}	%Err	n	σ_{Dlocal}	%Err	n	σ_{Dlocal}	%Err	n	σ_{Dlocal}	%Err	n	σ_{Dlocal}	%Err	n	σ_{Dlocal}	%Err	
0,00	218	1,0000	218	0	1,0000	218	0	1,0000	218	0	1,0000	218	0	-	-	-	-	-	-	-	-	-	Push-Pull
0,16	245	1,0977	240	2	1,0792	236	4	1,0212	223	9	1,1197	244	0	-	-	-	-	-	-	-	-	-	Bending
0,31	266	1,1381	248	7	1,1120	243	9	1,0420	227	14	1,1693	255	4	-	-	-	-	-	-	-	-	-	Bending
0,49	266	1,1726	256	4	1,1400	249	6	1,0649	232	13	1,2116	265	1	-	-	-	-	-	-	-	-	-	Bending
0,79	266	1,2184	266	0	1,1771	257	3	1,1020	241	10	1,2677	277	4	-	-	-	-	-	-	-	-	-	Bending
0.08% C, 0.4%Mn, 0.7% Ni, 0.07%Mo rolled (Heywood, 1962)																							
	Exp.	n	σ_{Dlocal}	%Err	n	σ_{Dlocal}	%Err	n	σ_{Dlocal}	%Err	n	σ_{Dlocal}	%Err	n	σ_{Dlocal}	%Err	n	σ_{Dlocal}	%Err	n	σ_{Dlocal}	%Err	
0,00	276	1,0000	276	0	1,0000	276	0	1,0000	276	0	1,0000	276	0	-	-	-	-	-	-	-	-	-	Push-Pull
0,17	290	1,0461	289	0	1,0820	299	3	1,0226	283	3	1,1248	311	7	-	-	-	-	-	-	-	-	-	Bending
0,26	316	1,0577	292	7	1,1027	305	3	1,0353	286	9	1,1562	320	1	-	-	-	-	-	-	-	-	-	Bending
0,66	319	1,0913	302	5	1,1623	321	1	1,0860	300	6	1,2470	345	8	-	-	-	-	-	-	-	-	-	Bending
0,79	304	1,1000	304	0	1,1778	326	7	1,1024	305	0	1,2706	351	16	-	-	-	-	-	-	-	-	-	Bending
SAE 4340 Hot Treated (Heywood, 1962)																							
	Exp.	n	σ_{Dlocal}	%Err	n	σ_{Dlocal}	%Err	n	σ_{Dlocal}	%Err	n	σ_{Dlocal}	%Err	n	σ_{Dlocal}	%Err	n	σ_{Dlocal}	%Err	n	σ_{Dlocal}	%Err	
0,00	556	1,0000	556	0	1,0000	556	0	1,0000	556	0	1,0000	556	0	-	-	-	-	-	-	-	-	-	Push-Pull
0,17	522	1,0258	571	9	1,0399	578	11	1,0083	561	8	1,0549	587	12	-	-	-	-	-	-	-	-	-	Bending
0,21	560	1,0291	572	2	1,0450	581	4	1,0105	562	0	1,0619	591	6	-	-	-	-	-	-	-	-	-	Bending
0,26	553	1,0323	574	4	1,0500	584	6	1,0129	563	2	1,0687	594	7	-	-	-	-	-	-	-	-	-	Bending
0,79	587	1,0559	587	0	1,0866	604	3	1,0383	577	2	1,1191	622	6	-	-	-	-	-	-	-	-	-	Bending

χ	σ_{Dlocal}	EICHLSEDER			SIEBEL			NEUBER			PETERSEN			BOLLENRATH			HEYWOOD			DIETMANN			Load
mm-1	Mpa																						
0.14% C, 0.5%Mn, 3.1% Ni, 0.9%Cr Hot Treated (Heywood, 1962)																							
	Exp.	n	σ_{Dlocal}	%Err	n	σ_{Dlocal}	%Err	n	σ_{Dlocal}	%Err	n	σ_{Dlocal}	%Err	n	σ_{Dlocal}	%Err	n	σ_{Dlocal}	%Err	n	σ_{Dlocal}	%Err	
0,00	372	1,0000	372	**0**	1,0000	372	**0**	1,0000	372	**0**	1,0000	372	**0**	-	-	-	-	-	-	-	-	-	Push-Pull
0,28	402	1,2063	448	**12**	1,0719	398	**1**	1,0208	379	**6**	1,0903	405	**1**	-	-	-	-	-	-	-	-	-	Bending
0,56	480	1,2918	480	**0**	1,1017	410	**15**	1,0411	387	**19**	1,1277	419	**13**	-	-	-	-	-	-	-	-	-	Bending
0.07% C, 0.2% Mn, 0.2% Si Normalized (Heywood, 1962)																							
	Exp.	n	σ_{Dlocal}	%Err	n	σ_{Dlocal}	%Err	n	σ_{Dlocal}	%Err	n	σ_{Dlocal}	%Err	n	σ_{Dlocal}	%Err	n	σ_{Dlocal}	%Err	n	σ_{Dlocal}	%Err	
0,00	204	1,0000	204	**0**	1,0000	204	**0**	1,0000	204	**0**	1,0000	204	**0**	-	-	-	-	-	-	**-**	**-**	**-**	Push-Pull
0,65	266	1,2543	256	**4**	1,1744	239	**10**	1,0949	223	**16**	1,2925	263	**1**	-	-	-	1,4757	301	**13**	1,3737	280	**5**	Push-Pull
1,18	291	1,3412	273	**6**	1,2340	252	**14**	1,1654	238	**18**	1,3925	284	**3**	-	-	-	1,6388	334	**15**	1,5017	306	**5**	Push-Pull
1,95	344	1,4396	293	**15**	1,3014	265	**23**	1,2626	257	**25**	1,5056	307	**11**	-	-	-	1,8240	372	**8**	1,6472	336	**2**	Push-Pull
3,34	365	1,5747	321	**12**	1,3941	284	**22**	1,4197	289	**21**	1,6610	339	**7**	-	-	-	2,0744	423	**16**	1,8438	376	**3**	Push-Pull
3,90	326	1,6217	331	**1**	1,4263	291	**11**	1,4793	302	**8**	1,7151	350	**7**	-	-	-	2,1605	440	**35**	1,9115	390	**19**	Push-Pull
5,92	326	1,7655	360	**10**	1,5249	311	**5**	1,6739	341	**5**	1,8805	383	**18**	-	-	-	2,4394	497	**52**	2,1305	434	**33**	Push-Pull
14,11	395	2,1821	445	**13**	1,8106	369	**7**	2,3014	469	**19**	2,3597	481	**22**	-	-	-	3,1801	648	**64**	2,7123	553	**40**	Push-Pull
22,93	511	2,5069	511	**0**	2,0333	414	**19**	2,8253	576	**13**	2,7333	557	**9**	-	-	-	3,8425	783	**53**	3,2326	659	**29**	Push-Pull
0.43% C, 2.64% Ni, 0.75% Cr, 0.65% Mn, 0.32% Si, 0.58% Mo, 0.05%V Hot treated (Heywood, 1962)																							
	Exp.	n	σ_{Dlocal}	%Err	n	σ_{Dlocal}	%Err	n	σ_{Dlocal}	%Err	n	σ_{Dlocal}	%Err	n	σ_{Dlocal}	%Err	n	σ_{Dlocal}	%Err	n	σ_{Dlocal}	%Err	
0,00	596	1,0000	596	**0**	1,0000	596	**0**	1,0000	596	**0**	1,0000	596	**0**	-	-	-	-	-	-	**-**	**-**	**-**	Push-Pull
0,65	606	1,0312	615	**2**	1,0883	649	**7**	1,0359	618	**2**	1,1171	666	**10**	1,2018	717	**18**	1,1894	709	**17**	1,3107	781	**29**	Push-Pull
1,18	606	1,0419	621	**3**	1,1185	667	**10**	1,0638	634	**5**	1,1572	690	**14**	1,2532	747	**23**	1,2543	748	**23**	1,4172	845	**39**	Push-Pull
1,95	697	1,0540	628	**10**	1,1527	687	**1**	1,1039	658	**6**	1,2025	717	**3**	1,2899	769	**10**	1,3280	792	**14**	1,5381	917	**32**	Push-Pull
3,34	744	1,0706	638	**14**	1,1996	715	**4**	1,1721	699	**6**	1,2647	754	**1**	1,3185	786	**6**	1,4276	851	**14**	1,7016	1015	**36**	Push-Pull
5,92	652	1,0940	652	**0**	1,2659	755	**16**	1,2896	769	**18**	1,3525	806	**24**	1,3398	799	**22**	1,5729	938	**44**	1,9400	1157	**77**	Push-Pull
0.44% C, 0.6%Mn (Heywood, 1962)																							
	Exp.	n	σ_{Dlocal}	%Err	n	σ_{Dlocal}	%Err	n	σ_{Dlocal}	%Err	n	σ_{Dlocal}	%Err	n	σ_{Dlocal}	%Err	n	σ_{Dlocal}	%Err	n	σ_{Dlocal}	%Err	
0,04	219	1,0160	223	**2**	1,0357	227	**4**	1,0046	220	**0**	1,0494	230	**5**	-	-	-	-	-	-	-	-	-	Bending
0,08	217	1,0226	224	**3**	1,0505	230	**6**	1,0091	221	**2**	1,0699	234	**8**	-	-	-	-	-	-	-	-	-	Bending
0,17	230	1,0329	226	**2**	1,0737	235	**2**	1,0192	223	**3**	1,1019	241	**5**	-	-	-	-	-	-	-	-	-	Bending
0,29	247	1,0434	229	**7**	1,0973	240	**3**	1,0333	226	**8**	1,1345	248	**1**	-	-	-	-	-	-	-	-	-	Bending
1,57	241	1,1009	241	**0**	1,2260	269	**11**	1,1684	256	**6**	1,3125	287	**19**	-	-	-	-	-	-	-	-	-	Bending
0.42% C, 0.6%Mn, 0,.25% Si (hot rolled) (Heywood, 1962)																							
	Exp.	n	σ_{Dlocal}	%Err	n	σ_{Dlocal}	%Err	n	σ_{Dlocal}	%Err	n	σ_{Dlocal}	%Err	n	σ_{Dlocal}	%Err	n	σ_{Dlocal}	%Err	n	σ_{Dlocal}	%Err	
0,08	231	0,9940	231	**0**	1,0534	244	**5**	1,0099	234	**1**	1,0768	249	**8**	-	-	-	-	-	-	-	-	-	Bending
0,17	225	0,9974	231	**3**	1,0779	249	**11**	1,0209	236	**5**	1,1121	257	**14**	-	-	-	-	-	-	-	-	-	Bending
0,29	221	0,9981	231	**4**	1,1028	255	**15**	1,0362	240	**8**	1,1479	266	**20**	-	-	-	-	-	-	-	-	-	Bending
1,57	230	0,9987	230	**0**	1,2388	287	**25**	1,1824	274	**19**	1,3437	311	**35**	-	-	-	-	-	-	-	-	-	Bending

χ	σ_{Dlocal}	EICHLSEDER			SIEBEL			NEUBER			PETERSEN			BOLLENRATH			HEYWOOD			DIETMANN			Load
mm-1	Mpa																						
0.45% C (Heywood, 1962)																							
	Exp.	n	σ_{Dlocal}	%Err	n	σ_{Dlocal}	%Err	n	σ_{Dlocal}	%Err	n	σ_{Dlocal}	%Err	n	σ_{Dlocal}	%Err	n	σ_{Dlocal}	%Err	n	σ_{Dlocal}	%Err	
0,04	225	0,9951	223	1	-	-	-	-	-	-	-	-	-	-	-	-	-	-	-	-	-	-	Bending
0,16	221	0,9903	222	0	-	-	-	-	-	-	-	-	-	-	-	-	-	-	-	-	-	-	Bending
1,57	218	0,9692	218	0	-	-	-	-	-	-	-	-	-	-	-	-	-	-	-	-	-	-	Bending
0.19% C (Heywood,1962)																							
	Exp.	n	σ_{Dlocal}	%Err	n	σ_{Dlocal}	%Err	n	σ_{Dlocal}	%Err	n	σ_{Dlocal}	%Err	n	σ_{Dlocal}	%Err	n	σ_{Dlocal}	%Err	n	σ_{Dlocal}	%Err	
0,08	169	1,0137	172	2	-	-	-	-	-	-	-	-	-	-	-	-	-	-	-	-	-	-	Bending
0,26	191	1,0250	174	9	-	-	-	-	-	-	-	-	-	-	-	-	-	-	-	-	-	-	Bending
1,57	180	1,0612	180	0	-	-	-	-	-	-	-	-	-	-	-	-	-	-	-	-	-	-	Bending
SAE 2345 Hot Treated (Heywood, 1962)																							
	Exp.	n	σ_{Dlocal}	%Err	n	σ_{Dlocal}	%Err	n	σ_{Dlocal}	%Err	n	σ_{Dlocal}	%Err	n	σ_{Dlocal}	%Err	n	σ_{Dlocal}	%Err	n	σ_{Dlocal}	%Err	
0,05	459	1,0161	467	2	1,0293	473	3	1,0036	461	0	1,0369	476	4	-	-	-	-	-	-	-	-	-	Bending
0,09	442	1,0211	469	6	1,0384	477	8	1,0062	462	5	1,0485	482	9	-	-	-	-	-	-	-	-	-	Bending
0,16	459	1,0278	472	3	1,0507	483	5	1,0107	464	1	1,0640	489	6	-	-	-	-	-	-	-	-	-	Bending
0,26	484	1,0359	476	2	1,0654	490	1	1,0178	468	3	1,0826	497	3	-	-	-	-	-	-	-	-	-	Bending
0,31	461	1,0393	478	4	1,0717	492	7	1,0213	469	2	1,0905	501	9	-	-	-	-	-	-	-	-	-	Bending
0,49	488	1,0492	482	1	1,0896	501	2	1,0331	475	3	1,1131	511	5	-	-	-	-	-	-	-	-	-	Bending
0,63	485	1,0556	485	0	1,1014	506	4	1,0422	479	1	1,1280	518	7	-	-	-	-	-	-	-	-	-	Bending
SAE 1020, strain relieved (Heywood, 1962)																							
	Exp.	n	σ_{Dlocal}	%Err	n	σ_{Dlocal}	%Err	n	σ_{Dlocal}	%Err	n	σ_{Dlocal}	%Err	n	σ_{Dlocal}	%Err	n	σ_{Dlocal}	%Err	n	σ_{Dlocal}	%Err	
0,04	193	1,0104	195	1	1,0431	202	4	1,0061	195	1	1,0693	207	7	-	-	-	-	-	-	-	-	-	Bending
0,08	193	1,0143	196	1	1,0589	205	6	1,0115	196	1	1,0947	212	9	-	-	-	-	-	-	-	-	-	Bending
0,16	193	1,0202	197	2	1,0833	210	8	1,0228	198	2	1,1340	219	13	-	-	-	-	-	-	-	-	-	Bending
0,31	200	1,0286	199	1	1,1178	216	8	1,0451	202	1	1,1895	230	15	-	-	-	-	-	-	-	-	-	Bending
0,49	200	1,0357	200	0	1,1472	222	11	1,0696	207	3	1,2369	239	19	-	-	-	-	-	-	-	-	-	Bending
SAE X4130 hot treated (Heywood, 1962)																							
	Exp.	n	σ_{Dlocal}	%Err	n	σ_{Dlocal}	%Err	n	σ_{Dlocal}	%Err	n	σ_{Dlocal}	%Err	n	σ_{Dlocal}	%Err	n	σ_{Dlocal}	%Err	n	σ_{Dlocal}	%Err	
0,05	449	1,0413	468	4	1,0248	460	2	1,0029	450	0	1,0324	464	3	-	-	-	-	-	-	-	-	-	Bending
0,09	449	1,0543	473	5	1,0326	464	3	1,0050	451	1	1,0425	468	4	-	-	-	-	-	-	-	-	-	Bending
0,16	449	1,0716	481	7	1,0430	468	4	1,0087	453	1	1,0561	474	6	-	-	-	-	-	-	-	-	-	Bending
0,31	482	1,1013	495	3	1,0607	476	1	1,0173	457	5	1,0794	485	1	-	-	-	-	-	-	-	-	-	Bending
0,66	515	1,1462	515	0	1,0877	488	5	1,0357	465	10	1,1146	501	3	-	-	-	-	-	-	-	-	-	Bending
SAE 1020, rolled (Heywood, 1962)																							
	Exp.	n	σ_{Dlocal}	%Err	n	σ_{Dlocal}	%Err	n	σ_{Dlocal}	%Err	n	σ_{Dlocal}	%Err	n	σ_{Dlocal}	%Err	n	σ_{Dlocal}	%Err	n	σ_{Dlocal}	%Err	
0,04	193	1,0437	202	4	1,0410	201	4	1,0056	195	1	1,0649	206	6	-	-	-	-	-	-	-	-	-	Bending
0,08	193	1,0619	205	6	1,0580	205	6	1,0112	196	1	1,0918	211	9	-	-	-	-	-	-	-	-	-	Bending
0,16	187	1,0875	210	13	1,0821	209	12	1,0223	198	6	1,1298	219	17	-	-	-	-	-	-	-	-	-	Bending
0,31	218	1,1237	217	0	1,1161	216	1	1,0441	202	7	1,1836	229	5	-	-	-	-	-	-	-	-	-	Bending
0,66	228	1,1786	228	0	1,1675	226	1	1,0900	211	8	1,2650	245	7	-	-	-	-	-	-	-	-	-	Bending

χ	σ_{Dlocal}	EICHLSEDER			SIEBEL			NEUBER			PETERSEN			BOLLENRATH			HEYWOOD			DIETMANN			Load
mm-1	Mpa																						
SAE 1035, rolled (Heywood, 1962)																							
	Exp.	n	σ_{Dlocal}	%Err	n	σ_{Dlocal}	%Err	n	σ_{Dlocal}	%Err	n	σ_{Dlocal}	%Err	n	σ_{Dlocal}	%Err	n	σ_{Dlocal}	%Err	n	σ_{Dlocal}	%Err	
0,04	238	1,0342	247	3	1,0366	247	4	1,0049	240	0	1,0461	249	5	-	-	-	-	-	-	-	-	-	Bending
0,08	245	1,0452	249	2	1,0484	250	2	1,0085	240	2	1,0652	254	4	-	-	-	-	-	-	-	-	-	Bending
0,16	245	1,0639	254	3	1,0685	255	4	1,0169	242	1	1,0922	260	6	-	-	-	-	-	-	-	-	-	Bending
0,31	269	1,0904	260	4	1,0969	261	3	1,0336	246	9	1,1304	269	0	-	-	-	-	-	-	-	-	-	Bending
0,66	269	1,1304	269	0	1,1398	272	1	1,0688	255	5	1,1882	283	5	-	-	-	-	-	-	-	-	-	Bending
SAE 1035, polished and annealed in vacuo (Heywood, 1962)																							
	Exp.	n	σ_{Dlocal}	%Err	n	σ_{Dlocal}	%Err	n	σ_{Dlocal}	%Err	n	σ_{Dlocal}	%Err	n	σ_{Dlocal}	%Err	n	σ_{Dlocal}	%Err	n	σ_{Dlocal}	%Err	
0,16	218	1,0544	229	5	1,0735	234	7	1,0189	222	2	1,1035	240	10	-	-	-	-	-	-	-	-	-	Bending
0,31	235	1,0770	234	0	1,1040	240	2	1,0375	226	4	1,1463	249	6	-	-	-	-	-	-	-	-	-	Bending
0,66	242	1,1111	242	0	1,1501	250	4	1,0766	234	3	1,2112	264	9	-	-	-	-	-	-	-	-	-	Bending
0.46% C, 0.7%Mn, 0,.2% Si, 0.12% Mo (Heywood, 1962)																							
	Exp.	n	σ_{Dlocal}	%Err	n	σ_{Dlocal}	%Err	n	σ_{Dlocal}	%Err	n	σ_{Dlocal}	%Err	n	σ_{Dlocal}	%Err	n	σ_{Dlocal}	%Err	n	σ_{Dlocal}	%Err	
0,04	238	1,0244	243	2	1,0338	246	3	1,0042	239	0	1,0448	248	4	-	-	-	-	-	-	-	-	-	Bending
0,08	249	1,0345	246	1	1,0478	249	0	1,0083	240	4	1,0634	253	2	-	-	-	-	-	-	-	-	-	Bending
0,26	275	1,0630	253	8	1,0873	258	6	1,0275	244	11	1,1157	265	4	-	-	-	-	-	-	-	-	-	Bending
0,98	267	1,1221	267	0	1,1690	278	4	1,0995	261	2	1,2240	291	9	-	-	-	-	-	-	-	-	-	Bending
SAE X4340-A (Heywood, 1962)																							
	Exp.	n	σ_{Dlocal}	%Err	n	σ_{Dlocal}	%Err	n	σ_{Dlocal}	%Err	n	σ_{Dlocal}	%Err	n	σ_{Dlocal}	%Err	n	σ_{Dlocal}	%Err	n	σ_{Dlocal}	%Err	
0,04	497	1,1111	519	4	-	-	-	-	-	-	-	-	-	-	-	-	-	-	-	-	-	-	Bending
0,08	497	1,0609	528	6	-	-	-	-	-	-	-	-	-	-	-	-	-	-	-	-	-	-	Bending
0,26	553	1,0430	553	0	-	-	-	-	-	-	-	-	-	-	-	-	-	-	-	-	-	-	Bending
SAE 4340 hot treated (Heywood, 1962)																							
	Exp.	n	σ_{Dlocal}	%Err	n	σ_{Dlocal}	%Err	n	σ_{Dlocal}	%Err	n	σ_{Dlocal}	%Err	n	σ_{Dlocal}	%Err	n	σ_{Dlocal}	%Err	n	σ_{Dlocal}	%Err	
0,04	511	1,0301	527	3	1,0169	520	2	1,0019	512	0	1,0260	525	3	-	-	-	-	-	-	-	-	-	Bending
0,08	511	1,0398	532	4	1,0223	523	2	1,0033	513	0	1,0344	529	3	-	-	-	-	-	-	-	-	-	Bending
0,16	539	1,0563	540	0	1,0316	527	2	1,0066	515	5	1,0486	536	1	-	-	-	-	-	-	-	-	-	Bending
0,31	560	1,0796	552	1	1,0447	534	5	1,0131	518	7	1,0687	546	2	-	-	-	-	-	-	-	-	-	Bending
0,66	570	1,1149	570	0	1,0645	544	5	1,0272	525	8	1,0992	562	1	-	-	-	-	-	-	-	-	-	Bending
0.1% C (Heywood, 1962)																							
	Exp.	n	σ_{Dlocal}	%Err	n	σ_{Dlocal}	%Err	n	σ_{Dlocal}	%Err	n	σ_{Dlocal}	%Err	n	σ_{Dlocal}	%Err	n	σ_{Dlocal}	%Err	n	σ_{Dlocal}	%Err	
0,07	245	1,0312	253	3	1,0570	259	6	1,0107	248	1	1,0928	268	9	-	-	-	-	-	-	-	-	-	Bending
0,12	256	1,0393	255	0	1,0718	263	3	1,0169	249	2	1,1169	274	7	-	-	-	-	-	-	-	-	-	Bending
0,26	260	1,0592	260	0	1,1082	272	5	1,0380	255	2	1,1760	288	11	-	-	-	-	-	-	-	-	-	Bending

χ	σ_{Dlocal}	EICHLSEDER			SIEBEL			NEUBER			PETERSEN			BOLLENRATH			HEYWOOD			DIETMANN			Load
mm-1	Mpa																						
0.3% C (Heywood, 1962)																							
	Exp.	n	σ_{Dlocal}	%Err	n	σ_{Dlocal}	%Err	n	σ_{Dlocal}	%Err	n	σ_{Dlocal}	%Err	n	σ_{Dlocal}	%Err	n	σ_{Dlocal}	%Err	n	σ_{Dlocal}	%Err	
0,07	270	1,0377	280	**4**	1,0491	283	**5**	1,0085	272	**1**	1,0683	289	**7**	-	-	-	-	-	-	-	-	-	Bending
0,12	285	1,0476	283	**1**	1,0619	287	**1**	1,0135	274	**4**	1,0861	293	**3**	-	-	-	-	-	-	-	-	-	Bending
0,26	289	1,0716	289	**0**	1,0931	295	**2**	1,0304	278	**4**	1,1296	305	**5**	-	-	-	-	-	-	-	-	-	Bending
0.45% C, 0.79% Mn, 0.18% Si Normalized (Heywood, 1962)																							
	Exp.	n	σ_{Dlocal}	%Err	n	σ_{Dlocal}	%Err	n	σ_{Dlocal}	%Err	n	σ_{Dlocal}	%Err	n	σ_{Dlocal}	%Err	n	σ_{Dlocal}	%Err	n	σ_{Dlocal}	%Err	
0,28	287	1,1228	322	**12**	1,0991	316	**10**	1,0339	297	**3**	1,1409	328	**14**	1,2122	348	**21**	1,2149	349	**21**	1,2152	349	**22**	Bending
0,84	313	1,2127	348	**11**	1,1716	336	**8**	1,0987	315	**1**	1,2440	357	**14**	1,3924	400	**28**	1,3720	394	**26**	1,3725	394	**26**	Bending
1,00	300	1,2320	354	**18**	1,1873	341	**14**	1,1165	321	**7**	1,2663	364	**21**	1,4381	413	**38**	1,4282	410	**37**	1,4288	410	**37**	Bending
1,68	321	1,3007	373	**16**	1,2427	357	**11**	1,1892	341	**6**	1,3451	386	**20**	1,4983	430	**34**	1,5261	438	**37**	1,5268	438	**37**	Bending
2,89	334	1,3947	400	**20**	1,3186	379	**13**	1,3089	376	**12**	1,4529	417	**25**	1,5623	449	**34**	1,6916	486	**45**	1,6925	486	**45**	Bending
3,00	359	1,4019	402	**12**	1,3244	380	**6**	1,3189	379	**5**	1,4612	419	**17**	1,5756	452	**26**	1,7416	500	**39**	1,7426	500	**39**	Bending
5,99	420	1,5684	450	**7**	1,4588	419	**0**	1,5745	452	**8**	1,6523	474	**13**	1,6246	466	**11**	2,0488	588	**40**	2,0502	589	**40**	Bending
8,39	391	1,6725	480	**23**	1,5428	443	**13**	1,7523	503	**29**	1,7717	509	**30**	1,6354	470	**20**	2,1726	624	**59**	2,1742	624	**59**	Bending
10,32	501	1,7457	501	**0**	1,6019	460	**8**	1,8831	541	**8**	1,8558	533	**6**	1,6481	473	**6**	2,3831	684	**37**	2,3850	685	**37**	Bending
0.42% C, 2.96% Ni, 0.68% Mn, 0.19% Si, 0.38% Mo (Heywood, 1962)																							
	Exp.	n	σ_{Dlocal}	%Err	n	σ_{Dlocal}	%Err	n	σ_{Dlocal}	%Err	n	σ_{Dlocal}	%Err	n	σ_{Dlocal}	%Err	n	σ_{Dlocal}	%Err	n	σ_{Dlocal}	%Err	
0,42	368	1,0966	404	**10**	1,2856	474	**29**	1,0505	387	**5**	1,1358	418	**14**	1,2135	447	**21**	1,2054	444	**21**	1,2510	461	**25**	Bending
1,06	403	1,1538	425	**6**	1,4546	536	**33**	1,1235	414	**3**	1,2162	448	**11**	1,3427	495	**23**	1,3421	494	**23**	1,4180	522	**30**	Bending
1,68	402	1,1933	440	**9**	1,5712	579	**44**	1,1892	438	**9**	1,2717	468	**16**	1,3826	509	**27**	1,4106	520	**29**	1,5017	553	**38**	Bending
4,25	470	1,3076	482	**2**	1,9091	703	**50**	1,4314	527	**12**	1,4324	528	**12**	1,4609	538	**15**	1,6857	621	**32**	1,8379	677	**44**	Bending
4,71	448	1,3240	488	**9**	1,9573	721	**61**	1,4708	542	**21**	1,4554	536	**20**	1,4609	538	**20**	1,6857	621	**39**	1,8379	677	**51**	Bending
8,39	486	1,4322	528	**9**	2,2773	839	**73**	1,7523	645	**33**	1,6075	592	**22**	1,4852	547	**13**	1,9152	705	**45**	2,1183	780	**60**	Bending
11,95	558	1,5159	558	**0**	2,5246	930	**67**	1,9875	732	**31**	1,7252	635	**14**	1,4978	552	**1**	2,1576	795	**42**	2,4146	889	**59**	Bending
0.45% C, 0.79% Mn, 0.18% Si Normalized (Heywood, 1962)																							
	Exp.	n	σ_{Dlocal}	%Err	n	σ_{Dlocal}	%Err	n	σ_{Dlocal}	%Err	n	σ_{Dlocal}	%Err	n	σ_{Dlocal}	%Err	n	σ_{Dlocal}	%Err	n	σ_{Dlocal}	%Err	
0,26	252	1,0838	274	**8**	1,0960	277	**10**	1,0318	260	**3**	1,1364	287	**14**	1,2029	304	**20**	1,1660	294	**17**	1,2084	305	**21**	Bending
0,95	277	1,1595	293	**6**	1,1827	299	**8**	1,1111	281	**1**	1,2597	318	**15**	1,4291	361	**30**	1,3320	336	**21**	1,4168	358	**29**	Bending
1,02	265	1,1655	294	**11**	1,1896	300	**13**	1,1192	283	**7**	1,2695	320	**21**	1,4254	360	**36**	1,3282	335	**27**	1,4119	356	**35**	Bending
1,68	270	1,2120	306	**13**	1,2427	314	**16**	1,1892	300	**11**	1,3451	340	**26**	1,4983	378	**40**	1,4196	358	**33**	1,5268	385	**43**	Bending
3,71	340	1,3152	332	**2**	1,3610	344	**1**	1,3842	349	**3**	1,5133	382	**12**	1,5930	402	**18**	1,6563	418	**23**	1,8239	460	**35**	Bending
6,09	354	1,4038	354	**0**	1,4625	369	**4**	1,5822	399	**13**	1,6576	418	**18**	1,6246	410	**16**	1,8367	464	**31**	2,0502	518	**46**	Bending
0.42% C, 2.96% Ni, 0.68% Mn, 0.19% Si, 0.38% Mo (Heywood, 1962)																							
	Exp.	n	σ_{Dlocal}	%Err	n	σ_{Dlocal}	%Err	n	σ_{Dlocal}	%Err	n	σ_{Dlocal}	%Err	n	σ_{Dlocal}	%Err	n	σ_{Dlocal}	%Err	n	σ_{Dlocal}	%Err	
0,32	370	1,0552	391	**6**	1,0906	404	**9**	1,0303	381	**3**	1,1180	414	**12**	1,1832	438	**18**	1,1455	424	**15**	1,2219	452	**22**	Bending
1,62	406	1,1250	417	**3**	1,2051	446	**10**	1,1467	425	**5**	1,2670	469	**16**	1,3845	513	**26**	1,3320	493	**21**	1,5065	558	**37**	Bending
2,37	426	1,1511	426	**0**	1,2480	462	**8**	1,2086	447	**5**	1,3228	490	**15**	1,4181	525	**23**	1,3991	518	**22**	1,6087	596	**40**	Bending

χ	σ_{Dlocal}	EICHLSEDER			SIEBEL			NEUBER			PETERSEN			BOLLENRATH			HEYWOOD			DIETMANN			Load
mm-1	Mpa																						
0.44% C, 1.75% Ni, 0.75% Cr, 0.8% Mn, 0.26% Si, 0.25% Mo Hot treated (Heywood, 1962)																							
	Exp.	**n**	**σ_{Dlocal}**	**%Err**	**n**	**σ_{Dlocal}**	**%Err**	**n**	**σ_{Dlocal}**	**%Err**	**n**	**σ_{Dlocal}**	**%Err**	**n**	**σ_{Dlocal}**	**%Err**	**n**	**σ_{Dlocal}**	**%Err**	**n**	**σ_{Dlocal}**	**%Err**	
0,16	539	1,0492	565	**5**	1,0420	562	**4**	1,0086	544	**1**	1,0566	569	**6**	1,0660	574	**7**	1,0632	573	**6**	1,1337	611	**13**	Bending
0,37	599	1,0739	579	**3**	1,0632	573	**4**	1,0193	549	**8**	1,0860	585	**2**	1,1351	612	**2**	1,1032	595	**1**	1,2184	657	**10**	Bending
1,02	605	1,1231	605	**0**	1,1052	596	**2**	1,0526	567	**6**	1,1428	616	**2**	1,2319	664	**10**	1,1783	635	**5**	1,3776	742	**23**	Bending
0.43% C, 0.54% Ni, 0.51% Cr, 0.84% Mn, 0.24% Si, 0.24% Mo Hot treated (Heywood, 1962)																							
	Exp.	**n**	**σ_{Dlocal}**	**%Err**	**n**	**σ_{Dlocal}**	**%Err**	**n**	**σ_{Dlocal}**	**%Err**	**n**	**σ_{Dlocal}**	**%Err**	**n**	**σ_{Dlocal}**	**%Err**	**n**	**σ_{Dlocal}**	**%Err**	**n**	**σ_{Dlocal}**	**%Err**	
0,16	497	0,9893	492	**1**	1,0459	520	**5**	1,0095	502	**1**	1,0593	527	**6**	1,0697	532	**7**	1,0680	531	**7**	1,1352	565	**14**	Bending
0,37	406	0,9840	489	**20**	1,0690	532	**31**	1,0214	508	**25**	1,0902	542	**33**	1,1423	568	**40**	1,1110	553	**36**	1,2209	607	**50**	Bending
1,02	484	0,9733	484	**0**	1,1149	535	**10**	1,0582	526	**9**	1,1498	572	**18**	1,2436	619	**28**	1,1919	593	**22**	1,3818	687	**42**	Bending
0.46% C, 0.57% Ni, 0.56% Cr, 1.06% Mn, 0.26% Si, 0.33% Mo Hot treated (Heywood, 1962)																							
	Exp.	**n**	**σ_{Dlocal}**	**%Err**	**n**	**σ_{Dlocal}**	**%Err**	**n**	**σ_{Dlocal}**	**%Err**	**n**	**σ_{Dlocal}**	**%Err**	**n**	**σ_{Dlocal}**	**%Err**	**n**	**σ_{Dlocal}**	**%Err**	**n**	**σ_{Dlocal}**	**%Err**	
0,16	506	1,0308	521	**3**	1,0395	526	**4**	1,0081	510	**1**	1,0537	533	**5**	1,0639	538	**6**	1,0615	537	**6**	1,1328	573	**13**	Bending
0,37	508	1,0463	529	**4**	1,0594	536	**6**	1,0181	515	**1**	1,0816	547	**8**	1,1310	572	**13**	1,1004	557	**10**	1,2170	615	**21**	Bending
1,02	545	1,0770	545	**0**	1,0989	556	**2**	1,0494	531	**3**	1,1355	574	**5**	1,2253	620	**14**	1,1736	594	**9**	1,3750	695	**28**	Bending
0.44% C, 0.52% Ni, 0.33% Cr, 1.18% Mn, 0.46% Si, 0.12% Mo Hot treated (Heywood, 1962)																							
	Exp.	**n**	**σ_{Dlocal}**	**%Err**	**n**	**σ_{Dlocal}**	**%Err**	**n**	**σ_{Dlocal}**	**%Err**	**n**	**σ_{Dlocal}**	**%Err**	**n**	**σ_{Dlocal}**	**%Err**	**n**	**σ_{Dlocal}**	**%Err**	**n**	**σ_{Dlocal}**	**%Err**	
0,16	439	1,0407	457	**4**	1,0526	463	**5**	1,0114	444	**1**	1,0657	468	**7**	1,0774	473	**8**	1,0753	473	**8**	1,1382	500	**14**	Bending
0,37	457	1,0612	466	**2**	1,0791	474	**4**	1,0255	451	**1**	1,0999	483	**6**	1,1576	509	**11**	1,1230	493	**8**	1,2257	539	**18**	Bending
1,02	484	1,1019	484	**0**	1,1316	497	**3**	1,0693	470	**3**	1,1660	512	**6**	1,2684	557	**15**	1,2126	533	**10**	1,3902	611	**26**	Bending
0.28% C, 0.79% Mn, 0.23% Si, 0.06% Cu (Heywood, 1962)																							
	Exp.	**n**	**σ_{Dlocal}**	**%Err**	**n**	**σ_{Dlocal}**	**%Err**	**n**	**σ_{Dlocal}**	**%Err**	**n**	**σ_{Dlocal}**	**%Err**	**n**	**σ_{Dlocal}**	**%Err**	**n**	**σ_{Dlocal}**	**%Err**	**n**	**σ_{Dlocal}**	**%Err**	
0,47	304	1,2567	382	**26**	1,1171	339	**12**	1,0489	319	**5**	1,1563	351	**16**	1,2023	365	**20**	1,1597	352	**16**	1,2276	373	**23**	Bending
0,72	319	1,3182	400	**25**	1,1452	348	**9**	1,0742	326	**2**	1,1935	362	**14**	1,2887	391	**23**	1,2181	370	**16**	1,3108	398	**25**	Bending
1,34	320	1,4338	435	**36**	1,1979	364	**14**	1,1341	344	**8**	1,2640	384	**20**	1,3915	423	**32**	1,3186	400	**25**	1,4541	442	**38**	Bending
23,70	858	2,8251	858	**0**	1,8326	557	**35**	2,4626	748	**13**	2,1101	641	**25**	1,5577	473	**45**	2,4283	737	**14**	3,0357	922	**7**	Bending
0.32% C, 0.41% Ni, 1.2% Cr, 0.52% Mn, 0.3% Si, 1W Hot treated (Heywood, 1962)																							
	Exp.	**n**	**σ_{Dlocal}**	**%Err**	**n**	**σ_{Dlocal}**	**%Err**	**n**	**σ_{Dlocal}**	**%Err**	**n**	**σ_{Dlocal}**	**%Err**	**n**	**σ_{Dlocal}**	**%Err**	**n**	**σ_{Dlocal}**	**%Err**	**n**	**σ_{Dlocal}**	**%Err**	
0,41	732	1,0538	771	**5**	1,0527	771	**5**	1,0175	745	**2**	1,0758	787	**8**	-	-	-	1,0748	787	**7**	1,1783	863	**18**	Bending
0,82	773	1,0762	788	**2**	1,0747	787	**2**	1,0348	757	**2**	1,1071	810	**5**	-	-	-	1,1245	823	**6**	1,2969	949	**23**	Bending
1,98	730	1,1181	818	**12**	1,1157	817	**12**	1,0815	792	**8**	1,1665	854	**17**	-	-	-	1,2075	884	**21**	1,4948	1094	**50**	Bending
11,79	943	1,2885	943	**0**	1,2826	939	**0**	1,4186	1038	**10**	1,4063	1029	**9**	-	-	-	1,5292	1119	**19**	2,2615	1655	**76**	Bending
Mo-Steel1 (Huck, 1981)																							
	Exp.	**n**	**σ_{Dlocal}**	**%Err**	**n**	**σ_{Dlocal}**	**%Err**	**n**	**σ_{Dlocal}**	**%Err**	**n**	**σ_{Dlocal}**	**%Err**	**n**	**σ_{Dlocal}**	**%Err**	**n**	**σ_{Dlocal}**	**%Err**	**n**	**σ_{Dlocal}**	**%Err**	
0,00	338	1,0000	338	**0**	1,0000	338	**0**	1,0000	338	**0**	1,0000	338	**0**	-	-	-	-	-	-	-	-	-	Push-Pull
0,05	344	1,0395	351	**2**	1,0370	351	**2**	1,0040	339,349	**1**	1,0397	351	**2**	1,0450	353	**3**	-	-	-	1,0989	371	**8**	Push-Pull
0,11	372	1,0558	357	**4**	1,0523	356	**4**	1,0080	340,693	**8**	1,0562	357	**4**	1,0816	366	**2**	-	-	-	1,1398	385	**4**	Push-Pull
0,25	372	1,0860	367	**1**	1,0806	365	**2**	1,0188	344,362	**7**	1,0866	367	**1**	1,1541	390	**5**	-	-	-	1,2155	411	**10**	Push-Pull
1,33	388	1,1986	405	**4**	1,1862	401	**3**	1,0967	371	**4**	1,2000	406	**5**	1,3243	448	**15**	-	-	-	1,4977	506	**30**	Push-Pull
2,50	380	1,2720	430	**13**	1,2550	424	**12**	1,1747	397	**4**	1,2739	431	**13**	1,3681	462	**22**	-	-	-	1,6814	568	**50**	Push-Pull
4,00	468	1,3440	454	**3**	1,3225	447	**4**	1,2681	429	**8**	1,3464	455	**3**	1,3907	470	**0**	-	-	-	1,8620	629	**34**	Push-Pull

χ	σ_{Dlocal}	EICHLSEDER			SIEBEL			NEUBER			PETERSEN			BOLLENRATH			HEYWOOD			DIETMANN			Load
mm-1	Mpa																						
Mo-Steel2 (Huck, 1981)																							
	Exp.	**n**	**σ_{Dlocal}**	%Err	**n**	**σ_{Dlocal}**	%Err	**n**	**σ_{Dlocal}**	%Err	**n**	**σ_{Dlocal}**	%Err	**n**	**σ_{Dlocal}**	%Err	**n**	**σ_{Dlocal}**	%Err	**n**	**σ_{Dlocal}**	%Err	
0,00	448	1,0000	448	**0**	1,0000	448	**0**	1,0000	448	**0**	1,0000	448	**0**	-	-	-	-	-	-	-	-	-	Push-Pull
4,88	428	0,9895	443	**4**	1,2420	556	**30**	1,2416	556	**30**	1,3124	588	**37**	1,3369	599	**40**	1,3276	449	**5**	1,9158	858	**101**	Push-Pull
8,00	442	0,9866	442	**0**	1,3098	587	**33**	1,3740	616	**39**	1,4000	627	**42**	1,3488	604	**37**	1,4195	480	**9**	2,1728	973	**120**	Push-Pull
S-816 (Huck, 1981)																							
	Exp.	**n**	**σ_{Dlocal}**	%Err	**n**	**σ_{Dlocal}**	%Err	**n**	**σ_{Dlocal}**	%Err	**n**	**σ_{Dlocal}**	%Err	**n**	**σ_{Dlocal}**	%Err	**n**	**σ_{Dlocal}**	%Err	**n**	**σ_{Dlocal}**	%Err	
0,00	393	1,0000	393	**0**	1,0000	393	**0**	1,0000	393	**0**	1,0000	393	**0**	-	-	-	-	-	-	-	-	-	Push-Pull
3,57	446	1,2856	505	**13**	1,1890	467	**5**	1,1696	460	**3**	1,2605	495	**11**	1,3172	518	**16**	1,2803	503	**13**	1,7781	699	**57**	Push-Pull
8,00	561	1,4275	561	**0**	1,2828	504	**10**	1,3506	531	**5**	1,3899	546	**3**	1,3392	526	**6**	1,4195	558	**1**	2,1646	851	**52**	Push-Pull
34NiCrMo6 H1 (Huck, 1981)																							
	Exp.	**n**	**σ_{Dlocal}**	%Err	**n**	**σ_{Dlocal}**	%Err	**n**	**σ_{Dlocal}**	%Err	**n**	**σ_{Dlocal}**	%Err	**n**	**σ_{Dlocal}**	%Err	**n**	**σ_{Dlocal}**	%Err	**n**	**σ_{Dlocal}**	%Err	
0,00	530	1,0000	530	**0**	1,0000	530	**0**	1,0000	530	**0**	1,0000	530	**0**	-	-	-	-	-	-	-	-	-	Push-Pull
0,25	613	1,0279	545	**11**	1,0758	570	**7**	1,0219	542	**12**	1,0962	581	**5**	1,1711	621	**1**	1,1025	584	**5**	1,2202	647	**6**	Push-Pull
1,00	636	1,0558	560	**12**	1,1517	610	**4**	1,0849	575	**10**	1,1924	632	**1**	1,3311	705	**11**	1,2049	639	**0**	1,4403	763	**20**	Push-Pull
8,00	614	1,1577	614	**0**	1,4290	757	**23**	1,5543	824	**34**	1,5441	818	**33**	1,4553	771	**26**	1,5797	837	**36**	2,2454	1190	**94**	Push-Pull
200,00	640	1,7887	948	**48**	3,1448	1667	**160**	6,0332	3198	**400**	3,7203	1972	**208**	1,4800	784	**23**	3,8983	2066	**223**	7,2271	3830	**499**	Push-Pull
34NiCrMo6 H2 (Huck, 1981)																							
	Exp.	**n**	**σ_{Dlocal}**	%Err	**n**	**σ_{Dlocal}**	%Err	**n**	**σ_{Dlocal}**	%Err	**n**	**σ_{Dlocal}**	%Err	**n**	**σ_{Dlocal}**	%Err	**n**	**σ_{Dlocal}**	%Err	**n**	**σ_{Dlocal}**	%Err	
0,00	314	1,0000	314	**0**	1,0000	314	**0**	1,0000	314	**0**	1,0000	314	**0**	-	-	-	-	-	-	-	-	-	Push-Pull
0,25	392	1,0516	330	**16**	1,0418	327	**17**	1,0106	317	**19**	1,0632	334	**15**	-	-	-	1,0671	335	**15**	1,2018	377	**4**	Push-Pull
1,00	425	1,1031	346	**18**	1,0837	340	**20**	1,0416	327	**23**	1,1265	354	**17**	-	-	-	1,1342	356	**16**	1,4036	441	**4**	Push-Pull
8,00	406	1,2917	406	**0**	1,2366	388	**4**	1,2961	407	**0**	1,3578	426	**5**	-	-	-	1,3795	433	**7**	2,1417	672	**66**	Push-Pull
200,00	437	2,4586	772	**76**	2,1832	686	**57**	4,2426	1332	**205**	2,7889	876	**100**	-	-	-	2,8974	910	**108**	6,7083	2106	**382**	Push-Pull

Appendix C

Algorithm for the calculation of the logarithmic correction of the slope k

Logarithmic correction according to the equation (4.52)

$$k_{correction} = k + A\ln(B \cdot \chi + 1)$$

in section 4.4.3.

Definition of the arrays dimensions

Array of the relative stress gradient value

χdato = Array[0, n];

Array of the experimental values of the slope k

ksper = Array[0, n];

Array of the computed value of the slope k according to formula (4.31)

kprev = Array[0, n];

Array of the computed value of the slope k according to formula (4.52)

klog = Array[0, n];

Array of the percentage error between experimental and predicted values of the slope k

errlog = Array[0, n];

χdato[[1]] = …. ;

χdato[[..]] = ….;

χdato[[n]] = ….;

ksper[[1]] =….;

ksper[[….]] = ….;

ksper[[n]] = ….;

kprev[[1]] = ….;

```
kprev[[…]] = ….;

kprev[[n]] = ….;

sqrlog[Alog_, Blog_] = 0;

For[i = 1, i ≤ n, i++,

   {

     klog[[i]] = kprev[[i]] + Alog Log[Blog χdato[[i]] + 1];

     errlog[[i]] = ksper[[i]] - klog[[i]];

     sqrlog[Alog_, Blog_] = sqrlog[Alog, Blog] + errlog[[i]]^2;

     }

   ];

minlog = Minimize[sqrlog[Alog, Blog], {Alog, Blog}];

Alog = minlog[[2, 1, 2]];

Blog = minlog[[2, 2, 2]];
```

Coefficients value of the equation (4.52)

"A"

Alog

"B"

Blog

$$\boxed{k_{correction} = k + A\ln(B\cdot\chi + 1)}$$

Appendix D

Protocol developed for a reliable computation of the slope

Legend

n	*Number of available data for the slope calculation*
χ	*Relative stress gradient of the component*
χ_i	*Not null relative stress gradient*
χ_k	*Null relative stress gradient*
k	*Slope of the S-N curve of the component*
k_k	*Slope of the S-N curve of the specimen with a null value of the relative stress gradient*
k_i	*Slope of the S-N curve of the specimen with a not null value of the relative stress gradient*
R^2	*The statistical goodness of fit indicator*

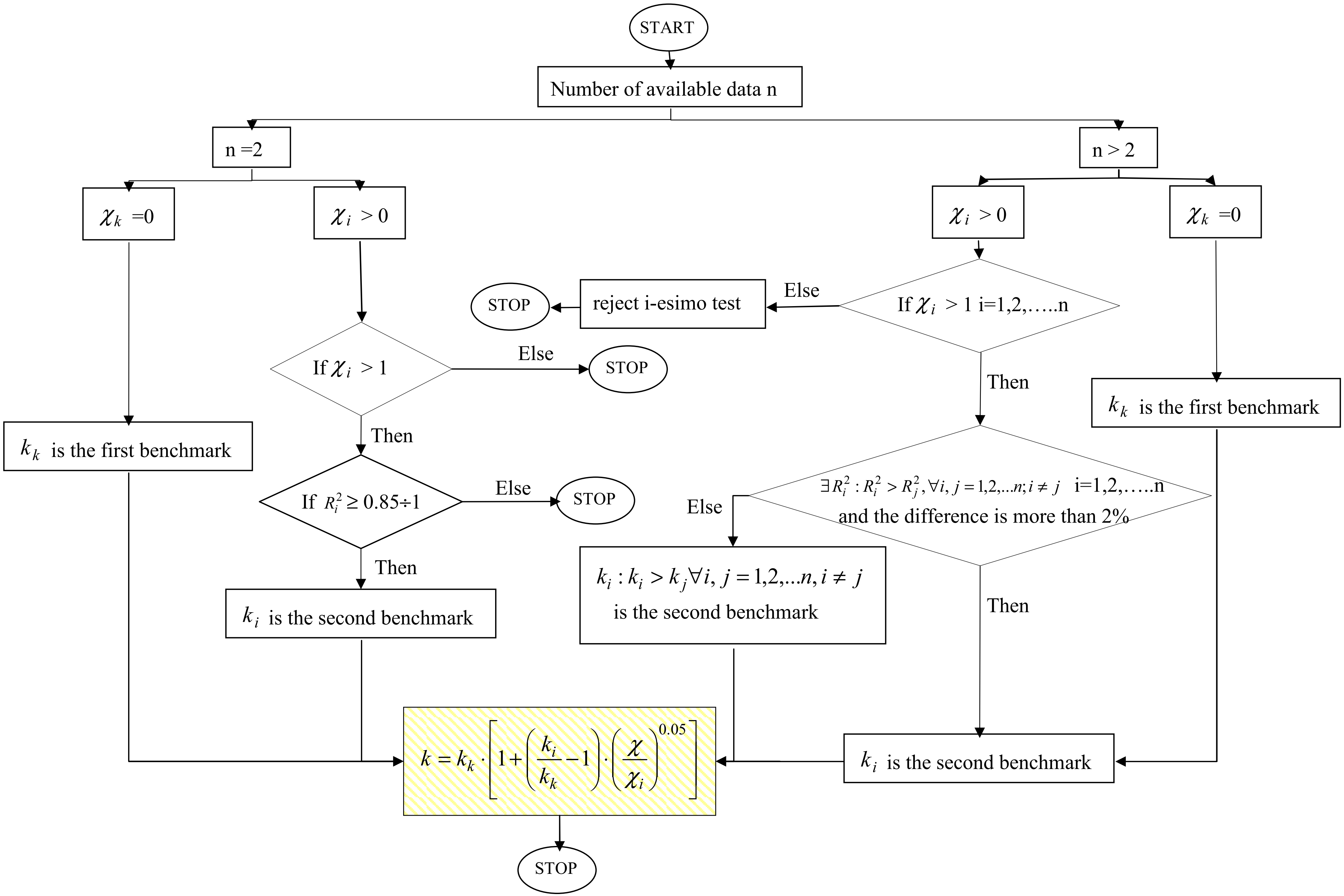

Appendix D: Protocol developed for a reliable computation of the slope

Appendix E

Comparison of experimental versus computed values of the slope k

Table caption

χ	Relative stress gradient of the component
k Experimental	Experimental value of the slope k
R^2	The statistical goodness of fit indicator
k Eichlseder	Slope of the S-N curve computed according to the equation (4.31)
k Log-correction	Slope of the S-N curve computed according to the equation (4.52)
k Novel formulation	Slope of the S-N curve computed according to the equation (4.53)
Type of load	Type of load applied

$$k = k_{\min} + \frac{k_{\max} - k_{\min}}{n^{K_k}} \tag{4.31}$$

$$k_{correction} = k + A\ln(B \cdot \chi + 1) \tag{4.52}$$

$$k_{estimated} = k_K \cdot \left[1 + \left(\frac{k_i}{k_K} - 1\right) \cdot \left(\frac{\chi}{\chi_i}\right)^{0.05}\right] \tag{4.53}$$

Material		χ [1/mm]	k Experimental	R^2	k Eichlseder	% Err	k Log-correction	% Err	A	B	k Novel Formulation	% Err	Type of load
C15	normalized	0,00	60,91	0,85	60,91	0	60,91	0	-1,5919	329294	60,91	0	Push-Pull
		1,05	16,73	0,99	40,92	145	20,61	23			16,73	0	Push-Pull
		2,10	24,35	0,86	36,15	48	14,74	39			15,18	38	Push-Pull
		4,20	16,14	0,93	31,30	94	8,79	46			13,56	16	Bending
C10	normalized	0,00	53,53	0,95	53,53	0	53,53	0	-0,7830	2235430	53,53	0	Torsion
		0,90	10,38	0,93	32,38	212	21,02	102			17,74	71	Torsion
		3,00	15,51	0,99	26,08	68	13,78	11			15,51	0	Torsion
		6,00	18,10	0,97	23,21	28	10,36	43			14,17	22	Torsion
13CrMo44	normalized	0,00	43,30	0,99	43,30	0	43,30	0	-0,4842	2168630	43,30	0	Torsion
		0,90	12,73	0,99	26,60	109	19,59	54			16,09	26	Torsion
		3,00	16,89	0,70	21,13	25	13,53	20			14,40	15	Torsion
		6,00	13,39	0,97	18,49	38	10,56	21			13,39	0	Torsion
Stg 45	glowed	0,00	42,17	0,90	42,17	0	42,17	0	-0,2722	2256580	42,17	0	Push-Pull
		0,30	24,51	0,92	29,92	22	19,42	21			21,91	11	Bending
		1,05	20,60	0,99	25,58	24	14,10	32			20,60	0	Push-Pull
		4,20	19,54	0,97	21,99	13	9,41	52			19,05	2	Push-Pull
C45	normalized	0,00	30,47	0,94	30,47	0	30,47	0	-0,8210	37500	30,47	0	Push-Pull
		1,05	12,82	0,90	25,24	97	16,55	29			14,14	10	Push-Pull
		2,10	11,23	0,95	23,87	113	14,61	30			13,56	21	Push-Pull
		4,20	12,96	1,00	22,40	73	12,58	3			12,96	0	Push-Pull
		7,00	16,94	0,93	21,33	26	11,09	35			12,51	26	Push-Pull
C45	hardened	0,00	30,56	0,69	30,56	0	30,56	0	-1,8697	8	30,56	0	Push-Pull
		0,30	30,00	0,71	28,00	7	28,00	7			18,64	38	Bending
		1,05	22,04	0,95	26,27	19	22,04	19			17,87	19	Push-Pull
		4,20	16,95	0,99	23,62	39	16,95	39			16,95	0	Push-Pull
24NiCrMoV14-6		0,00	21,76	1,00	21,76	0	21,76	0	-2,9778	460	21,76	0	Push-Pull
		0,04	15,74	0,95	20,00	27	11,17	29			4,39	72	Torsion
		0,08	5,41	0,97	19,29	256	8,35	54			3,75	31	Torsion
		0,11	3,55	0,97	18,94	434	7,17	102			3,48	2	Torsion
		0,53	2,00	0,97	16,26	713	-0,11	106			2,00	0	Torsion

Material	χ [1/mm]	k Experimental	R^2	k Eichlseder	% Err	k Log-correction	% Err	A	B	k Novel Formulation	% Err	Type of load
36NiCrMo4	0,00	11,71	0,89	11,71	0	11,71	0			11,71	0	Push-Pull
	1,13	5,02	0,98	11,31	125	5,39	7	-0,7132	3601	5,02	0	Push-Pull
	2,14	5,59	0,95	11,17	100	4,78	14			4,80	14	Push-Pull
	3,19	3,93	0,95	11,05	181	4,38	11			4,66	19	Push-Pull
Mo-steel-1	0,00	18,00	-	18,00	0	18,00	0			18,00	0	Push-Pull
	0,05	8,00	-	16,51	106	10,38	30			7,53	6	Push-Pull
	0,11	5,50	-	15,96	190	9,46	72			7,16	30	Push-Pull
	0,25	8,50	-	15,02	77	8,08	5	-0,5188	2609800	6,68	21	Push-Pull
	1,33	4,50	-	12,28	173	4,46	1			5,69	27	Push-Pull
	2,50	4,00	-	10,97	174	2,83	29			5,30	33	Push-Pull
	4,00	5,00	-	9,94	99	1,56	69			5,00	0	Push-Pull
Mo-steel-2	0,00	20,00	-	20,00	0	20,00	0			20,00	0	Push-Pull
	4,88	7,00	-	20,56	249	6,40	9	-2,6852	24	6,24	12	Push-Pull
	8,00	6,00	-	20,44	188	7,60	7			5,90	0	Push-Pull
S-816	0,00	13,00	-	13,00	0	13,00	0			13,00	0	Push-Pull
	3,57	6,00	-	8,08	47	5,50	0	-1,0560	3	3,88	30	Push-Pull
	8,00	4,00	-	6,88	97	3,50	0			3,50	0	Push-Pull
34niCrMo6-H1	0,00	14,00	-	14,00	0	14,00	0			14,00	0	Push-Pull
	0,25	4,90	-	13,13	168	8,61	76			4,50	8	Push-Pull
	1,00	3,30	-	12,35	274	7,47	127	-0,2575	170464000	3,82	16	Push-Pull
	8,00	2,70	-	10,09	274	4,67	73			2,70	0	Push-Pull
	200,00	2,70	-	4,79	78	-1,45	154			0,73	73	Push-Pull
34niCrMo6-H2	0,00	11,00	-	11,00	0	11,00	0			11,00	0	Push-Pull
	0,25	6,70	-	10,10	51	8,06	20			5,45	19	Push-Pull
	1,00	4,40	-	9,36	113	7,14	62	-0,1268	40901300	5,05	15	Push-Pull
	8,00	4,40	-	7,54	71	5,06	15			4,40	0	Push-Pull
	200,00	4,40	-	4,89	11	1,99	55			3,25	26	Push-Pull

Appendix F

Specimens data of 28NiCrMoV steel used for fatigue bending experimental tests

Table caption

K_t	*Elastic stress concentration factor*
K_f	*Fatigue notch factor*
χ	*Relative stress gradient*
HR	*Hardness Rockwell*
Roughness R_a	*Measured average roughness*
Average roughness	*Average value of* R_a *over the performed measurements*

Specimen Code	Specimen type	Nominal dimension: ϕ / ϕ at notch root	Nominal dimension: notch radius	Real dimension: ϕ / ϕ at notch root		Real dimension: notch radius		K_t	K_f	χ	HR	Roughness Ra 1	Roughness Ra 2	Roughness Ra 3	Average Roughness
	[Smooth/Notched]	[mm]	[mm]	[mm]	%Err	[mm]	%Err			[1/mm]		[µm]	[µm]	[µm]	[µm]
B2	Smooth	6,5 u0,05	-	6,468	0,5	-	-	1,01	-	0,31	22	0,1	0,1	0,1	0,1
D2	Smooth	6,5 u0,05	-	6,468	0,5	-	-	1,01	-	0,31	21	0,1	0,0	0,0	0,0
B1	Smooth	6,5 u0,05	-	6,524	0,4	-	-	1,01	-	0,31	21	0,1	0,0	0,0	0,0
C1	Smooth	6,5 u0,05	-	6,412	1,4	-	-	1,01	-	0,31	19	0,1	0,0	0,1	0,1
C2	Smooth	6,5 u0,05	-	6,454	0,7	-	-	1,01	-	0,31	19	0,1	0,2	0,1	0,1
D1	Smooth	6,5 u0,05	-	6,435	1,0	-	-	1,01	-	0,31	20	0,1	0,0	0,0	0,0
G1	Smooth	6,5 u0,05	-	6,464	0,6	-	-	1,01	-	0,31	20	0,1	0,1	0,1	0,1
G2	Smooth	6,5 u0,05	-	6,478	0,3	-	-	1,01	-	0,31	20	0,0	0,1	0,0	0,0
H2	Smooth	6,5 u0,05	-	6,468	0,5	-	-	1,01	-	0,31	20	0,0	0,0	0,3	0,1
H1	Smooth	6,5 u0,05	-	6,542	0,6	-	-	1,01	-	0,31	20	0,1	0,0	0,1	0,1
										0,31		**average**			
										0,00		**standard deviation**			
ε 2	Notched	6,5 u0,05	1	6,513	0,2	1,045	4,5	1,78	1,73	2,22	19	-	-	-	-
J2	Notched	6,5 u0,05	1	6,504	0,1	1,014	1,4	1,78	1,73	2,28	22	-	-	-	-
V1	Notched	6,5 u0,05	1	6,512	0,2	0,951	4,9	1,78	1,73	2,41	20	-	-	-	-
Y1	Notched	6,5 u0,05	1	6,502	0,0	0,988	1,2	1,78	1,73	2,33	20	-	-	-	-
ε 1	Notched	6,5 u0,05	1	6,503	0,0	0,994	0,6	1,78	1,73	2,32	19	-	-	-	-
λ 2	Notched	6,5 u0,05	1	6,525	0,4	1,021	2,1	1,78	1,73	2,27	20	-	-	-	-
V2	Notched	6,5 u0,05	1	6,524	0,4	1,064	6,4	1,78	1,73	2,19	20	-	-	-	-
J1	Notched	6,5 u0,05	1	6,483	0,3	1,047	4,7	1,78	1,73	2,22	19	-	-	-	-
λ 1	Notched	6,5 u0,05	1	6,511	0,2	0,982	1,8	1,78	1,73	2,34	21	-	-	-	-
Y2	Notched	6,5 u0,05	1	*		-				-	19				
										2,29		**average**			
										0,70		**standard deviation**			
L2	Notched	6,5 u0,05	0,5	6,524	0,4	0,576	15,2	2,07	1,94	3,78	22	-	-	-	-
N1	Notched	6,5 u0,05	0,5	6,543	0,7	0,492	1,6	2,07	1,94	4,37	20	-	-	-	-
M2	Notched	6,5 u0,05	0,5	6,517	0,3	0,450	10,0	2,07	1,94	4,75	19	-	-	-	-
U2	Notched	6,5 u0,05	0,5	6,528	0,4	0,481	3,8	2,07	1,94	4,46	21	-	-	-	-
M1	Notched	6,5 u0,05	0,5	6,528	0,4	0,493	1,4	2,07	1,94	4,36	17	-	-	-	-
R1	Notched	6,5 u0,05	0,5	6,543	0,7	0,457	8,6	2,07	1,94	4,68	20	-	-	-	-
Q2	Notched	6,5 u0,05	0,5	6,506	0,1	0,476	4,8	2,07	1,94	4,51	19	-	-	-	-
T1	Notched	6,5 u0,05	0,5	6,523	0,4	0,574	14,8	2,07	1,94	3,79	21	-	-	-	-
R2	Notched	6,5 u0,05	0,5	6,514	0,2	0,516	3,2	2,07	1,94	4,18	20	-	-	-	-
Q1	Notched	6,5 u0,05	0,5	6,513	0,2	0,475	5,0	2,07	1,94	4,52	19	-	-	-	-
										4,34		**average**			
										0,33		**standard deviation**			

Appendix F: Specimens data of 28NiCrMoV steel used for fatigue bending experimental tests

Appendix G

Results of experimental tests

Table caption

R	*Stress ratio*
Number of cycles	*Number of cycles to failure or 10^7 cycles (run-out)*
% Err	*Percentage error on nominal dimensions*

Specimen Code	Specimen type	Notch radius	Load		Alternating Stress		R	Frequency	Number of cyle	Broke
			Kg	M_b	Nominal	Real				
	[Smooth/Notched]	[mm]		[Nmm]	[MPa]	[MPa]		[cycle/sec]		[Yes/No]
C1	Smooth	-	16,6	9979	370	374	-1	50	10000026	No
G2	Smooth	-	20,4	11749	436	440	-1	50	10000029	No
H2	Smooth	-	20,4	11749	436	440	-1	50	1044500	Yes
B2	Smooth	-	22,6	12774	474	479	-1	50	348517	Yes
D2	Smooth	-	22,6	12774	474	479	-1	50	205425	Yes
H1	Smooth	-	25,7	14219	527	533	-1	50	197694	Yes
C2	Smooth	-	25,7	14219	527	533	-1	50	106053	Yes
B1	Smooth	-	27,9	15244	565	571	-1	50	62382	Yes
D1	Smooth	-	27,9	15244	565	571	-1	50	72065	Yes
G1	Smooth*	-	-	-	-	-	-	100	-	-
J2	Notched	1,0	11,3	7509	279	487	-1	50	10000032	No
V1	Notched	1,0	12,4	8022	298	521	-1	50	98796	Yes
λ 1	Notched	1,0	12,4	8022	298	521	-1	50	375356	Yes
ε 2	Notched	1,0	13,5	8534	317	554	-1	50	90743	Yes
J1	Notched	1,0	13,5	8534	317	554	-1	50	460864	Yes
Y1	Notched	1,0	14,6	9047	336	587	-1	50	174274	Yes
ε 1	Notched	1,0	14,6	9047	336	587	-1	50	213837	Yes
λ 2	Notched	1,0	15,5	9466	351	625	-1	50	147433	Yes
V2	Notched	1,0	16,6	9979	390	681	-1	50	85972	Yes
Y2	Notched **	1,0	-	-	-	-	-	-	-	-
U2	Notched ***	0,5	-	-	-	-	-	-	-	-
T1	Notched	0,5	10,2	6997	260	537	-1	50	1035380	Yes
L2	Notched	0,5	10,2	6997	260	537	-1	50	10000029	No
R2	Notched	0,5	11,3	7509	279	577	-1	50	304906	Yes
Q2	Notched	0,5	12,4	8022	298	616	-1	50	278772	Yes
Q1	Notched	0,5	12,4	8022	298	616	-1	50	247825	Yes
M2	Notched	0,5	13,5	8534	317	655	-1	50	110617	Yes
R1	Notched	0,5	13,5	8534	317	655	-1	50	283659	Yes
N1	Notched	0,5	15,5	9466	351	727	-1	50	59196	Yes
M1	Notched	0,5	15,5	9466	351	727	-1	50	87978	Yes

Appendix H

Stereographic illustrations of the fracture surfaces of the tested specimens

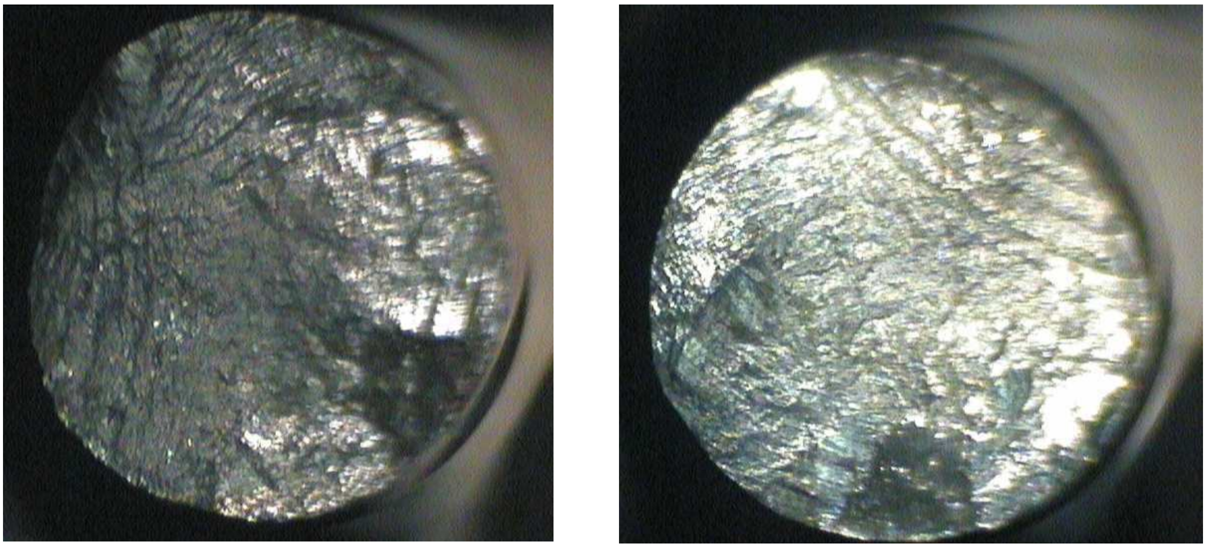

(474 MPa; 348517 cycles to failure)
***B2**: illustration of the metal structure of the fracture surface from stereo Microscope*

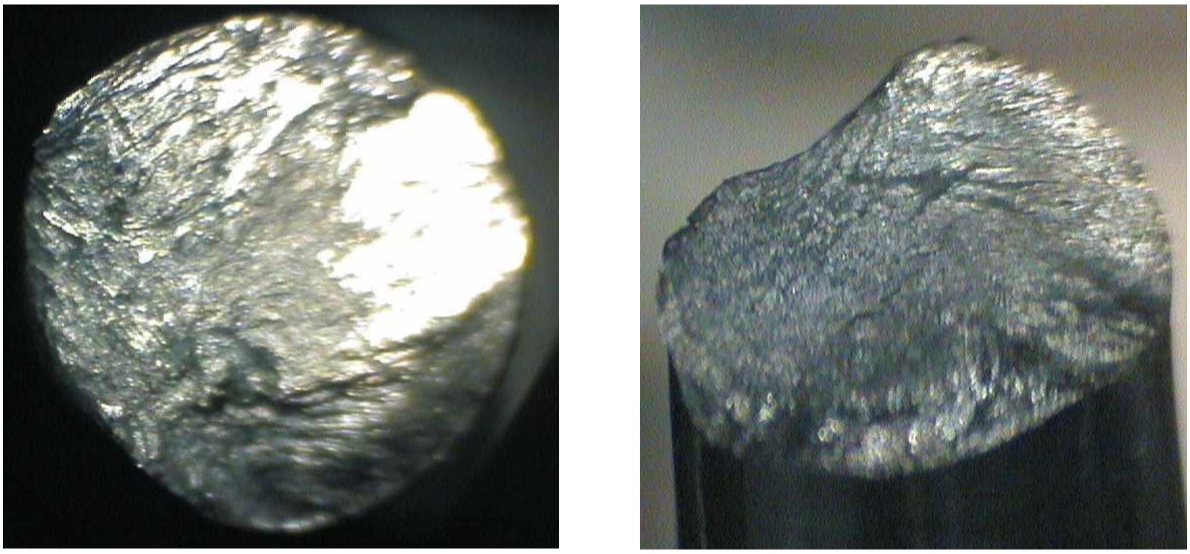

(474 MPa; 205425 cycles to failure)
***D2**: illustration of the metal structure of the fracture surface from stereo Microscope*

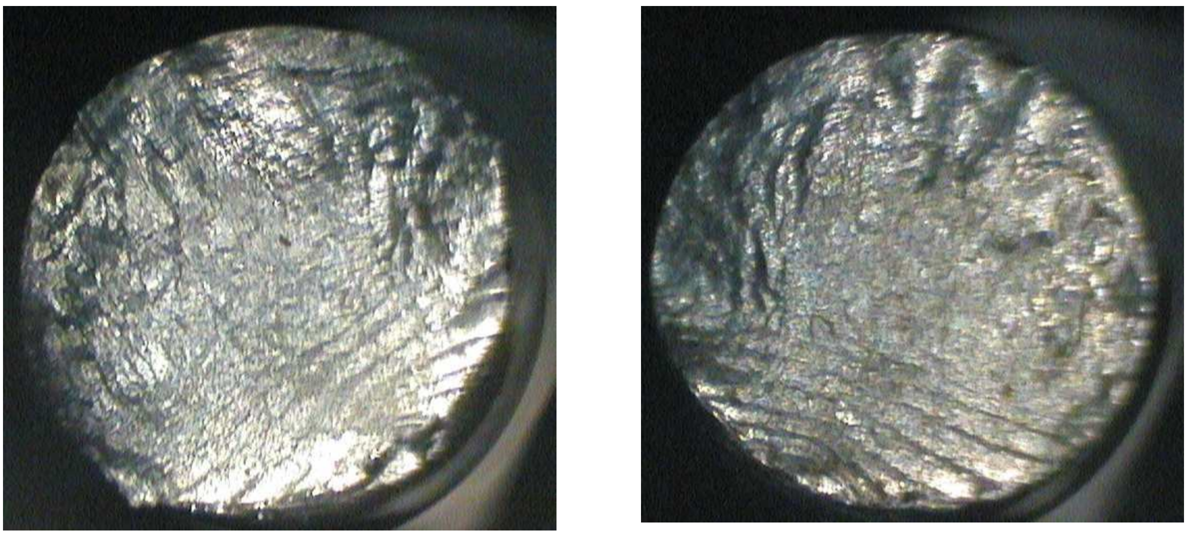

(565 MPa; 62382 cycles to failure)
***B1**: illustration of the metal structure of the fracture surface from stereo Microscope*

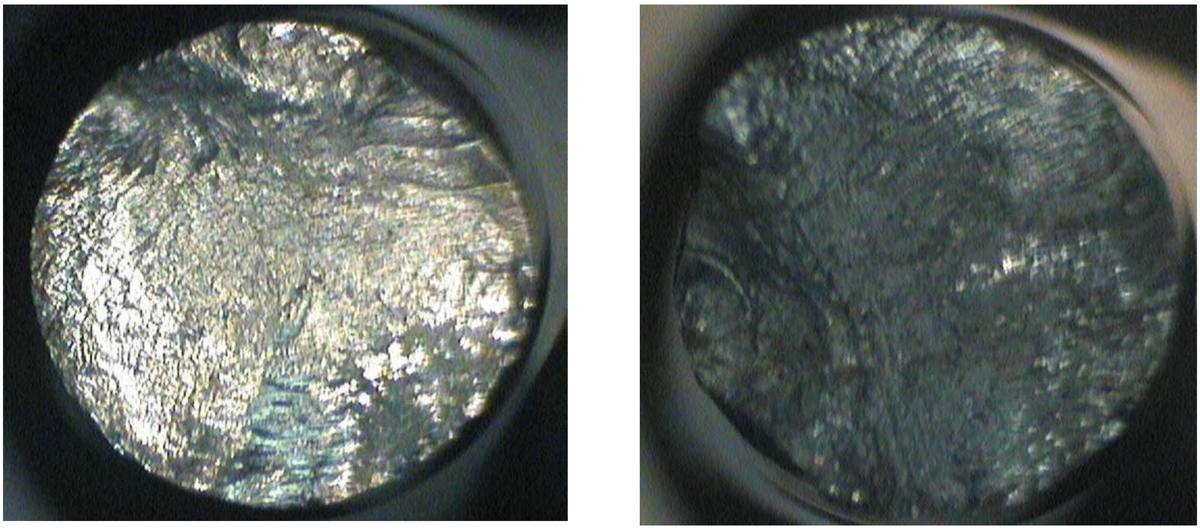

(527 MPa; 106053 cycles to failure)
***C2**: illustration of the metal structure of the fracture surface from stereo Microscope*

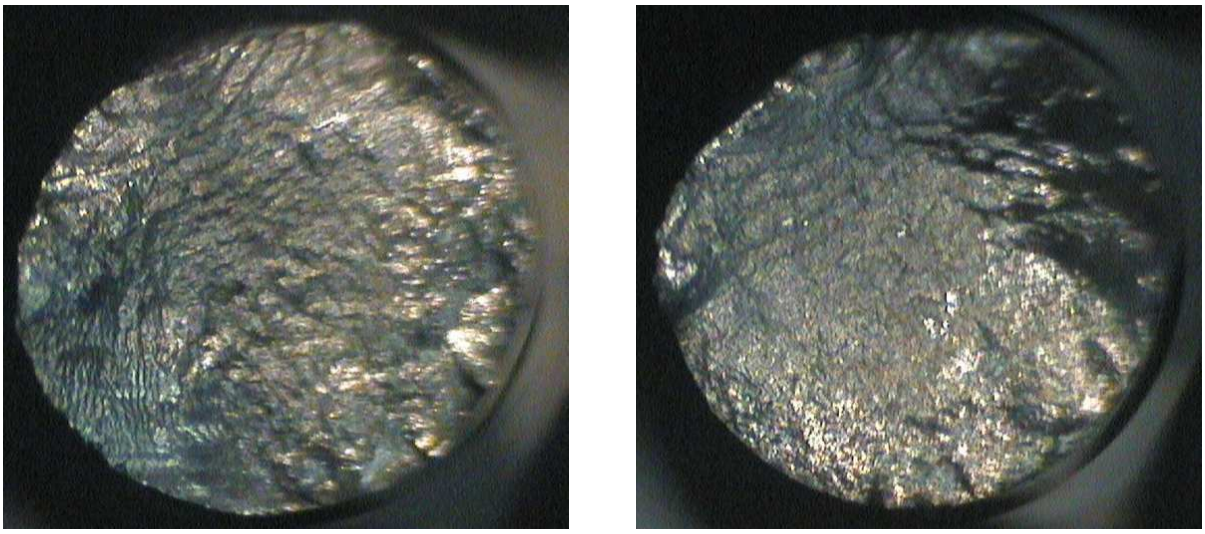

(565 MPa; 72065 cycles to failure)
***D1**: illustration of the metal structure of the fracture surface from stereo Microscope*

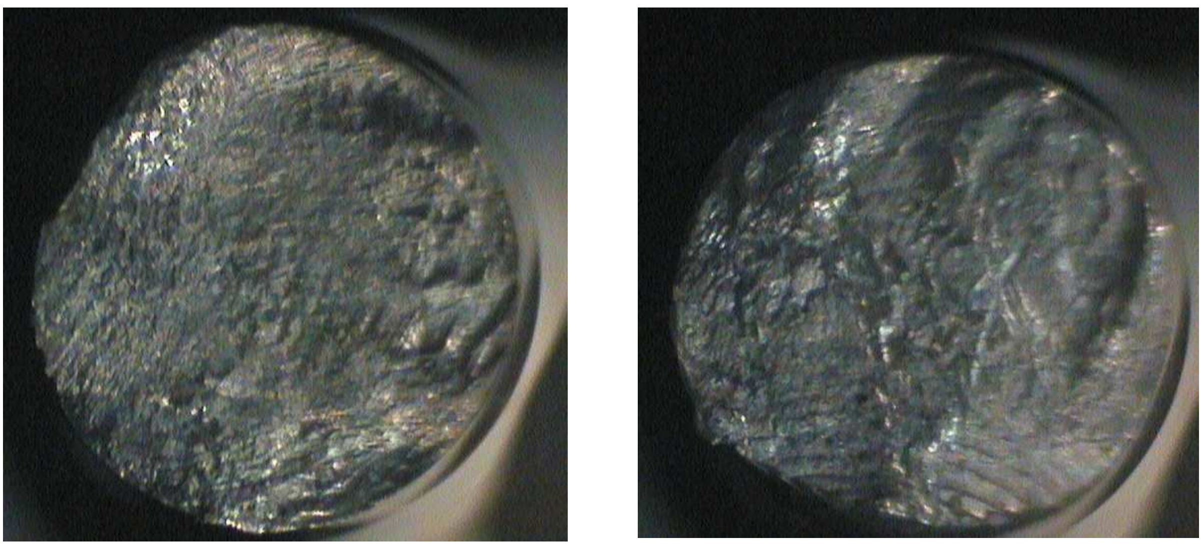

(436 MPa; 1044500 cycles to failure)
***H2**: illustration of the metal structure of the fracture surface from stereo Microscope*

(527 MPa; 197694 cycles to failure)
***H1**: illustration of the metal structure of the fracture surface from stereo Microscope*

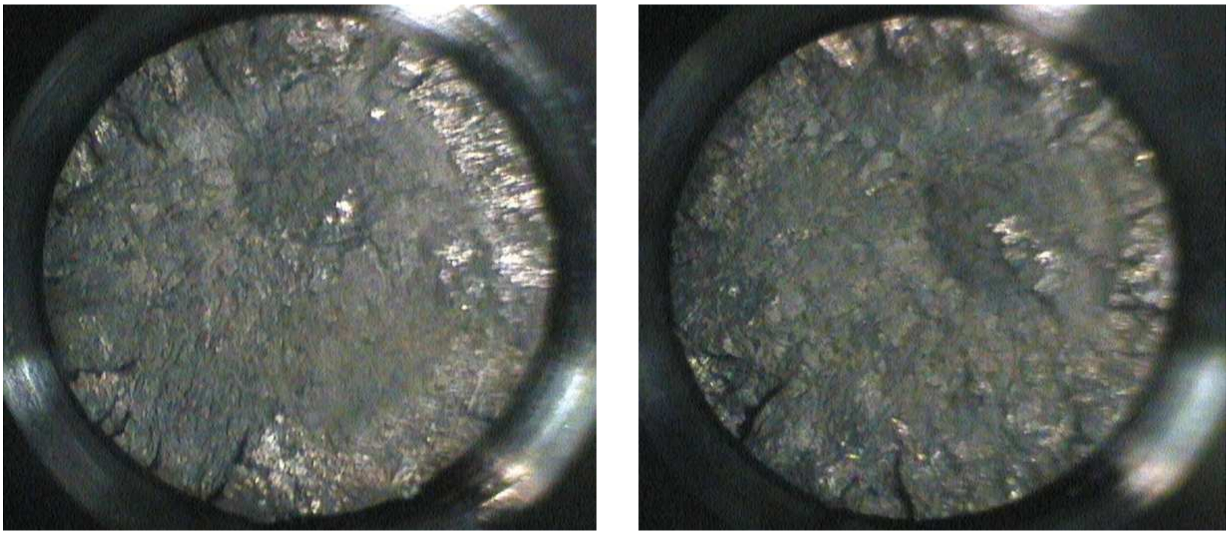

(317 MPa; 554 MPa local stress; 90743 cycles to failure)

***ℰ2**: illustration of the metal structure of the fracture surface from stereo Microscope*

(298 MPa;521 MPa local stress; 98796 cycles to failure)

***V1**: illustration of the metal structure of the fracture surface from stereo Microscope*

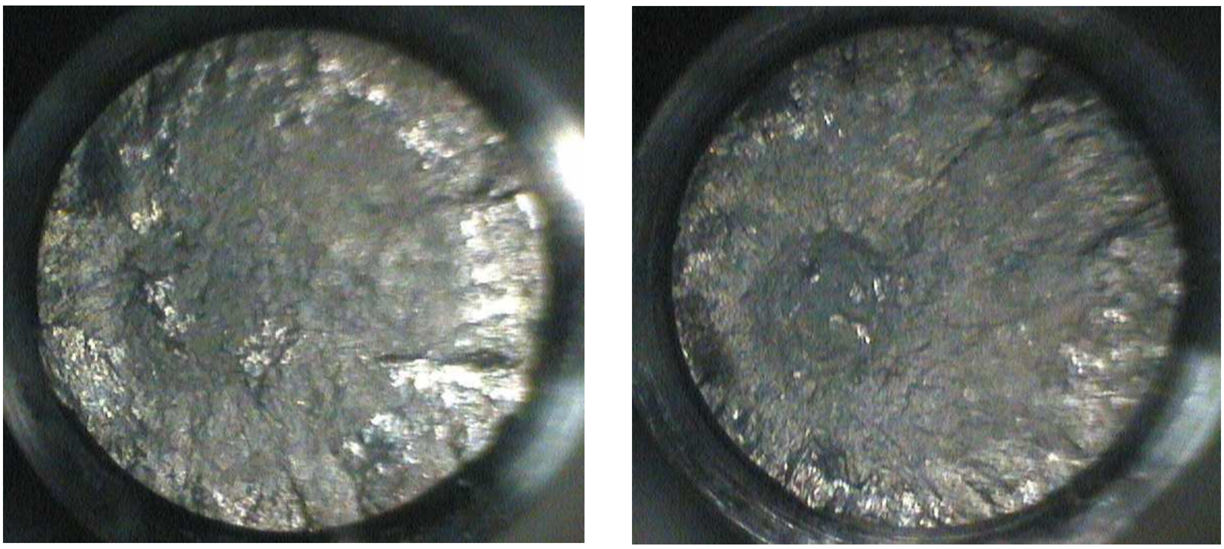

(336 MPa;587 MPa local stress; 174274 cycles to failure)

***Y1**: illustration of the metal structure of the fracture surface from stereo Microscope*

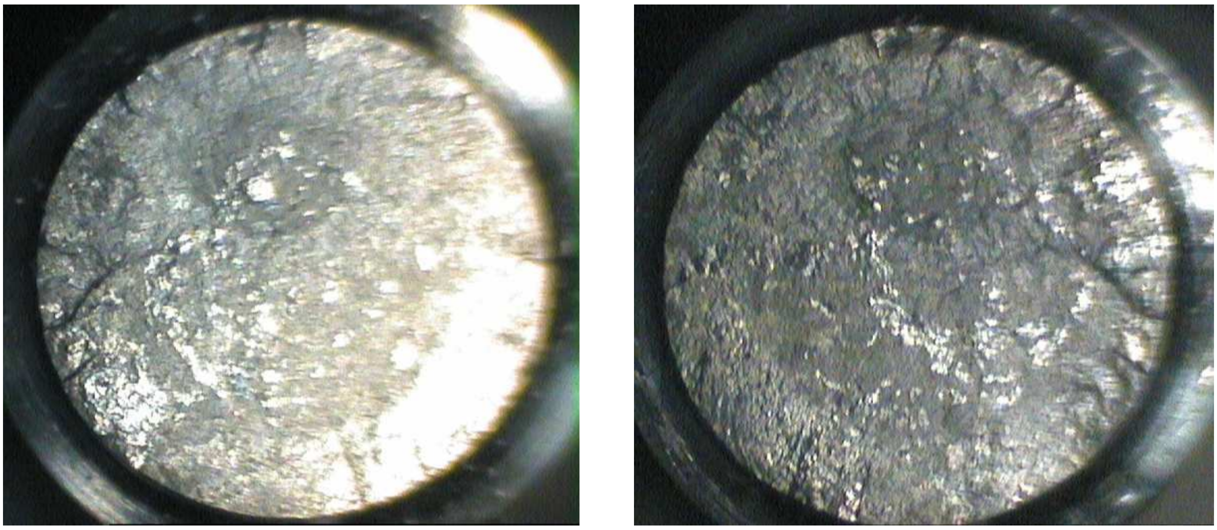

(336 MPa;587MPa local stress; 213837 cycles to failure)

***ε1**: illustration of the metal structure of the fracture surface from stereo Microscope*

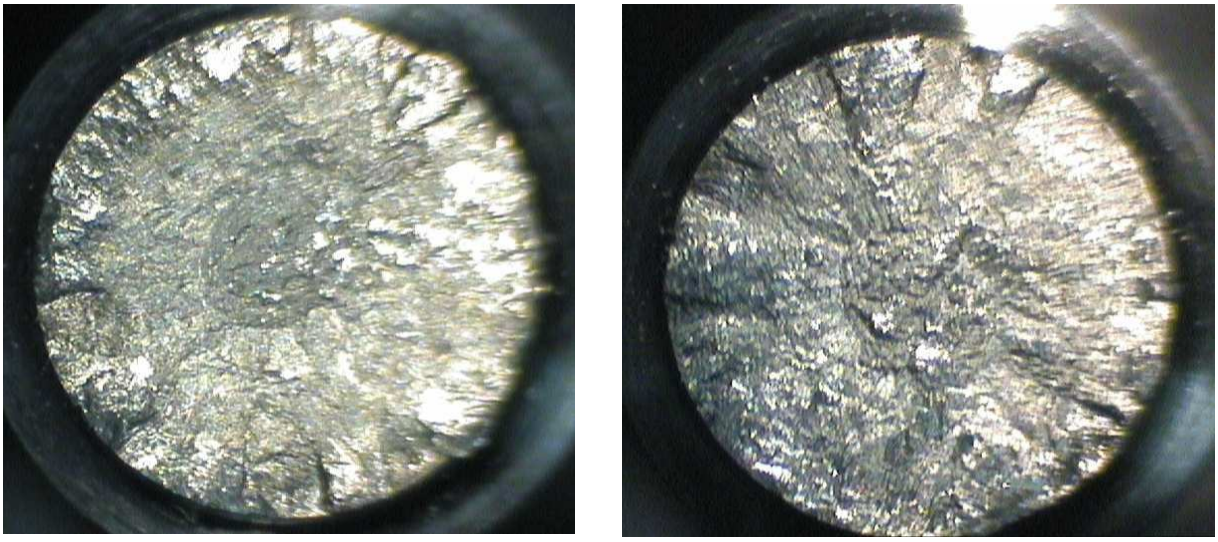

(351 MPa;625MPa local stress; 147433 cycles to failure)

***λ2**: illustration of the metal structure of the fracture surface from stereo Microscope*

(390 MPa;681 MPa local stress; 85972 cycles to failure)

***V2**: illustration of the metal structure of the fracture surface from stereo Microscope*

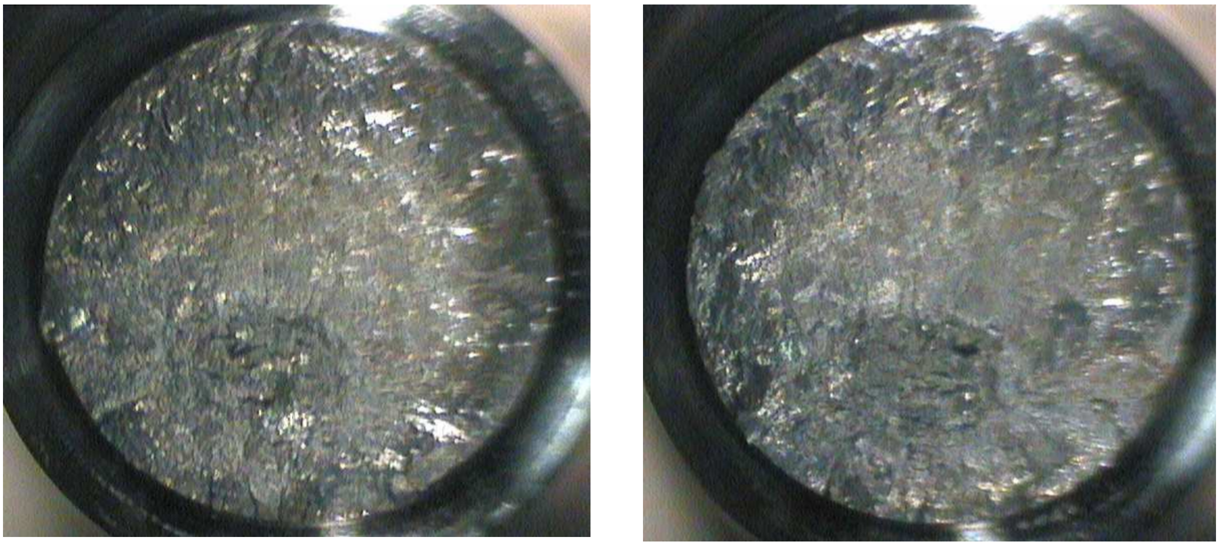

(317 MPa;554 MPa local stress;460864 cycles to failure)
J1*: illustration of the metal structure of the fracture surface from stereo Microscope*

(298 MPa;521 MPa local stress; 348517 cycles to failure)
λ1*: illustration of the metal structure of the fracture surface from stereo Microscope*

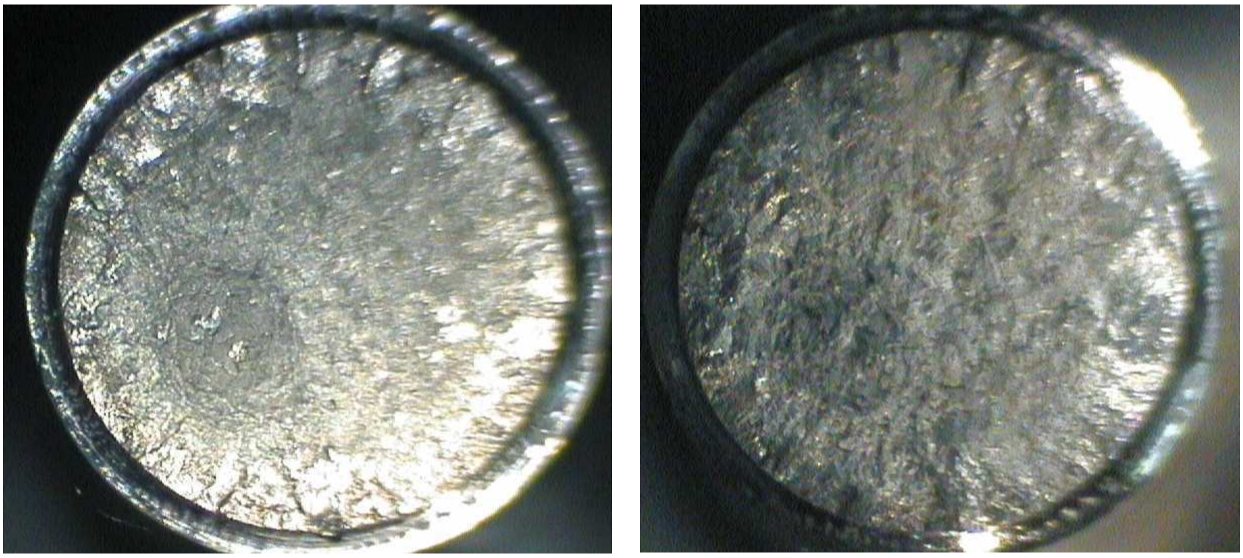

(351 MPa;727 MPa local stress; 59196 cycles to failure)
***N1**: illustration of the metal structure of the fracture surface from stereo Microscope*

(317 MPa;655 MPa local stress;110617 cycles to failure)
***M2**: illustration of the metal structure of the fracture surface from stereo Microscope*

(351 MPa;727 MPa local stress; 87978 cycles to failure)
***M1**: illustration of the metal structure of the fracture surface from stereo Microscope*

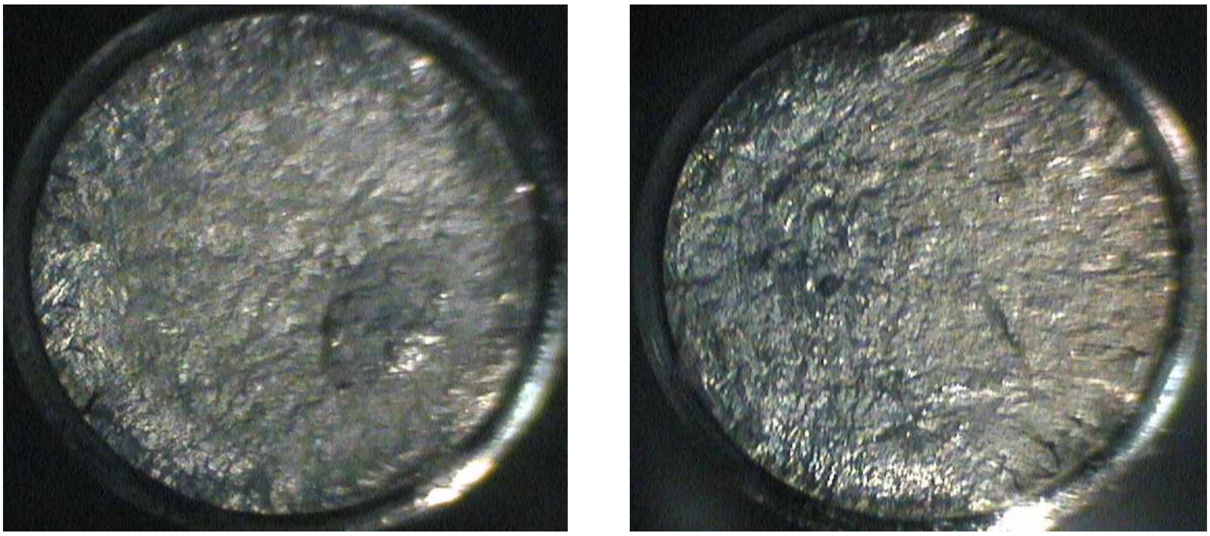

(317 MPa;655 MPa local stress; 283659 cycles to failure)
***R1**: illustration of the metal structure of the fracture surface from stereo Microscope*

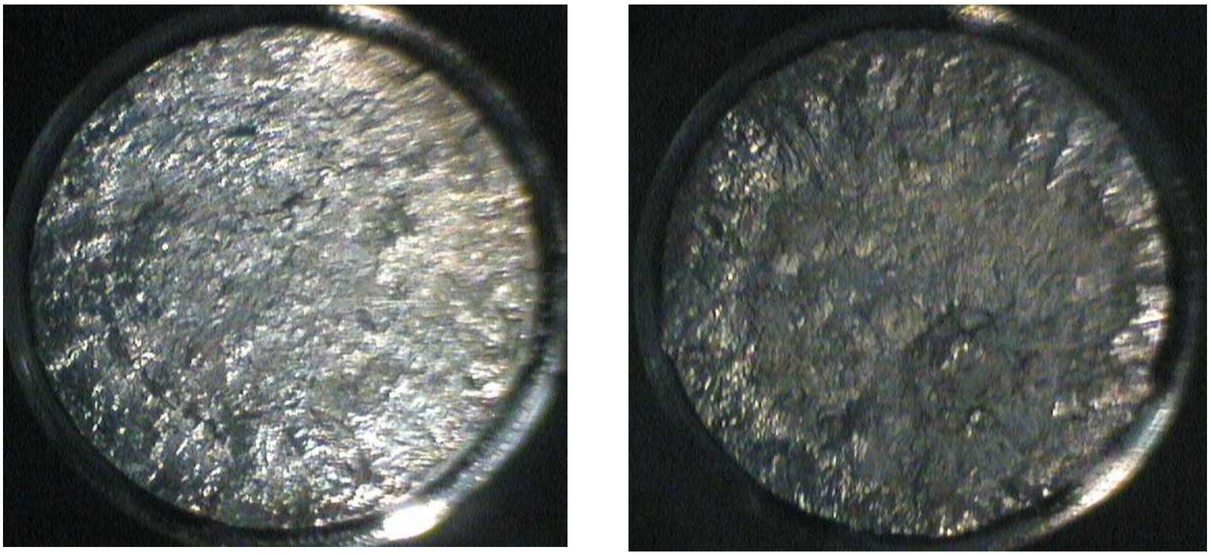

(298 MPa;616 MPa local stress; 278772 cycles to failure)
***Q2**: illustration of the metal structure of the fracture surface from stereo Microscope*

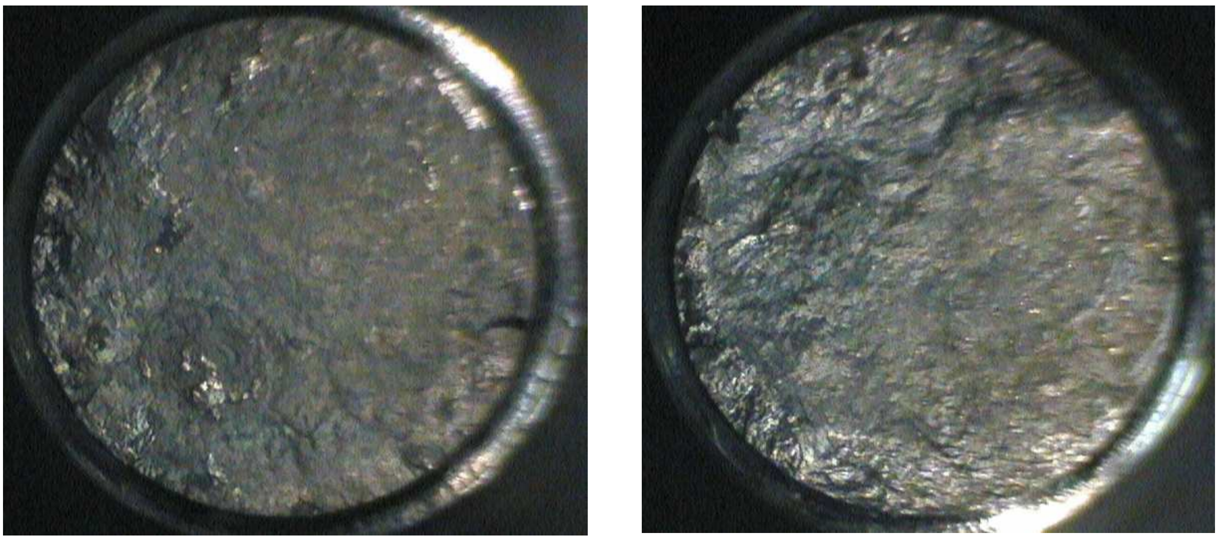

(260 MPa;537 MPa local stress;1035380 cycles to failure)
***T1**: illustration of the metal structure of the fracture surface from stereo Microscope*

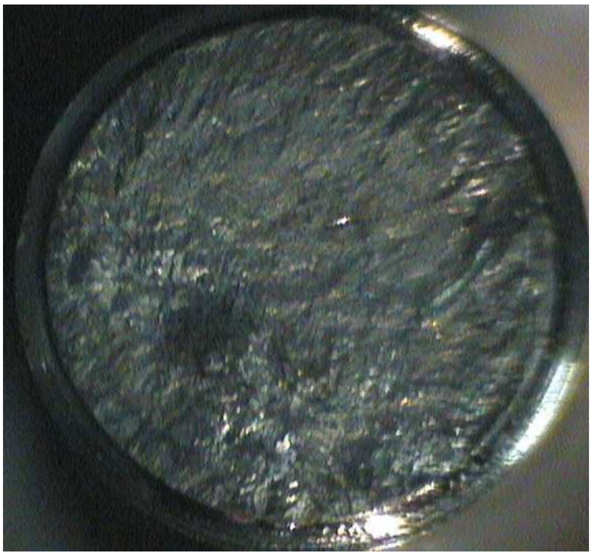
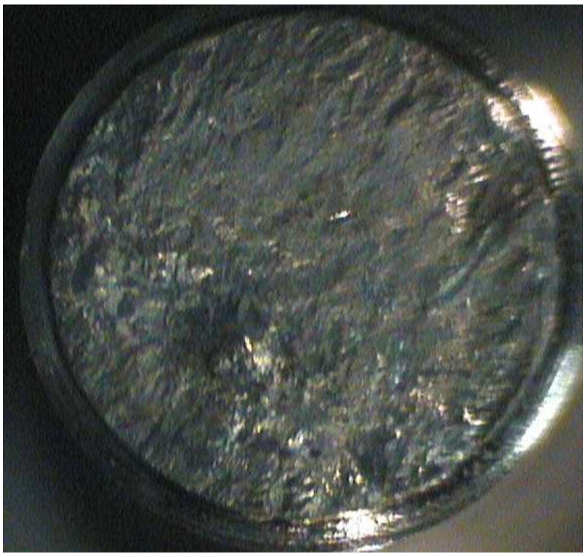

(279 MPa;577 MPa local stress; 304906 cycles to failure)
***R2**: illustration of the metal structure of the fracture surface from stereo Microscope*

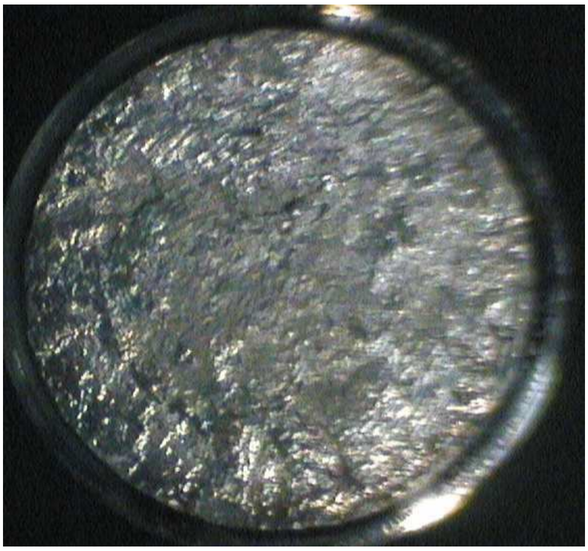


(298 MPa;616 MPa local stress; 247825 cycles to failure)
***Q1**: illustration of the metal structure of the fracture surface from stereo Microscope*